Direct Search for Dark Matter with the DarkSide Experiment

Paolo Agnes

UNIVERSITÉ SORBONNE PARIS CITÉ

Thèse préparée

à l' UNIVERSITÉ PARIS DIDEROT

ÉCOLE DOCTORALE STEP'UP — ED N°560

Laboratoire Astro-Particules et Cosmologie

Direct Search for Dark Matter with the DarkSide Experiment

par

Paolo Agnes

Thèse de doctorat de Sciences de la Terre et de l'Environnement
dirigée par Pr Alessandra Tonazzo et Dr Davide Franco
présentée et soutenue publiquement le
30 Septembre 2016
devant un jury composé de:

Alessandra Tonazzo	Directrice de thèse
Professeur (Université Paris Diderot)	
Davide Franco	Directeur de thèse
Chargé de recherche (CNRS - APC)	
Stavros Katsanevas	Président du jury
Professeur (Université Paris Diderot)	
Corinne Augier	Rapporteur
Professeur (Université Claude Bernard Lyon 1)	
Marco Selvi	Rapporteur
Professeur adjoint (Bologna University)	
Cristiano Galbiati	Examinateur
Professeur (Princeton University)	
Andrea Giuliani	Examinateur
Directeur de recherche (CNRS - CSNSM)	

Acknowledgements

I would like to express my sincere gratitude to all the members of the thesis committee, in particular to Corinne Augier and Marco Selvi, who attentively read the manuscript and provided precious comments for its improvement. Thanks to the president of the jury and director of the APC Laboratory, Stavros Katsanevas, and to Andrea Giuliani and Cristiano Galbiati for the motivation and support they offered me in several circumstances.

I am particularly grateful to Alessandra: she firstly welcomed me at the APC as a *stagiare* and I probably wouldn't have had the opportunity to come here for my PhD otherwise. I appreciated every discussion with her, she was always straight to the point and she gave me valuable advice for my thesis, teaching matters and future perspectives.

A huge thanks to Davide, who patiently followed me on a day-by-day basis and from whom I learned so much. Many of the results discussed in this work originated from the fruitful discussions with him and his guidance. I am grateful for the time he spent with me, transmitting his passion for this job, teaching me the right way of doing it and for always putting me under ~~a high~~ the correct level of pressure.

I would like to thank the members of the DarkSide Collaboration for the continuous exchange and dedication with which they all are contributing to this experiment's success. I am glad to be part of this great environment, it is a perfect one for a young physicist to grow in and develop his or her expertise.

Thanks to members of the *Neutrinos* group of the APC, to the office mates and to the small (not so small) Italian colony of the lab, for making the work place so welcoming.

I feel I owe a lot to my parisian friends. Either we met many years ago or in the recent months, either we lived together or we meet to have (many) beers, you made me really enjoy my time in Paris. Many already left and others will leave soon, I wish them to always be able to find their *petit club* :) .

Grazie ai delicatissimi amichetti pavesi. Non riuscirei a fare a meno della sensazione di sentirmi a casa ogni volta che ci vediamo, ovunque ci vediamo.

Grazie ai miei genitori, che mi hanno sempre dato con fiducia e generosità tutto ciò di cui potessi aver bisogno, e anche di più.

E infine grazie a Elena, per l'enorme supporto che mi ha offerto negli ultimi anni. E soprattutto congratulazioni: i tuoi successi mi rendono orgoglioso e rappresentano una motivazione aggiuntiva a fare sempre meglio!

Abstract

French version

L'Univers est principalement constitué d'un ensemble d'éléments non baryoniques et non lumineux appelé la matière noire. L'un des candidats actuellement favorisés est une particule massive interagissant faiblement avec la matière ordinaire (WIMP) issue du Big Bang. Le programme DarkSide vise à la détection directe de WIMPs à l'aide d'une chambre à projection temporelle utilisant de l'argon liquide en double phase. La première étape de l'expérience, DarkSide-50 (46 ± 0,7 kg de masse active) est en cours d'exécution. Une première campagne, avec un remplissage d'argon atmosphérique(AAr), a produit la meilleure limite sur la section efficace WIMP-nucleon jamais obtenue par une expérience à base d'argon. La deuxième phase, avec un remplissage d'argon souterrain (UAr, appauvri en ^{39}Ar), représente une étape importante vers la construction de DarkSide-20k, une expérience à bas bruit de fond avec une masse fiducielle de 20 t. Ce travail est principalement consacré à la description de la simulation Monte Carlo de DarkSide (G4DS), et à ses applications. G4DS, basé sur GEANT4, fournit la description géométrique de chaque détecteur du programme DarkSide ; il a été calibré afin de reproduire la réponse de DarkSide-50 avec une précision de l'ordre de 1% et intègre un modèle spécifiquement développé pour la description des mécanismes d'ionisation et de scintillation dans l'argon liquide, étalonné sur des données expérimentales. Les principales applications de la simulation comprennent l'estimation du bruit de fond dû aux neutrons et gammas pour DarkSide-50, la mesure du facteur d'appauvrissement de l'^{39}Ar en UAr par rapport à l'AAr et les études de conception pour DarkSide-20k.

Abstract

English version

A wide range of observational evidence suggests that the matter content of the Universe is dominated by a non-baryonic and non-luminous component: dark matter. One of the most favoured candidate for dark matter is a big-bang relic population of Weakly Interacting Massive Particles (WIMPs). The DarkSide program aims to the direct detection of WIMPs with a dual-phase liquid argon TPC and a background free exposure. The first phase of the experiment, DarkSide-50, is running since Oct 2013 and has (46 ± 0.7) kg active mass. A first run, with an atmospheric argon fill (AAr), provided the most sensitive limit ever obtained by an argon-based experiment. The current run, with an underground argon fill (UAr, depleted in ^{39}Ar), represents a milestone towards the construction of DarkSide-20k, a low-background dual-phase TPC with a fiducial mass of 20 t. This work is been mainly devoted to the description of G4DS, the DarkSide Monte Carlo simulation, and to its applications. G4DS is a GEANT4-based simulation, it provides the geometry description of each detector of the DarkSide program, it is tuned to reproduce the DarkSide-50 response at the percent level and incorporates a custom model for ionisation and scintillation mechanisms in liquid argon, tuned on real data. The principal applications of the simulation include the estimate of the neutron and gamma backgrounds for DarkSide-50, the measurement of the ^{39}Ar depletion factor in UAr with respect to AAr and the design studies for DarkSide-20k.

Table of contents

Introduction

It is now widely known that the matter content of the Universe is dominated but by a non-luminous and non-baryonic component: dark matter. Several direct and indirect observations, ranging from the studies of the internal motions of galaxies, to the large scale inhomogeneities in the cosmic microwave background radiation, support this conclusion. However, we are still lacking the answer to one of the most important open question in fundamental physics: what is the precise nature of this matter?

One possibility for the dark matter, motivated by considerations in elementary particle physics and cosmology, is that it consists of as-yet undiscovered elementary Weakly Interacting Massive Particles (WIMPs). WIMPs are distributed such that a dark matter halo is pervading our galaxy, and the motion of the Earth within the halo should result in WIMP-nucleus elastic interactions of sufficient energy to be detected directly by a ground based sensitive detector. Such a detector must be designed to have low energy detection threshold (a typical nuclear recoil is expected to deposit ≤ 100 keV), large active mass (the current limit on the WIMP-nucleon cross section is 1.1×10^{-46} cm^2 for a 50 GeV/c^2 WIMP [1]) and a strong background suppression.

Noble liquids are particularly suited for this kind of search because of their high ionization and scintillation yields and scalability to large masses. Liquid argon offers in addition to this a spectacular discrimination of the electron recoils background (up to a factor 10^8 [2]) based on the time profile of the scintillation pulse. The DarkSide Collaboration is carrying out a direct WIMP search program, through a staged approach, using a dual-phase Liquid Argon Time Projection Chamber (LAr TPC) and an active Liquid Scintillator Veto (LSV).

The current phase of the experiment, DarkSide-50, is running at *Laboratori Nazionali del Gran Sasso* (LNGS, in Italy) since October 2013 and produced the first physics results [3, 4]. Because of the reduced dimension of the detector (the active mass is $\sim$ 50 kg), DarkSide-50 is not sensitive enough to improve the current limit on the WIMP-nucleon cross section, but the recent null result is the most sensitive background-free search ever performed with a liquid argon target. Moreover, it is the first limit ever obtained with an underground argon fill (which is depleted in ^{39}Ar with respect to the atmospheric argon). Since the ^{39}Ar contamination in atmospheric argon is currently the major limitation to the size of a large argon TPC, the procurement of underground depleted argon represents a milestone towards

the construction of DarkSide-20k, the next phase detector, with a fiducial mass of 20 t and planned to reach an exposure of 100 t y.

My involvement in the DarkSide project have been mainly related to the simulation. After a preliminary discussion on the dark matter physics (Chapter 1) and on the DarkSide-50 experiment (Chapter 2), I will introduce, in Chapter 3, G4DS, the DarkSide simulation tool. G4DS incorporates the full simulation chain from the fundamental physics (based on GEANT4) to the electronics response. We devoted particular attention to the tuning at the %-level of the TPC response and veto systems and developed a custom model for the description of the scintillation and ionization mechanisms in liquid argon (called PARIS: Precision Argon Recoil Ionization and Scintillation).

Chapter 4 contains two MC-based studies of the neutron and electron recoil backgrounds for DarkSide-50. For the first result, we developed a machine for the production and propagation of (α, n) radiogenic neutrons within the DarkSide-50 geometry. Neutrons are the most dangerous background for a direct WIMP search detector, since they can mimic a WIMP-induced nuclear recoil, but their interactions in the sensitive volume can be rejected by looking at the energy depositions in the LSV. We established the expected neutron rate for a given exposure and estimated the veto efficiency to tag them. For the electron recoil background study we simulated the β and γ radioactivity naturally present in all the detector components. The major outcome of this study is the measurement of the ^{39}Ar depletion factor in underground argon.

I discuss in Chapter 5 about the pulse shape discrimination in liquid argon. Nuclear and electron recoils can be easily separated at high energy, but the two populations overlap at low energy (< 20 keV$_{ee}$). In particular I propose a model for the determination of the electron recoil leakage in the nuclear recoil expectation region.

In Chapter 6 I describe two results based on G4DS simulations and related to the next phases of the DarkSide program. The first one concerns the design of the DarkSide-20k experimental setup: we demonstrated that without a liquid scintillator sphere around the TPC cryostat it is impossible to obtain a background-free exposure. The last part of this Chapter is dedicated to the foreseen Argo experiment, the ultimate liquid argon TPC, with active (fiducial) mass of 300 t (100 t). I will not present the sensitivity to WIMPs of such a detector, but I will focus on the solar neutrino physics potential.

Chapter 1

Searching for Dark Matter

For the first time in 1933, Zwicky discovered that a significant fraction of the mass content of a massive objects cluster is not luminous baryonic matter. He selected a sample of 8 galaxies in the Coma Cluster, a cluster containing more than 1000 objects, 99 Mpc away from the Milky Way [5]. He found that the amount of luminous matter was not enough to justify the velocity dispersion of those galaxies around the center. This discovery turned out to be one of the most profound scientific insights of the 20th century.

In this Chapter I will list and briefly discuss the subsequent observations that contributed to establishing our (partial) knowledge of dark matter properties. I will then introduce the dark matter particle candidates, focusing on the most favored one: the Weakly Interacting Massive Particle (WIMP). In the last part I will present the current status of the search for WIMPs.

1.1 Evidence for Dark Matter

1.1.0.1 Velocity Dispersion

One of the most convincing evidence of the existence of dark matter comes from the study of velocity dispersion curves. The study firstly done by Zwicky was repeated for other galaxies and in the Milky Way [6, 7]. The rotational velocity v of an object orbiting at distance r around the galaxy center scales like $v(r) \propto \sqrt{M(r)/r}$, where $M(r)$ is the mass inside the orbit. For distant objects, with r extending outside the visible part of the galaxy, the distribution of velocities is expected to decrease like $v(r) \propto \sqrt{1/r}$. However, the velocity dispersion appears to be constant in many spiral galaxies like the Milky Way.

The tension can be solved assuming the existence of a dark matter halo with mass density $\rho(r) \propto 1/r^2$. This density is expected to drop faster at some unknown large radius, in order to keep finite the amount of dark matter included at large radii. To date, the density profile of dark matter halos is still under debate.

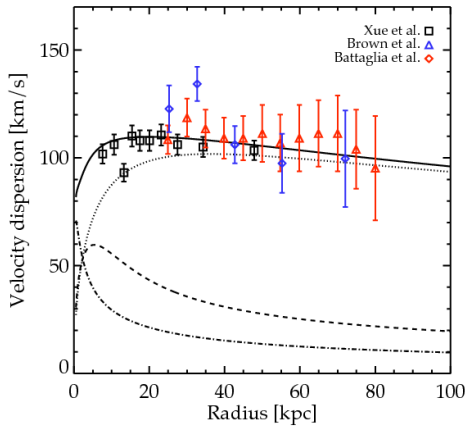

Fig. 1.1 Velocity dispersion versus distance from the galactic center in the Milky Way. The dot-dashed curve is the predicted velocity dispersion from the bulge potential, the dashed curve is from the disk potential, and the dotted curve is from the dark matter halo. The solid curve is the sum of all three components. The velocity dispersion is assumed to be isotropic. See ref. [8] for more details.

Figure 1.1 shows the comparison between the velocity dispersion measurements from three different observation samples of Milky Way stars and a model which describes the contributions of three matter components (the matter bulge and disk, and the dark matter halo [8]).

1.1.0.2 The Bullet Cluster

The bullet cluster consists in a system of two galaxy clusters that recently (on cosmological time-scale) collided. Figure 1.2 shows one optical and one X-ray picture of the clusters. The optical image is dominated by the galaxies, while the X-ray image indicates the current position of gas clouds, heated because of the collision. The gravitational potential contours (measured by gravitational lensing) are drawn in green on the two pictures. The 8σ shift [9] between the barycenter of gravitational potential and the hot gas distributions can be interpreted assuming that the original clusters included galaxies, gas clouds and dark matter and that they were moving towards each other. While the baryonic matter (hot gas clouds) slows down and gets heated because of mutual interaction, the dark matter clusters, constituting most of the mass of the clusters, go through each other.

From theoretical models and hydrodynamics simulations it is possible to set a limit for the self-interaction cross section (σ_{SI}) of dark matter [10]:

$$\frac{\sigma_{SI}}{m_\chi} < 1.25\ \mathrm{cm}^2\mathrm{g}^{-1}$$

where m_χ denotes the mass of the dark matter particle. The uncertainty on this limit is large and it depends on the hypotheses on the ratio between luminous and dark matter and on the collision model. Nonetheless, it is consistent with other measurements (e.g. [11]).

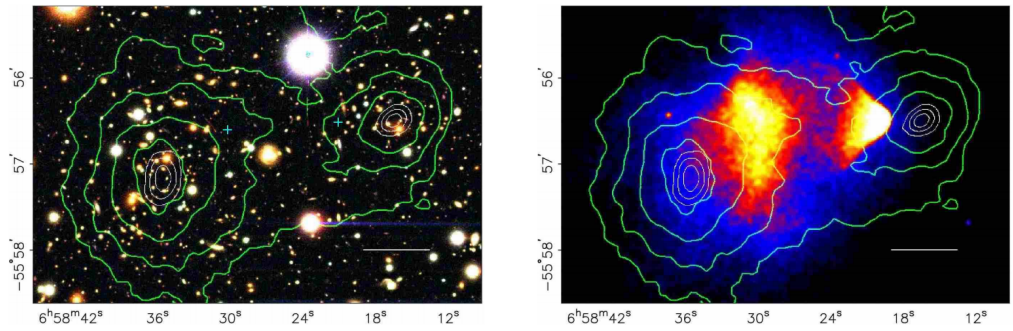

Fig. 1.2 The bullet cluster: optical image taken with the Magellan telescope (left) and X rays image taken with Chandra. In both the pictures, the gravitational potential contours, calculated using the gravitational lensing, are drawn in green. See ref. [9] for more details.

1.1.1 Cosmological Proofs

As soon as large hydrodynamics simulations of structures formation in the Universe were available, it appeared clear that dark matter must be non-relativistic (cold). The current cosmological model, the Lambda Cold Dark Matter model (ΛCDM), is founded on the assumption that the Universe is homogeneous and isotropic (the cosmological principle) at large scale. Three terms contribute to the total energy density of the Universe ρ_T:

$$\rho_T = \rho_r + \rho_m + \rho_\Lambda$$

where ρ_r is the radiation density, ρ_m the matter density and ρ_Λ the dark energy density. Those quantities are usually given in terms of fraction of total density $\Omega_i = \rho_i/\rho_c$, being ρ_c the critical density, required for the universe to be flat and homogeneous.

The ΛCDM model has six free parameters. These parameters can be constrained by fitting the CMB (Cosmic Microwave Background), the relic diffuse black body emission at 2.726±0.010 K [12]) power spectrum. The PLANCK data have largely improved the resolution of the small (∼ 10 μK) anisotropies of the CMB [13]. Nonetheless, complementary observations are required to break the degeneracy between Ω_Λ and Ω_m.

The additional data comes for instance from the measurements of gravitational lensing, observations of distant supernovae and the discovery of baryon acoustic oscillations. I will briefly discuss these observations in what follows, as well as the BBN (the Big Bang Nucleosynthesis), which represents an independent method to separate the two contributions to Ω_m: the baryonic matter density Ω_b and the non-baryonic one Ω_c. The best estimates of the density fractions are then summarized in Table 1.1.

1.1.1.1 Distant Supernovae

Type Ia supernovae are originated from the thermonuclear disruption of carbon–oxygen white dwarfs. Since the white dwarfs are known to have uniformly a similar mass, the energy

Component	Symbol	Measurements
Photons	Ω_r	$\sim 5.46 \times 10^{-5}$
Dark Energy	Ω_Λ	0.6911 ± 0.0062
Matter Content	Ω_m	0.3089 ± 0.0062
Baryonic matter	Ω_b	0.0486 ± 0.00072
Non-baryonic matter	Ω_c	0.2589 ± 0.0041

Tab. 1.1 Measurements of cosmological parameters at 1σ. These values are obtained combining the PLANCK CMB data with external constraints from lensing, BAOs and SNe and assuming the standard ΛCDM model with six free parameters [13].

output of type Ia supernovae is roughly constant and they can be used as standard candles and efficient distant indicators. From the SNe data alone, fitting the relation between distance and redshift, it is possible to constraint the ratio between the matter and dark energy density. A recent work, performed on a sample of 740 spectroscopically confirmed SNe Ia with redshift z between 0.01 and 1.2, reports $\Omega_m = 0.295 \pm 0.034$ (stat+sym) as described in [14].

Combining the SNe data with the CMB data, it is possible to constrain the baryonic contribution to Ω_m.

1.1.1.2 Gravitational Lensing

The mass profile of galaxy centers or galaxy clusters can be measured by looking at the gravitational lensing distortions, as reviewed in [15]. One can distinguish the strong and the weak lensing regime. The strong lensing takes place when the light from a bright source is passing by a massive object and arrives at the observer traveling along multiple paths, deflected by large angles. The strength of the deflection is proportional to the square root of object mass.

Most of the light visible from the Earth is not affected by strong lensing. On the contrary, massive objects can deflect the light propagation from distant sources along the line of sight by a small amount, so that the image of the distant galaxies is distorted. The effect is not measurable on the single source, but galaxies along adjacent lines of sight are sheared by similar amount. By means of a convolution, the shear field is converted to a map of the mass distribution along the line of sight.

The analysis of the mass distribution in galaxy clusters shows that the baryonic matter is not enough to account for all the matter content of the clusters.

1.1.1.3 Baryon Acoustic Oscillations

Before photon decoupling form baryons, the CMB anisotropies supported the expansion of baryon clusters, because of radiation pressure. When the local density drops, because of the expansion, photons decouple from baryons and baryons are free to collapse. The baryonic matter gravitational collapse produces an expansion shock-wave, which gives

birth to typical large scale (150 Mpc) acoustic oscillation patterns in the baryonic matter distribution [16]. The typical amplitude of the first oscillation peak is small when compared to the CMB anisotropies, but the identification and the fit of the acoustic peak provide an independent constraint of cosmological parameters such as the dark matter content of the Universe.

1.1.1.4 Big Bang Nucleosynthesis

The current abundancies of light elements in the Universe can be effectively understood in terms of very well established Standard Model Physics. The agreement between prediction and observation spans over several orders of magnitude and provide strong constraint on the new physics beyond the Standard Model.

Until 1 s after the Big Bang, when $T \sim 1$ MeV, the weak interactions were in thermal equilibrium, fixing the ratio between proton and neutrons to $n/p = e^{-Q/T}$ where $Q = 1.293$ MeV is the neutron to proton mass difference. At the freeze-out temperature $T_{fr} \approx 1$ MeV the Universe expansion rate is larger than the neutron-proton conversion rate. The n/p ratio is then fixed to $(n/p)_{T_{fr}} = e^{-Q/T_{fr}} = 1/6$. Neutrons are free to decay (with half-life $\tau^n_{1/2} = 885.7 \pm 0.8$ s) until the nuclear reactions start and lead to nuclei formations. Their relative abundance decreases down to 1/7.

The first phase of the nuclei formation is dominated by a still high density of photons, which delays the deuterium production reaction $p(n,\gamma)$D. Only when the temperature drops below $T \approx 0.1$ MeV, nuclei can begin to form without being immediately photo-dissociated. The Big Bang nucleosynthesis stops roughly three minutes after the Big Bang, when the temperature is low enough to prevent nuclear fusion. Nearly all the neutrons are now bound in the lightest stable nucleus, the ^{4}He, leading to the relic mass fraction of ~ 0.25. The measured traces of deuterium (D/H = $(2.82 \pm 0.21) \times 10^{-5}$) and ^{7}Li (Li/H = $(1.7 \pm 0.06 \pm 0.44) \times 10^{-10}$) primordial mass fractions are in good agreement with the expectations.

Since the rates of the reactions mentioned above depend on the density of baryons, constraining the photon density from the CMB observations, one can derive the baryonic fraction of the critical density [17],

$$\Omega_b = \frac{\rho_b}{\rho_c} = (0.021 \div 0.025)\ h^{-2} = (4.57 \div 5.44) \times 10^{-2} \tag{1.1}$$

for the present Hubble parameter $h = H_0/(100\ \text{km/s/Mpc}) = 0.6781 \pm 0.00092$ [13]. This range is in reasonable agreement with the one obtained from the CMB observations (including the mentioned constraints) discussed above in Table 1.1.

1.1.2 Dark Matter Halos

In picture derived so far, dark matter constitutes most of the mass of the Universe ($\sim$ 85%). The dark matter particle must be stable, non-relativistic and almost non-collisional, but of course subjected to gravity.

At small scale, as it happens for baryons, the dark matter distribution is highly non-uniform. The mass content of a galaxy is dominated by dark matter, believed to cluster in the form of halos around the center of the galaxy. Combining the observations with theoretical assumptions and simulations, it is possible to make predictions on the geometry and velocity distribution of dark matter particles within a dark matter halo surrounding a galaxy. The available data and N-body simulations of the universe history show that the dark matter halos also maintain a generally uniform structure.

The phase-space distribution $f(\boldsymbol{r}, \boldsymbol{v}, t)$ of a non-collisional self-gravitating fluid follows the Boltzmann equation [18]:

$$\frac{\partial f}{\partial t} + \boldsymbol{v} \cdot \nabla f - \nabla \phi \cdot \frac{\partial f}{\partial \boldsymbol{v}} = 0 \tag{1.2}$$

where ϕ is the gravitational potential. This potential must satisfy the Poisson equation, which depends on the dark matter density distribution $\rho(\boldsymbol{r})$:

$$\nabla^2 \phi = 4\pi G \rho(\boldsymbol{r}) = 4\pi G \int f(\boldsymbol{r}, \boldsymbol{v}, t_0) d^3 r \tag{1.3}$$

where t_0 stands for the current time.

A simple solution to the Boltzmann equation, for a spherical dark matter density profile $\rho(r) \propto 1/r^2$ and isotropic velocity dispersion, is the following Maxwell-Boltzmann distribution:

$$f(\boldsymbol{v}) = \left(\frac{3}{2\pi\sigma_v^2}\right)^{3/2} \exp\left(-\frac{3\boldsymbol{v}^2}{2\sigma_v^2}\right) \tag{1.4}$$

where σ_v is the WIMP velocity dispersion in the halo. The most probable speed is $v_0 = \sqrt{2/3}\sigma_v$ and the average speed is $2v_0/\sqrt{\pi}$.

1.1.2.1 The Standard Dark Matter Halo Model

There is no strong evidence that the above hypotheses are realized in the Milky Way, but the described model can be applied to define the standard dark matter halo model, describing the halo properties in the Solar System vicinity. This will be particularly useful in future applications.

In a first approximation, the halo is believed to be static. This assumption is founded on the non-collisional nature of dark matter particles and it is confirmed by the results of the N-body simulation described in [19]. According to this simulation, the dominant component ($\sim$ 75%) of the dark matter tangential velocity distribution is centered around

0. This means that the bulk component of the WIMP motion relative to an observer on the Earth is dominated by the motion of the observer.

The velocity of the observer $\boldsymbol{v_{obs}}$ can be parameterized as:

$$\boldsymbol{v_{obs}}(t) = \boldsymbol{v_{\odot}} + \boldsymbol{v_E}(t) \tag{1.5}$$

where $\boldsymbol{v_{\odot}}$ is the speed of the Sun with respect to the stationary halo and $\boldsymbol{v_E}$ the relative motion of the Earth with respect to the Sun. The Sun is orbiting around the center of the Milky Way at a speed of 254 ± 16 km/s towards the Cygnus constellation at a radius $R_{\odot} = 8.4 \pm 0.6$ kpc from the center of the galaxy [20].

In the traditional description, the motion of the Sun is composed by the sum of the Local Standard of Rest velocity $v_{LSR} = (0, 220, 0)$ km/s in the galactic frame reference and the Sun peculiar velocity $v_{\odot,pec} = (10, 13, 7)$ km/s with respect to the LSR [21]. The average velocity of the Earth can be approximated by the Sun velocity (~ 232 km/s), but the Earth is orbiting around the Sun at a speed of 29.9 km/s. The orbit around the Sun induce a modulation in the relative speed of the Earth-halo system, that will be discussed in Sect. 1.2.2.

For the numerical applications, the standard halo model parameters are:

- $\boldsymbol{\rho_0 = 0.3\ \mathrm{GeV/c^2/cm^3}}$**.** This is the mean value usually adopted in particle astrophysics for the local dark matter halo density [22]. A detailed comparison of different measurements is reported in [23].

- $\boldsymbol{v_0 = 220\ \mathrm{km/s}}$**.** The traditional value measured for the Sun orbital velocity is taken as a reference for the galactic circular speed. The underlying assumption is that at the Sun distance the rotational curve has already reached the asymptotic value.

- $\boldsymbol{\sigma_v = \sqrt{3/2}\, v_0 \simeq 270\ \mathrm{km/s}}$. In the assumption of isotropic velocity distribution, the velocity dispersion is related to the rotational speed of the galaxy around its center. The local circular speed and the peak speed are also considered identical [24].

- $\boldsymbol{v_{esc} \lesssim \infty}$**.** The escape velocity v_{esc} is the minimum velocity needed in the galactic reference frame to escape the gravitational attraction. The 90% CL interval for the escape velocity is 498 km/s $< v_{esc} <$ 608 km/s, with a most probable value of 544 km/s [25]. For the Maxwell-Boltzmann velocity distribution with the parameters described above, the fraction of WIMPS with velocity larger than 544 km/s is less than 1%.

1.1.3 Dark Matter Candidates

The observations mentioned above are suggesting that $\sim 85\%$ of the total mass content of the Universe is made of non-relativistic dark matter. The dark matter particles must be stable (their lifetime must be larger than the age of Universe) and the self-interaction as well as the ordinary matter interaction cross sections are suppressed. A dark matter candidate must also satisfy the requirement of the correct relic abundance in the present Universe.

Many models of physics beyond the Standard Model are currently predicting a particle with the required properties, and so far none of them is confirmed by observations. Some of the most motivated candidates from both cosmology and particle physics are listed below.

1.1.3.1 Sterile Neutrinos.

It is well established that the SM fails in predicting the neutrino masses. A possible expansion of the Standard Model which allows to solve this problem consists in adding one or three generations of sterile massive neutrinos. Sterile neutrinos would also be a natural explanation for the abundance of non-baryonic matter in the Universe. They would be detectable through their (tiny) mixing with active neutrinos. No theory can predict their exact mass scale but the keV range is not excluded by cosmological constraints (mainly limits from the Lyman-α forest data). Such a light dark matter particle would be relativistic and can not account for all the cold dark matter content of the Universe. For a more detailed discussion, refer to [26].

The 3.55 keV excess found in X-rays spectra from nearby galaxy clusters [27] can for instance be interpreted as due to the decay of a $\simeq 7.1$ keV dark matter particle, namely a sterile neutrino, through the reaction $\nu_s \rightarrow \nu + \gamma$. The mixing angle with active species would be in the range $\sin^2\theta_s = (5.5 \div 50) \times 10^{-12}$ [28]. The significance of this peak must be confronted with the uncertainty on the background models. Moreover, spatial origin of this line do not match with the expectations. In any case, even accepting this excess as a dark matter decay signal would exclude most of the possible sterile neutrinos production mechanisms [29].

A massive sterile neutrino is also appealing because, thanks to the see-saw mechanism, it would bring to a sub-eV mass scale for active states.

1.1.3.2 Axions.

Axions are light neutral pseudoscalar bosons that couple weakly to normal matter and radiation. They can be massive if there is a small explicit symmetry breaking, either already in the Lagrangian or due to quantum effects such as anomalies. Their coupling to Standard-Model particles is suppressed by the energy scale that characterizes the symmetry breaking. For a more detailed review refer to [30].

Axions are of particular interest because the Peccei-Quinn (PQ) mechanism remains perhaps the most credible scheme to allow the CP conservation in QCD. Even if no CP violation is observed in QCD, a CP violating term appears in the QCD Lagrangian and the mentioned PQ mechanism is an elegant solution for the suppression of this term.

Axions also represent a good candidate for the cold dark matter of the universe. While a thermally produced axion population would be too hot, the Misalignment Mechanism can lead to the production of cold dark matter [31]. Nonetheless, the ory doesn't predict the mass scale of axions. Masses of the order of μeV are excluded by the constraint on the relic density from the ΛCDM cosmological paradigm. Masses larger than 1 eV are instead disfavored by

other observations. Many experiments are currently being designed and realized to explore the meV mass range.

1.1.3.3 WIMPS.

Postulating a broad class of Weakly Interactive Massive Particles is particularly interesting because they would naturally have the correct relic density if produced during the Big Bang. This feature is referred to as the WIMP miracle and it will be described below. The weak interaction makes WIMPs detectable through non gravitational methods. The Standard Model does not predict such a particle, but the introduction of a new one with mass at the weak scale ($m_{weak} \sim 10$ GeV $\div$ 1 TeV) would also justify the mass of the Higgs boson to be smaller than the Planck mass [32] (solving the so called gauge hierarchy problem).

These arguments are very strong and made WIMPs the paradigmatic and most studied dark matter particle candidate.

1.1.4 The WIMP miracle

The current dark matter population may have been produced in the early Universe as a thermal relic of the Big Bang. After the Big Bang in fact, the Universe is dense and hot and all the particles are at the rmal equilibrium (the annihilation rate is equal to the production rate):

$$\chi + \overline{\chi} \rightleftharpoons X + \overline{X}.$$

When the temperature T drops below the dark matter particle mass m_χ, the production rate is suppressed and the number of dark matter particles drops exponentially as $e^{-m_\chi/T}$. In addition to the cooling, the Universe is also expanding: the dark matter particle gas becomes so diluted that the annihilation rate becomes negligible. This "freeze out" process implies that the number density of dark matter particles approaches asymptotically the rmal relic density.

The evolution of a WIMP thermal relic's number density n, shown in Figure 1.3, is quantitatively described by the Boltzmann equation:

$$\frac{dn}{dt} = -3Hn - \langle \sigma_A v \rangle \left(n^2 - n_{eq}^2 \right) \tag{1.6}$$

where H is the Hubble expansion rate of the Universe,[1] $\langle \sigma_A v \rangle$ represents the WIMP effective annihilation cross section and n_{eq} is the WIMPs density at the equilibrium.

[1] $H = \dot{a}/a$, where $a(t)$ is the scale factor for a distance $d(t)$ with respect to its value at the Big Bang d_0: $d(t) = a(t)d_0$.

For a rough analysis [32] we can define the freeze out to be the time when $n\langle\sigma_A v\rangle = H$. The solution of the equation gives the relic density at the freeze out n_f:

$$n_f \sim \left(m_\chi T_f\right)^{3/2} e^{-m_\chi/T_f} \sim \frac{T_f^2}{M_{Pl}\langle\sigma_A v\rangle} \tag{1.7}$$

where T_f is the freeze out temperature and M_{Pl} the Planck mass. It has to be noted that in the exponential part the ratio $x_f \equiv m_\chi/T_F$ is independent of dark matter particles properties. The typical expected value is $x_f \approx 20$.

the rmal relic density assumes the form:

$$\Omega_\chi h^2 = \frac{m_\chi n_0}{\rho_c} = \frac{m_\chi T_0^3}{\rho_c}\frac{n_0}{T_0^3} \sim \frac{m_\chi T_0^3}{\rho_c}\frac{n_f}{T_f^3} \sim \frac{x_f T_0^3}{\rho_c M_{Pl}}\langle\sigma_A v\rangle^{-1} \tag{1.8}$$

where h is the reduced Hubble constant,[2] n_0 and T_0 are the present day number density and temperature. This expression is remarkably independent of the mass of the dark matter particle. The numerical calculation of the last term brings to

$$\Omega_\chi h^2 \simeq \frac{\left(3\times10^{-27}\right)\ \mathrm{cm^3 s^{-1}}}{\langle\sigma_A v\rangle}. \tag{1.9}$$

The above equation can be inverted to get the expected scale of the dark matter annihilation cross section:

$$\langle\sigma_A v\rangle \simeq \frac{\left(3\times10^{-27}\right)\ \mathrm{cm^3 s^{-1}}}{\Omega_\chi h^2} \simeq 2.5\times10^{-26}\ \mathrm{cm^3 s^{-1}}. \tag{1.10}$$

The above value is extremely close to the typical weak interaction cross section σ_{weak}, defined as:

$$\sigma_W \simeq \frac{\alpha_{weak}^2}{m_W^2} \simeq \left(1.5\times10^{-26}\right)\ \mathrm{cm^3 s^{-1}} \tag{1.11}$$

where $\alpha_{weak} \simeq 0.01$ is the weak coupling constant and m_W the mass of the $W^\pm$ boson. This homology suggests that a dark matter particle candidate could interact by means of the weak force. This coincidence is often referred to as **the WIMP miracle**: a Big Bang relic population of weakly interacting particles, with mass in the 10 GeV - TeV range, would naturally have the correct present density. Moreover, as already mentioned, the introduction of a new particle at the m_{weak} scale still represent an elegant way to solve the gauge hierarchy problem.

As for the weak interaction, in many theories it is only the mass scale that sets the annihilation cross section. The cross section of equation (1.10) can be parameterized as follows:

$$\sigma_A v = k\frac{g_{weak}^4}{16\pi^2 m_\chi^2} \times \left(1\ \mathrm{OR}\ v^2\right) \tag{1.12}$$

[2] The Hubble constant in units of 100 km.s^{-1}.Mpc^{-1}.

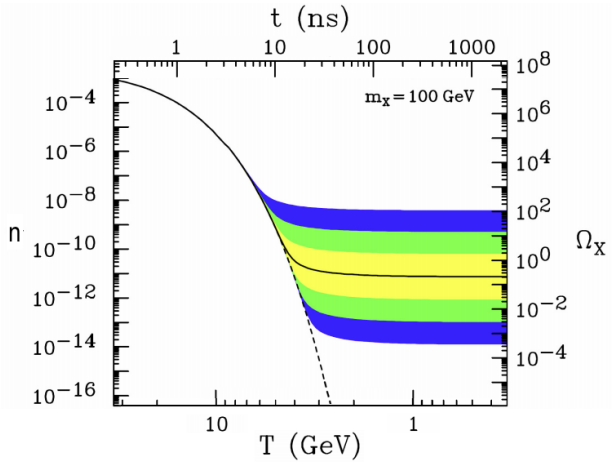

Fig. 1.3 Comoving density n and the resulting relic density Ω_χ for a 100 GeV WIMP as a function of temperature T and time t (p-wave annihilation assumed). The density decreases exponentially until the *freeze out* ouccurs. The solid contour corresponds to the annihilation cross section which leads to the correct relic density. Color regions are for cross sections that differ 10, 100 and 1000 times from this value. Picture extracted from [32].

where $g_{weak} \simeq 0.65$ is the weak gauge coupling and k a factor to accounting for deviations from the estimate. In the second term, the factor v^2 is present (absent) in case of p-wave (s-wave) annihilation. If the p-wave is suppressed, the annihilation cross section $\langle \sigma_A v \rangle$ is energy independent.

1.1.5 Supersymmetric WIMPs and Detection Principles

The Supersymmetry (SUSY) [33] is a theory proposed to solve the gauge hierarchy problem and to allow the gauge unification at high energy. It is a particularly interesting theory for the dark matter physics, because it naturally predicts a stable GeV-TeV particle.

According to the MSSM (the Minimal SUSY Standard Model), it exists a super-symmetric fermion (boson) partner for each boson (fermion). The symmetry must be broken, otherwise the SM particle and their partners would have the same mass. A new parity has to be introduced, in order to suppress the decays of SM particles through vertexes that involve super-symmetric partners (for example the proton decay: $p \rightarrow \pi^0 e^+$). The R parity can be defined as:

$$R = (-1)^{3(B-L)+2S}$$

where B and L are the baryonic and leptonic number and S the spin. The value of R is 1 for SM particles and -1 for their super-symmetric partners. The conservation of this number prevents a super-symmetric particle to decay into SM products, implying that the lightest SUSY particle (LSP) is stable.

In the MSSM, the LSP is the lightest neutralinos χ_1^0. The four neutralinos χ_i^0 (ordered by increasing masses) are linear combinations of the higgsino (the superpartner of the Higgs boson), the bino (the superpartner of the U(1) gauge field corresponding to weak hypercharge) and the winos (the superpartners of the W bosons).

The neutralino is a stable Majorana particle, with no electric or color charge, with a mass in the range GeV $< m_\chi <$ TeV. These properties make it a good WIMP candidate. The MSSM, is a theory with $\sim$ 100 free parameters. However, some constrained scenarios, where the

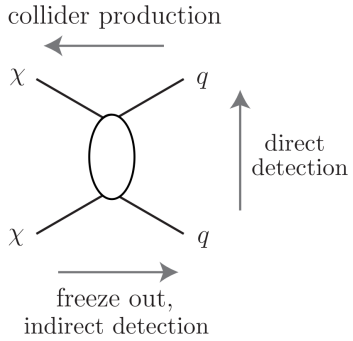

Fig. 1.4 Schematic Feynman diagram of possible dark matter detection principles. From right to left: production at colliders; from bottom to top: direct detection via elastic scattering on nuclei; from left to right: indirect detection through identification of decay products. Picture extracted from [34].

number of free parameters is reduced are possible and provide specific predictions for WIMP mass and interaction cross section. Two examples are the cMSSM (the constrained MSSM) and the pMSSM (the phenomenological MSSM). The first model, the simplest, with only 5 free parameters, has become disfavored after the recent experimental evidence. The pMSSM model is based on some experimentally motivated assumptions (as the R-parity conservation and the absence of new CP violations) and it allows to reduce the number of free parameters number down to 19.

As another possibility, in the case when the mass of the interaction mediator or the mass of the WIMP is much larger than the weak scale, even simpler theories are available. These so called effective theories don't require the scan through multidimensional parameter spaces, at the cost of a less complete information obtained with a model-dependent dedicated analysis.

WIMPs can in principle be detected in different ways, as summarized in Figure 1.4.

The direct detection channel, exploiting the elastic scattering of WIMPs off ordinary nuclei will be discussed in the next section. In this section I will focus on the indirect detection and colliders production channels: if the annihilation of WIMPs has SM particles in the final state, it is possible to measure the WIMP coupling to SM particles by looking at the annihilation products; additionally, it would be possible to produce WIMPs in colliders though the inverse reaction.

1.1.5.1 Indirect searches

If dark matter particle decays or the self-annihilation of dark matter particles produces SM particles, some experiments could measure an unexpected signal. Such an excess is expected to come from region of the Universe where the local density of dark matter is higher, like the center of the Milky Way or the center of the Sun (where WIMPs could be gravitationally trapped). Three annihilation products are usually considered: (a) photons (in the X and γ energy range) (b) neutrinos and (c) anti-matter.

The X and γ astronomy offers the cleanest signature and the evidence for an excess peaked around m_χ (for the $\gamma\gamma$ and γZ channels) is often referred as "smoking gun". The Fermi-LAT collaboration reported in 2012 on a feature centered around 130 GeV in the

spectrum obtained looking at the center of the galaxy [35], which was later no more visible in extended data sample [36].

Another ~ GeV excess is found in the central region of the Milky Way γ-rays spectrum, but the interpretation as a WIMP annihilation signal is not exhaustive, because of the small intensity of the excess and the large uncertainties on the models to describe the foreground objects [37, 38].

The previous limits from the Fermi-LAT satellite on the WIMP self-annihilation cross section in the $\gamma\gamma$ and $Z\gamma$ channels are $\langle\sigma v\rangle_{\gamma\gamma} < (0.03 \div 4.6) \times 10^{-27}$ cm^3/s and $\langle\sigma v\rangle_{Z\gamma} < (0.02 \div 10.1) \times 10^{-27}$ cm^3/s for WIMP masses of 63 - 200 GeV [39]. Those results are complementary to those from the HESS ground-based telescope, which is sensitive to the higher WIMP masses: $\langle\sigma v\rangle < 3 \times 10^{-24}$ cm^3/s for a ~ TeV WIMP [40].

The Fermi-LAT collaboration also established a lower limit on the WIMP lifetime (for masses in the 14 to 400 GeV range) for the $\chi \rightarrow \nu\gamma$ channel, which spans in the range $4 \div 30 \times 10^{28}$ s [39].

A possible consequence of WIMPs being gravitationally trapped in the center of the Sun is a large annihilation rate which depends on the WIMP-proton cross section. At the equilibrium, the number of captured WIMPs is equal to the annihilating ones. All the final state particles but neutrinos would thermalize inside the celestial body.

Neutrino observatories such as IceCube and SuperKamiokande set strong limits on the WIMP-proton cross section, by looking for an excess in the neutrino rate coming from the Sun. No positive signal is observed: limits can be put on the $b\bar{b}$, $\tau^+\tau^-$ and W^+W^- channels. The most stringent limits come from SuperKamiokande (~ 1×10^{-40} cm^2 from the $\tau^+\tau^-$ channel for a GeV WIMP [41]) and IceCube (~ 0.25×10^{-40} cm^2 from the W^+W^- channel for a TeV WIMP [42]).

The PAMELA experiment measured an excess in the positron flux in the vicinity of the Earth. This result represents another example of signal from an unknown origin interpreted as possibly due to dark matter self annihilation. The excess lays in the $10 \div 100$ GeV energy range [43]. However, the antiproton flux measured by the same detector is in good agreement with the expectations, requiring a leptophilic dark matter candidate. The strength of the signal is also ~ 100 times larger than expected from the relic abundance. These constraints favor the interpretation of this excess in terms of other galactic sources, as pulsars. This statistical significance of this excess has been increased by the AMS experiment [44]. A galactic origin seems to be the most favored explanation, nonetheless the are theories that predict such a signal from dark matter particle decay, such as [45].

1.1.5.2 WIMP Searches at LHC

The constraint to the pMSSM model from the ATLAS collaboration are described in [46]. The inclusive reactions that produce squarks and gluinos are expected to have large cross section. Gluinos and squarks are expected to decay into neutralinos (the LSP), implying large missing

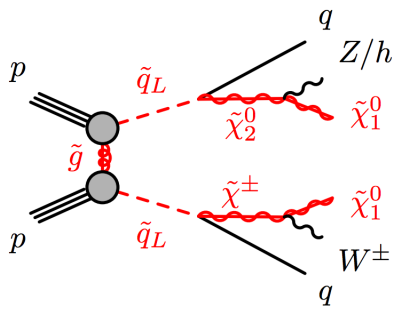

Fig. 1.5 Feynman diagram of a one-step decay topology of the squark in the phenomenological MSSM [46]. Two protons interact exchanging a gluino $\tilde{g}$ and produce a pair of left-handed squarks $\tilde{q}_L$ which in turn decay in neutralinos $\tilde{\chi}_i^0$ or charginos $\tilde{\chi}_i^\pm$ (linear combinations of charged higgsinos and winos). Both the heavy neutralino and the chargino decay in the LSP, the light neutralino $\tilde{\chi}_1^0$.

transverse energy in the event signature, along with jets. Figure 1.5 shows an example of Feynman diagram for the production of squarks. No evidence for new particles has been observed: this implies that SUSY, if realized in nature, must be broken at higher energy. Some theories predict such a symmetry breaking and the pMSSM limits on the mass of squarks can be set at the order of $m_{\tilde{q}} >$ TeV.

Since a WIMP could interact with a nucleon through the exchange of a squark, the limits on the squark masses can be translated into limits on the WIMP-nucleon cross section. The coupling is in fact proportional to $1/m_{\tilde{q}}^4$: if the squark mass is much larger than the Higgs mass, the squark contribution is suppressed with respect to the one arising from the exchange of a Higgs or Z^0 boson.

The LHC data can also be interpreted in the framework of model-independent effective field theories. Dark matter is only assumed to be a Dirac fermion, but the cross section only differs by a factor of 2 when considering a Majorana fermion. The characteristic signature of the WIMP production in a pp interaction at the LHC remains the missing transverse energy E_T^{miss}. Specific searches are carried out selecting monojet events, mono-photon events and mono-W/Z events.

No significant excess is found in the selected channels with respect to the Standard Model predictions. Assuming the validity of the effective interaction theory, the derived limits on the WIMP-nucleon cross section are competitive with the ones obtained with direct detection experiment. In particular at low WIMP mass the results driven from colliders dominate the exclusion.

1.2 Direct Search for WIMPs

An experiment for direct detection of WIMP is designed to detect the elastic scattering of dark matter particles on ordinary nuclei. As will be discussed in what follows, the event rate is expected to be of the order of ~ 1 event/ton/yr in noble liquids (assuming a cross section of 10^{-47} cm^2) and the typical recoil energy $\lesssim$ 100 keV. Those conditions impose severe requirements for a successful experiment: a large exposure and a low energy detection threshold.

Another essential requirement is the extreme reduction of external known backgrounds. Direct search experiments are usually installed in underground facilities, to be shielded from cosmic rays, and built with low-radioactivity materials. Discrimination techniques can be put in place in order to distinguish between nuclear and electronic (beta or gamma induced) recoils. Cosmogenic and radiogenic neutrons are the most pernicious background, since they can mimic a WIMP signal. A possible solution is the installation of one or more active or passive shielding around the sensitive target.

In this section I will discuss the expected event rate and signature of WIMP interactions (Sections 1.2.1 to 1.2.4). The following results are strongly dependent on the halo model, introduced in Section 1.1.2. In Section 1.2.5 I will present the summary of the recent experimental results.

1.2.1 Event Rate Calculation

I will briefly recall the standard derivation of the expected event rate in a designed target, as firstly suggested in [47]. The differential density of dark matter particles dn is given by:

$$dn = \frac{n_0}{k} f(\boldsymbol{v}, \boldsymbol{v_E}) d^3 v \tag{1.13}$$

where $n_0 = \rho_0 / m_\chi$ is the number density of DM particles, with local density ρ_0 and mass m_χ, $\boldsymbol{v}$ the velocity of the WIMP in the Earth reference system and $\boldsymbol{v}_E$ the velocity of the Earth with respect to the static DM halo. k is a normalization factor such that

$$\int_0^{v_{esc}} dn = n_0 \tag{1.14}$$

where v_{esc} is the escape velocity from the galaxy gravitational field.

The event rate per unit mass dR on a target with atomic mass A is:

$$dR = \frac{N_A}{A} \sigma(q)\, v\, dn \tag{1.15}$$

where N_A is the Avogadro's constant, $q = \sqrt{2 m_T E}$ is the nucleus recoil momentum and $\sigma(q)$ the WIMP-nucleus cross section and v the WIMP velocity.

Combining the above equations (1.13) and (1.15):

$$dR = \frac{N_A}{A} \frac{\rho_0}{m_\chi} \sigma(q) \frac{v f(\boldsymbol{v}, \boldsymbol{v_E})}{k} d^3 v \tag{1.16}$$

Assuming the elastic scattering between a WIMP with kinetic energy $E = \frac{1}{2} m_\chi v^2$ and a nucleus at rest, one can express the recoil energy of the nucleus in terms of the scattering angle θ (in the center of mass frame) with the formula:

$$E_R = \frac{E r (1 - \cos\theta)}{2} \tag{1.17}$$

with $r = 4m_\chi m_N/(m_\chi + m_N)^2$. If the scattering is isotropic, the recoils energies are uniformly distributed in $0 \leq E_R \leq Er$, so that:

$$\frac{dR}{dE_R} = \int_{E_{min}}^{E_{max}} \frac{1}{Er} dR(E) = \frac{2}{m_\chi r} \int_{v_{min}}^{v_{max}} \frac{1}{v^2} dR(v) \tag{1.18}$$

The integration lower limit corresponds to the minimum velocity a WIMP must have to produce a nuclear recoil of energy E_R: $v_{min} = \sqrt{(m_N E_R)/2\mu^2}$, with $\mu = m_\chi m_N/(m_\chi + m_N)$ is the reduced mass of the WIMP-nucleus system. The upper limit $v_{max} = v_{esc}$ is the maximum speed, in the galactic frame, that a gravitationally bound WIMP can have.

Using equation (1.16) one can write:

$$\frac{dR}{dE_R} = \frac{N_A}{A} \rho_0 \sigma(q) \frac{m_N}{2\mu^2 m_\chi} \times \frac{1}{k} \int_{v_{min}}^{v_{max}} \frac{f(\boldsymbol{v}, \boldsymbol{v_E})}{v} d^3 v \tag{1.19}$$

In general, the cross section can be expressed as:

$$\sigma(q) = \sigma_0 F^2(q) \tag{1.20}$$

where σ_0 is the cross section at zero momentum transfer and $F(q)$ represents the nuclear form factor. The form factor is needed to describe the decrease of the effective total cross section when the transferred momentum is such that the wavelength h/q becomes much smaller than the nucleus radius. On the contrary, the σ_0 factor takes into account all the dependence on the specific physics model. In general, both the zero momentum cross section and the form factor differ for even and odd nuclei, because of the target nucleus spin. If the target nucleus has spin different from 0, both the spin-dependent and spin-independent contributions must be taken into account when computing the WIMP-nucleus cross section.

We will give the expressions of the spin-dependent and spin-independent contributions in Sections 1.2.1.1 and 1.2.1.2 respectively. The last term of Equation 1.15, the inverse mean velocity $\frac{1}{k} \int_{v_{min}}^{v_{max}} \frac{f(\boldsymbol{v}, \boldsymbol{v_E})}{v} d^3 v$, is calculated in Section 1.2.1.3.

1.2.1.1 Spin-independent Contribution

The spin-independent zero momentum cross section σ_o^{SI} is given by:

$$\sigma_0^{SI} = \frac{4}{\pi} \mu^2 [Z f_p + (A - Z) f_n]^2 \tag{1.21}$$

where μ is the reduced mass of the WIMP-nucleus system, and f_p and f_n are the coupling of WIMPs with the proton and the neutron respectively. Since in most of the models $f_p \approx f_n$,

the spin-independent cross section is usually given in terms of WIMP-proton cross section:

$$\sigma_0^{SI} = \sigma_p \left(\frac{\mu}{\mu_p}\right)^2 A^2 \tag{1.22}$$

with μ_p being the WIMP-proton reduced mass.

The nuclear form factor calculations start from the Fourier transform of the nuclear density function. In a first approximation, considering the nucleus as a solid sphere, the factor $F(qr_n)$ can be expressed as:

$$F(qr_n) = 3\frac{\sin(qr_n) - qr_n\cos(qr_n)}{(qr_n)^3} = 3\frac{j_1(qr_n)}{qr_n} \tag{1.23}$$

where $j_1(qr_n)$ indicates the first Bessel function and r_n, the nuclear radius, introduced to make the qr_n product dimensionless.

Considering a more physical nuclear density distribution, like the Fermi distribution

$$\rho(r) = \rho_0 \left[1 + \exp\left(\frac{r-c}{a}\right)\right]^{-1} \tag{1.24}$$

leads to the following analytical form for the $F(qr_n)$ factor:

$$F(qr_n) = 3\frac{j_1(qr_n)}{qr_n} \times \exp\left(-\frac{q^2 s^2}{2}\right) \tag{1.25}$$

where c is the typical nucleus radius, a a parameter that describe the density decrease and s a measure of the nucleus skin thickness.

It is found that r_n satisfies the following relation

$$r_n^2 = c^2 + \frac{7}{3}\pi^2 a^2 - 5s^2 \quad \text{fm}^2 \tag{1.26}$$

for a and s experimentally determined to be 0.52 fm and 0.9 fm respectively and

$$c = \left(1.23 \times A^{\frac{1}{3}} - 0.6\right) \quad \text{fm.} \tag{1.27}$$

1.2.1.2 Spin-dependent Contribution

The spin-dependent zero momentum cross section σ_0^{SD} is often expressed, for a target nucleus with atomic mass A, Z protons and spin J, as:

$$\sigma_0^{SD} = \frac{32}{\pi} G_F^2 \mu_N^2 \frac{J+1}{J} [a_p \langle S_p \rangle + a_n \langle S_n \rangle]^2 \tag{1.28}$$

where G_F is the Fermi constant and μ_N the reduced mass of the WIMP-nucleon system. $\langle S_i \rangle$ are the expectation values of the spin content of the proton and neutron groups inside the nucleus and a_p and a_n are the effective WIMP-nucleon couplings.

The spin-dependent nuclear form factor F^2_{SD} can be parameterized in terms of effective couplings as well, by means of the definition of isoscalar ($a_0 \equiv a_p + a_n$) and isovector ($a_1 \equiv a_p - a_n$) couplings:

$$F^2_{SD}(q) = \frac{S(q)}{S(0)} = \frac{1}{S(0)}\left[a_0^2 S_{00}(q) + a_0 a_1 S_{01}(q) + a_1^2 S_{11}(q)\right] \tag{1.29}$$

From detailed nuclear shell model calculations one can derive the independent form factors: the pure isoscalar S_{00}, the pure isovector S_{11} and the interference term S_{01}. A useful approximation is given by:

$$F^2_{SD}(q) \approx \exp\left(-\frac{q^2 R_A^2}{4}\right) \tag{1.30}$$

with

$$R_A = 1.7A^{1/3} - 0.28 - 0.78\left(A^{1/3} - 3.8 + \sqrt{(A^{1/3} - 3.8)^2 + 0.2}\right)$$

1.2.1.3 The Earth's Motion

We lastly need to evaluate the mean inverse speed:

$$\eta(E_r, t) \equiv \frac{1}{k}\int_{v_{min}}^{v_{max}} \frac{f(\boldsymbol{v}, \boldsymbol{v_E})}{v} d^3 v$$

We will rely on the standard halo model and assume the Maxwellian velocity distribution described in Section 1.1.2. Because of the finite value of the escape velocity v_{esc}, the Maxwellian distribution f_0 is modified as follows:

$$f_0(\boldsymbol{v}) = \begin{cases} \frac{1}{N_{esc}}\left(\frac{3}{2\pi\sigma_v^2}\right)^{3/2} \exp\left(-\frac{3\boldsymbol{v}^2}{2\sigma_v^2}\right) & \text{for} |\boldsymbol{v}| < v_{esc} \\ 0 & \text{otherwise.} \end{cases} \tag{1.31}$$

where most probable velocity $\overline{v_0} = \sqrt{2/3}\sigma_v$ and N_{esc} a normalization factor:

$$N_{esc} = \text{erf}\left(\frac{v_{esc}}{\overline{v_0}}\right) - \frac{2}{\sqrt{\pi}}\frac{v_{esc}}{\overline{v_0}} e^{-\left(\frac{v_{esc}}{\overline{v_0}}\right)^2} \tag{1.32}$$

such that, for $v_{esc} \to \infty$, $N_{esc} \to 1$.

Because of the motion of the Earth in the WIMP rest frame, the WIMP velocity distribution in the Earth frame can be written as:

$$f(\boldsymbol{u}) = f_0(\boldsymbol{u} + \boldsymbol{v_{obs}}) \tag{1.33}$$

The parameters of the already introduced standard halo model are: $\overline{v_0}$ = 220 km/s, σ_v = 270 km/s, v_{obs} = 232 km/s and v_{esc} = 544 km/s. A useful parameterization of the mean

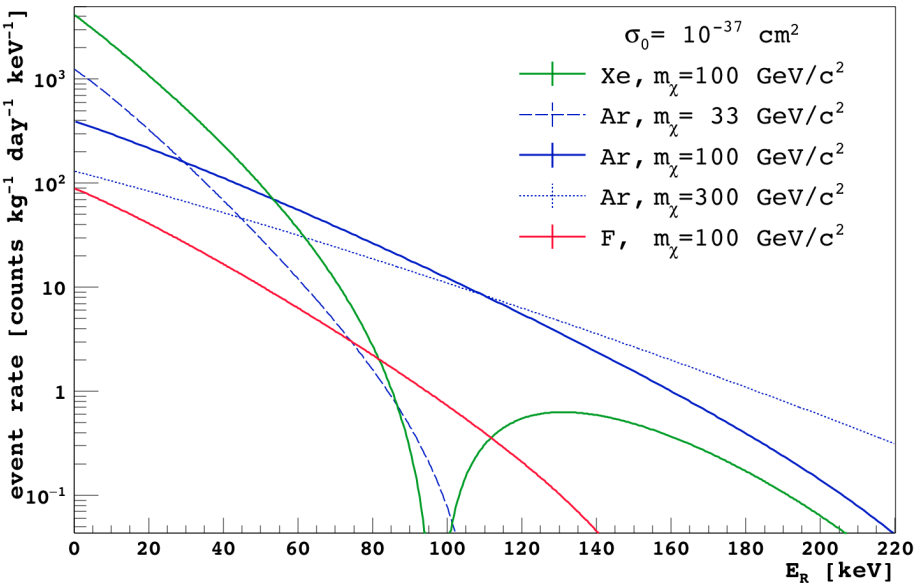

Fig. 1.6 Expected differential event rate for different target materials. A spin-independent cross section with $\sigma_0 = 10^{-37}$ cm^2 is assumed. Expected rates in xenon (green), argon (blue) and fluorine (red) for a WIMP mass of 100 GeV/c^2 are compared. In the argon case, the spectra for a 3 times smaller (dashed line) and larger (point line) WIMP mass is also shown.

inverse speed is found in [21]:

$$\eta(E_r,t) = \begin{cases} \frac{1}{\overline{v_0}y} & \text{for } z<y, x<|y-z| \\ \frac{1}{2N_{esc}\overline{v_0}y}\left[\text{erf}(x+y)-\text{erf}(x-y)-\frac{4}{\sqrt{\pi}}ye^{-z^2}\right] & \text{for } z>y, x<|y-z| \\ \frac{1}{2N_{esc}\overline{v_0}y}\left[\text{erf}(z)-\text{erf}(x-y)-\frac{2}{\sqrt{\pi}}(y+z-x)e^{-z^2}\right] & \text{for } |y<z|<x<y+z \\ 0 & \text{for } y+z<x \end{cases} \tag{1.34}$$

where

$$y \equiv \frac{v_{obs}}{\overline{v_0}}, \qquad x \equiv \frac{v_{min}}{\overline{v_0}} \qquad \text{and} \qquad z \equiv \frac{v_{esc}}{\overline{v_0}}$$

where v_{min} is defined in Eq. 1.18.

1.2.1.4 Differential Event Rate

We now have all the elements to compute the differential WIMP event rate for any target according to Equation 1.19. Figure 1.6 shows the expected event rate (assuming a spin-independent cross section) for different targets (xenon, argon anf fluorine), assuming a 100 GeV/c^2 WIMP. The mean inverse velocity is averaged over the year. Being the cross section proportional to A^2 of the target, the absolute rate is larger for xenon, but suppressed at high recoil energy because of the nuclear form factor.

In the argon case, the spectrum shape dependence on the WIMP mass is also shown (dashed and point lines).

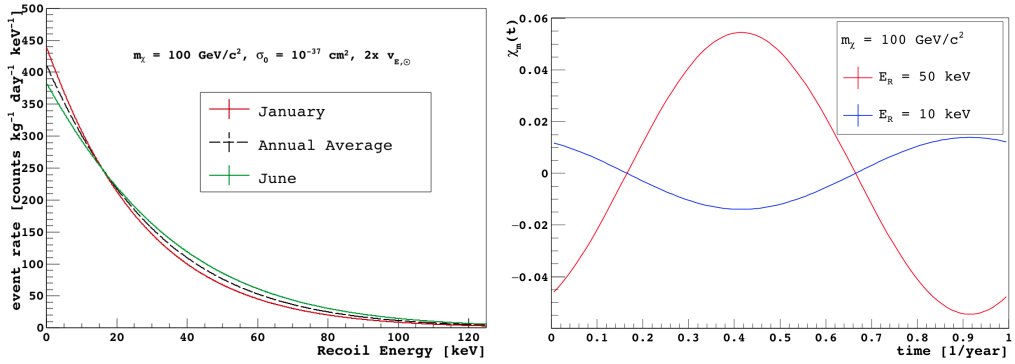

(a) Seasonal variation of $\frac{dR}{dE}$(t)

(b) Amplitude of the modulation

Fig. 1.7 Annual modulation of the expected event rate for a WIMP mass of 100 GeV/c^2 on a argon target. (a) $dR/dE(t)$ as a function of the season. The dashed line represents the averaged curve, equal to the solid blue curve of Fig. 1.6. To enhance the effect, the orbiting speed of the Earth around the Sun is increased by a factor of 2. (b) Expected amplitude of the annual modulation. On the x-axis, 1 = 0 = January 1st. The modulation is expected to invert phase for $E_R^0 = \mu^2 v_{min}/m_T \simeq 16.5$ keV for an Ar target.

1.2.2 Annual Modulation

One of the possible signatures of a WIMP signal is the annual modulation, described in this Section. Because of the motion of the Earth around the Sun, the velocity of the observatory in the galactic reference system $\boldsymbol{v_{obs}}$ can be expressed as

$$\boldsymbol{v_{obs}}(t) = \boldsymbol{v_\odot} + v_E[\hat{\boldsymbol{\epsilon_1}}\cos\omega(t-t_1) + \hat{\boldsymbol{\epsilon_2}}\cos\omega(t-t_1)] \tag{1.35}$$

where $\boldsymbol{v_\odot}$ is the Sun velocity, $\boldsymbol{v_E}$ is the orbital velocity of the Earth around the Sun, $\omega = 2\pi$/year and t_1 the fraction of the year before the Spring equinox. The $\hat{\boldsymbol{\epsilon_1}}$ and $\hat{\boldsymbol{\epsilon_2}}$ are unitary vectors describing the direction of the Earth at the Spring equinox and and the Summer solstice respectively in the galactic reference system.

The time dependence of the $\boldsymbol{v_{obs}}$ magnitude can be written as:

$$v_{obs}(t) = \sqrt{v_\odot^2 + v_E^2 + 2\,b\,v_E\,v_\odot\cos\omega(t-t_c)} \tag{1.36}$$

where $b = 0.49$ is a geometrical factor, accounting for the different inclinations of the Earth orbit with respect to the Sun orbit plane and t_c is the time of the year at which v_{obs} is maximized. Since $v_\odot \gg v_E$, the above equation can be approximated by:

$$v_{obs}(t) \simeq v_\odot\left[1 + b\frac{v_E}{v_\odot}\cos\omega(t-t_c)\right] \tag{1.37}$$

This few-% variation in the velocity of the Earth through the WIMP static halo implies a time-dependent change in the inverse mean speed, which reflects in a modulation of the event rate. The time-dependent event rate can be parameterized as the sum of a time-

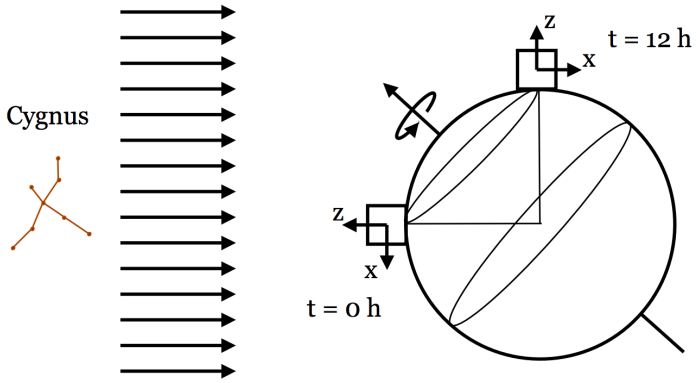

Fig. 1.8 The daily rotation of the Earth introduces a modulation in recoil angle, as measured in the laboratory frame. [48]

averaged component and a modulation one:

$$R(t) = R_0 + R_m(t) = R_0 \left[1 + \chi_m(t)\right] \tag{1.38}$$

where $\chi_m(t) = R_m(t)/R_0$ is the magnitude of the relative modulation.

Using the assumptions of the standard halo model, the relative modulation over a wide range of specific recoil energies is:

$$\chi_m(x,t) \approx \cos\omega(t-t_c) \times \begin{cases} -0.034(1-x^2/x_p^2), & \text{for } x < x_p \\ 0.014(x/x_p - 1)(x/x_p + 3.7), & \text{for } x_p < x \lesssim z \end{cases} \tag{1.39}$$

where x is again defined as $v_{min}/\overline{v_0}$, $t_c = 0.415$ (June 1), $z = v_{esc}/\overline{v_0} = 2.47$, $x_p = 0.89$ is the value at which the phase inversion occurs.

The amplitude of the modulation becomes large for $x \geq z$ and the shape is no longer cosine-like. The overall rate is though strongly suppressed and this deviation can be ignored.

Figure 1.7 (a) shows the seasonal variation of the shape of the recoil energy spectrum (for illustrative purposes the effect has been enhanced). The right panel shows the amplitude of the modulation for two recoil energies.

This few-% annual modulation represents a strong signature of a WIMP signal (if the background does not show the same behavior). Nonetheless, in order to be exploited, a large statistics data sample is required (of the order of 10^3 events distributed over the whole year).

1.2.3 Directionality

The Solar System is traveling towards the Cygnus constellation. In the assumption of a static dark matter halo, the rotation of the Earth around its axis makes a detector cross the WIMP with different angles during the day. For a detector able to discriminate the recoils direction, the anisotropy in the angular distribution can be exploited to distinguish between WIMP

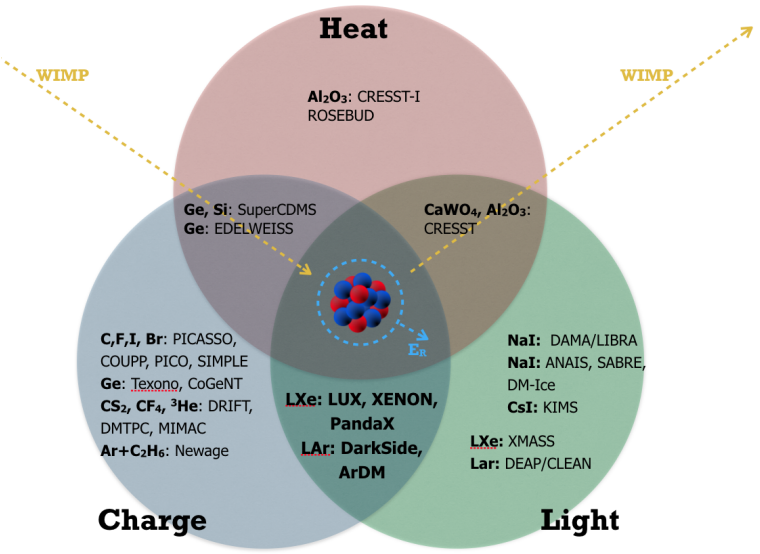

Fig. 1.9 Direct detection of dark matter. Current experiments exploit one or more detection techniques at the same time.

events and background, as sketched in Figure 1.8. The majority of the backgrounds is in fact expected to be isotropic in the Galactic reference.

A directional detector could make use of non-isotropic response scintillators (such as stilbene) or gaseous targets in an electric field. In the latter case, the amount of collected ionization charges depends on the inclination of the track with respect to the drift field.[3] To improve the spatial resolution of the track, one can lower the pressure of the target, at the cost of a large sensitive mass (and thus exposure).

The direction signal is much larger than the one coming from the annual modulation (the backscattering probability for an elastic collision is several times larger than the forward one). A detector with good angular resolution could reject the case of isotropic recoils with only a small sample of events (of the order of 10). For a 95% CL identification of the median inverse recoil direction a sample of ~ 31 events is required (assuming a zero background detector) [49].

1.2.4 Complementarity

Several experiment are currently looking for interactions of WIMPs. A recoiling nucleus deposits its energy in the form of scintillation, ionization and phonons. Some of the currently running detectors are designed to be sensitive to more than one of those channels. As a results, the energy resolution is usually better and in some cases this improves the background discrimination power.

[3] This effect can be described with the so called columnar recombination model and it might be also exploited in liquid targets.

In general, if a dark matter particle is detected, the use of different target materials and detection techniques is crucial. The signals from different detectors can in fact unambiguously constraint the WIMP properties (such as the WIMP mass and the nature of the interaction) and eventually rule out possible theoretical models. We can refer to Figure 1.6 to illustrate the different shapes of the nuclear recoil energy spectrum produced by a WIMP in different targets.

In the past 15 years, some experimental collaborations claimed the detection of WIMP dark matter. The observations, sometime supported by a strongly significant annual modulation [50], are challenged by other experiments which obtained negative results in the same phase-space region. The state-of-the-art of the direct search for dark matter is reviewed in more details in the next Section.

Complementarity must also be considered in a broader way [28]: the LHC is a unique channel for exploring the interactions with Standard Model particles; the scattering of dark-matter particles off various materials in direct-detection experiments can provide insight into the local density and velocity distribution of dark matter; the indirect detection through astrophysical measurements permits tracing the distribution of dark matter in the sky. It is therefore mandatory that all the three strategies of dark matter detection be continued.

1.2.5 State of the Art

To compute the total cross section of non-relativistic dark matter particle with nuclei it is convenient to separate the spin-dependent (SD) and spin-independent (SI) contributions. In the SI case, the cross section is proportional to the atomic mass of the target nucleus, so that heavy nuclei such Xe and Ge are usually preferred. To test the SD interaction, possible targets are ^{19}F, ^{23}Na, ^{73}Ge, ^{127}I, ^{129}Xe, ^{131}Xe and ^{137}Cs.

For a fixed detection energy threshold, the smaller the WIMP mass, the smaller the accessible fraction of the WIMP energy spectrum. The sensitivity of the experiment is usually given as a function of the WIMP mass. Because of the threshold effect, the sensitivity naturally drops for low WIMP masses. Moreover, for large masses, assuming a fixed mass density, the WIMP flux decreases $\propto 1/m_\chi$: for the same exposure, the sensitivity of a given experiment also decrease for increasing WIMP-masses.

The first WIMP detectors were made by ultra-pure semiconductors, passively shielded and installed underground. Experiments such Heidelberg-Moscow produced the first limits in the mass-cross section space (SI). The technical challenge was to lower the threshold maintaining a low background. A threshold as low as 400 eV has been achieved for the first time by the CoGeNT collaboration [51] thanks to the technique of Point Contact Ge detectors. The collaboration claimed as well the evidence for a signal at low energy, showing annual modulation. Nonetheless, the strength of this evidence has decreased over the time after a more careful analysis of surface events.

Another positive signal comes from the DAMA/LIBRA experiment. The collaboration reported the result for an exposure of 1.33 ton.y of NaI scintillation crystals detector with a 9.3σ evidence of annual modulation. This result favors two allowed region in the mass-cross section plane, centered around $m_\chi \sim 50$ GeV ($m_\chi \sim 7$ GeV) and $\sigma_{\chi p} \sim 7 \cdot 10^{-42}$ cm^2 ($\sigma_{\chi p} \sim 10^{-40}$ cm^2). Some inconsistencies appears between the data from the two phases (DAMA [50] and DAMA/LIBRA [52]): the amplitude of the annual modulation in the second data-set is for instance 0.43 ± 0.13 times the value obtained from the first, with a discrepancy of more than 4σ's. Moreover, the regions allowed by these data in the mass-cross section plane have been excluded by several subsequent experiments.

In order to test the DAMA results, other detectors have been (and will be) operated with the same technique by different collaborations. In particular the KIMS [53] experiment excluded the parameters region allowed by DAMA with an exposure of 24 t.d of CsI crystals. The SABRE [54] and DM-ICE [55] collaborations are instead aiming to run experiments with NaI crystals in the Southern hemisphere: if the seasonal modulation is due to a residual background, the phase of the modulation is expected to be inverted.

The CRESST experiment couples the scintillation detection with the bolometric technique and it is operated at the temperature of 10 mK. The scintillation light from $CaWO_4$ crystals provides discrimination between nuclear and electronic recoils. The collaboration claimed a positive result in 2012 [56], partially challenged after the upgrade of the detector. In the phase-II, a very low threshold is achieved (~ 300 eV) and the collaboration set the best limit for very low WIMP masses ($\sim 10^{-38}$ cm^2 for $m_\chi \lesssim 1$ GeV) [57].

Germanium bolometers are designed to access the ionization charge and the phonons at the same time and are implemented in detectors such CDMS and Edelweiss [58]. Operating the crystals in the standard mode allows to discriminate nuclear and electronic recoils. The combined analysis from the two experiments gives the best limit obtained with the bolometric technique for large WIMP masses [59]. The CDMS collaboration showed that, operating the detector with higher bias voltage, it is possible to lower the detection threshold to ~ 170 eV (at the cost of losing the discrimination capability). They produced a limit which is currently the best one in the 2 to 6 GeV WIMP mass range ($\sim 10^{-40}$ cm^2) [60].

In the high WIMP mass region, the field is dominated by noble liquids experiments. They can be operated in single phase (XMASS [61], ArDM[4] [62], DEAP-CLEAN [63]) or double phase (LUX [64, 1], XENON [65], Panda-X [66, 67] and DarkSide [3, 4]) to access the scintillation light or both the scintillation and ionization charges respectively. The first part of the next chapter is entirely dedicated to the double-phase detection technique and the comparison between argon and xenon as targets.

In the spin-dependent sector, one can distinguish the limit on the WIMP-proton and WIMP-neutron cross section. Since the xenon isotopes ^{129}Xe and ^{131}Xe have an odd number of neutrons, the LUX experiment gives the best limit on the WIMP-neutron cross section. For

[4] Currently being upgraded to operate in dual-phase

the WIMP-proton cross section the best limits are set by indirect observations by the SuperK and ICeCube experiments (these limits are however model dependent). The COUPP and PICASSO collaborations joined together to run the PICO experiment [68]. This experiment, a metastable liquid bubble chamber, has the advantage to be insensitive to electromagnetic interactions and thus to be in principle free from β and γ backgrounds.

Figure 1.10 summarizes the status of the SI and SD searches. The sensitivity of the experiments probing the spin-independent cross section will be limited by the neutrino coherent scattering on nuclei, which represents an irreducible background. If the WIMP-nucleon cross section is found to be smaller than the ν-nucleon one, only a directional detector could statistically separate the two components.

The NEW-AGE [70], MIMAC [71] and DRIFT [72] collaborations are giving promising results in this direction, operating TPC filled with gaseous mixtures. The main limitation at the moment is the mass of the target: up to now, these experiment are only able to test a parameter region already excluded by other experiment.

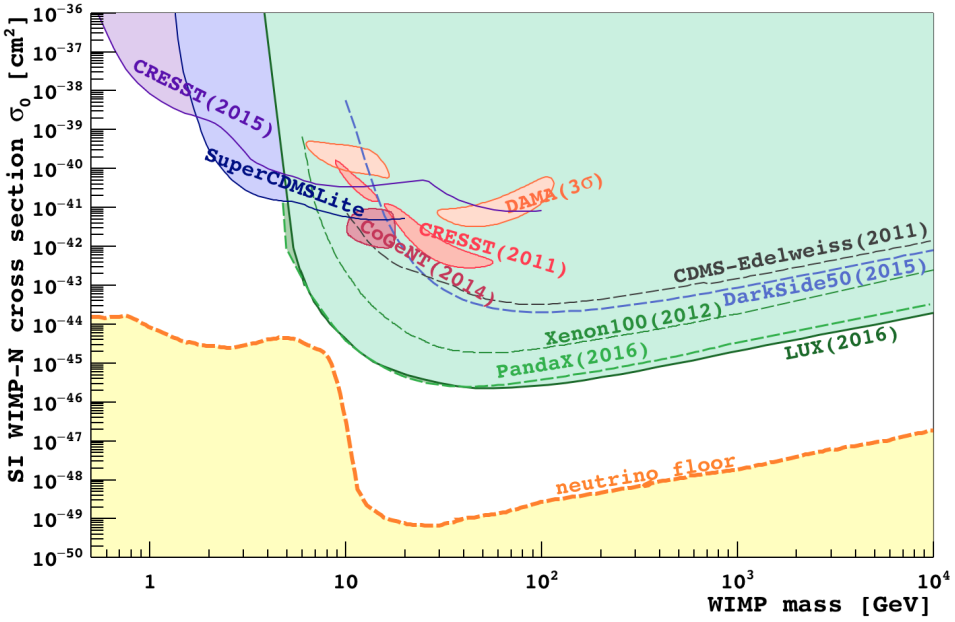

(a) SI exclusion plot

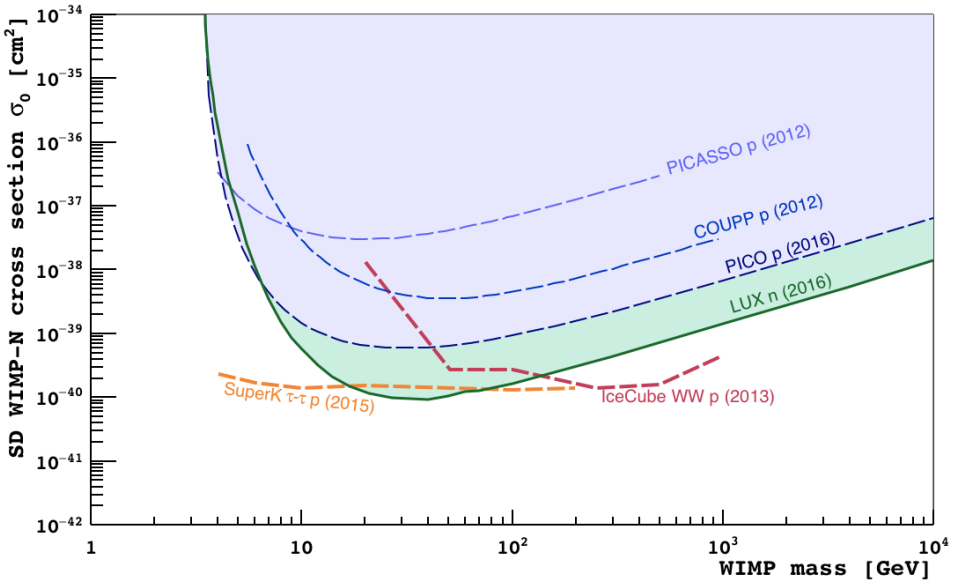

(b) SD exclusion plot

Fig. 1.10 Spin-independent (a) and spin-dependent (b) exclusion plots. In the spin-dependent (SD) plot, the yellow area is the neutrino floor [69]. In the spin-independent (SI) plot, solid lines correspond to the WIMP-neutron exclusion, while the dashed lines correspond to the WIMP-proton cross section.

Chapter 2

The DarkSide Program and the DarkSide-50 Results

In this Chapter I will describe the basics of the WIMP direct detection technique with a noble liquid dual-phase time projection chamber (TPC). I will then focus on the DarkSide program and in particular on the DarkSide-50 experiment.

2.1 Direct Search with Noble Liquids

WIMPs are expected to interact with the nuclei of the target, inducing low energy (< 100 keV) nuclear recoils (NR). Thus, a direct detection experiment must have a low energy detection threshold and excellent background rejection. The possible backgrounds includes:

- NR's induced by radiogenic and cosmogenic neutrons;
- α particle emitted from the detector surfaces;
- electron recoils (ER) from β and γ internal and external contamination.

Moreover, a good energy resolution and large sensitive targets are also required.

Noble liquids are suitable targets for the direct detection of massive dark matter particles. Among noble liquids, argon and xenon are the most widely used ones, but neon and krypton could in principle be valid alternatives. They are relatively in-expensive, naturally stable, dense and easy to be chemically purified; they have large ionization and scintillation yields; they are and transparent to the scintillation light and the electron mobility is large. Because of these features, sensitive volume can in principle easily be scaled to large masses without large degradation of possible signals.

In addition to this, the ratio between ionization and scintillation is different for nuclear and electron recoils. This feature is exploited in dual-phase detectors for the ER background discrimination. The rejection power of this technique is of the order of 10^3 (one electron recoil over 10^3 is mis-reconstructed as a nuclear recoil). A dual-phase TPC additionally

provides 3D position reconstruction of the interaction vertexes, a useful tool for the rejection of surface background.

The high density (~ 3 kg/l) and very high intrinsic radio-purity are additional advantages of xenon. In addition to this, a xenon target is self-shielded against external radiation: the mean free path of thermal neutrons is of the order of the cm and the range of 50 keV gammas is less than 1 mm in liquid xenon. As a comparison, in liquid argon these quantities are respectively 50 cm and 1 cm.[1] These are the reason why the xenon-based experiment are leading the field.

On the other hand, liquid argon offers more advantages in terms of discrimination between nuclear and electron recoils. The shape of the primary scintillation pulse is strongly dependent on the nature of the recoiling particle. The limiting constraint on the mass of a liquid argon detector comes from the internal radioactivity, far from being negligible in atmospheric argon (~ 1 Bq/kg).

The next two sections contain the description of the detection principles in a dual-phase TPC, a description of the pulse shape discrimination (PSD) technique and a discussion about the argon internal radioactivity.

2.1.1 dual-phase Time Projection Chambers

A particle interaction in a noble liquid target produces ionization, heat and atomic excitation. The mean energy required to produce a ion pair or an exciton (the conversion work function) is of the order of 10 eV. The heat fraction information is usually lost: this results in a slightly higher value for the work function. The work function from recoil energy to excitation or ionization is assumed to be constant with respect to the recoil energy and the same for the ratio between excitons and ionization pairs $\alpha = N_{ex}/N_{ion}$. These ratios are $\alpha_{Xe} = 0.06 \div 0.2$ in liquid xenon and $\alpha_{Ar} = 0.21$ in liquid argon for electron recoils [73].

In liquid argon (but the mechanism is the same in all the noble liquids), an excited atom forms with a neutral atom an excited dimer that subsequently decays by radiative emission:

$$\mathrm{Ar}^* + \mathrm{Ar} \rightarrow \mathrm{Ar}_2^* \rightarrow 2\mathrm{Ar} + \gamma \tag{2.1}$$

For high LET[2] tracks (such as nuclear recoils) the bi-excitonic quenching is believed to play an important role. The collision between two excitons can cause the emission of a low energy electron that loses his energy before recombining:

$$\mathrm{Ar}^* + \mathrm{Ar}^* \rightarrow \mathrm{Ar}^+ + \mathrm{Ar} + \gamma. \tag{2.2}$$

[1] The range for radiogenic neutrons is approximately the same in argon and xenon (~ 15 cm). All the quoted numbers are estimated by means of a dedicated GEANT4 simulation.

[2] *Linear Energy Transfer.*

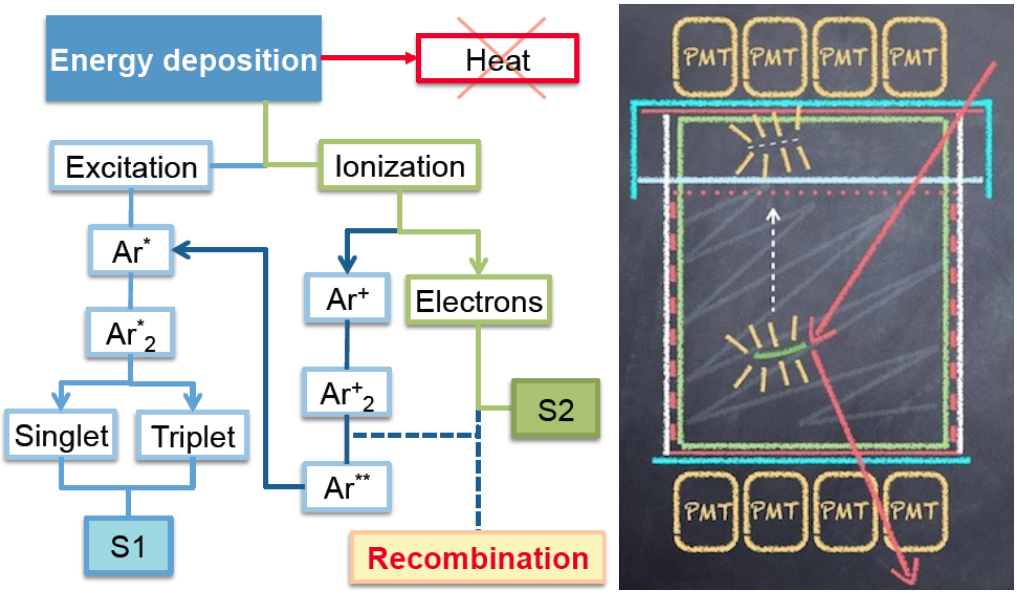

(a) (b)

Fig. 2.1 A scheme of ionization and scintillation mechanisms (a) and a cartoon of a dual-phase noble liquid TPC (b).

This process reduces the number of emitted scintillation photons since two excitons eventually produce only one photon and might be the main responsible for the nuclear recoil quenching. On the contrary, the emission efficiency (the ratio of emitted photons per exciton) is assumed to be 1 for electron recoils.

If ionization occurs, the positive ions form charged dimers with neutral atoms. The free electrons thermalize and can be later captured by dimers (recombination). This leads as well to the formation of excited dimers and thus to emission of scintillation light:

$$\mathrm{Ar}^+ + \mathrm{Ar} \rightarrow \mathrm{Ar}_2^+,$$

$$\mathrm{Ar}_2^+ + e^- \rightarrow \mathrm{Ar}_2^* \rightarrow 2\mathrm{Ar} + \gamma \tag{2.3}$$

Since both the processes lead to the same excited state Ar_2^*, the emitted photon energy is the same. Moreover, since the excitation energy of the dimers is smaller than the excitation energy of free atoms, the self-absorption in a pure target is negligible. The emitted light is in the VUV range for liquid argon and xenon, peaked at 128 nm and at 178 nm respectively.

A small α ratio means that most of the scintillation light is due to recombination of free ions and electrons. One can define the maximum photon yield for the deposited energy E assuming the recombination of all the ion pairs, $N_{ph} = E/W_{ph}$. The effective work function W_{ph} for xenon and argon is experimentally determined to be 13.7 eV and 19.5 eV, leading to a maximum photon yield of 73 and 51 photons/keV respectively [73].

As already mentioned, the fraction of the recoil energy dissipated by ionization is different depending on the dE/dx of the recoiling particle. For the same recoil energy, electron recoils will show a higher ratio between ionization and excitation with respect to nuclear recoils. The ionization electrons can be drifted away from the interaction region, dense in dimers, by means of an electric field and then be measured. Only free electrons that escape recombination contribute to the ionization signal, so that ionization and scintillation are anti-correlated. Moreover, the ratio between the two contributions is affected by the electric drift field strength, through the field dependence of the recombination probability.

A scheme of the processes described above is given in Figure 2.1 (a).

The ionization component can be measured extracting the free electrons in a gaseous region on top of the liquid and accelerating them by means of a stronger field. This mechanism produces scintillation in the gas (electro-luminescence). The prompt scintillation light signal is usually called S1, while the delayed signal produced by the electrons extracted in the gas is called S2.

In a dual-phase noble liquid TPC, the sensitive volume is usually immersed in a constant electric field (typical strengths of the order of $10^2 \div 10^3$ V/cm). A gaseous region with typical height of ~ 1 cm is created on top of the liquid by heating the liquid and a transparent grid is placed a few mm below the liquid surface to allow the formation of the extraction and acceleration fields.

One or more arrays of photo-detectors (usually photo-multipliers) observe the sensitive volume. Since the scintillation light of noble liquids is in the VUV region, VUV sensitve photo-cathodes or a wavelength shifter coating of the inner walls of the TPC are required. A cartoon of a dual-phase TPC detector is given in Figure 2.1 (b).

The segmentation of the light detector array allows the localization of the interaction in the plane normal to the drift direction, while the vertical position is given by the ionization electron drift time (measured as a time difference between S2 and S1). As already mentioned, the 3D vertex reconstruction is an effective tool for the background rejection. Moreover, the events in which the incoming particle interacts more than once in the sensitive volume (at different vertical positions) can be identified since they will show multiple ionization-induced pulses.[3]

2.1.2 Pulse Shape Discrimination in Liquid Argon

The excitation of a noble element atom involves two states, the singlet $^1\Sigma_u^+$ and the triplet $^3\Sigma_u^+$. The energy difference between the two states is small, so that they cannot be distinguished spectroscopically. However, the decay time constant of the two states is different. While in liquid xenon the two decay constants are $\tau_1 \sim 4$ ns and $\tau_2 \sim 22$ ns, they differ by more than

[3] A multi-sited event produces more than one ionization clouds that are drifted and extracted in the gaseous region. If the vertical position of the recoils is different, the drift electrons will arrive at the liquid surface at different times.

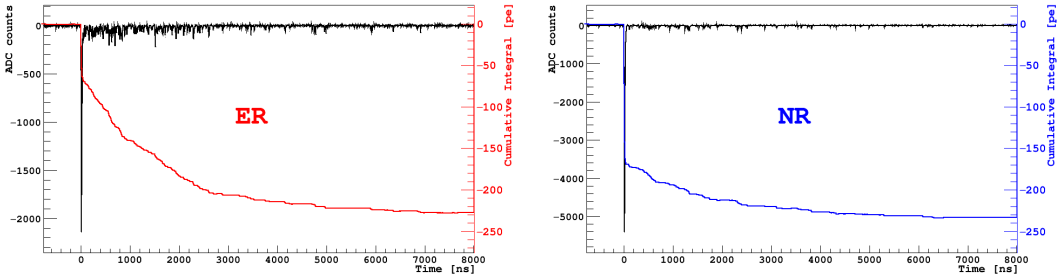

(a) Electron recoil (b) Nuclear recoil

Fig. 2.2 Comparison of two typical waveforms for ER (left) and NR (right) in liquid argon. The two examples are chosen to have approximately the same integral: in the ER case, the prompt fraction of the signal is smaller with respect to the NR case. The solid curves represents the cumulative integral of the waveforms in both the cases.

a factor of 200 in liquid argon: $\tau_1 \sim 7$ ns and $\tau_2 \sim 1.6\,\mu$s [74]. In both the expressions, the subscript 1 stands for the singlet and 2 for the triplet.

It was shown in [75–77] that the relative intensity of the singlet (or prompt) component is smaller for higher deposited energy density. The typical singlet fraction for electron recoils is about 0.3 and about 0.7 for nuclear recoils in liquid argon. Figure 2.2 shows two typical DarkSide-50 scintillation pulses, of approximately the same size. The one on the left corresponds to an ER, while the one on the right to a NR.

One can measure the fraction of prompt component (which decays completely in a few tens of nanoseconds) by computing the ratio between the integral of a scintillation pulse in the first tens of nanoseconds and the total integral. The SCENE collaboration [78] has shown that the maximum separation is achieved by defining f_{90} as estimator of the prompt fraction of the signal $S(t)$:

$$f_{90} = \frac{\int_0^{90\text{ns}} S(t)dt}{\int_0^{7\mu\text{s}} S(t)dt} \tag{2.4}$$

where the upper limit of 7 μs is chosen to allow the late part of the signal to fully decay.

By means of the f_{90} parameter it is possible to achieve a discrimination between nuclear and electron recoils up to a factor $\sim 10^8$ in liquid argon [2]. It must be noted that the separation is less accentuated at low energy ($\sim$ few keV_{ee}),[4] when the mean value of the prompt fraction for electronic and nuclear recoils tend to approach the intermediate value of 0.5, while it is larger at higher energies.

The pulse shape discrimination (PSD) is a prerogative of liquid argon and offers a unique tool for the background rejection. An argon detector can in principle be free from all the known β and γ backgrounds to an unprecedented level. We will further discuss about the pulse shape discrimination in Chapter 5.

[4] keV_{ee} = keV electron equivalent.

2.1.3 Low-radioactivity Argon

Argon is relatively abundant in the Earth atmosphere (0.94%) and this makes the extraction of this gas from the air convenient. Because of cosmogenic activation through the reaction ^{40}Ar $(n,2n)$ ^{39}Ar, there is a significant amount of ^{39}Ar in atmospheric argon (^{39}Ar/ ^{40}Ar $\simeq 8\times10^{-16}$). The ^{39}Ar isotope is a beta-emitter, with half-life of 269 years and endpoint at 565 keV. As a result, the total activity of atmospheric argon is $A_{atm} = 1.01 \pm 0.01 \pm 0.08$ Bq/kg [79]. To prevent dead-time saturation and pile-up in a detector with long acquisition window (as required for TPCs), the mass of the sensitive volume can not be too large. [5]

The extraction of argon from underground sources can solve this issue, because of the long isolation from the atmosphere. In particular, the CO_2 from the Kinder Morgan well (in Colorado) has been discovered to contain argon with a concentration of approximately 500 ppm. An extraction plant has been installed and the operations started in 2009. A preliminary chromatographic separation of the extracted gas gives a mixture of He, N and Ar (at ~ 5%). After a subsequent cryogenic distillation it was then possible to obtain a 99.95% pure sample of argon, at the production rate of the order of 0.5 kg/day [80, 81].

In April 2015 the DarkSide TPC was filled for the first time with a batch of underground argon and the data taking with low-radioactivity filling started. A reduction in the ^{39}Ar concentration was found to be as large as a factor of 1400 ± 200 (see Chapter 4). This impressive result opens new scenarios in the field of the direct detection of dark matter. The liquid argon target technology can be now applied in large dual-phase detectors.

2.2 The DarkSide Program

The DarkSide experiment is designed for direct detection of WIMP-induced nuclear recoils in a liquid argon target. The goal is to reach a background-free multi-ton scale exposure through a staged approach. The DarkSide-10 prototype [82] was build at Princeton and operated at *Laboratori Nazionali del Gran Sasso* (LNGS) between 2011 and 2013. The detector was meant to prove the feasibility of a dual-phase liquid argon TPC. Figure 2.3 (a) shows a schematic of the inner detector.

The DarkSide-50 detector design aimed to perform a dark matter search and actually the provided limit is the best one ever obtained with a liquid argon target (corresponding to a combined atmospheric and underground argon exposure of about $4.7{\cdot}10^3$ kg.d). Thanks to the implemented background suppression and identification techniques, no WIMP-like event survived the analysis cuts. This result will be discussed later in this Chapter.

[5] The acquisition window length (set by the the maximum drift time of ionization electrons) scales with the vertical dimension of the detector and decreases when the drift field is increased. With a drift field of 200 V/cm, the maximum drift time is ~ 1 ms/m, while the activity of a cubic meter of atmospheric argon is 1.4 kHz.

The design goal for the DarkSide-20k stage is an exposure of 100 ton.y, achievable with 5 years of run of a 20 tons detector. The main features of the current and future phase of the DarkSide program can be summarized as follows:

- **Background suppression.** The experiment is placed underground, at the LNGS (*Laboratori Nazionali del Gran Sasso*) facility, to reduce cosmic rays irradiation. It is built with radio-pure materials and mounts low-radioactivity photo-detectors. The key point of the future development is the use of low-radioactivity argon, to strongly reduce the internal background.
- **Background identification.** The PSD is the main tool for the discrimination between nuclear recoils and external β- and γ-backgrounds. Additional discrimination is possible thanks to the different ratio between ionization and scintillation.

  Moreover, the dual-phase TPC design allows position reconstruction of the interaction vertexes. This means that surface events and multi-sited events are efficiently rejected.

In addition, both the current experiment and the next phase will be equipped with a high efficiency active neutron veto. By looking at the coincidence between TPC and veto events it is possible to reject neutrons that interact only once within the sensitive volume and then leave the TPC.

The neutron veto is made of a cocktail of liquid scintillator (Pseudo-cumene, PC), wavelength shifter (PPO) and TMB, $B(OCH_3)_3$, a molecule containing boron. The ^{10}B has a very high thermal neutron capture cross section (3840 barn) and its isotopic abundance is around 20%. With natural boron made TMB and a TMB concentration of 5% in the scintillator, the mean capture time of MeV neutrons is $\sim$ 22 μs [83] (the two quantities are inversely proportional).

The $^{10}B\ (n,\alpha)\,^{7}Li$ neutron capture reaction produces:

- a ^{7}Li in the ground state and one 1775 keV α with 6.4% BR
- an excited $^{7}Li^{*}$, along with a 1471 keV α with 93.6% BR. The de-excitation of the $^{7}Li^{*}$ implies the emission a 478 keV γ.

The emitted α particle is short-ranged in the scintillator mixture. If the neutron capture produced only γ's (as in the case of captures on Gd or H), the veto efficiency would be limited by the escape probability of the γ.

On the other hand, the α light output is expected to be heavily quenched (in the 40 - 60 keV electron equivalent range [83]). The requirement for using such a scintillator consists in keeping an high light yield (in order not to miss the α when emitted without the γ). Implementing the same technology in the DarkSide-20k phase is even more challenging, because of the larger dimensions. The veto light yield measured in DarkSide-50 is higher than 500 pe/MeV, making the detection of the single α largely possible.

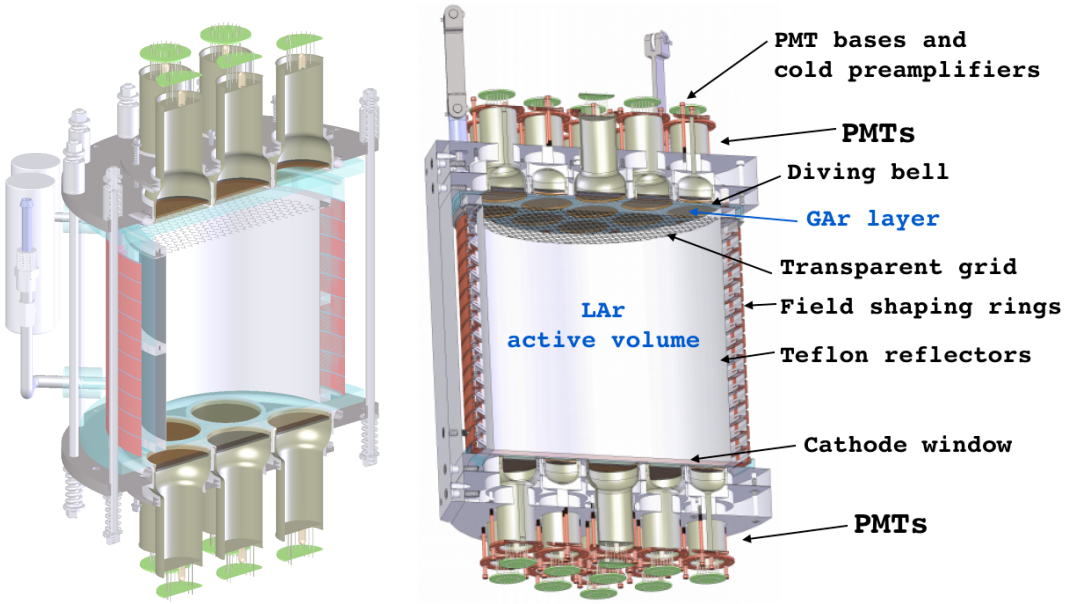

(a) The DarkSide-10 TPC (b) The DarkSide-50 TPC

Fig. 2.3 The DarkSide-10 and DarkSide-50 time projection chambers, cutaway drawings, not in scale. In both the drawings, the field rings are in copper red, the teflon reflector in white and fused silica in light blue. On top of the liquid volume is visible the stainless steel mesh for creating the extraction field. The 10 kg prototype was equipped with 10 3 inches PMTs, while 38 PMTs are mounted on DarkSide-50. The two TPCs are immersed in liquid argon in a vacuum cryostat.

2.3 The DarkSide-50 Experiment

Figure 2.4 shows the layout of the DarkSide-50 experimental setup. It is installed in the Hall C of LNGS (under 3400 mwe of rock), inside the water tank used as Counting Test Facility (CTF [84]) by the Borexino collaboration. The 11 m-diameter, 10 m-high cylindrical tank is filled with pure water and currently equipped with 80 large area PMTs (ETL 9351). It serves as water Cerenkov detector (WCD) for vetoing events induced by cosmic muons. The inner surfaces are covered with Tyvek reflectors, to maximize the light collection.

A 4 m diameter stainless steel sphere is placed at the center of the water tank, filled with 30 tons of liquid scintillator and mounting 110 low-radioacitivty and high QE photo-multiplier tubes (PMTs), the Hamamatsu R5912.

The TPC vacuum-insulated cryostat is hanging from the ceiling of the WCD into the liquid scintillator veto (LSV) sphere. Roughly 150 kg of liquid argon are necessary to fill the inner vessel and the re-circulation loop. The structure of the TPC (shown in Fig. 2.3 (b)) is made of teflon (PTFE) reflector. The cylindrical walls of the TPC are surrounded by 15 T-shaped copper rings for the uniform drift field creation. The sensitive volume cylinder (35.6 cm both diameter and height at warm) contains (46.4 ± 0.7) kg of liquid argon. The large uncertainty is mainly due to the uncertainty on the shrinking factor of teflon at the liquid argon temperature.

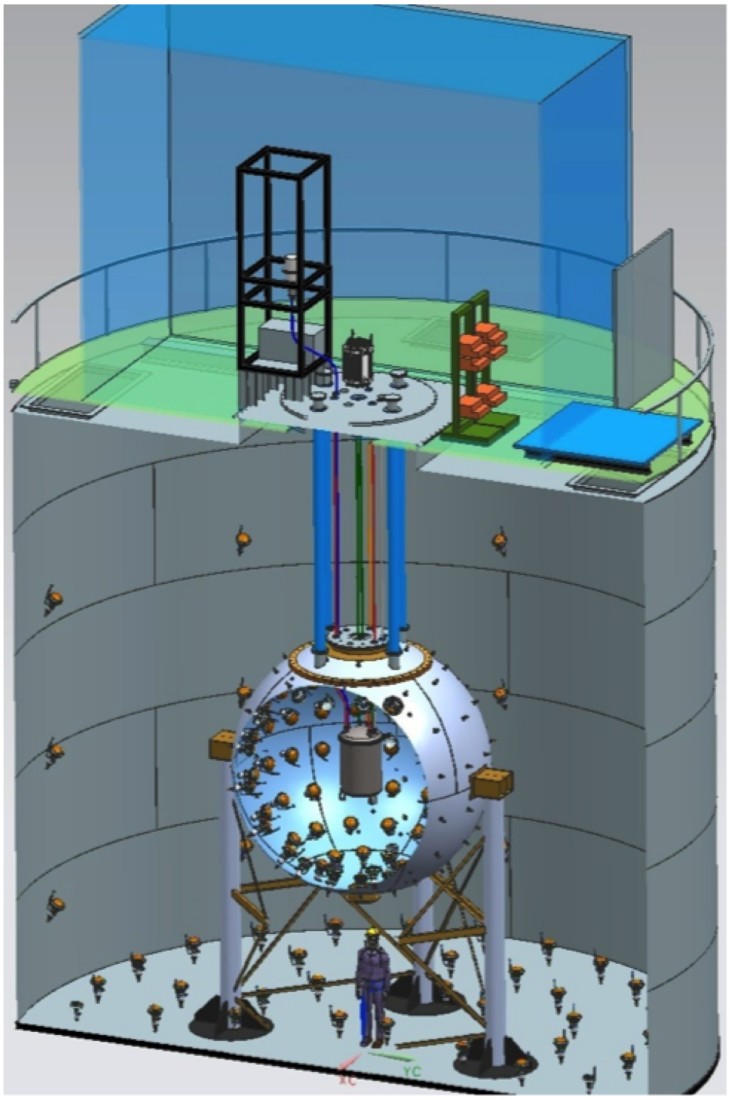

Fig. 2.4 The DarkSide-50 layout.

The top and bottom caps serve as support for the 38 Hamamatsu R11065 PMTs (3 inches area, high efficiency photocathode) and the PMT bases, including custom designed cold pre-amplifier.

The top and bottom surfaces of the cylindrical sensitive volume are quartz windows, 6 mm and 12 mm thick respectively. The top window acts as diving bell, so that a 1 cm gas layer can be maintained even when the TPC is fully immersed in liquid argon. At the gas liquid surface a stainless steel mesh is placed to maintain an higher extraction field in the gas. The wire are 10 μm thick and separated by 2 mm. The high voltage electrodes, evaporated on both the surfaces of the quartz windows, are made of indium tin oxide (ITO). The inner window faces serve as anode (top) and cathode (bottom) while the outer faces are maintained at the mean PMT voltage.

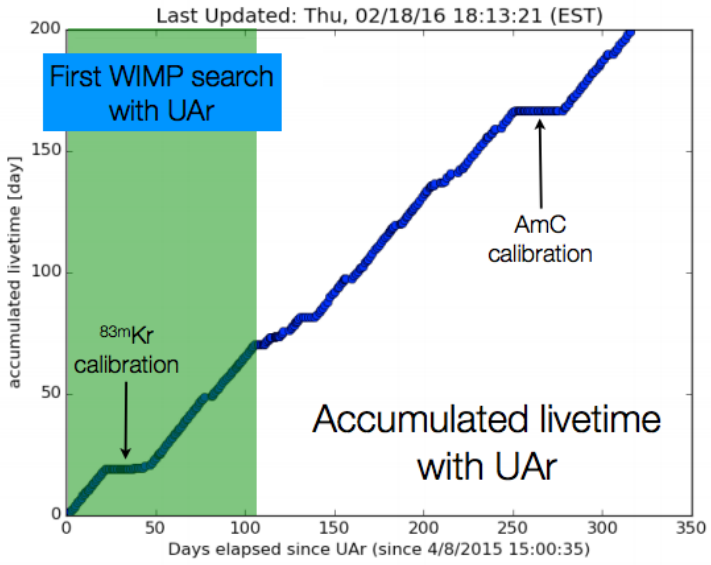

Fig. 2.5 Accumulated lifetime since the 8th April 2015, last updated on the 18th February 2016.

The nominal drift, extraction and electroluminescence fields are 200 V/cm, 2.4 kV/cm in the liquid and ~ 4.2 kV/cm in the gas respectively. The choice of the drift field was driven by the evidence of S1 quenching for higher drift field.

The inner surfaces of the TPC are coated with TPB (Tetra-phenyl-butadiene) a typical wavelength shifter, to convert the 128 nm scintillation light of liquid argon in visible light (the TPB emission peak occurs at 420 nm).

2.3.1 Electronics, Detector Operation and Stability

The electronics and data acquisition systems are separated for the TPC and the vetoes, but thanks to a common run controller several data taking configurations are allowed. Even if an independent trigger for each detector is possible, the WIMP search mode is designed to have a shared trigger (the waveforms of the three detectors are acquired when at least three TPC PMTs give signal in a 100 ns time window).

The cold pre-amplifiers allow to operate the TPC PTMs at low gain (and so low bias voltage), to prevent the observed sporadic light emissions, while maintaining high signal-to-noise ratio. The maximum dynamic range of the electronics chain is set by the voltage swing of the amplifier to the equivalent of ~ 1500 pe. At room temperature, the signal coming from the TPC PMTs is further amplified 10 times and digitized at 250 MHz frequency with a 12 bits board.

The detector is successfully taking data in stable mode since October 2013. In the first phase of the atmospheric argon (AAr) data taking the total event rate exceeded 50 Hz. The energy spectrum was dominated by the ^{39}Ar events. In order to save disk space, events with

more than ~ 600 pe were tagged and prescaled by a factor 33. The total acquisition rate was reduced to 13 Hz.

In the current data taking, started in April 2015 with an underground argon (UAr) fill, the total acquisition rate is of the order of 1.5 Hz and no prescaling is required.

In the WIMP search configuration, the detector is acquiring data with a livetime loss of roughly 2%. The plot of the accumulated lifetime, including the calibration campaigns, is shown in Figure 2.5. This efficiency loss is mainly due to occasional maintenance and to periodical laser calibration of the PMTs. For the latter, the light from a pulsed laser source is brought inside the TPC by means of an optical fiber. The feed-through of the fiber is placed in the vicinity of the central PMT in the bottom array, pointing upwards. Two laser runs are taken daily and the single electron response (SER) is evaluated with a statistical method independent on any assumption on the expected functional shape. A 2.5% decrease in the mean value of the SER has been observed over the course of 7 months.

Electronegative impurities in LAr can capture ionization electrons and induce a S2 intensity dependence on the drift distance. The liquid argon purity, thanks to the continuous re-circulation and filtering, is improving over the time. The currently measured value of the electron lifetime is compatible with being > 5 ms. When compared to the maximum drift time, it corresponds to a maximum S2 reduction of 7% for events at the bottom of the TPC with respect to events at the top.

2.3.2 Calibrations

We deployed several calibration sources to accurately evaluate the TPC response. Gaseous ^{83m}Kr can be injected inside the argon re-circulation loop. This nuclide decays to the ground state emitting two conversion electrons with energy of 32.1 and 9.4 keV with half-life of the intermediate state of 152 ns [85]. The two βs are so close in time that the two scintillation pulses partially overlap. The double decay is treated as a single one with reference energy value of 41.5 keV. The lifetime of the decay is 1.83 hrs: the detector is free of ^{83m}Kr 12 hours after the injection.

Several ^{83m}Kr calibration campaigns have been performed during the data taking for both the AAr and the UAr fills and for different drift fields. As an example, Figure 2.6 shows the S1 spectrum obtained during the AAr campaign with the ^{83m}Kr source at null drift field. Thanks to these data is possible to measure the light yield of the detector, summarized in Table 2.1 for the AAr and UAr campaigns. The ~ 2% increase in the light yield of the UAr data sample must be attributed to an upgrade of the reconstruction software between the two campaigns. The dominant uncertainty is due to the systematic error on the calibration of the PMTs.

Run	Drift Field	Light Yield [pe/keV]
AAr	200 V/cm	7.0 ± 0.3
AAr	Zero	7.9 ± 0.4
UAr	200 V/cm	7.3 ± 0.1
UAr	Zero	8.1 ± 0.2

Tab. 2.1 Light yields measured in DarkSide-50 using the ^{83m}Kr calibration.

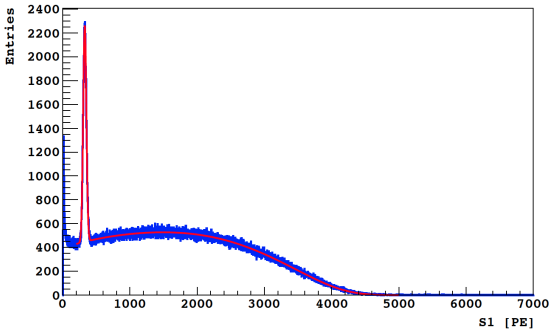

Fig. 2.6 S1 spectrum acquired by DarkSide-50 with the ^{83m}Kr source on obtained with null drift field and AAr fill of the detector. The ^{83m}Kr peak is superimposed to the ^{39}Ar beta spectrum.

2.3.2.1 Response Corrections

By selecting events in the ^{83m}Kr peak we found some asymmetries in the TPC response. In particular the average light yield varies along the vertical direction by $\pm \sim 10\%$ with respect to the center of the TPC. The events at the bottom produce more light with respect to the ones at the top. The reason for this is believed to be the total reflection induced by the gas layer on top of the liquid volume. On the other hand, the S1 radial dependency is smaller than 3%.

The S2 signal is instead strongly varying along the radial direction. The events at the center have S2 more than 3 times larger with respect to the events at the maximum radius. The reason for this effect is the non-uniformity of the extraction field, due to the sagging of the fused silica window or to the non-uniform thickness of the gas pocket.

Since these effects are well reproduced by the MC simulation of DarkSide-50, we will discuss them in Chapter 3.

2.3.2.2 External Calibrations

Thanks to the CALibration Insertion System (CALIS [86]) we deployed several sources, external to the TPC. The CALIS system allow to dip the source from the top of the WCD, along the vertical direction, until it reaches the same height of the cryostat. We chose three reference positions, corresponding to the vertical position of the center of the TPC and its top and bottom surfaces.

We deployed γ sources (^{57}Co, ^{133}Ba, ^{137}Cs and ^{22}Na) and neutron sources (^{241}Am^{9}Be, AmBe in what follows, and ^{241}Am^{13}C, or AmC).

The ^{57}Co decay consists in the emission of one electron and some gammas. The three main gamma lines are 122 keV (85.6%), 136.5 keV (10.7%) and 14.4 keV (9.16%). The ^{133}Ba β decay is accompanied as well by several gammas. The three main lines are 356 keV (62%), 81.0 keV (34%) and 302.9 keV (18.3%). The ^{137}Cs is another β emitter, producing also a gamma line at 661.6 keV (B.R. 85%). The activity of these sources is of the order of the kBq.

The chosen ^{22}Na source has instead a larger activity (~ 30 kBq). The data taking was performed without the gas pocket, because of the high trigger rate (> 100 Hz). The motivation for such a test was the possibility of acquiring a large sample of electron recoils to improve our understanding of the PSD capabilities.

The ^{22}Na β^+-decay produces, after the annihilation of the positron, a pair of 511 keV gammas (and a 1274 keV one). The energy spectrum of the TPC events is peaked in the low energy region. In one day of data taking, a statistics almost equivalent to the entire AAr campaign data has been collected. The analysis of these data in currently ongoing, while the source has not been used further because of some fatigue effect shown by the TPC PMTs.

Three neutron sources have been used to calibrate the TPC response to nuclear recoils and to measure the veto neutron capture detection efficiency. They all contains ^{214}Am and the working principle is the following: the α's emitted by the ^{214}Am are absorbed in a material with high (α, n) neutrons production cross section (^{9}Be or ^{13}C).

Two AmBe samples with different activities (10 Bq and 2000 Bq) were deployed. The emitted neutron spectrum is broad and relatively well known. Three decay channels are available for the ^{9}Be:

- single neutron with 36% BR.
- one neutron accompanied by a 4.4 MeV gamma (from ^{12}C de-excitation after α-absorption) with 65% BR.
- one neutron accompanied by 4.4 MeV and 3.2 MeV gamma for the remaining 3%.

The ^{241}Am gamma activity for the 10 Bq neutron activity source is about 170 kBq. The most important line is the 60 keV gamma with branching ratio of 35%. To prevent these low-energy gammas to reach the TPC or the veto, a minimum shield of 2 mm of Pb must be placed around the source.

We also produced and deployed an AmC source. The main advantage of this source is the lack of correlated gamma emission. This can be achieved by slowing down the α's produced by the ^{241}Am with a thin gold foil placed between the Am and the C absorber. Neutrons are emitted at a rate of roughly 1 Bq and have a broad energy spectrum centered around 4.6 MeV.

The external source gave important inputs for the calibration of the DarkSide-50 MC tool. We will give a discussion of this calibration in Chapter 3.

2.4 The DarkSide-50 WIMP Searches

Two main papers were published in the last three years by the DarkSide-50 Collaboration. In the first one [3] we reported on the analysis of a first 50-days lifetime data-set, acquired with an atmospheric argon fill. This data-set is largely dominated by ^{39}Ar β-spectrum. This result highlighted the power of the pulse shape discrimination: we collected a large statistics of electron recoils (1.5×10^{7}) in the [8, 40] keV$_{ee}$ energy range and we did not find any WIMP-like

Period	Experimental phase	Scintillator mixture
Nov. 2013 - June 2014	Phase-I	PC 50%, TMB 50%, PPO 2.5 g/l
Feb. 2015 - present	Phase-II	PC 95%, TMB 5%, PPO 1.4 g/l

Tab. 2.2 Scintillator mixtures used in the different periods of DarkSide-50 running. Fractions of PC and TMB are mass fractions

candidate. This large statistics corresponds to more than 20 years of DarkSide-50 run with a UAr fill.

The second publication [4] is dedicated to the analysis of the first 70 days lifetime data-set obtained with UAr. DarkSide-50 is the first experiment to run with a depleted argon fill and the measured depletion factor is ~ 1400.

The limit on the cross-section calculated by combining the AAr and UAr exposure (2.0 $\times 10^{-44}$cm^2 for a WIMP mass of 100 GeV/c^2), is currently the best one obtained with an argon target.

The elastic scattering of a WIMP off an Ar atom is expected to produce a single sited nuclear recoil with no coincident energy deposit in the vetoes. The AAr and the UAr data-sets have been taken with two different veto configurations. During the first phase the LSV was loaded with 50% high-activity TMB, producing 150 kHz of ^{14}C events in the full veto (33 t). Since the high-rate can reduce the veto efficiency, the TMB has been replaced before the UAr data taking (the current mixture is 95% PC and 5% TMB). The veto acquisition window was than extended from the initial width of 70 μs to 200 μs to account for the larger mean neutron capture time. The estimation of the veto efficiency is discussed in Chapter 4. In Table 2.2 is reported the veto composition for the different phases of the data taking.

Besides the LSV, additional discrimination between neutrons and WIMP candidates is done by looking at the number of interactions in the sensitive target. WIMPs are expected to interact only once in the sensitive target, while the mean free path in LAr for a $\sim$ MeV neutron is of the order of 10 cm. A multi-sited event will show multiple ionization signals.

In addition to this, to reject the $\gamma-$ and $\beta-$induced ER background we can rely on the PSD.

At the nominal drift field of 200 V/cm, the electron drift velocity is 0.93 ± 0.01 mm/μs. The maximum drift time is ~ 376 μs. After each trigger, a 440 μs acquisition window is opened and the PMT waveforms are acquired. Raw data are processed by the reconstruction software, which takes care of:

- the identification of the baseline mean and RMS,
- the calculation of the sum of the 38 channels,
- the identification of the pulses (start and end times, duration, integral, f_{90}...),

- the extraction of other parameters useful for the analysis and the calculation of corrected variables, e.g. S1 corrected by the vertical position or S2 corrected by the radial distance,
- the integration of the information from the veto DAQ system.

We developed a set of standard cuts to identify WIMP candidates. I will briefly discuss these cuts in the next Section.

2.4.1 Event Selection

The set of standard cuts is defined for the AAr run and then slightly tuned to be applied to the UAr analysis. A preliminary selection is applied to remove full runs identified as problematic from the data-sets. We distinguish between quality cuts (that imply a net loss of lifetime) and physics cuts. A summary of the cuts is reported in Table 2.3.

2.4.1.1 Quality cuts

- **Q_CUT 1**. We select events for which all the PMTs were active and the waveforms are correctly acquired for all the channels.
- **Q_CUT 2**. Only events for which the baseline was found for each channel are selected.
- **Q_CUT 3**. We removed short-lifetime events. The electron emission (due to photo-ionization) from the cathode, when illuminated with scintillation light, is responsible for low energy signals (echoes) that follows the scintillation pulse by a fixed amount of time, corresponding to the maximum drift time. The echo production probability is proportional to light pulse intensity, so that S2 signals are more likely to produce echoes. Echoes will be discussed in more detail in Appendix B since their presence can affect the lifetime calculation.

  A fixed inhibit of 810 μs is employed after each acquisition window in order to prevent triggers on echoes or on S2 tails. We only accept events which follow the previous event by at least 1.35 ms (440 μs acquisition window +810μs inhibit time). The mean event rate during the AAr run was about 50 Hz, reduced to 13 Hz after the application of a prescale rule (a suppression by a factor of 33 of the events with more than 600 pe in the first pulse). The pile-up probability is respectively ∼7% and ∼ 2%, implying a net reduction of the lifetime. The mean acquisition rate during the UAr campaign is of the order of 1 Hz and the pile-up probability is negligible.
- **Q_CUT 4**. We remove events with a lifetime larger than 1 s in the AAr data-set (the mean acquisition rate is larger than 10 Hz even after the prescale of high energy events). Those events are related to occasional DAQ problems. This cut is not applied in the UAr analysis.

Cut	Cut Description	AAr data-set	UAr data-set
Q_CUT 1	Number of channels	== 38	
Q_CUT 2	Sum channel baseline found		
Q_CUT 3	Lifetime + inhibit time	> 1.35 ms	
Q_CUT 4	Lifetime	< 1 s	—
Q_CUT 5	Veto is present		
CUT 6	Prompt window charge	< 10 pe	< 1 pe
CUT 7	High energy LSV or CTF	See text	
CUT 8	Number of pulses	(==2) OR (==3 AND has_s3)	
CUT 9	Pulse start in the expected 100 ns trigger time window		
CUT 10	No S1 pulse saturation		
CUT 11	Max fraction of light on 1 PMT (%)	< 99%	< 95%
CUT 12	Valid S2:	f_{90} of S2 < 0.2	
CUT 13	Minimum S2:	S2 (corrected) > 100	
CUT 14	S1 range:	60 < S1 < 450	20 < S1 < 450
CUT 15	Drift time FV:	(40.0 μs < tdrift < 334.6 μs)	

Tab. 2.3 Summary of the standard quality and physics cuts. Cuts are slightly tuned for AAr and UAr analysis. Refer to the text for more details.

- **Q_CUT 5**. Only events with corresponding data from the veto detectors are considered. The veto cuts are discussed in the physics cuts section.

The effect of quality cuts is a net reduction of the lifetime (by roughly the 4.5% for both the AAr and UAr campaigns). After the quality cuts, the available statistics for the AAr corresponds to 47.1±0.2 days lifetime. For the UAr, the lifetime after the application of these cuts is 70.9 days.

2.4.1.2 Physics cuts

- **CUT 6**. Events with a prompt coincidence in the veto are rejected. The prompt coincidence is typically attributed to a thermalization signal of a radiogenic neutron. A coincidence window is defined around the TPC trigger. A fixed threshold is defined according to the data-set and events with a signal above the threshold are rejected. For the AAr analysis the prompt window extends from -10 ns to 200 ns around the TPC trigger and the detection threshold is set to 10 pe. During the UAr data acquisition the rate in the veto was strongly suppressed and so the accidentals rate. The threshold has been lowered to 1 pe and the prompt window extends from -50 ns to 250 ns around the TPC trigger. The improvement of the veto efficiency due to the increased sensitivity to the thermalization signal is discussed at the end of Section 4.1.
- **CUT 7**. Events with a signal in the veto compatible with a neutron capture signal are rejected. During the AAr run, the mean capture time of neutrons in the LSV was 2.2 μs. Two sliding delayed regions of interest (ROIs) are defined for the capture signals. The event is rejected if more than 80 pe are found in any 300 ns window included in the [300

ns, 8.8 μs] interval. This signal is attributed to the capture on ^{10}B. The second window is required to veto events which thermalize in detector materials with larger capture time (such as stainless steel). Event with more than 110 pe in any 300 ns window going from 8.8 μs to the end of the acquired veto waveform are rejected.

After the upgrade of the veto and the TMB removal, the mean neutron capture time increased to 22 μs. A single 500 ns sliding delayed window is defined to account for capture signal. The detection threshold is fixed to 3 pe (6 pe) and the acquisition window to 140 μs (200 μs). In addition to this, events with more than 3 pe in a 500 ns window prior the TPC signal (up to 8 μs) are rejected, to prevent events with a gamma interaction in the veto and a delayed neutron interaction in the TPC.

Finally, muon events are defined as events with more than 200 pe in the WCD (for AAr data-set) or >400 pe in the WCD and >1000 in the LSV (UAr data-set). All events acquired within 2 s after a muon are rejected.

- **CUT 8**. Events with more than two pulses (one S1 and one S2) are rejected. Events with three pulses are accepted if the third pulse is consistent with an echo of the S2 pulse.

  The acceptance of this cut is reduced by the loss of events with a more sophisticated topology. For instance, events with S1 echoes or both S1 and S2 echoes are rejected. Other acceptance losses are due to pile-up and to the failing in two pulses separation. The pulse-finder algorithm has ∼ 1 efficiency in the energy range of interest, but when two pulses are too close it can fail in separating them.

  The total acceptance for this cut is $0.95^{+0.00}_{-0.01}$ in the AAr data-set. We don't expect a large variation in the UAr run, even if the pile-up rate is larger in the AAr data-set.

- **CUT 9**. The cut is designed to remove events for which the first pulse was not reconstructed in the expected trigger window (100 ns width). This cut mainly removes "junk" events like triggers on the tails of previous events.

- **CUT 10**. Events saturating the electronics are rejected. The S1 saturation starts to appear for S1 > 1000 pe, meaning that in the WIMP search region we don't expect acceptance losses due to saturation.

- **CUT 11**. The maximum light fraction cut removes events concentrated on a single PMT. They are believed to be Cerenkov events (their f_{90} is ≈ 1), as confirmed by MC simulations. The cut is S1 and channel dependent. We implemented the cut looking at the light fractions distribution for each PMT as a function of the energy and cut a fixed fraction of the tails of these distributions. The relative fraction of Cerenkov events is increased in the UAr campaign, due to the lower rate of other events. For the AAr (UAr) analysis we retained 99% (95%) of the events.

- **CUT 12**. We applied some pulse shape discrimination on the S2 signal. In particular we required S2 to have $f_{90} < 0.2$. The typical S2 signal rise time is $\sim 1\mu s$ so that f_{90} is typically ~ 0.05.
- **CUT 13**. Since the typical S2 signal is > 1000 pe, we also require the S2 pulse amplitude, corrected by the radial dependence, to be larger than 100 pe.
- **CUT 14**. We selected events in the [60, 450] pe range for the AAr data. Assuming a constant light yield of (7.0 ± 0.3) pe/keV, achieved in the AAr period and very close to the measured light yield in the UAr campaign, this range corresponds to [8.5, 64.3] keV_{ee}. The upper edge of the energy range is arbitrarily chosen. However, the impact of moving it on the experiment sensitivity is minimum because of the exponentially decreasing shape of the expected energy spectrum of WIMP-induced nuclear recoils.

  The lower edge of the energy range depends instead on the collected statistics, in the following way. We want to maximize the NR acceptance while minimizing the ER background. We require the ER background to be lower than 0.1 events and choose the S1 threshold accordingly. The NR and ER f_{90} distributions are well separated for S1 > 100 pe. At low energy they tend to overlap and, as the collected statistics of ER increases, the NR acceptance decreases. In the 70 days UAr campaign data, the energy threshold is set to S1 ≈ 20 pe. At this value of S1 the NR acceptance is 0 because of the ER leakages.
- **CUT 15**. The fiducial volume is limited only in the vertical direction. The vertical position of the event is determined by the electron drift time. We accepted only the events with 40.0 μs < tdrift < 334.5 μs. The maximum drift time is ~ 376 μs. The same cut is applied in both the AAr and UAr data analysis. The total fiducial mass after this cut is (36.9 ±0.6) kg. The uncertainty on the FV comes primarily from the uncertainty on the teflon shrinking factor at low temperature.

  We did not apply a radial fiducialization, even if the detector allows a good resolution in the x-y plane (< 1 cm). From material essay we actually expect surface contamination of $< 10\,\alpha/d/m^2$. This class of events has been investigated but none of these events survive the previous standard cuts [87].

Table 2.4 shows the acceptance of the physics cuts, as estimated during the AAr analysis. They are substantially flat over the whole WIMP expectation energy range. Figure 2.7 shows the dependence on the energy of the cut acceptance calculated during the UAr analysis (mainly thanks to the AmBe calibration data). The reduction of the asymptotic value down to ~ 75% in the WIMP region is mainly due to the different definition of the maximum light fraction cut (the CUT 11 was designed to remove 1% of the events in the AAr data-sets and 5% in the UAr data-set).

Cut	Acceptance
CUT 6: prompt LSV	0.95
CUT 7: delayed LSV and WCD	0.94
CUT 8: single scatters	$0.95^{+0.00}_{-0.01}$
CUT 9: first pulse time	$1.00^{+0.00}_{-0.01}$
CUT 10: no S1 saturation	1.00
CUT 11: max S1 fraction per PMT	0.99
CUT 12: S2 pulse shape	1.00
CUT 13: mimum S2	$0.99^{+0.01}_{-0.04}$
CUT 14: S1 range	1.00
Total	$0.82^{+0.01}_{-0.04}$

Tab. 2.4 Cuts acceptance for the AAr data-set. Errors are systematics, since the statistical error is negligible.

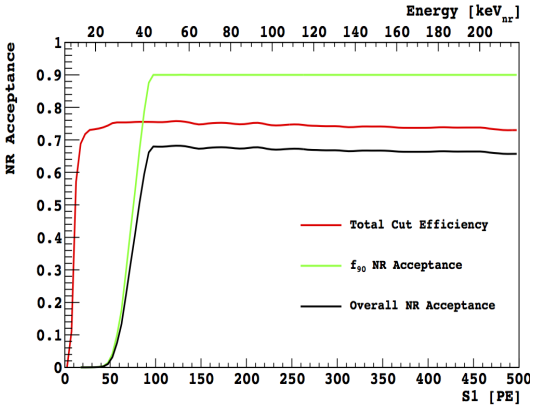

Fig. 2.7 Combined acceptance of the physics cuts (red), acceptance of the f_{90} NR cut (green) and the final cumulative NR acceptance in UAr data (black) as a function of S1.

2.4.2 Null Result of the WIMP Searches

For both analyses we defined a WIMP search region in the (S1,f_{90}) plane, for which the NR acceptance is high enough. The WIMP search region extends from 60 pe (20 pe) to 460 pe for the AAr (UAr) data. The WIMP search regions are shown in Figures 2.8 (a) and (b) along with all the collected data (events in the energy range passing the selection cuts). The lower edge of the WIMP box comes from the intersection of the 90% NR acceptance curve with the curve corresponding to the extrapolated 0.01 ER events/(5-pe bin) leakage into the WIMP search region.

We adopted two procedures to compute the NR acceptance bands. For the AAr data-set, we relied on the SCENE measurements [78, 88]. The SCENE experiment aimed to the characterization of nuclear recoils in liquid argon. The experimental setup consists in a small TPC (to avoid multiple interactions) exposed to a pulsed neutron beam. The neutron beam is pointing the center of the TPC and a neutron detector can rotate around the TPC. Since the scattering angle is known, the energy of the neutron is reconstructed by the kinematics of the interaction.

The SCENE Collaboration measured the NR f_{90} distributions for several NR energies and determined the corresponding acceptance curves. We linearly interpolated between the discrete points (for 90% acceptance) after scaling for the difference of the detectors light yields.

For the UAr data-set, we used the outcome of DarkSide-50 NR calibration with an AmBe source. The result is in good agreement with the predictions made from SCENE data, as shown in Figure 2.9.

The prediction on the ER leakages in the WIMP search region are obtained with an analytical fit of the f_{90} distribution for 5 pe S1 slices. The model describes the ratio of two

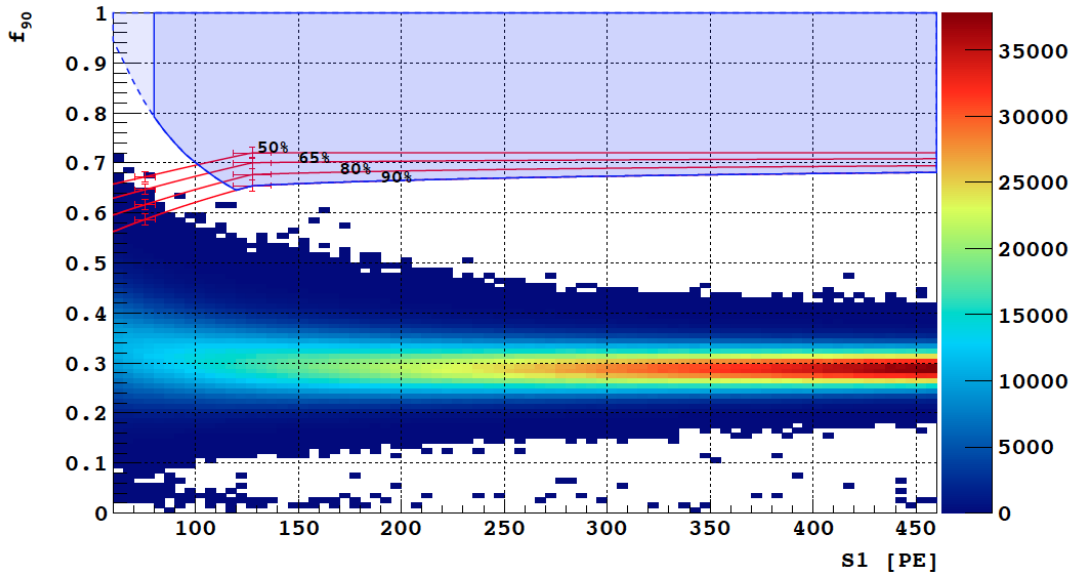

(a) AAr data

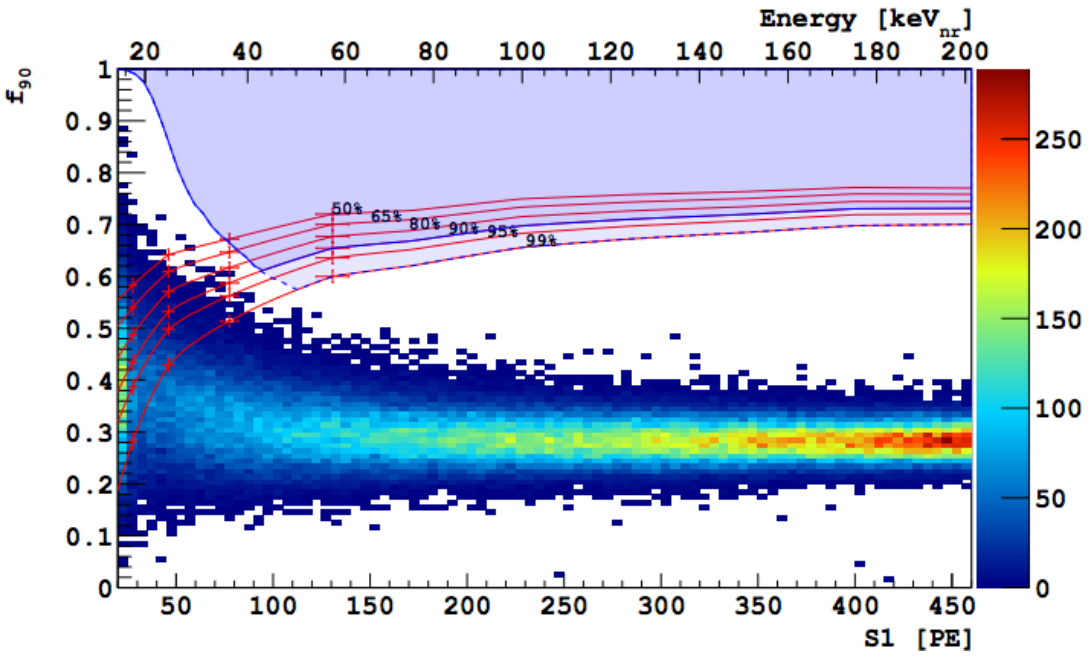

(b) UAr data

Fig. 2.8 Distribution of events in the f_{90} vs S1 plane surviving all cuts in the energy region of interest for the AAr (top) and UAr (bottom) campaigns. The shaded blue are with solid blue outline represents the WIMP search region. The red curves represents the NR acceptance cruves, while the points are directly derived from the SCENE measurements. Refer to the text, and especially to Chapter 5, for the description of the derivation of the f_{90} contours.

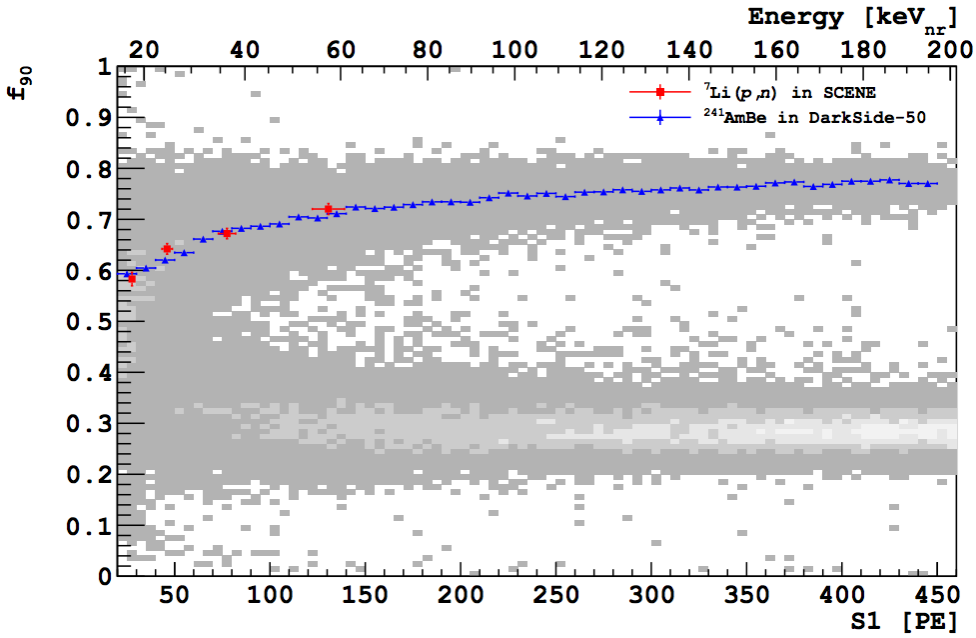

Fig. 2.9 f_{90} NR median vs. S1 from a high-rate in situ AmBe calibration (blue) and scaled from SCENE measurements (red points). Grey points indicate the upper NR band from the AmBe calibration and lower ER band from γ-ray- and β decay-induced background events. Events in the region between the NR and ER bands are due to inelastic scattering of high energy neutrons, accidentals, and correlated neutron and γ-ray emission by the AmBe source.

correlated normally distributed variables (the prompt and prompt+late fractions of S1). I will discuss the calculation of the ER leakages in the Chapter 5.

It should be mentioned that the presented results does not make use of the ionization to scintillation ratio cut (S2/S1). The pulse shape discrimination technique is enough to guarantee the background-free condition in these datasets. However, the discrimination based on the S2/S1 ratio represents an additional tool for event-by-event rejection of WIMP candidates.

2.4.3 Projected Sensitivity

The combined analysis of the AAr and UAr data-sets brings to the exclusion curve shown in Figure 2.10. To compute the limit, we implemented a toy MC, scanning over a wide mass range according to the following procedure:

1. For the given WIMP mass, compute the differential event rate dR/dE for a large value of the WIMP-nucleon cross section $\sigma_0 = 10^{-37}$ cm^2.
2. Generate a sample of nuclear recoil energies E_r, for a DarkSide-50 equivalent exposure.
3. Compute S1 and for these recoils, using the DarkSide-50 light yield and resolution and including the quenching.
4. Sample f_{90} for the generated events according to the analytical model.

Mass	Cross section
100 GeV	2.0×10^{-44} cm^2
1 TeV	8.6×10^{-44} cm^2
10 TeV	8.0×10^{-43} cm^2

Tab. 2.5 Summary of the limits on the spin independent WIMP-nucleon cross section obtained by the AAr and UAr DarkSide-50 combined data at 90%.

5. Measure the number N of nuclear recoils enter the WIMP search region.
6. Scale the cross section by $2.3/N$ to get the sensitivity (at the 90% CL) for the given WIMP mass.

From the combined data set, we derived the upper limits on the spin independent WIMP-nucleon cross section summarized in Table 2.5. The exclusion curves are shown in Figure 2.10, along with the curves from other experiments.

2.5 Conclusions

I firstly discussed in this Chapter the basics of the WIMP direct detection technique with a noble liquid target dual-phase TPC. Noble liquids (xenon and argon in particular) are particularly well suited for this kind of searches because of their numerous advantages with respect to other materials. Liquid xenon based experiments are at the moment the most sensitive, but the DarkSide Collaboration demonstrated that argon is a valid alternative: the internal radioactivity can be suppressed thanks to the extraction of argon from the underground and the pulse shape discrimination offers a unique handle for the background rejection.

I then illustrated the DarkSide program, which aims to the construction of a large TPC (20 t active mass, designed to reach a 100 t.y exposure) though a staged approach. The prototype phase (DarkSide-10) is concluded and the intermediate detector (DarkSide-50) is currently running.

I described in the last part of the Chapter the results of the WIMP searches performed by the DarkSide-50 experiment.

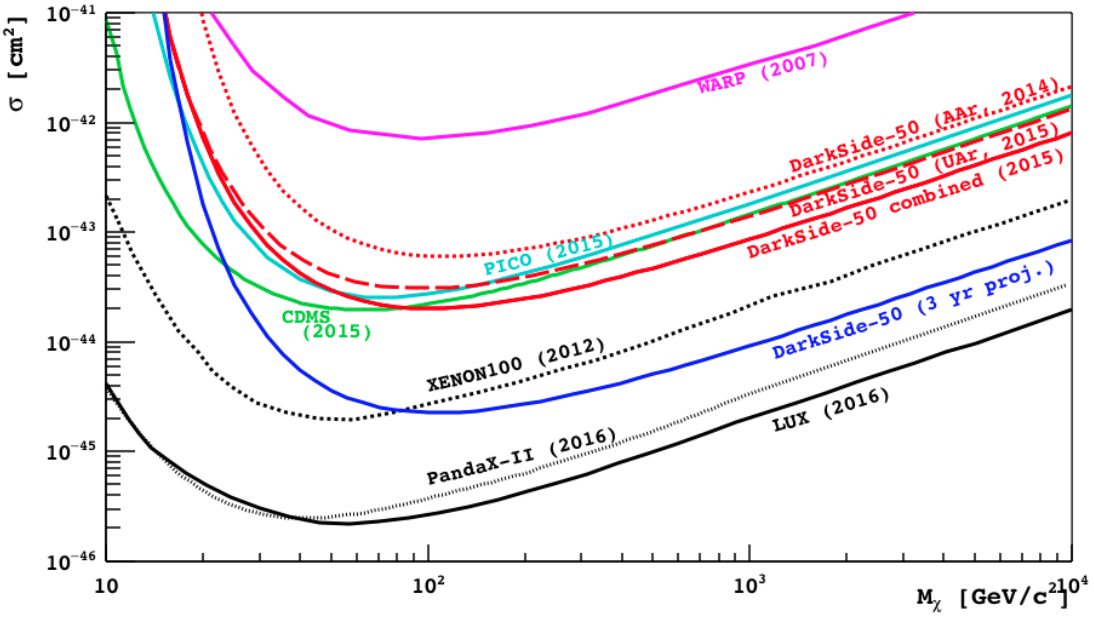

Fig. 2.10 Spin-independent WIMP-nucleon cross section 90% C.L. exclusion plots for the DarkSide-50 AAr (dotted red) and UAr campaigns (dashed red), and combination of the UAr and AAr campaigns (solid red). Also shown are results from LUX [64] (solid black), XENON100 [65] (dashed black), PandaX-I [66] (dotted black), CDMS [89] (solid green), PICO [68] (solid cyan), ZEPLIN-III [90] (dash dotted black) and WARP [2] (magenta).

Chapter 3

G4DS, the DarkSide simulation tool

I will discuss in this Chapter G4DS , the DarkSide simulation tool. I will firstly give a general introduction on the simulation structure (Section 3.1), while Section 3.2 is dedicated to the simulation of the electronics.

In Section 3.3 I will discuss the simulation of the TPC response both to electron and nuclear recoils. I will describe as well the PARIS model (*Precision Argon Response for Ionization and Scintillation*), a custom model we developed and tuned for both S1 and S2.

In the last Section I will briefly discuss the calibration of the liquid scintillator veto (LSV).

3.1 A GEANT4 based MC code

G4DS is a GEANT4-based (GEANT4.10.0 [91]) simulation toolkit specifically developed for DarkSide. The code is designed with a modular architecture in order to describe the energy and time responses of all the detectors foreseen by the DarkSide program, namely DarkSide-10, DarkSide-50 and DarkSide-20k. For each of them, G4DS provides a rich set of particle generators, detailed geometry descriptions, properly tuned physical processes and the full optical propagation of photons produced by scintillation in liquid argon and by electroluminescence in gaseous argon.

The main goals of G4DS are: the accurate description of the light response (to calibrate the energy responses in S1 and S2 and the time response expressed by the f_{90} variable); the tuning of the analysis cuts and the estimate of their efficiencies; the prediction of the electron and nuclear recoil backgrounds.

G4DS tracks photons until their conversion to photoelectrons, which occurs when a photon reaches the active region of a photosensor and survive to the quantum efficiency. The conversion of the photoelectron into a charge signal is handled by the electronic simulation described in the next section.

The event structure in G4DS contains primary and optional variables. Primary variables includes information related to the particle generation, like the particle type, initial kinetic energy and position, and to the detector observable (the time and photo-sensor id of each

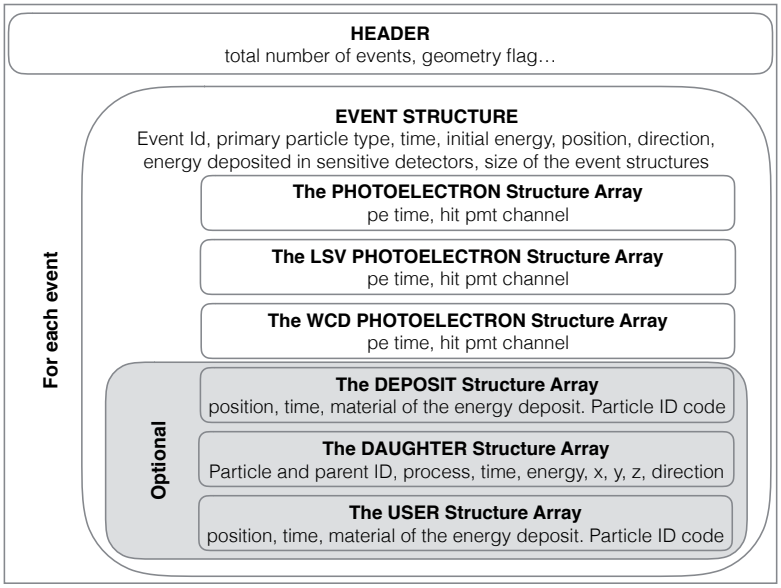

Fig. 3.1 The G4DS output file structure.

detected photon). Optional variables can be activated either to improve the comprehension of the physical processes, by storing each energy deposit, secondaries directly produced by the generated particle, or photon absorption on any detector material, or to debug the code (developer custom variables). The event structure, summarized in Figure 3.1, is written so that, if the optional variables are disabled, there is no loss of disk space.

Each DarkSide experiment is composed by the detector core, the TPC and a veto system. For DarkSide-50 and DarkSide-20k, the veto system includes two detectors: a liquid scintillator sphere, surrounding the TPC, and an external water-based detector. Each of them is accurately described in G4DS, but, if needed, can be independently de-activated in order to reduce the CPU time required for the simulation.

A particular attention was dedicated to the description of the physical processes. Despite in G4DS there is the possibility to choose between different electromagnetic physics lists, the *G4EmLivermorePhysics* perfectly fits with the energy range and the accuracy required by DarkSide. For what concerns the hadronic physics lists, the need of a very high accuracy in the low energy neutron propagation, from fraction of eV to a few MeV, obliged us to define a custom made one based on high-precision models for neutron interactions. Nonetheless, the standard GEANT4 hadronic physics lists are available and can be activated to study a different type of events, like the cosmic muon propagation and the production of cosmogenic isotopes.

The light generation in liquid and gaseous argon required a dedicated custom–made new GEANT4 physical process, since effects like excitation, ionization, nuclear quenching, and electron-ion recombination effects are poorly known in argon, especially in presence

of electric field. We developed a theoretical model, called PARIS (Precision Argon Recoil Ionization and Scintillation), based on an effective description of the recombination effect, which, once opportunely tuned on calibration data, is able to provide an accurate description of the light response in both S1 and S2. A dedicated section of this chapter is devoted to the description of the PARIS model.

Another critical ingredient of G4DS is the tuning of optical parameters of the materials, through which light is propagated, and of the surfaces, where light can be absorbed, reflected, or diffused. The tuning of the optics was entirely based on properly chosen observables: those must be independent on the energy and type of the particle responsible of the light generation, to avoid degeneracies with the tuning of the PARIS model. As described in Section 3.3.1, the variables related to the channel occupancy and asymmetries in the collection of the light between the top and bottom PMT arrays do not require any knowledge about the amount of deposited energy and represent the best candles through which optics can be tuned.

G4DS is equipped with several event generators, in order to meet the specific needs of each physics goal. Beyond the simplest one, the Particle Gun, G4DS can generate specific forbidden beta decays, like the ^{39}Ar and ^{85}Kr ones, complex vertexes, single radioactive decays and chain segments, cosmic muon and neutron fluxes as measured at LNGS, and AmBe and AmC neutron sources. In this context, it is worth to mention that G4DS accept also as input custom made FLUKA [92] and TALYS [93] simulation outputs: the first one to study cosmogenic isotope productions and the second for the prediction of (α,n) neutron energy spectra and hence the evaluation of the nuclear recoil background.

3.2 The Simulation of the Electronics

The reconstruction of DarkSide-50 data is managed by a dedicated software (`darkart`), based on the `art` framework [94]. The waveforms of the TPC photomultipliers are stored for each trigger and passed to the reconstruction algorithms chain. Those algorithms take care of the baseline subtraction, identification and integration of the pulses (S1 and possibly multiple S2's), extraction of several parameters useful for the analysis (PMT light fractions, f_{90}...).

We developed a module of this software, to simulate the electronics and to provide to the reconstruction chain the same data format as real data. The module reads the time of arrival and the hit channel ID of each photoelectron and overlays the typical single pe time response to the baseline. The template PMT time response is obtained averaging over the 38 PMTs. A value for the charge is sampled from the real PMT single pe response (SER), assuming that the PMT response is perfectly linear. The average SER distribution is fit by a Gaussian + exponential function, with μ = 153 ADC counts and σ = 64 ADC counts. The dynamic range of the ADC boards is about 4000 counts: when the vertical amplitude of the signal exceeds this value, electronics saturation occurs.

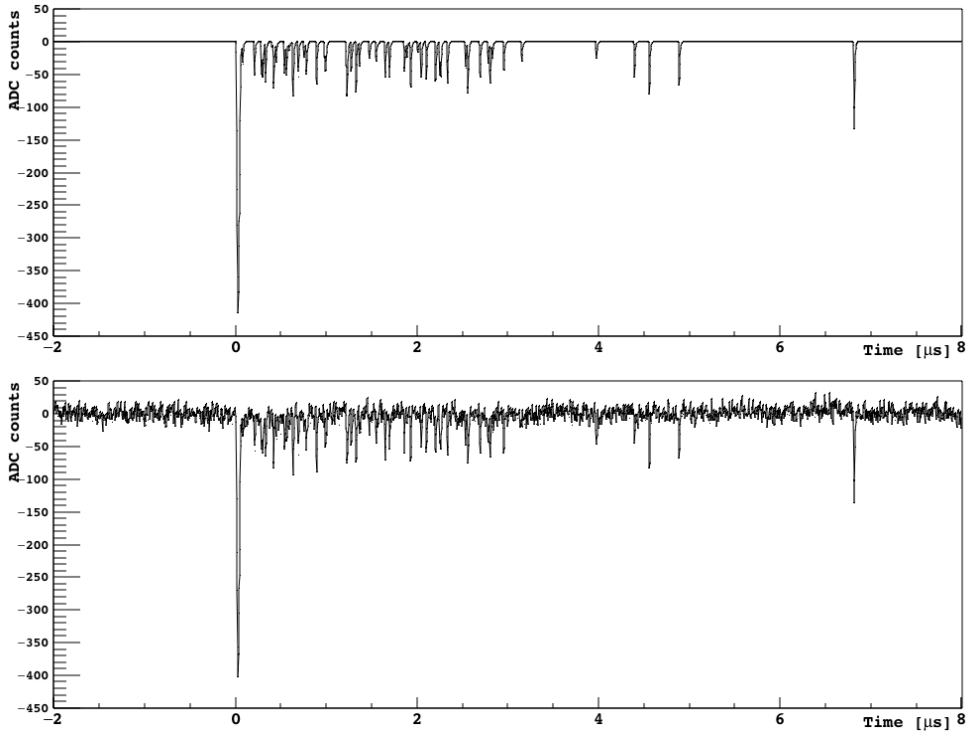

Fig. 3.2 Example of reconstructed G4DS S1 waveform after the overlay of a flat (top) and of a true (bottom) baseline. A baseline run is taken periodically, triggering the acquisition with a pulser, to monitor and study the evolution of the electronic noise.

We periodically acquire pure baseline runs (using a pulsed trigger) in order to monitor the detector stability and the noise. These data can be optionally used to build simulated waveforms, by adding Monte Carlo simulated pulses to real baselines. Alternatively, baseline fluctuations and noise can be generated directly by the electronic simulation. In addition to this, fake scintillation and LED light pulses can be generated directly by the electronic simulation, bypassing the G4DS output, in order to better understand the impact of the electronics.

The overlayed waveform can optionally be quantized, to simulate the ADC digitization of the voltage signal. It is then passed to the reconstruction algorithms. Figure 3.2 shows one G4DS S1 pulses, reconstructed with a flat (top) and with a true (bottom) baseline.

Figure 3.3 shows the comparison between the reconstructed S1 integral after the `darkart` reconstruction versus the true number of photoelectrons from the simulation. The left panel corresponds to the flat baseline case (with no quantization) while the right panel to the true baseline (with quantization). We do not expect (and we don not observe) any bias in the overlay of a flat baseline with a continuous signal. The real baselines, on the other hand, are directly taken from DarkSide-50 data and they are digitized in 12 bits. Adding a continuous signal to a digitized waveform and then applying the quantization again would induce a bias in the reconstructed signal integral. In order to correct for this effect, we apply a vertical jitter

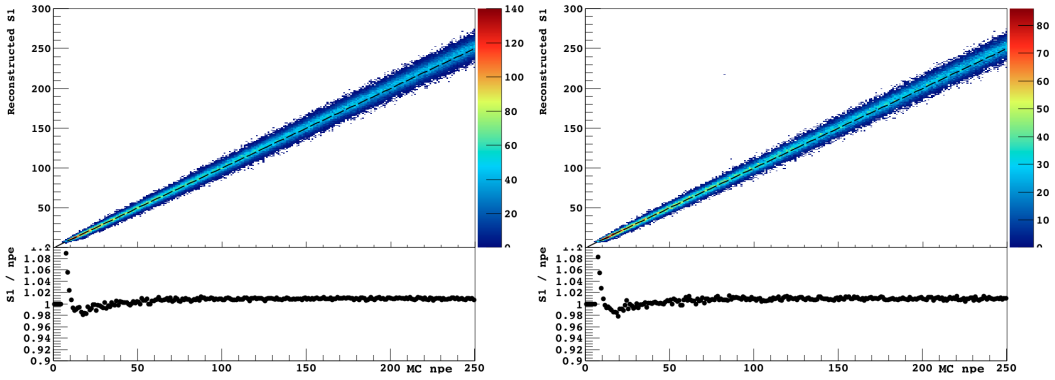

Fig. 3.3 The reconstructed S1 vs the true number of simulated pe's. The flat baseline case, with no quantization, is shown on the left; the overlay of a true baseline on the right. In the latter case, the (~ 2%) observed bias is expected. In both the plots, the dashed line represents the S1 = npe curve.

(uniformly distributed between 0 and 1 ACD counts) to the simulated signal and then round to the closer integer.[1]

Figure 3.4 shows the spread of the reconstructed signals as a function of the simulated number of pe's (npe). In both cases, the main contribution to the sigmas arises from the SER, so that $\sigma \propto \sqrt{\text{npe}}$. In particular, according to the SER input parameters ($\sigma_{SER} = 0.418 \times \mu_{SER}$), we expect $\sigma^2_{SER} = 0.418 \times \text{S1}$. The prediction of this contribution is shown in dashed blue. The fit with a more general function, assuming a constant term and a dependency on both npe and $\sqrt{\text{npe}}$ is shown in red. The fit results are in good agreement with the sole contribution coming from the SER, meaning that the reconstruction process is not inducing a significant smearing.

The overlay of a true baseline with PMT time response for each pe can take a very long time according to the S1 amplitude and simulated waveform length. Because the reconstruction code only induces a smearing and this effect is smaller with respect to the one induced by the internal TPC optics, a study based on the S1 variable only does not require the full `darkart` reconstruction. It is however required for studies of the f_{90} variable (which is affected, for example, by the integration of the noise) or to validate the position reconstruction algorithms.

Moreover, one goal of the reconstruction code is the identification of multiple S2's events in order to reject gamma and neutron events interacting more than once in the sensitive volume. In order to maintain the same rejection capability, we developed an alternative method for the identification of multi-sited events, described in the next paragraph.

3.2.1 The Clustering of the Deposits

The pulse-finder performance in resolving two consecutive and partially overlapping S2 pulses depends on the pulses amplitude and time profile. Figure 3.5 (a) shows the time

[1] We can either perform rounding to the closer integer, or to the closer superior or inferior integer.

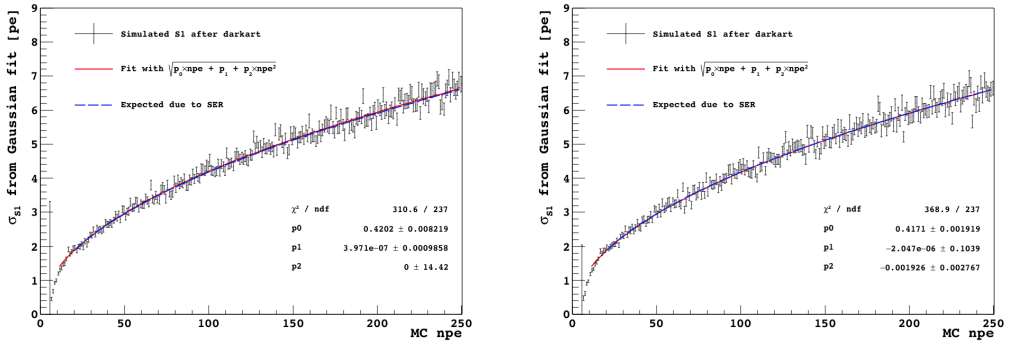

Fig. 3.4 The smearing of the reconstructed S1 vs the true number of simulated pe's. The flat (real) baseline case is shown on the left (right). For each MC npe value, the reconstructed S1 projection is fitted with a Gaussian. The sigma vs npe plot is then fitted allowing a dependency on npe, $\sqrt{\text{npe}}$ and a constant term (red line). The fit shows a good agreement with the prediction with a sole contribution from the SER ($\sigma \propto \sqrt{\text{npe}}$), shown in blue.

difference between two consecutive resolved S2 pulses in AAr data. The minimum time difference between two signals is ~ 3.5 µs. Since the mean drift velocity of free electrons at the nominal field of DarkSide-50 (200 V/cm) is ~ 0.93 mm/µs, this time difference corresponds to a difference in the vertical position of the interaction of about 3.5 mm.

Ideally, the light pattern on the top array of photo-sensors could be exploited to identify simultaneous pulses separated in the x-y plane, but this method is not implemented in the current DarkSide-50 analysis procedure.

G4DS simulates the physical tracks of ionizing particles as a sequence of consecutive steps in the medium and computes the energy lost at each step until the particle interacts or looses all its energy. In general, each recoil in liquid argon implies several steps and they can be recorded in the output file deposit structure (position, time, deposited energy). The resolution of the detector is not good enough to distinguish the single deposits and we want to reproduce this behavior.

We define *cluster* a group of energy deposits close to each other in space and in time, so that they will be reconstructed as a single pulse. In particular, we group together in one cluster the deposits that are close in the vertical direction ($\Delta z < 3.5$ mm, while no condition is applied in the x-y plane) and with a time difference of less than 3.5 µs. These clustering condition implies that a gamma scattering twice in the horizontal plane will be reconstructed as a single pulse event. The cluster position and time are then computed as the weighted average of the deposits contributing to the cluster.

We tuned the clustering algorithm by means of a simulation with the full optics. We limited our tuning to the resolution of S2 pulses, assuming that the time profile of the signal does not induce a significant bias. The number of reconstructed pulses is compared to the number of clusters identified by the clustering algorithm performed on the same simulation with different clustering conditions. Figure 3.5 (b) shows the result of the scanning on several

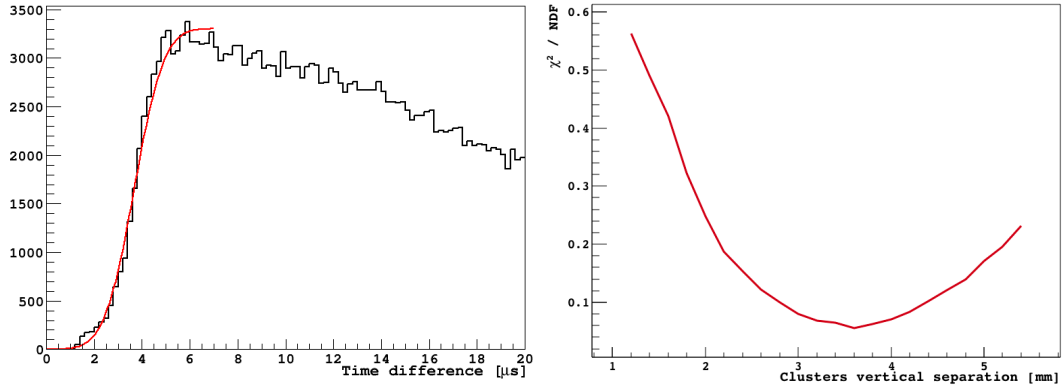

(a) Time difference between consecutive pulses

(b) χ^2 profile for the clustering tuning

Fig. 3.5 (a) Time difference between two consecutive S2 pulses and (b) tuning of the clustering algorithm. The plot on the left is obtained from AAr data after the application of the standard quality cuts and selecting event with at least 3 pulses in the waveform. The fit with an Error Function of the time difference between the third and the second pulse shows that 50% efficiency in resolving two S2 pulses is at 3.68 ± 0.02 μs. The plot on the right is obtained after the reconstruction of a G4DS ^{57}Co simulation. The distribution of the number of pulses is compared to the number of clusters found by the clustering algorithm for different values of the minimal vertical separation. The χ^2 is computed on the bins with more than two pulses after the normalization to the one pulse bin.

values of the minimum distance between two energy deposits to be considered as separate clusters. We used a χ^2 estimator to evaluate the compatibility between the reconstructed number of pulses and the number of clusters, considering only events with more than two pulses.

We cross checked this clustering condition using the distribution of the number of pulses observed in real data from external calibration sources and found a good agreement.

3.3 The TPC Response

The DarkSide TPC's are designed to readout the scintillation light and the ionization charges produced in the liquid argon. These processes are fairly well characterized experimentally but we are lacking a microscopic physical description. The NEST Collaboration developed a model [95] (Noble Element Simulation Technique) currently used for the XENON and LUX experiments. The goal of the model is the description of the recombination probability of electron and ions from a microscopic point of view. The model distinguishes between two regimes: long tracks are treated with the Doke-Birks formalism [96] while for short tracks the Thomas-Imel box model [97] is better suited. However, NEST is not entirely predictive and requires a data-driven tuning of some parameters.

The NEST predictions are in good agreement with the data collected in liquid xenon; we implemented this model in G4DS, to simulate the response of liquid argon, but we failed

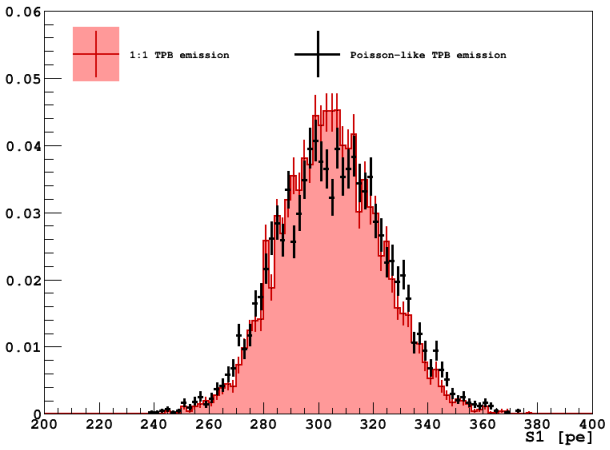

Fig. 3.6 Comparison between the Poisson-like (black) and the 1:1 (red) TPB absorption-emission mechanism. We simulated the ^{83m}Kr's electrons and selected events with drift time in the [100,300] µs range. Since the Poisson distribution increases the mean number of emitted photons, we scaled accordingly the initial scintillation yield. The S1 spread induced by the Poisson process is negligible with respect to the one induced by the internal optics.

in reproducing the DarkSide-50 data. We then opted for a semi-empirical model, based on the extraction of the recombination probability as a function of the recoil energy from DarkSide-50 data.

In order to remove any possible bias due to the detector resolution we firstly tuned the optical response of the DarkSide-50 TPC, as described in the next Section. We then proceeded to the tuning of our model for the scintillation and ionization for both electron and nuclear recoils.

3.3.1 The Optical Tuning

Since we performed the tuning of the optical response before the energy calibration, we only selected, for the data-MC comparison, observables that are free from any assumption on the energy of the considered events, namely the light yield as a function of the z coordinate, the top/bottom asymmetry, the S1 and S2 channel occupancy.

The propagation of scintillation photons within the geometry of the detector is affected by the optical properties of each detector volume and of the interfaces between materials. We had to define more than 30 values (refractive indices, absorption lengths, surface reflectivities, wavelength-shifter properties) to implement the optical simulation. In some cases the optical parameters are experimentally well known, in other cases we had to make some assumptions.

For example, the internal walls of the TPC are covered with TPB,[2] a commonly used wavelength shifter. Since the thickness of this layer is not precisely known, we tuned the absorption length in the material and the refractive index, in order to prevent UV photons to be trapped because of internal reflection. In addition to this, the authors of [98] found experimentally that the emission efficiency per absorbed UV photon is ~ 1.2 at 128 nm (but their measurement is compatible with 1.0 at less than 2σ). From theoretical considerations it seems unlikely to have a Poisson-like absorption-emission mechanism with mean 1.2, but we tested this hypothesis in our implementation of the wavelength shifter. We observed

[2] *Tetra-phenyl-butadiene*, evaporated on the inner detector surfaces.

Parameter	G4DS value	Expectation	Comment
LAr attenuation length at 128 nm	1.6 m	See text	Tuned
LAr Rayleigh scattering length at 128 nm	~ 45 cm	See text	Tuned
LAr rindex at 128 nm	1.47	1.47 [99]	Tuned
LAr rindex at 420 nm	1.25	1.25 [99]	Tuned
LAr layer rindex	1.27	See above	Tuned
Quartz rindex at 420 nm	1.47	1.468 [a]	Tuned
Quartz transmittance at 128 nm	0	0	Assumed
Thickness of condensed LAr layer	0.1 mm	0 mm	Tuned
Grid transparence to normal incidence	0.95	0.95	Measured
Grid reflectivity at 10 degrees and 420 nm	0.6	0.6	Measured
Grid reflectivity at 10 degrees and 128 nm	0.16		Extrapolated
PTFE Reflectivity for visible light	0.98	0.98	Measured
PTFE Reflectivity for VUV light	0.075		Extrapolated

Tab. 3.1 Selection of some meaningful parameters for the optical tuning. Some parameters are fixed to the value measured in the laboratory on actual samples. For all the tuned parameters, with the exception of liquid argon absorption and Rayleigh scattering lengths, only a pair of values is used, to distinguish between the VUV and the visible range.

[a] http://refractiveindex.info/?shelf=main&book=SiO2&page=Malitson

that the induced additional smearing is negligible with respect to the one induced by the internal optics. We then opted to make this material absorb UV photons and emit visible light isotropically in 1:1 proportion. Figure 3.6 shows the comparison between a simulation with Poisson-like emission and a simulation with 1:1 absorption-emission.

The anode and cathode electrodes are as well thin layers (30 nm) of ITO[3] deposited on the top and bottom surfaces of the fused silica windows. The optical properties of fused silica covered with ITO have been extensively measured in the laboratory. We did not implement the geometry of these thin layers, but assigned the specific optical properties to the interfaces between the coated fused silica and liquid or gaseous argon.

We used the same approach for the description of the steel grid placed just below the liquid surface. The grid is required to maintain a constant drift field in the active region and a uniform extraction field in the gas. We did not simulate the geometrical shape of the grid, but assigned to a thin layer of stainless steel the optical properties measured in the laboratory (namely the transmission coefficient and the reflectivity as a function of the incident angle and wavelength).

Some optical parameters have a larger effect than others on the selected observables. The major source of asymmetry in the detector response is the gas pocket, since it is present only in the upper part of the TPC. In addition, we inferred the presence of a thin condensation layer of LAr at the bottom of the top window of the TPC. Without this thin volume it is almost impossible to reproduce the top-bottom asymmetry observed in data.

[3] *Indium Tin Oxide.*

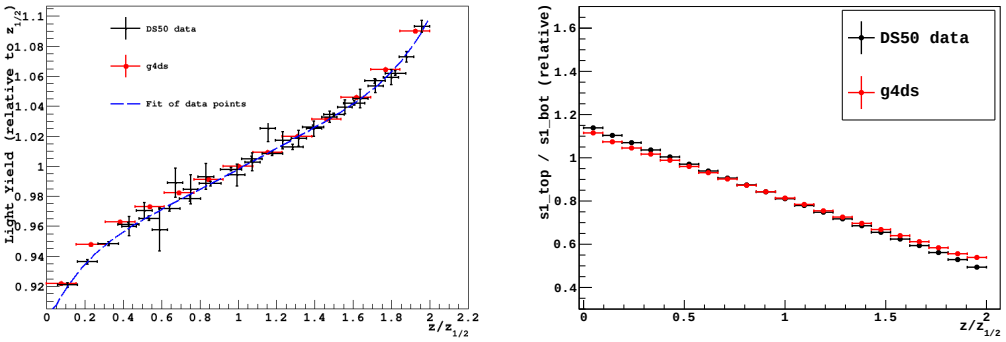

Fig. 3.7 Relative light collection (left) and top-bottom asymmetry in light collection (right) as a function of the vertical position of the event. The normalization is relative to the center of the TPC, so that $z/z_{1/2} = 0$ corresponds to the top, $z/z_{1/2} = 2$ correspond to the bottom. In the left plot, the blue dashed line is a 5 degree polynomial fit of he data points.

In order to reproduce the TPC response at the %-level we had to slightly tune the parameters with the largest impact, simultaneously scanning over them. In general we distinguished between the optical properties in the visible and in the VUV regimes. The simulations consist in shooting single photons with 128 nm wavelength with a uniform spatial distribution in the TPC (for the S1 signal) or in the gas pocket (for the S2 signal). A photon is detected when it hits one of the PMT windows, and survives a binomial selection to take into account the PMT quantum efficiency. Even though we are interested in an effective description, the deviations from the expectation values are in general small. Table 3.1 shows the result of the tuning for some meaningful parameters.

Fig. 3.7 (left) shows a comparison of the light collection efficiency as a function of the vertical position of the event in data and in G4DS. The relative light yield is inferred by selecting the ^{83m}Kr peak and by using the endpoint of the ^{39}Ar spectrum. The vertical position is obtained by measuring the time difference between S2 and S1. The $\pm$10% variation of the light yield within the TPC is properly reproduced in G4DS.

Figure 3.7 (right) shows the dependency on the vertical position of the top-bottom asymmetry (the ratio between the light seen from the top array of PMTs and from the bottom array). Data points are obtained computing event by event this ratio for single-scatter events, mainly due to ^{39}Ar decays.

Figure 3.9 left (right) shows the comparison of the average S1 (S2) channel occupancy. Channels from 0 to 18 (19 to 37) correspond to the PMTs top (bottom) array. The channels 0 and 19 are located at the center of the two PMT arrays. The other PMTs are disposed in concentric rings with increasing radii, according to the map of Figure 3.8. The outermost PMTs are partially covered by the TPC walls ($\sim$ 60% of the photo-cathode is active). As expected, the bottom array is seeing on average more S1 light. For uniformly distributed S2 signals, the bottom array is uniformly illuminated (except for corner PMTs), while a decrease in the collection efficiency is observed when going from the center to the edge of the TPC.

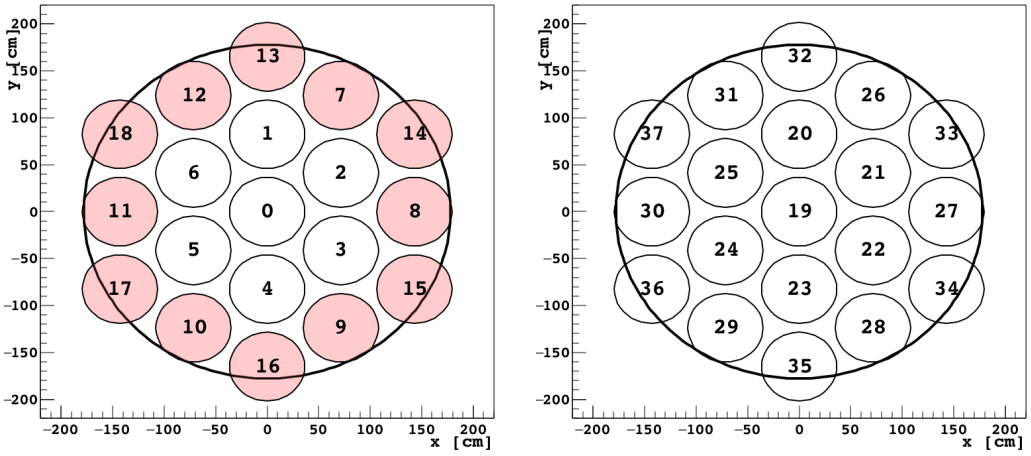

(a) Top array (b) Bottom array

Fig. 3.8 Top and bottom PMT array mapping in G4DS. The TPC edge are shown in solid black. The PMTs are arranged in three concentric circles with increasing radius around the central one. The colored channels in the top array are the only ones used to compute the S2-ring variable, used for the S2 calibration as discussed in Section 3.3.4.

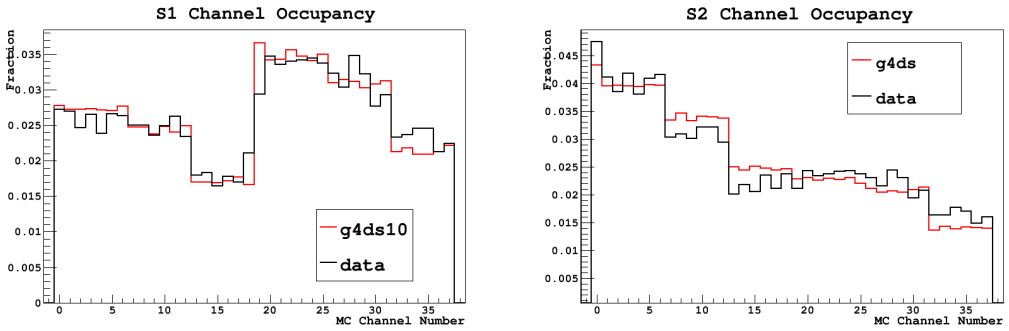

Fig. 3.9 S1 (left) and S2 (right) channel occupancy in data and G4DS.

After the tuning, the average detection efficiency (for VUV photons isotropically generated in the liquid argon volume) is $15.7 \pm 0.1\%$. Since we are interested in an effective description of the TPC response, we will allow some freedom in our model for the scintillation in liquid argon. In particular, we will introduce a scaling factor for the predicted number of scintillation photons for a given recoil. This scaling, in any case close to the unity, accounts for any possible difference in the total number of detected photoelectrons.

3.3.1.1 The Sagging Model

The analysis of ^{83m}Kr data and the average S2 channel occupancy show a radial dependence of the S2 scintillation yield. In particular, the S2 value for the events reconstructed at the center of the TPC appears to be a factor of 4 larger with respect to the S2 of the events reconstructed at the TPC edge. This effect can be reproduced by a variation in the multiplication

electric field, increasing towards the center of the gas pocket. Most likely the field variation is caused by the sagging of the top fused silica window, which makes the distance between the flat grid and the anode decrease. Another possibility is the non-uniform thickness of the condensation LAr layer.

The effect is currently well determined in real data and a radial correction for the S2 photon yield per electron is implemented in G4DS in order to accurately reproduce it.

3.3.1.2 Absorption and Rayleigh Scattering in Liquid Argon

Ultra-pure noble liquids are transparent to their scintillation light, however, the impurities inside the liquid (typically N_2, O_2 or Xe), even at the ppm level, can induce a significant absorption of the VUV light. This effect has been studied, for example, for the N_2 case in [100] and for the O_2 case in [101].

In any case, a direct measurement of the absorption length in a pure target is difficult, because of the effect of the Rayleigh scattering, which becomes the dominant effect at high purity. There is some tension between the calculation of this parameter (90 cm [102]) at 128 nm and the experimental measurements. In [99] the reported value for the Rayleigh scattering length is 55 ± 5 cm, while in [103] the lower limit on the measured attenuation length is 1.1 m.

On the other hand, the precise knowledge of this parameter can have a large impact on the design of larger liquid argon TPCs.

The DarkSide-50 TPC, in spite of the reduced dimensions compared to the typical attenuation length, is sensitive to both the scattering and the absorption lengths. The maximum travel distance of VUV photons is about 40 cm, under the assumption that when the VUV light reaches the TPC walls it is either absorbed or converted to visible light. This assumption is true in G4DS, according to the implemented model for the TPB.

Figure 3.10 shows the relative light yield variations for events distributed in concentric shells of the sensitive volume. We observe the same behavior in G4DS. Assuming that the description of the internal optics of the TPC is accurate in G4DS, we can study the combined effect of the absorption length and Rayleigh scattering in liquid argon from DarkSide-50 data. This study is currently ongoing.

3.3.2 The PARIS Model for Ionization and Scintillation in LAr

The tuning of the TPC response is a prerequisite for the calibration of the energy response. The scintillation and ionization mechanisms, introduced in Section 2.1, and summarized in Fig. 2.1 are not precisely characterized for liquid argon. We then developed a custom–made model based on an effective parameterization of the recombination probability of free electrons.

In liquid argon, the energy deposited by external radiation is mainly dissipated through the production of N_i electron-ion pairs and N_{ex} excited atoms. Some fraction of the energy

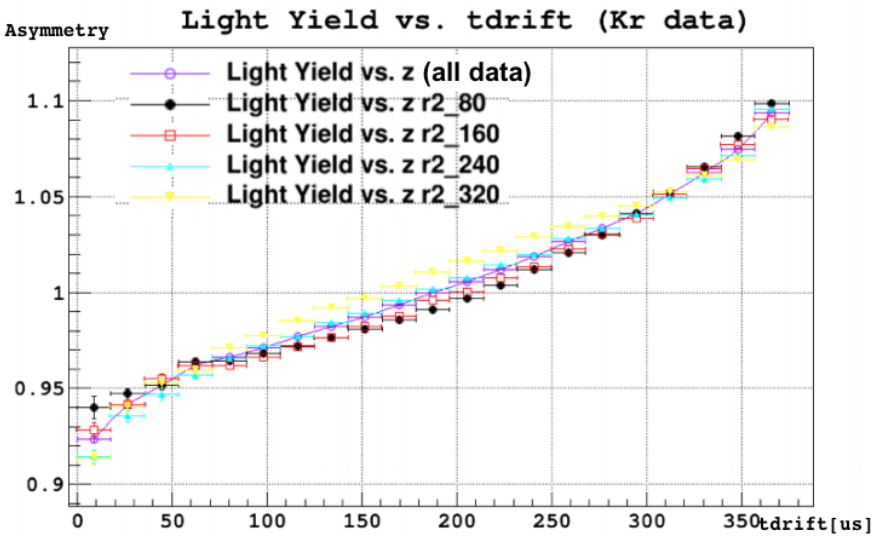

Fig. 3.10 Dependence of the light yield on the vertical position of the event and radial dependence. The purple line corresponds to the light yield averaged over all the radial positions. Black line: events with R < 8.9 cm, red line: 8.9 < R < 12.6 cm, light blue line: 12.6 < R < 15.5 cm and yellow line: 15.5 < R < 17.8 cm.

goes into sub-excitation electrons, that is free electrons with energy lower than the first excited level.One can write:

$$E_0 = N_i E_i + N_{ex} E_{ex} + N_i \epsilon \tag{3.1}$$

where E_0 is the total deposited energy, E_i and E_{ex} the average conversion energy for ionization and excitation respectively and ϵ the mean energy of sub-excitation free electrons. The latter accounts for energy dissipation through heat and it is lost.

The ionization work function W_i is defined as the average energy required for atomic ionization $W_i = E/N_i$, where E denotes the visible energy ($E = E_0 - N_i\epsilon$). The excitation work function is usually different, so that we can define an effective work function W as

$$W = \frac{E}{N_i + N_{ex}} = \frac{W_i}{1 + \frac{N_{ex}}{N_i}} \tag{3.2}$$

The effective work function sets the maximum number of scintillation photons that can be produced (assuming maximal recombination). The near-100% conversion efficiency of excited or recombined atoms to lead to scintillation is experimentally well established.

The ratio $f \equiv N_{ex}/N_i$ is assumed to be independent on the recoil energy but it is different according to the track type. Moreover, the fraction of energy dissipated by heat is much larger for nuclear recoils with respect to electronic recoils. The nuclear recoil quenching is described by the Lindhard theory [104], as discussed in Section 3.3.5. A constant reduction factor is observed in some scintillators, but some energy dependence is not excluded in noble liquids. The commonly-used assumption is that the portion of nuclear recoil energy

dissipated by electrons creates excitons and ions with the same efficiency as pure electron recoils.

In presence of an electric field, only a fraction of ionization electrons undergo recombination. The number of primary scintillation photons N_γ, which contribute to the S1 signal, is then:

$$N_\gamma = N_{ex} + \mathbf{R} \times N_i \tag{3.3}$$

where **R** denotes the recombination probability, which depends on the local ionization density and on the applied electric field. The remaining non-recombined free electrons are drifted away and contribute to the S2 signal. The number of free electrons N_e,

$$N_e = (1 - \mathbf{R}) \times N_i \tag{3.4}$$

and the number of scintillation photons N_γ are then fully anti-correlated.

The PARIS model is based on an effective parameterization of the recombination probability as a function of the recoil energy, extracted from DarkSide-50 data.

We fixed $f = 0.21$ and $W = 19.5$ eV, as suggested in many works [73, 105], to compute N_γ and N_i for electron recoils. Since Compton and photo-electric interactions both produce an electron, we did not distinguish between β decays and γ-induced electron recoils in liquid argon. We assume that all the fluctuations in the ratio between excitons and ions and the number of recombined ions are described by a Poissonian smearing of the predicted number of scintillation photons. This is the simplest assumption on the statistics of the photon emission. Since the optical propagation is properly tuned and the effect of the electronics on the energy response resolution is correctly simulated, any observation of an extra component in the resolution term, from data-MC comparison, should be addressed to the statistics governing the LAr photon emission. The results of this comparison are shown in the next Section.

In G4DS, the recombination probability is calculated as a function of the initial track energy (the GEANT4 vertex kinetic energy), while the number of produced species (excitons or ions) is computed for each energy deposit.

The model is currently tuned on DarkSide-50 S1 data for both ER and NR. It is well established that the f value for nuclear recoils is significantly different from 0.21. However, we assumed the same effective work function to compute the number of species for a given recoil energy. The partition between excitons and ions is then realized assuming $f = 1$. This is the same approach used in [95] and causes no loss of generality: the effect of a different work function can be absorbed in the absolute scale of the quenching function.

3.3.3 The S1 Response

3.3.3.1 The Extraction of the Recombination Probability from Electron Recoils Data

We defined an analytical parameterization of the recombination probability as a function of the recoil energy which depends on 6 free parameters p_i:

$$\mathbf{R} = p_0 \times \left(1 - p_1 \times e^{p_2 E} \times e^{p_3 E^{p_4}}\right) + p_5 \tag{3.5}$$

We used the S1 energy spectrum obtained with DarkSide-50 during the AAr campaign, dominated by the ^{39}Ar β-decay, taken at the nominal drift field of 200 V/cm. In order to reduce the external γ's, which can distort the spectral shape, we selected single sited events at the center of the TPC, applying strong cuts both on the vertical direction ($100 <$ drift time < 200 µs) and on the radius ($R < 4$ cm). Starting from the theoretical shape of the ^{39}Ar β-decay, we performed an analytical fit of the data leaving free the recombination probability.

The ^{39}Ar β-decay is a first forbidden decay: because of the difference in the spin of the parent and daughter nuclei, the emitted electron must carry away a large angular momentum. There is no experimental data available on the true shape of the decay spectrum but, in principle, it can be calculated applying the forbiddness, the Fermi, and the electron screening corrections to the allowed shape [106]. The Fermi correction accounts for the finite dimension of the nucleus, while the electron screening correction is of the order of 1% and can be neglected. The allowed and forbidden β-spectra are compared in Figure 3.11.

The shape correction is applied by multiplying the allowed shape by a shape factor F, defined as

$$F(T) = a \times \left((T + m_e)^2 - m_e^2\right) + b \times (Q - T)^2 \tag{3.6}$$

where T is the electron kinetic energy, m_e the mass of the electron and Q the endpoint (565 keV). The two factors a and b are assumed to be equal.

In order to further constrain the recombination probability at low energy, we simultaneously fit the ^{37}Ar and the ^{83m}Kr peaks. The first nuclide is found in the early runs of the UAr campaign and has an half life of 35.5 days. The decay consists an electron capture decay, followed by the emission of X-rays (the most important lines are at $\sim$ 2.62 keV with 8.4% BR). The two ^{83m}Kr conversion electrons are treated independently in G4DS, since we want to model the recombination probability as a function of their two recoil energies (9.4 and 32.1 keV).

The shape of the recombination probability extracted from this data is shown in Figure 3.12. At high energy, we assume a constant value equal to p_5. Using the recombination probability extracted from AAr data, we simulated ^{39}Ar , ^{37}Ar and ^{83m}Kr. The comparison of the simulations with the real data is shown in Figure 3.13. These plots demonstrate also that the combined effect of the internal optics and the model statistical assumptions allow us to recover the detector resolution.

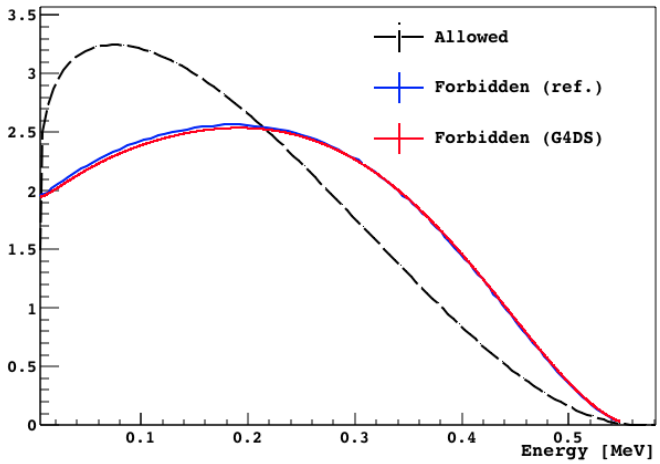

Fig. 3.11 Forbidden shape of ^{39}Ar β-decay. The allowed shape is compared to the one computed in [106] and to the one calculated with $a = b = 1$.

The S1 and S2 observables can be expressed in terms of number of scintillation photons and ion pairs:

$$S1 = g_1(N_{ex} + \mathbf{R} \times N_i) = g_1 N_\gamma \tag{3.7}$$

$$S2 = g_2 N_e = g_2(1 - \mathbf{R}) N_i \tag{3.8}$$

where g_1 is the average S1 photon detection efficiency and g_2 the mean number of photo-electrons detected per ionization electron extracted in the gas. The non-flat shape of the input β-spectrum allows to constraint the absolute scale of the recombination probability looking only to the S1 variable. However, the value of g_1 and g_2 parameters may be different in the real detector and in G4DS. In G4DS two scaling factors for the N_γ and g_2 variables are left as free parameters and fine tuned on data. In order to account for a possible difference in g_1, we re-scaled N_γ in order to match the global S1 light output of the TPC. We found that the scaling factor is very close to the unity (the best fit is ~ 1.01). The scaling of the S2-yield is described in the next section.

3.3.3.2 Validation of the S1 Calibration

In our analytical fit procedure for the extraction of the recombination probability, we computed the fraction of energy that goes into scintillation for each bin of the input energy spectrum according to the PARIS model and then we apply a convolution with a Gaussian to simulate the detector resolution. We assumed a constant light yield and a variance proportional to S1.

We periodically acquired external gamma calibration data that could ideally have been used to further constrain the shape of the recombination probability. However, since the

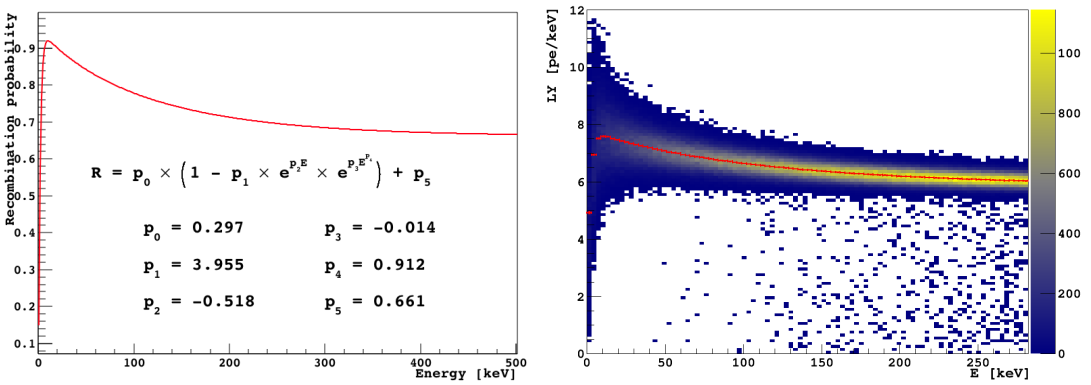

Fig. 3.12 The recombination probability extracted from DarkSide-50 data (left) and the G4DS light yield (right). The right points in the right panel represent the average trend.

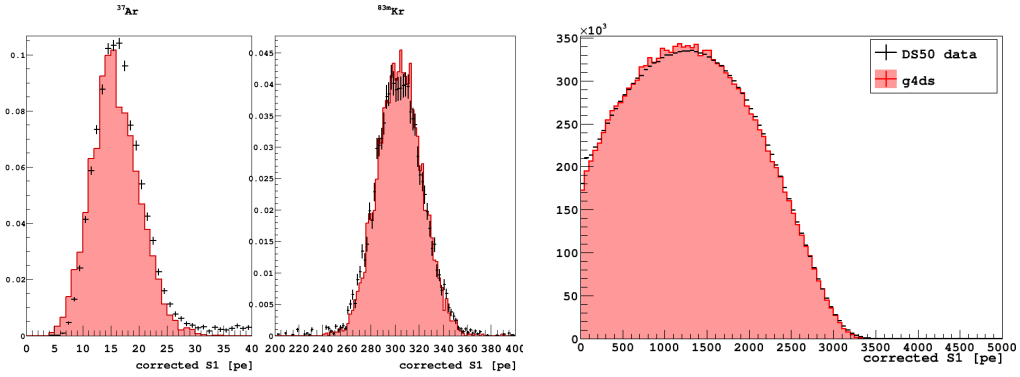

Fig. 3.13 The ^{37}Ar, ^{83m}Kr and ^{39}Ar S1 spectra in data (black) and G4DS (red) Single sited events are selected without any radial cut (to increase the statistics) but with 40 < tdrift < 330 µs.

samples of events collected with the external calibration sources are typically non-uniform in drift time and x-y distributions, the detector response might be biased with respect to the response to internal calibrations (^{39}Ar , ^{37}Ar and ^{83m}Kr).

The internal optical tuning of G4DS accounts for all the non-uniformities due to the spatial distribution of the events. We then opted to use the external calibration sources for the validation of the fit results. In particular we used ^{57}Co and ^{133}Ba external calibration data. Figure 3.14 shows the comparison between data and G4DS for the single and multiple scatter spectra after the background subtraction. We tuned our model on single scattering events but we found a good agreement for the multiple pulses spectra as well.

The shown source data are acquired with the source placed outside the DarkSide-50 cryostat in a central position with respect to the sensitive volume.

The simple statistical assumptions included in the PARIS model for the LAr photon emission distribution allow us to accurately reproduce the DarkSide-50 data, without the need to add extra smearing components.

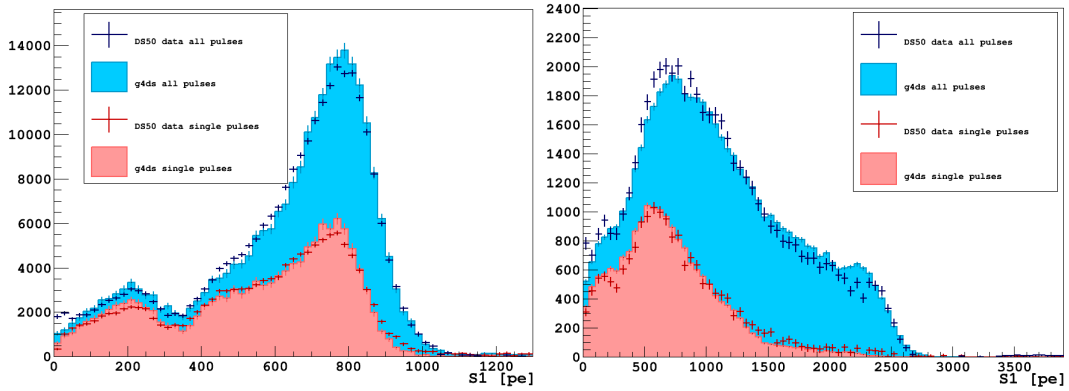

(a) ^{57}Co (b) ^{133}Ba

Fig. 3.14 Single and multiple scatter spectra of calibration sources in DarkSide-50 data and G4DS. The normalization for the ^{39}Ar background subtraction in data is performed by the area in a region where no source events are expected.

3.3.4 The S2 Response

The S2 signal is proportional to the number of ionization electrons that survive recombination. In the real detector, they are drifted by the electric field and extracted in the gas region. According to the purity of the liquid, some of them are captured by impurities.

In G4DS, the simulation of the ionization electrons does not involve the actual particle tracking. For each energy deposit in the active target, we calculate the number of electrons N_e surviving the recombination according to the PARIS model. Each electron is translated up to the gas pocket region, taking into account the electron diffusion and mobility. The drift time delay is calculated assuming a constant drift velocity of 0.93 mm/µs. The scintillation light is emitted uniformly during the electron drift in the gas pocket, so that the rise time of the signal is about 1 µs. The time profile of the scintillation light pulse is then described by the fast and slow decay constants with the relative weight of 0.3 and 0.7 respectively.

The functional shape of the recombination probability extracted from S1 data allows us to reproduce the ^{39}Ar S2 spectrum, assuming a photon yield of ~ 245 ph/e$^-$ and Poisson fluctuations. Because of the light collection efficiency this number converts to ~ 39 photoelectron/e$^-$. Figure 3.15 shows the comparison between data and G4DS. The data sample is chosen to minimize the effect of the S2 radial dependency: only the events with the maximum light fraction detected by the central top PMT are accepted. However, the saturation of central PMTs can induce a significant bias. We opted to use a saturation free observable: S2ring, namely the S2 signal recorded by the outermost PMTs (the colored ones in Figure 3.8 left).

The right panel of Figure 3.15 shows the comparison between the photoelectron yield per single electron in both data and G4DS. We selected pulses occurring at a fixed drift time equal to the maximum one (tdrift = 376±5 µs) and with the most of the light concentrated on

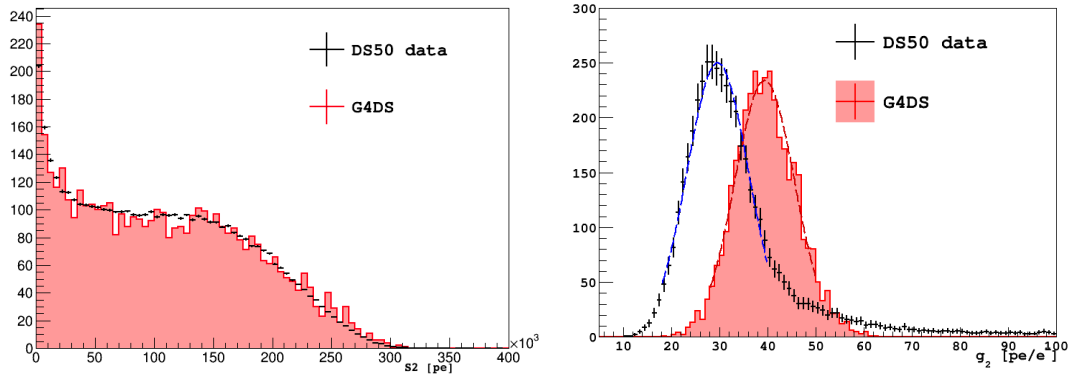

(a) Full ^{39}Ar S2 spectrum (b) Single ionization e^- events spectrum

Fig. 3.15 The ^{39}Ar S2 spectrum (a) and the single electron pe yield (b) in data and G4DS. In (a), a strong radial cut is applied in both G4DS and real data in order to avoid spectral distortion due to the S2 radial dependency. In particular, only events with S2 below the central top PMT have been selected. The MC statistics is poorer because of the large CPU time required for the simulation. In (b) are also shown Gaussian fits to the spectra. The mean value from fit is 29.6 ± 0.1 for data (blue line fit) and 39.4 ± 0.1 in G4DS (red line fit). See the text for further details.

the top central PMT. These events (echoes) are believed to be due to electron emission from the cathode when illuminated by the S1 signal, as discussed in Chapter 2.

The value of the S2 photoelectron yield is higher with respect to the one observed in data by roughly ~ 30%. The reason for this discrepancy is still under investigation. A possible explanation could be a bias of the reconstruction software, responsible for an artificial reduction of the reconstructed S2 pulse integral. The effect can depend on the time profile of the signal, which is not precisely modeled for such low energy events.

3.3.5 Tuning of the Quenching for Nuclear Recoils

The nuclear recoils are quenched in noble liquids because the fraction of energy released through collisions with ions is much larger with respect to the electron recoil case. The quenching factor in liquid argon is relatively well determined at high energy to be of the order of 0.25 [107]. There exists large uncertainty at low energy (< 20 keV$_{ee}$) where the theoretical models predicts a decrease of the quenching while some experimental measurements show the opposite behavior (see for example [108]).

We calibrated the nuclear recoil quenching thanks to the deployment of an AmBe source. As already presented in Section 2.3.2, three decay channels are available for the ^{9}Be:

- single neutron with 36% BR.
- one neutron accompanied by a 4.4 MeV gamma (from ^{12}C de-excitation after α-absorption) with 65% BR.
- one neutron accompanied by 4.4 MeV and 3.2 MeV gamma for the remaining 3%.

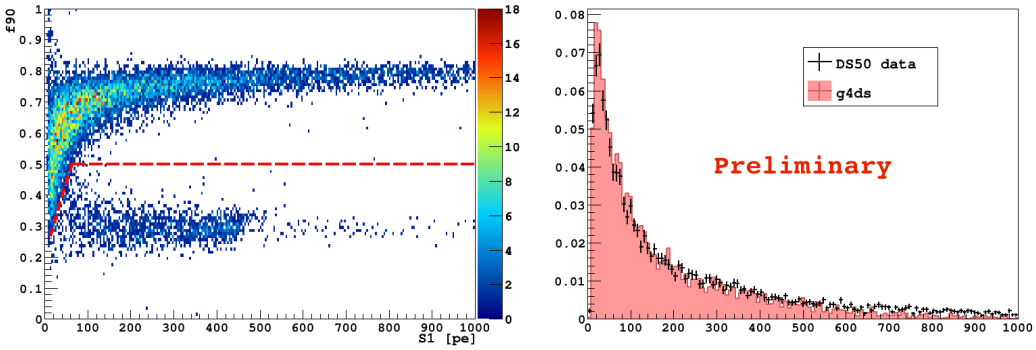

(a) Pure neutron sample selection

(b) AmBe neutron energy spectrum

Fig. 3.16 The pure AmBe neutron sample is selected looking for a veto coincidence. Only single scatters with f90 > 0.45 are accepted. The data and G4DS energy spectra are compared in the rightmost plot. The normalization is done in the [100, 400] pe range.

The ^{241}Am gamma activity for 10 Bq neutron activity is about 170 kBq. The most important line is the 60 keV gamma with branching ratio of 35%.

With this source it is not trivial to extract a pure sample of neutron recoils from data without reducing significantly the statistics. We isolated single scatter events with a 4.4 MeV signal in the veto prior to the TPC trigger. The selected sample is cleaned from gammas and ^{39}Ar events by means of the minimal f_{90} cut shown in Figure 3.16 (a). The neutron energy spectra for the selected events is shown in the panel (b).

The only parameter to be tuned within G4DS is the nuclear recoil quenching as a function of the recoil energy. We assumed that the recombination probability as a function of the quenched energy is the same one extracted for electron recoils. We implemented in G4DS the model proposed and described by Mei *et al* in [109], which incorporates both the Lindhard theory and the Birks' saturation law [110]. We prepared a G4DS sample, simulating only the neutrons from the AmBe and neglecting the gammas, running G4DS in the full optics mode. The simulated neutron energy spectrum is compared to the one from real data in Figure 3.16 (b). We observe a good agreement in first approximation, but a more refined analysis is required to evaluate our discrimination power between the model proposed by Mei *et al* and the pure Lindhard one.

3.3.6 The PSD parameter (f_{90})

Since the decay time constant of the singlet excited state of the Ar atom is ~ 6 ns, the fast component of the scintillation pulse is emitted within a few tens of nanoseconds after the recoil takes place. The total delay induced by the light propagation inside the detector, the TPB absorption-emission mechanism and the PMTs detection time spread are believed to be of the order of $\sim 1 \div 10$ ns. The pulse shape discrimination parameter (f_{90}) used for the

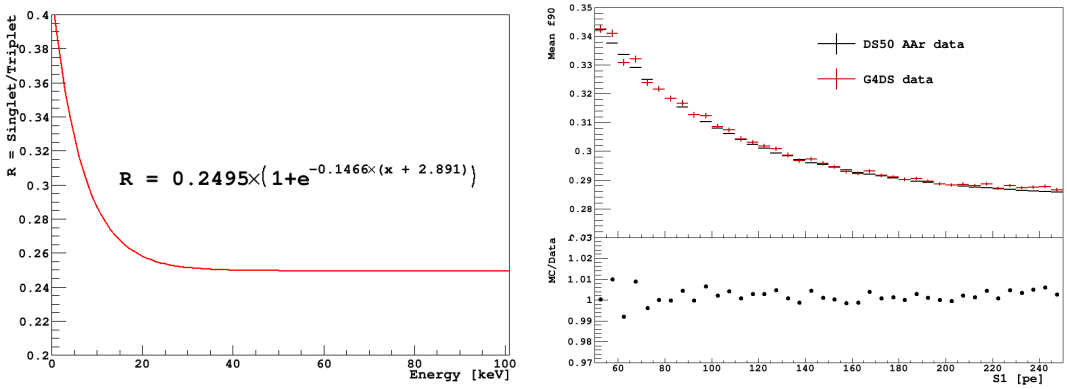

(a) Singlet to triplet ratio in G4DS

(b) Data-MC comparison (f90 mean)

Fig. 3.17 Singlet to triplet ratio *R* for electron recoils (a) and comparison data-MC (b). This function in (a) is used in G4DS to compute the fast component probability. The functional form has been derived from AAr data. In (b) the AAr f90 distribution means are compared to the ones obtained from the full G4DS simulation chain of ^{39}Ar events. The relative difference is lower than 1% in the considered energy range [50,250] pe .

DarkSide-50 analysis is defined as the fraction of the S1 pulse occurring in the first 90 ns of the pulse itself. Since only a small fraction of the slow component (with time constant of 1.6 µs) is integrated within this small time window (~ 0.5%), f_{90} is almost equal to the ratio between singlet and triplet.

The ratio between singlet and triplet for electron recoils is about 0.3 for energies above 10 keV. However, since it depends on the local ionization density, it is expected to increase at lower energy. In G4DS , the fast or slow decay time constant is assigned to each exciton assuming binomial fluctuations. The probability of the singlet state is sampled as a function of the recoil energy, according to the functional shape shown in Figure 3.17 (a). This function is extracted from AAr data, by means of an analytical fit with model that describes the ratio of two correlated Gaussians. I will discuss the details of this model in a Chapter 5. We assume that the sample of AAr data is a pure sample of electron recoils and we simulated ^{39}Ar events with G4DS to compare the f_{90} distributions. Figure 3.18 shows this comparison for different S1 intervals. We can evaluate the agreement between the datasets by looking at the mean values of the f_{90} distributions for each S1 bin. Figure 3.17 (b) shows the f_{90} means in top panel and the relative difference in the bottom panel. The maximum disagreement in the position of the distribution mean is in general lower than ~ 1%.

Since the calculation of the f_{90} parameter involves the integration of the waveform, the full reconstruction chain is required to recover the correct width of the distributions. A more accurate tuning of the singlet to triplet ratio would require a massive production and reconstruction. Nonetheless, the tuning of the single to triplet ratio and the validation of the distribution width would represents a powerful method for the prediction of the electron recoils band in the f_{90} vs S1 plane. In the low energy range, the WIMP search region

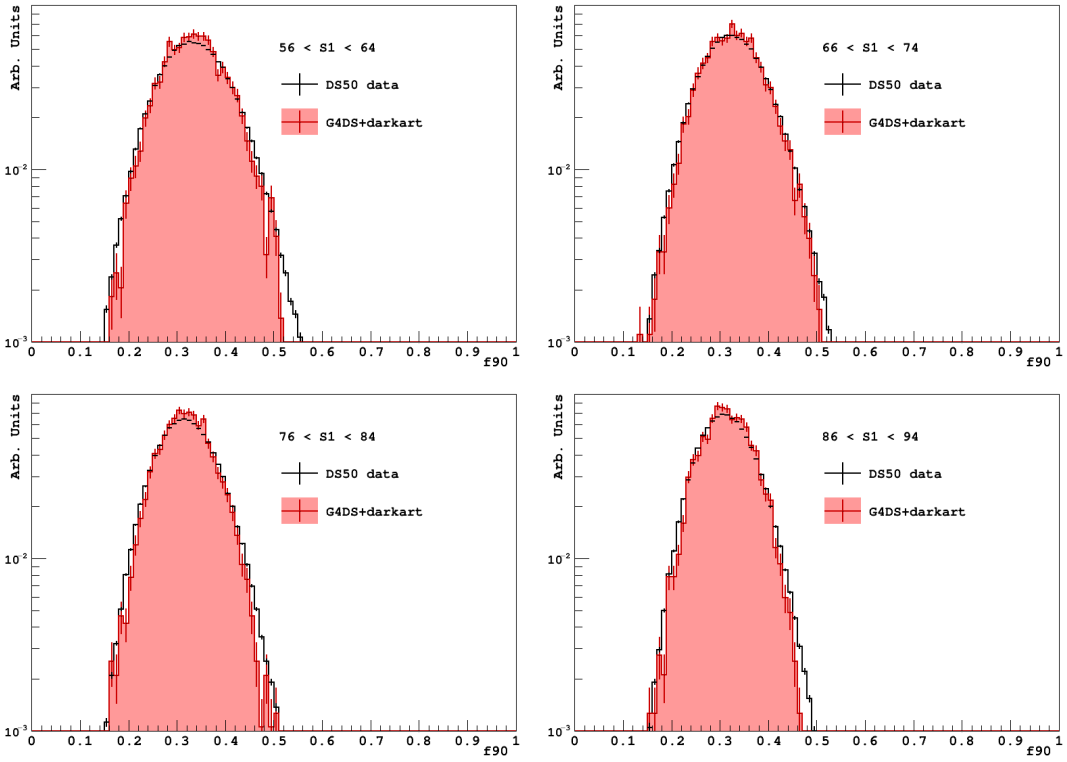

Fig. 3.18 Real AAr f_{90} distributions and G4DS simulations for several S1 intervals. The selected sample includes single scatter events with 40 µs < tdrift < 330 µs.

is ultimately determined by the prediction on the electron recoil leakage in the nuclear expectation band.

3.4 The LS Veto Response

The TPC is surrounded by a liquid scintillator veto sphere (LSV). The sphere has 4 m diameter and is equipped with 110 8 inches photo-multipliers. The LSV is made of a solution of PC and TMB. In the final configuration, the relative mass fraction are 95% and 5% respectively. Some PPO is dissolved in the scintillator (with 1.4 g/l concentration) to act as wavelength shifter.

The model for scintillation in GEANT-4 is exhaustive for most of the electromagnetic processes occurring inside the scintillator. The model is based on the Birks' saturation law [110], which describes the scintillation yield as a function of the interacting particle energy. The Birks parameter is set to 0.109 mm/MeV, as reported in [111]. This value is in good agreement with the calculations described in [112].

We tuned the global scintillation yield using external calibration sources. In addition to the ^{57}Co and ^{133}Ba sources, we included the ^{137}Cs source. The average light yield required to reproduce the calibration spectra is of 423 ± 27 pe/MeV.

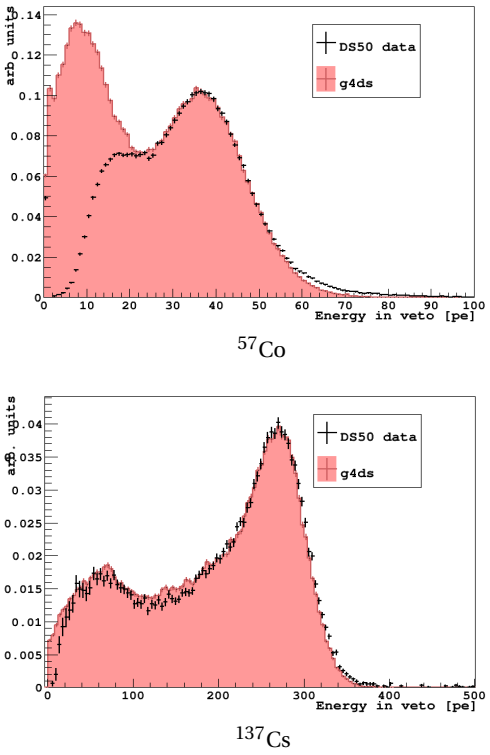

Fig. 3.19 The comparison between the calibration sources veto spectra and the MC ones for ^{57}Co, ^{133}Ba and ^{137}Cs. The discrepancy at low energy is due to the trigger threshold, based on a multiplicity cut. The requirement is that at least 22 (6) PMTs must detect at least one photoelectron in a 200 ns coincidence time window for the ^{133}Ba and ^{137}Cs (^{57}Co) sources.

Figure 3.19 shows the comparison between data and MC for the three calibration sources. The data spectra represent the calibration source contribution after the statistical subtraction of the background. The background and signal shapes are obtained running the veto in the self-trigger configuration (without being triggered by the TPC). The veto PMTs work in the single photo-electron regime and the veto waveforms are scanned in order to find clusters of hits. One cluster is accepted only if at least 22 PMTs were hit. This multiplicity cut imply a trigger inefficiency for low energy signals.

3.5 Conclusions

In this Chapter, I discussed the status of G4DS, the DarkSide simulation tool, a GEANT4-based full simulation of all the detectors of the DarkSide program. It includes the accurate simulation of the DarkSide-50 optical and electronics responses and a custom-made physical model for the ionization and scintillation in liquid argon (the PARIS model).

The PARIS model is based on a modelization of the recombination probability of ionization electrons as a function of the recoil energy. It is currently tuned on the DarkSide-50 data at 200 V/cm for both electron and nuclear recoils. The model has been tuned using internal electron sources and the statistical assumptions we made have been cross checked with external calibration sources. The model can in principle be extended to other noble liquids operating at different electric drift fields.

The G4DS simulation package has been intensively used within the DarkSide Collaboration. In the next Chapters I will report about some of the most relevant studies related to the DarkSide-50 experiment and based on MC simulations (the evaluation of neutron and gamma backgrounds in Chapter 4) and to the future phase of the experiment (the design studies for DarkSide-20k in Chapter 6).

Chapter 4

Background Estimates for DarkSide-50

Neutrons are the most dangerous background for the WIMP search of the DarkSide experiment, since a neutron induced single-sited nuclear recoil has the same signature as a WIMP interaction. This background can be suppressed in DarkSide-50 by means of the active veto. I will firstly discuss in this Chapter the evaluation of the neutron induced background and the related veto efficiency.

In the second part I will show the results of a spectral analysis I carried out in order to identify all the components contributing to the ER background. Thanks to this analysis we measured the ^{39}Ar activity in UAr and the depletion factor with respect to the AAr.

Both these results are based on G4DS simulations.

4.1 Neutron Background and Veto Efficiency Studies

Neutrons have cosmogenic or radiogenic origin. The work presented in [113], based on FLUKA simulations [92], shows that the muon-induced (cosmogenic) neutron background is negligible with respect to the radiogenic contribution for an experiment of the size of DarkSide-50.

Concerning the radiogenic background, we distinguish between spontaneous fission and (α,n) neutrons. We present in this Section an estimate of the expected (α,n) neutron rate for the AAr campaign and a study of the veto efficiency to these neutrons. The spontaneous fission neutron yield is typically smaller compared to (α,n) neutron yield for low-Z materials and thus this contribution has been neglected.

The composition of the Liquid Scintillator Veto (LSV) is discussed in the Chapter 2. The loading with TMB allows the exploitation of the large neutron capture cross section of ^{10}B. The veto efficiency depends on the detection efficiency of the capture products. I will discuss a complete analysis of the systematics related to this aspects.

4.1.1 Radiogenic Neutrons Flux and Energy Spectra

Long lived decay chains such as ^{238}U and ^{232}Th produce several α particles with energy in the MeV range. α particles have a very short range and have high probability to be absorbed inside the material. The α's absorption can induce neutron emission. The total yield of these (α, n) neutrons depends on the specific activity of the decay chains in each detector component and the specific neutron yield per decay of the material.

As suggested in [114], the total neutron yield Y for one α particle in a thick monoatomic target is

$$Y = \frac{N_A}{A} \int_0^{E_0} \frac{\sigma(E)}{S^m(E)} \mathrm{dE} \tag{4.1}$$

where N_A is the Avogadro's constant, A the atomic mass of the target, E_0 is the initial energy of the α, $\sigma(E)$ the n production cross section and $S^m(E)$ the total mass stopping power.

The neutron yield of a full decay chain in a composite material is obtained by summing up the contributions of the various α's (weighted for their BR's) and the various isotopic contribution (weighted by the mass fractions).

The differential neutron yield for the i-th element of the target and j-th α of the chain can be expressed as:

$$Y_i(E_n) = \frac{N_A}{A_i} \sum_j \frac{R_\alpha(E_j)}{S_j^m(E_j)} \int_0^{E_j} \frac{\mathrm{d}\sigma(E_\alpha, E_n)}{\mathrm{d}E_\alpha} \mathrm{d}E_\alpha \tag{4.2}$$

where $\frac{R_\alpha(E_j)}{S_j^m(E_j)}$ represents the flux of the j-th α, $R_\alpha(E_j)$ is the j-th α production rate and E_j its initial energy. The equation is true under the hypothesis of a thick target, where the α energy attenuation in the medium is the dominant process and the α's flux is invariant until the energy is attenuated to zero. This assumption, that simplifies the calculations, leads to an upper limit in the estimate of the neutron yield, since, in general, the probability for a neutron to be emitted after the capture of one α particle decreases with the α energy.

The α production rate (R_α) depends on the specific concentration $[X]$ of the decay chain father. If the concentration is expressed in ppm/g/y:

$$R_\alpha(E_j) = 10^{-6}\,[X]\,\frac{N_A}{A}\frac{\ln 2}{\tau_{1/2}} B_j \tag{4.3}$$

where A is the atomic mass of the chain parent, $\tau_{1/2}$ the half life of the decay and B_j the branching ratio of the α. The list of considered α's includes all the decays with a branching ratio larger than 0.5% and it is shown in Table 4.1.

The differential neutron production cross section $\frac{\mathrm{d}\sigma(E_\alpha, E_n)}{\mathrm{d}E_\alpha}$ is calculated by the TALYS software package [93], where all the production channels are considered according to the TENDL neutron cross section database [115]. The mass stopping power is computed with

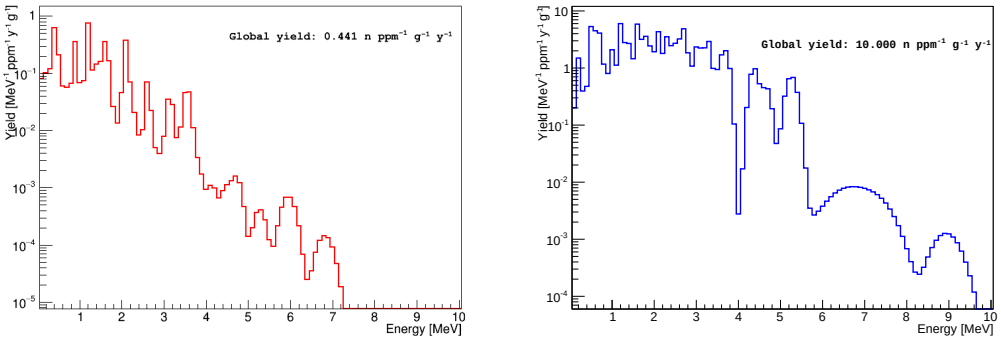

Fig. 4.1 Two examples of (α, n) neutron spectra computed from ^{238}U and ^{232}Th decay chains in a target made of stainless steel (left) and teflon (right).

the TRIM/SRIM package [116]. This approach, suggested in [114], gives results consistent within a factor of 2 with [117] and with the prediction of SOURCES [118][1], as shown in [119].

We computed the differential (α, n) neutron spectra for several detector materials, namely:

- Fused silica (windows): O (0.532 mass fraction), Si (0.468)
- Stainless steel (cryostats): Mn (0.012), Si (0.0047), Cr (0.181), Ni (0.082), Fe (0.724)
- Borosilicate glass (PMT windows): Li (0.0047), B (0.0529), Na (0.046), Si (0.3243), Al (0.0318), O (0.5215), Ba (0.0179)
- Ceramic (PMT stems): Al (0.53), O (0.47)
- Teflon (reflectors): C (0.238), F (0.762)
- Copper
- Titanium
- Silicon

We chose to use the natural isotopic abundances for each element and validate the calculations with the spectra found in [114]. The Appendix A is dedicated to a more detailed description of the spectra production.

All the detector components have been screened before the commissioning of the detector. The majority of them were γ-counted and actual measurements of the radioactive contamination or upper limits are stored in a database. When possible, the measurement for at least two gamma lines for each chain are reported: typically ^{234}Th, ^{234m}Pa and ^{226}Ra for the ^{238}U chain, ^{228}Th and ^{228}Ra for the ^{232}Th chain. When no explicitly stated, the ^{235}U concentration is assumed to be 0.0072 of the concentration of ^{238}U and the secular equilibrium is assumed for the decay chains. When the result of the gamma counting leads to

[1] SOURCES-4A is another code for the calculation of neutron yields and spectra. It is based on the EMPIRE neutron cross-section database and experimental data.

^{238}U			^{232}Th			^{235}U		
Parent	E (keV)	BR (%)	Parent	E (keV)	BR (%)	Parent	E (keV)	BR (%)
^{238}U	4151	21%	^{232}Th	3947	21.8%	^{235}U	4212	9%
^{238}U	4198	79%	^{232}Th	4012	78.2%	^{235}U	4366	19%
^{234}U	4722	28.5%	^{228}Th	5340	27.5%	^{235}U	4397	57%
^{234}U	4775	71.5%	^{228}Th	5423	72.5%	^{235}U	4502	4%
^{230}Th	4620	23.4%	^{224}Ra	5449	5.1%	^{235}U	4570	11%
^{230}Th	4687	76.6%	^{224}Ra	5685	94.9%	^{231}Pa	5040	62.5%
^{226}Ra	4601	5.6%	^{220}Rn	6288	100%	^{231}Pa	4951	26.5%
^{226}Ra	4784	94.4%	^{216}Po	6778	100%	^{231}Pa	4736	8.8%
^{222}Rn	5490	100%	^{212}Bi	6051	25%	^{231}Pa	4853	1.9%
^{218}Po	6002	100%	^{212}Bi	6090	9.7%	^{227}Ac	4945	1.2%
^{214}Po	7687	100%	^{212}Po	8784	64.1%	^{227}Th	6010	26.9%
^{210}Po	5304	100%				^{227}Th	5714	44.1%
						^{227}Th	5750	21%
						^{227}Th	5830	3.8%
						^{227}Th	5670	2.3%
						^{223}Ra	5520	10%
						^{223}Ra	5606	26%
						^{223}Ra	5747	10.5%
						^{223}Ra	5716	53.5%
						^{219}Rn	7226	2.4%
						^{219}Rn	7675	66.2%
						^{219}Rn	7720	0.9%
						^{219}Rn	7982	30.5%
						^{215}Po	7386	100%
						^{211}Bi	6278	16.2%

Tab. 4.1 List of the α's included in the (α, n) neutron energy spectra calculation.

different concentration values for the upper and lower parts of a chain (both ^{232}Th or ^{238}U), the breaking of the secular equilibrium is assumed at the radon position.

The conversion from the activity measurement (A_X, in mBq/kg or mBq/unit) to the concentration in g/g of the X decay chain is computed as follows:

$$[X] = \frac{A_X t_{1/2}}{\ln 2} \frac{A}{N_A} \tag{4.4}$$

where $\tau_{1/2}$ is the half-life of the decay chain parent, A is its atomic mass and N_A the Avogadros's constant.

The estimate of the absolute neutron yield per detector component is performed by scaling the computed neutron yield per decay by the concentration of the contaminants. Table 4.2 summarizes the absolute neutron yield for the most relevant materials. The yield from the PMTs represents the dominant contribution by far. Nonetheless, the uncertainty is large, due to the fact that two measurements of different photodetectors gave different results for the upper part of the ^{238}U chain.[2] Moreover, since only a measurement of the full device is available, we attributed all the activity to the borosilicate glass PMT stem. This hypothesis has to be considered as a worst-case scenario, because of the large (α, n) neutron cross section of the borosilicate glass.

4.1.2 The Simulation Procedure

We simulated neutrons originating from the materials listed in Table 4.2 and propagate them through the full geometry of DarkSide-50. We did not simulated the full optics inside the TPC and the veto, in order to save CPU time, and based the study only on the energy depositions. The neutron spectrum for each decay chain is calculated with TALYS, while the normalization is done according to the measured contamination. The results shown in this Section only refer to the neutrons coming from the PMT stems.

4.1.2.1 TPC Variables

In order to reproduce the TPC response without simulating the optics, the energy deposits in the liquid argon are grouped according to the clustering algorithm described in Chapter 3.

We extracted the fraction of recoil energy that produces scintillation according to the PARIS model, including a constant quenching factor for nuclear recoils (we assumed 0.25 [108]). This fraction of the deposited energy for each cluster is then translated in the number of photoelectrons by applying a Poisson smearing and assuming a light yield of 7.0 pe/keV.

To distinguish between electron and nuclear recoils we implemented a pulse shape discrimination based on the contribution of electron and nuclear recoils to the quenched energy in each cluster. The time distribution for each deposited energy can be described as

[2]

Material	Activity [mBq/PMT]			n yield [n/decay]	n yield [n/y]
One PMT (borosilicate)	^{232}Th:	6 ± 1		1.074e-05	2.038
	^{238}U upper (a):	190 ± 40		4.262e-06	24.05
	^{238}U upper (b):	90 ± 40		4.262e-06	10.77
	^{238}U lower:	19 ± 1.2		8.682e-06	4.91
	^{235}U:	7 ± 1		1.371e-05	3.01
Total	(a)				**34.0 (1292)**
1 PMT (38 PMTs)	(b)				**20.72 (787.4)**
Material	Activity [mBq/kg]		Equivalent conc. [g/g]	n yield [n/decay]	n yield [n/y]
Stainless steel	^{232}Th:	0.8 ± 0.3	(1.96 ±0.6)e-10	2.607e-06	10.4 ± 3.2
	^{238}U upper:	< 51	< 4.2e-9	2.427e-09	< 0.6
	^{238}U lower:	0.4 ± 0.2	(3.2±1.6)e-11	1.12e-06	2.2 ± 1.1
	^{235}U:	< 15	< 0.0072 × 4.2 e-9	2.607e-06	< 20.7
Total (159.3 kg)					**< 34.08**
Teflon	^{232}Th:	—	< 2e-13	7.81e-05	< 0.09
	^{238}U:	—	< 1e-12	8.3e-05	< 1.5
	^{235}U:	—	< 0.0072 × 1e-12	9.786e-05	< 0.1
Total (50 kg)					**< 1.7**
Fused silica	^{232}Th:	—	< 4e-11	1.602e-06	< 0.025
	^{238}U:	—	< 7e-11	1.644e-06	< 0.14
	^{235}U:	—	< 0.0072 × 7e-11	1.809e-06	<0.005
Total (3.2 kg)					**< 0.17**

Tab. 4.2 Summary of neutron yield for some detector components in DarkSide-50. Two measurements for the upper part of ^{238}U chain are available for R-1165 PMTs ((a) and (b) in the table). When only limits are available, the concentration of ^{235}U is constrained by the concentration of ^{238}U.

the sum of two exponentials with different time constants:

$$f^i(t) = f_p^i \times \frac{1}{\tau_1} \exp\left(-\frac{t}{\tau_1}\right) + (1 - f_p^i) \times \frac{1}{\tau_2} \exp\left(-\frac{t}{\tau_2}\right) \tag{4.5}$$

where i is the type of the recoil (electron or nuclear), $\tau_1 = 7$ ns and $\tau_2 = 1600$ ns. f_p^i represents the relative contribution of the two exponentials to the time distribution and is different for electron and nuclear recoils. We used $f_p = 0.3$ for electron recoils and $f_p = 0.7$ for nuclear recoils.

In general a mixture of electron and nuclear recoils can contribute to the same deposited energy and the time distribution will then be the sum of the time distribution for electron and nuclear recoils weighted by the relative contribution of the two recoils to the deposited energy:

$$f(t) = W \times f^e(t) + (1 - W) \times f^n(t) \tag{4.6}$$

where W represent the fraction of quenched energy deposited by electron recoils with respect to the total fraction.

To distinguish between electron and nuclear recoils we defined the f_{90} parameter as the charge contained in the first 90 ns of the waveform divided by the total charge.

We define one event as electron-like, and so we reject it, if the f_{90} equivalent parameter is smaller than 0.5.

In conclusion, the most relevant variables used for the selection cuts in the TPC are:

- **nclustersTPC**: number of clusters in the TPC;
- **cl_npeTPC**: number of pe in the cluster;
- **cl_timeTPC**: cluster time;
- **cl_zTPC**: z position in the TPC, converted in drift time (**tdrift**)
- **cl_f_{90}like**: f_{90} equivalent parameter defined as the fraction of quenched energy deposited by electrons with respect to the total quenched deposited energy .

The drift time cut and the spatial distribution of the single cluster in the TPC are shown in Fig. 4.2.

4.1.2.2 Veto Variables

Each energy deposition in the veto is quenched according to the plots in Fig. 4.3. The veto light yield is fixed to 520 pe / MeV, and energies are converted into pe's via a pure Poisson smearing.

To mimic the cuts implemented in the real veto analysis, we identified three time windows (prompt, late and delayed) and implemented the following variables:

- **prompt_timeVeto**: time of the first deposit in the veto, in the [-10, 200] ns window;

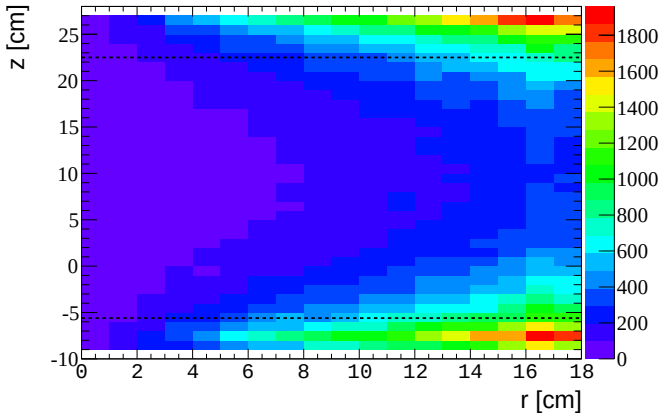

Fig. 4.2 Spatial distribution of single clusters in the TPC assuming neutrons coming from the PMT stems. The horizontal dashed lines represent the z cuts.

- **delayed_timeVeto**: starting time of the delayed sliding window;
- **late_timeVeto**: starting time of the late sliding window.
- **prompt_npeVeto**: sum of all the pe's in the [-10, 200] ns window from the TPC event;
- **delayed_npeVeto**: integral of the 300 ns window with maximum charge, in the [200, 8800] ns window;
- **late_npeVeto**: integral of the 300 ns window with maximum charge, in the [8800, 4e5] ns window;

The prompt window corresponds to the region where it is expected a thermalization signal from a neutron interacting in the veto just before or after the TPC trigger. The late and delayed windows are designed for the identification of the capture signal. Since the mean capture time in the LSV is 2.2 μs, the delayed windows corresponds to the region where the capture on ^{10}B are expected, while the late window serves to count the captures on other materials. They require a sliding window algorithm in order to identify the maximum charge collected during 300 ns in the [200, 8800] ns and [8800,4e5] ns windows respectively.

4.1.2.3 TPC and Veto Selection Cuts for the Phase-I Analysis

We implemented TPC cuts in order to isolate WIMP-like events:

- Number of scattering centers: we selected only one cluster events in the active liquid argon volume.
- f_{90} equivalent: the most of the energy is deposited by a nuclear recoil.
- Energy cut: we identified two energy ranges, the first is [60, 200] pe and the second is [60, 450] pe.

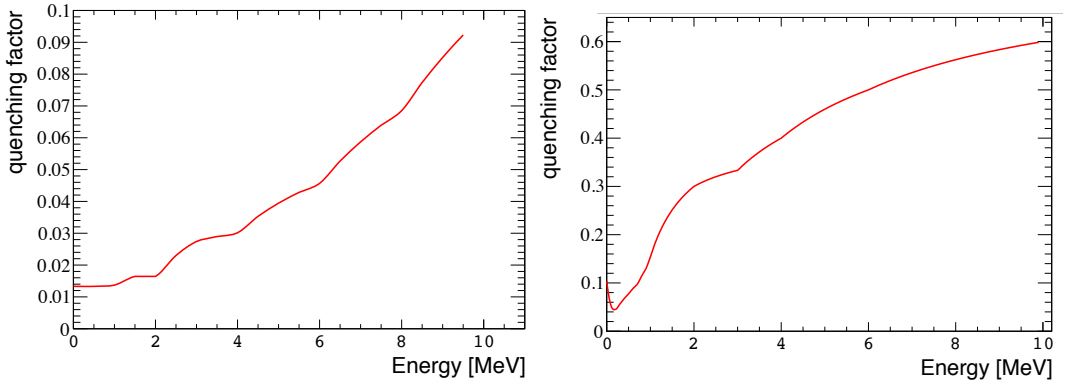

(a) α quenching

(b) Proton quenching

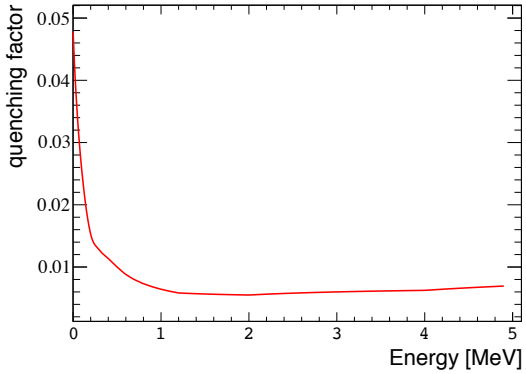

(c) Heavier nuclei quenching

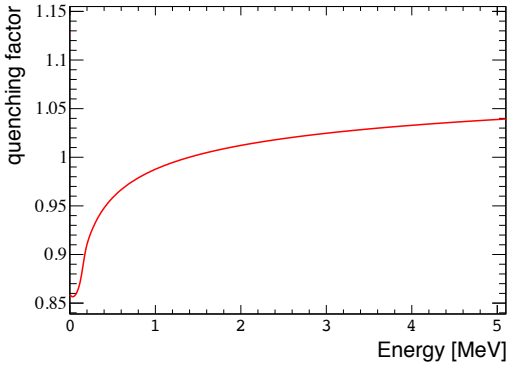

(d) Electron quenching

Fig. 4.3 Scintillator veto quenching functions. The quenching factor for the electrons in the veto is larger than 1 above ~1.5 MeV. This due to a bug, which, however, should have a minimal impact, since we do not expect high energy electrons.

The Phase-I of the data acquisition (ended in Jun 2014 and corresponding to the first 50 days of AAr run) was characterized by high activity ^{14}C in the TMB loading of the LSV. The total TMB loading was 50% and the measured rate in the veto (at the beginning of the 50 days data-set) was of the order of ~ 150 kHz. This very high rate prevented to lower the detection threshold. In addition to this, even if the mean capture time of neutrons was ~ 2.2μs, the veto acquisition gate was set to 70μs, to include signals from captures in other materials (like the cryostats steel).

During June 2014 and February 2015 the high-activity TMB was firstly removed from the LSV and, after a few months of data taking, replaced with radio-pure TMB, in concentration of 5%. The activity in the veto dropped down to less than 0.3 kHz and the Phase-II started. Because of the reduction of the TMB loading, the neutron mean capture time has increased to ~ 22μs. Therefore, the acquisition window is extended to 220 μs. This study described in this section refers to the DarkSide-50 Phase-I. The improvement of the veto efficiency obtained during the Phase-II is briefly discussed at the end of the Section.

Using the variables introduced in the previous section, we reproduced the set of veto cuts applied in the DarkSide-50 Phase-I analysis:

- **Prompt Cut**: Veto TPC events for which the region of interest from -10 ns to 200 ns of the sum waveform has an integral above 10 pe.
- **Delayed Cut**: Veto TPC events for which the charge in a 300 ns window with greatest charge in the first 8.8 μs after the prompt time is above 80 pe.
- **Late Cut**: Veto TPC events for which the charge in a 300 ns window with greatest charge between the end of the delayed window and the end of the acquisition window is above 110 pe.

The estimate of the rejection efficiency is obtained by looking at the numbers of events selected by the TPC Cuts (N_{TPC}) and by each of the veto cuts (N_{Veto}) applied on the events selected by the TPC Cuts. The efficiency of the veto is defined as:

$$\epsilon = \frac{N_{Veto}}{N_{TPC}}. \tag{4.7}$$

Analogously, the veto inefficiency is defined as 1 - ϵ, and it represents the fraction of WIMP-like events not tagged by the veto.

The overall efficiency is estimated by applying all the veto cuts in sequence on the same data sample selected by the TPC cut. Taking into account the set of events in the TPC (before the veto cuts) with total S1 in the [60,200] pe and [60,450] pe energy ranges, the single cluster cut removes ~57% of the events. The f_{90}like cut removes ~20% of the TPC single cluster events. The drift time cuts remove, among the single cluster events, 47.5% and 51.6% of the events in the TPC in the two energy ranges.

Cut	Cut rejection power	Number of surviving events
		1000000
No TPC energy depositions	5	~200000
ER vs NR	2	~100000
Energy cut	1.4	71420
Single cluster	1.6	44600
Fiducial volume	1.4	31900
Overall	**32**	

Tab. 4.3 Cut–by-cut rejection power in the TPC in the [60,450] pe energy range.

Cut	[60–200] pe Veto inefficiency (%)	[60–450] pe Veto inefficiency (%)
TPC cut	100	100
Prompt cut	11.9 ± 0.1	10.1 ± 0.1
Delayed cut	31.0 ± 0.2	30.7 ± 0.1
Late cut	94.5 ± 0.3	94.7 ± 0.3
All Vetos	3.0 ± 0.1	2.5 ± 0.1

Tab. 4.4 Inefficiency of the veto cuts for the two TPC energy ranges. The light yield in the veto is fixed at 520 pe/MeV.

The first results are quoted in Table 4.4 for the [60,200] pe energy range and for the [60, 450] pe energy range. The study of the possible systematics is described in what follows. The results will be presented only for the [60,450] pe energy range.

4.1.3 Study of the Systematics

4.1.3.1 Impact of the Variation of LS Light Yield on the Veto Efficiency

In these simulations, the veto light yield has been fixed to 520 pe/MeV, but the uncertainty on the true value were large. We performed a study of the effect of different values of LY on the veto efficiency in our simulation and the results are shown in Tab. 4.5 in the [60,450] pe S1 range. As expected, increasing the LY, has the effect of increasing the efficiency of the veto.

4.1.3.2 Impact of the LS Noise on the Veto Efficiency

The noise in the LSV, due to the contamination of ^{14}C, to the large number of reflections for each photon and to the rate of low multiplicity events, can affect the veto efficiency. At the beginning of the data taking, there was a noise in the Liquid Scintillator of ~ 6.1 pe in a random 210 ns window. The effect of the noise can be interpreted as a decrease of the threshold for the neutron tagging in the prompt cut to 3.9 pe. Similarly the amount of noise in a 300 ns sliding window in the [200,8800] ns window used for the delayed cut was 35 pe

Cut	LY of 480 pe/MeV ineff. (%)	LY of 520 pe/MeV ineff. (%)	LY of 560 pe/MeV ineff. (%)	LY of 600 pe/MeV ineff. (%)
TPC cut	100	100	100	100
Prompt cut	10.5 ± 0.3	10.1 ± 0.1	9.7 ± 0.3	8.9 ± 0.3
Delayed cut	32.0 ± 0.5	30.7 ± 0.1	29.9 ± 0.5	29.6 ± 0.5
Late cut	94.7 ± 0.9	94.7 ± 0.3	94.2 ± 0.9	94.0 ± 0.9
All Vetos	2.7 ± 0.2	2.5 ± 0.1	2.1 ± 0.1	1.9 ± 0.1

Tab. 4.5 Inefficiency of the veto for different veto light yields (LY) in the [60,450] pe energy range.

(reducing the effective threshold to 45 pe) and of 54 pe in the [8800,4e5] ns window (reducing the threshold to 56 pe for the delayed cut).

For the prompt cut we implemented the noise as derived from data, while for the late and delayed cut we scaled the values of the noise in a random 210 ns window to a 300 ns window:

$$n_{delay,late} = n_{prompt} \times 300/210. \tag{4.8}$$

By using $n_{prompt} = 6.1$ pe, the expected noise for the delay and late components is expected to be $n_{delay} = 8.7$ pe.

To correctly simulate the noise we started from the energy spectrum in a random 200 ns window. For each neutron interaction in the prompt window we sampled a value of the noise from that distribution. For this study we did not take into account the part of the distribution with negative values of pe. For the delayed and the late cuts we followed the same procedure scaling the noise by 300/210.

The simulation was done with a LY in the Veto of 520 pe/MeV. As expected, the effect of the noise is to increase the efficiency of the cuts and the effect is particularly visible in the prompt cut where the neutron detection threshold is relatively small. We observed an exponential decrease over time (with a decay constant of $\sim$ 1 month) of the mean value of the noise spectrum. The origin of this effect is unclear, but we repeated the noise calculations starting from a noise spectrum taken at the end of the AAr campaign. The mean value reduction is about 50%. For later runs the veto efficiency is, as expected, reduced. This behaviour is shown in table 4.6 for the [60,450] pe range and it is similarly observed in the [60,200] pe range.

The fluctuations of the noise to values larger than the threshold induce false neutron tagging. This effect is more important for the prompt cut because the threshold (10 pe) is close to the typical noise we have in a 210 ns window. To give an idea of the magnitude of this effect, 3.7% of the events that are rejected by the prompt cut have a number of photoelectrons deposited in the veto by the neutron smaller than 4.

An additional effect, not included in the simulation, is the possibility to reject an event because of a large noise either in the delayed or in the late veto window. We estimate that the noise distribution fluctuate to values larger than 80 pe (110 pe) in the 2.8% (1.0%) of the

Cut	Without noise ineff. (%)	With noise ineff. (%)
TPC cut	100	100
Prompt cut	10.1 ± 0.1	6.6 ± 0.1
Delayed cut	30.7 ± 0.1	29.6 ± 0.2
Late cut	94.7 ± 0.3	94.3 ± 0.4
All Vetoes	2.5 ± 0.1	1.6 ± 0.1

Tab. 4.6 Effect of the addition of the noise on the veto efficiency in the [60–450] pe energy range.

Cut	Quenching model from fig. 4.3 (a)	Fixed quenching factor $Q_F = 1./25$	Fixed quenching factor $Q_F = 1./50$
	ineff. (%)	ineff. (%)	ineff. (%)
TPC cut	100	100	100
Prompt cut	6.6 ± 0.1	6.9 ± 0.1	6.9 ± 0.1
Delayed cut	29.6 ± 0.2	29.6 ± 0.2	32.2 ± 0.2
Late cut	94.3 ± 0.4	94.4 ± 0.4	94.8 ± 0.4
All Vetos	1.6 ± 0.1	1.7 ± 0.1	1.9 ± 0.1

Tab. 4.7 Effect of changing the α quenching on the veto efficiency in the [60–450] pe energy range. Noise model from run 227 is also included.

cases (assuming that all the counts are due to noise and not to neutron capture). Since the inefficiency of the veto cuts has been estimated to be $\sim 2\%$, the additional rejection power due to fluctuation of the noise in the delay and late cuts is negligible.

4.1.3.3 Systematics Due to the α Quenching in the LS

The neutron capture on ^{10}B leads to the emission of one α particle in the Liquid Scintillator (with 1.47 MeV or 1.77 MeV energy). These α are heavily quenched in the scintillator and the light output is expected to be equivalent to a 30 to 60 keV_{ee} energy deposit. The results discussed so far are obtained with the quenching function plotted in Fig. 4.3.

We have estimated the systematics due to the uncertainties in the model of the quenching of the α. Including in the simulation of the noise, we have varied the quenching factor of the α from 30 to 60 keV_{ee}. The results on the efficiency are shown in Tab. 4.7: as expected, increasing the quenching factor from 1/25 (~ 60 keV_{ee}) to 1/50 (~ 30 keV_{ee}) slightly decrease the veto efficiency but the effect is not larger than 0.5%.

4.1.4 Phase-I Results

In conclusion, we estimate for the Phase-I run an efficiency of the veto of $\sim 98\%$. The observed changes of the efficiency for variation of light yield, noise and α quenching model are shown in Tab. 4.8. The fluctuations are of the order of 1%.

	Veto LY ineff. (%)	Noise ineff. (%)	α quenching ineff. (%)
Inefficiency	[1.9 - 2.7]	[1.6 - 2.5]	[1.6 - 1.9]

Tab. 4.8 Effect of variation of LY, noise and α quenching model in the [60,450] pe energy range. The dependency on the LY was estimated without including the noise and that's why the absolute inefficiency is larger.

We focused on the expected number of neutrons coming from the PMTs (the largest source of radiogenic neutrons) in 47.2 days. We assumed the worst–case scenario (all the neutrons coming from the borosilicate stems) and we used the activities reported in 4.2. Since two measurements are available for the ^{238}U chain (190 ± 40 mBq/PMT and 90 ± 40 mBq/PMT) we took the average between the two cases. We then expect

$$N = 130 \pm 25.6 \pm 6.5 \tag{4.9}$$

neutrons from the 38 PMTs in 47.2 days of data acquisition. The statistical uncertainty is computed taking the largest one among the two measurements, and the systematic error represents the difference between the two mean values, outside the statistical errors. It's worth noting that the uncertainties calculated above are not exhaustive: the errors on the neutrons cross section, for instance, are not included in this study.

Scaling the averaged number of expected neutrons by the fraction of neutrons surviving to the TPC cuts, we expect $0.936 \pm 0.18 \pm 0.05$ neutrons in the [60,200] pe window and $1.31 \pm 0.26 \pm 0.07$ in the [60,450] pe window. This estimate translates the number quoted in [3] for the AAr run.[3] The Collaboration quoted larger uncertainties in order to account for all the effects which are not considered in this study (for instance we set the neutron acceptance to 1).

By scaling for the veto inefficiency, we can then conclude that the expected number of neutrons from the PMTs during the 47.2 days in the Phase-I configuration, surviving the TPC cuts, and not tagged by the veto are:

$$\textbf{in the [60,200] pe window: } \mathbf{0.026\ ^{+0.011}_{-0.007}}$$

$$\textbf{in the [60,450] pe window: } \mathbf{0.029\ ^{+0.013}_{-0.007}}$$

4.1.4.1 Upgrade to the Phase-II

The removal of high-activity TMB allowed to reduce the threshold in the veto down to 6 pe in the prompt window (instead of 10 pe, as during the Phase-I) and so improve the efficiency to thermalization signal. Furthermore, the light yield measured in the scintillator during Phase-II is ~ 550 pe/MeV [83] (instead of 520 pe/MeV).

[3] ~ 1.3 *neutron-induced events, with large (> factor of 2) uncertainties*

From a combined analysis of AmBe source data and MC simulations, we demonstrated that the neutron rejection power for the neutron capture signal alone is ≥ 99.1% for the Phase-II. The main limit on the neutron capture efficiency is due to residual neutron captures on ^{1}H, happening in ~8% of cases. Simulation and ^{241}AmBe calibration data indicate that 8% of the 2.2 MeV γ-rays from neutron captures on ^{1}H escape the LSV without depositing energy. The maximum possible rejection power of the neutron capture channel alone, if every neutron capture were detected, with a 5% concentration of TMB, would be then ~ 99.3%. The remaining inefficiency in the neutron capture rejection power comes from the tails in the neutron capture time distribution that extend outside of the acquisition window, which happens to ~0.2% of neutrons that thermalize in the LSV. An additional ~0.05% of the neutrons are, according to the simulation, lost in captures in materials other than the LSV.

4.2 Gamma Background: a MC-based Spectral Fit

We will give in this Section a description of a G4DS-based spectral analysis of DarkSide-50 data, performed in order to evaluate the external gamma background and to measure the residual ^{39}Ar activity in the underground argon.

4.2.1 The simulation procedure

The full TPC spectra acquired during the AAr and UAr campaigns are shown in Figure 4.4. At low energy, the ^{39}Ar β-decay is the dominant component in the AAr sample, while several gamma full absorption peaks are visible in both the datasets above the ^{39}Ar endpoint. The spectra extend up to ~ 2.6 MeV[4] and those peaks can be accurately identified. In order to extract the residual ^{39}Ar activity in the UAr, we have first to understand and subtract from the UAr spectrum all the other components.

We developed a fit procedure based on MC spectra. In particular, we simulated with G4DS all the β and γ radioactivity coming from the detector components listed below:

- **TPC sensitive volume:** ^{39}Ar , ^{85}Kr, ^{42}Ar chain and ^{222}Rn chain.
- **Cryostats:** ^{60}Co, ^{40}K decays and ^{238}U, ^{232}Th and ^{235}U full decay chains. The ^{238}U and ^{232}Th chains are broken in order to account for possible deviations from the secular equilibrium. A uniform distribution in the cryostats geometry is assumed.
- **PMTs:** ^{60}Co, ^{40}K decays and ^{238}U, ^{232}Th and ^{235}U full decay chains. The ^{238}U and ^{232}Th chains are broken in order to account for possible deviations from the secular equilibrium. We believe that most of the activity comes from the borosilicate glass stems in the back of the PMTs.
- **Fused silica windows:** ^{40}K decay and ^{238}U, ^{232}Th and ^{235}U full decay chains. The material is expected to have higher levels of radiopurity with respect to the others, but, because of its placement, very close to the sensitive volume, even a small activity can produce a significant signal.

We introduced an additional component, the ^{85}Kr, assuming a uniform spacial distribution in the sensitive volume. The presence of ^{85}Kr in UAr was totally un-expected and no specific purification procedure has been put in place before the filling of the detector. The ^{85}Kr forbidden β-decay endpoint is at 687 keV and this make quite difficult to resolve this spectral shape from the one of ^{39}Ar . However, the fitter was not converging before the addition of this component. The ^{85}Kr decay has a 0.434% BR allowed channel, with endpoint at 173 keV to the excited state of ^{85}Rb. The de-excitation consists in the emission of a 514 keV gamma with $\tau_{1/2} = 1.015$ µs. Looking for the $\beta+\gamma$ coincidence in UAr data allowed us to confirm the presence of ^{85}Kr and to cross check the measured activity.

[4] The highest energy gamma line found in nature, coming from the ^{208}Tl in the ^{232}Th decay chain.

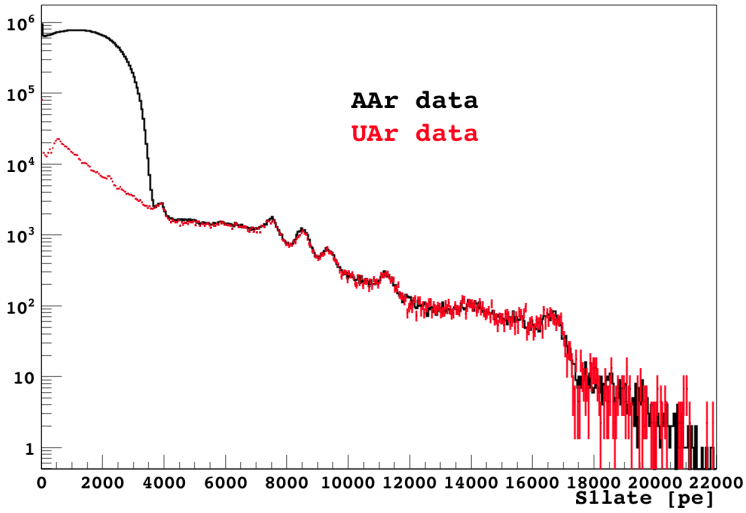

Fig. 4.4 Normalized energy spectra for the AAr (black) and UAr (red) campaign. No change in light yield has been observed after the filling of the detector with UAr. The data selection did not include a rejection of multi-sited events, so that some high energy full absorption peaks are visible.

We considered a possible contamination of ^{42}Ar, a nuclide with anthropogenic origin, even if we do not expect it to be present in UAr. The ^{42}Ar decay ($\tau_{1/2}$ = 32.9 y) leads to unstable ^{42}K ($\tau_{1/2}$ = 12.36 h). Both these decays are β decays, with endpoint 599 keV and 3525 keV respectively. The ^{42}K decay is accompanied by a 1524 keV gamma with 18% BR.

Most of the simulated radioactivity, originated in various materials, is due to the same decays or decay chains, so that the TPC energy spectrum show some similarities. We identified three observables in order to break the degeneracy between the spectral shapes: the standard S1 and drift time variables for single scattering events and S1late variable (defined as $(1-f_{90})\times$S1) for the multiple pulse data.

While the multiple pulse spectrum contains the full absorption peaks, the single scattering events sample (S1 vs drift time) embeds the information on the spacial distribution of the contaminants in the detector materials. For instance, the drift time distribution of events generated in the PMTs is different from the one of events generated in the cryostat (concentrated at the top and bottom of the drift volume and uniform respectively).

Figure 4.5 contains the S1 vs drift time distributions of single scatter events produced by the ^{232}Th decay chain contamination in the cryostats, in the PMT stems and in the fused silica. The bottom right panel shows the comparison of the S1late spectra of the all pulses dataset for the same background components. While the PMTs and cryostats induce a similar energy spectrum in the TPC, the two components show a different drift time distribution of the events. On the other hand, the contamination in the fused silica windows is closer to the TPC active volume and show different features in the TPC energy spectrum while the events are concentrated at the top and at the bottom of the active volume as in the PMT case.

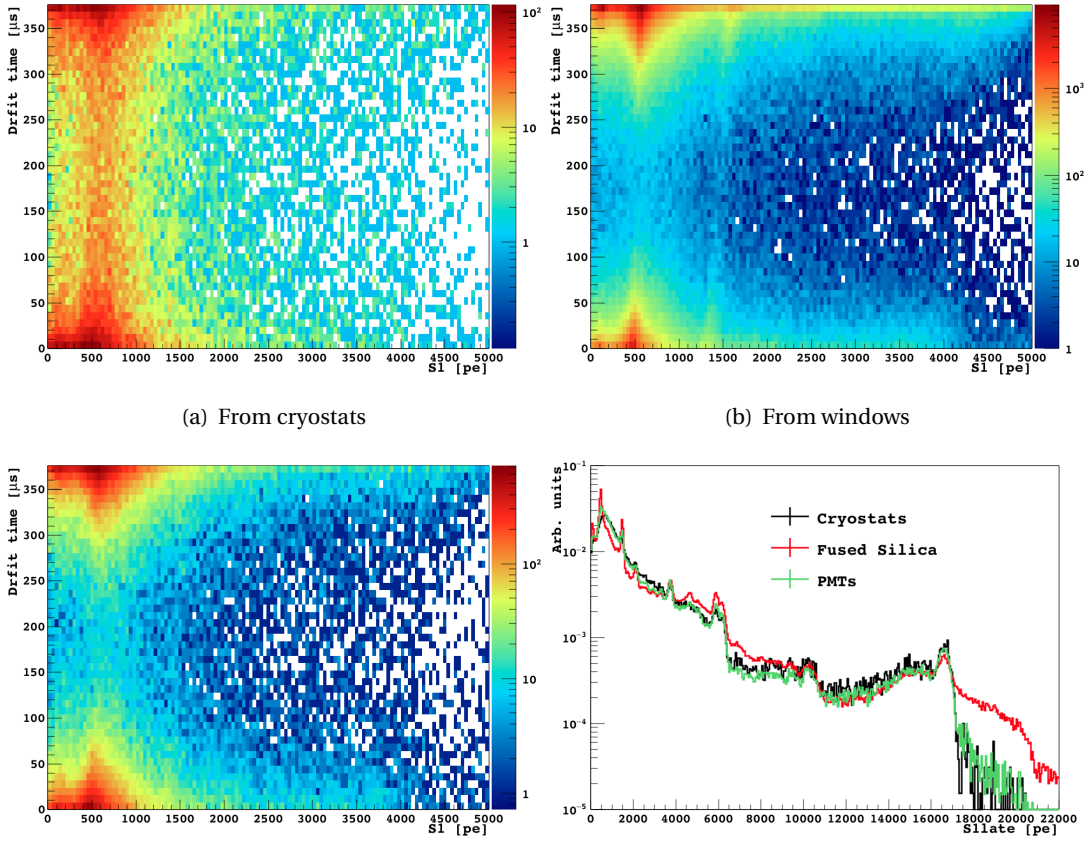

(a) From cryostats

(b) From windows

(c) From PMTs

(d) All pulese spectra

Fig. 4.5 G4DS simulations of the TPC spectra for the ^{232}Th decay chain in different detector materials. Comparison of the single scatter S1 vs drift time distributions and the all pulses spectra. See text for further details.

For the production of the (S1, drift time) 2D histograms we relied on the full G4DS simulation chain, described in Chapter 3. The use of the S1 variable is limited to the [0, 5000] pe energy range (slightly above the endpoint of the ^{39}Ar $\beta-$spectrum), because the saturation starts to be non-negligible at higher energy. In order to build the full energy spectrum, we opted for the **S1late** variable since it does not suffer from saturation induced distortion. The construction of the S1late is described in the next paragraph.

4.2.1.1 Null Field S1late Energy Scale and Spectral Corrections

The vertical saturation of the ADC boards is expected to be present only during the first tens of nanosecond of the typical scintillation pulse, because the fast component of the scintillation pulse is concentrated in this time window, while the slow component is emitted on a several microsecond time scale.

We defined f_{90} in Chapter 2 as the fraction of the pulse occurring in the first 90 nanoseconds of the signal S:

$$f_{90} = \frac{\int_0^{90\text{ns}} S(t)dt}{\int_0^{7\mu\text{s}} S(t)dt}. \tag{4.10}$$

The effect of saturation is totally absorbed in the f_{90} deviation from the true value. In this sense, the S1late variable (S1late = (1 - f_{90}) × S1) is free from saturation induced distortions. Actually the value of f_{90} is dependent on the reconstructed start time of the pulse too. However, this effect is believed to be small and so it is neglected in the S1late energy scale calibration.

A drawback of using this variable is a loss of resolution (since the typical value of the (1-f_{90}) factor for ERs is $\sim$ 0.7). For this reason we chose to use data acquired without the electric field. If no electric field is present in the liquid argon sensitive volume, almost all the deposited energy is converted into scintillation light. The S1 light yield of the TPC is higher with respect to the case where the drift field is present (in DarkSide-50: $\sim$ 8 pe/keV at null field and $\sim$ 7 pe/keV at the nominal field of 200 V/cm).

In the all-pulses spectrum the non-uniformity induced by the internal optics make the full absorption peaks disappear because of the large width. The full absorption peaks are in fact due to multi-sited events, since the gamma progressively looses its energy via Compton scatterings. Each interaction can occur at different z in the sensitive volume, where the light collection efficiency is different. We need to apply a correction in order to recover the detector resolution.

The S1 value is usually corrected for the z-dependence of the light collection efficiency due to internal optics, according to the fit function shown in Figure 3.7 (left). Nonetheless, without the electric field there is no S2 and thus no information of the drift time. On the contrary, we can then exploit the z-dependence of the top-bottom asymmetry (TBA, shown in Figure 3.7 right) in the light collection to recover the average position of the event. In presence of multi-scattering events the TBA will be the weighted average of the single deposits.

Figure 4.6 (a) shows the field off S1late spectrum, TBA corrected (in black), taken during the UAr campaign. It is compared to the spectrum before the TBA correction (in blue, scaled by a factor of 10 for easier comparison). In order to compute the absolute light yield, we identified some of the natural radioactivity full absorption peaks. A few ^{83m}Kr calibration runs are also included in the dataset, to add one point at low energy (41.5 keV). At high energy, the peaks of ^{208}Tl (2614 keV), ^{214}Bi (1764 keV), ^{40}K (1461 keV), ^{60}Co (1332 keV and 1173 keV) are visible. The sub-MeV energy region includes many gamma lines from the ^{232}Th, ^{238}U and ^{235}U decay chains and the identification is not straightforward. For instance, the 583 keV line of ^{208}Tl from the ^{232}Th chain overlaps with the 609 keV line of ^{214}Bi from the ^{238}U decay chain. At lower energy the density of gamma lines is larger and we only used one of the most prominent one (the 352 keV line from ^{214}Pb).

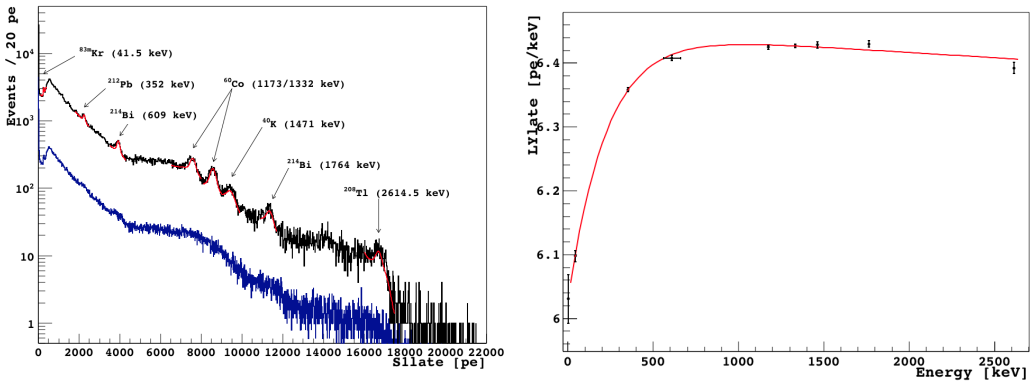

(a) Null field spectrum (S1late)

(b) Null field light yield (S1late)

Fig. 4.6 S1late null field spectrum (a) and corresponding light yield (b). The peaks are fitted after the local background subtraction. In (a), the spectrum reconstructed by means of the top/bottom asymmetry (black) is compared to the one without light yield correction (blue, scaled by a factor of 10 for easier comparison).

We fit each of those peaks with a Gaussian after the subtraction of the local background. The mean S1late value is divided by the true energy to obtain the light yield. We then found that the light yield LY_{late} [pe/keV] dependency on the energy E is well described by the following function:

$$LY_{late} = \frac{6.45}{1+0.07\cdot e^{-E/0.13}} - 3.4\times10^{-5}\cdot E. \tag{4.11}$$

The S1late light yield and width of the peaks are used to build the S1late MC spectra. We simulated each background component and sampled the spectrum of the deposited energy inside the TPC sensitive volume.

4.2.1.2 Spectra Normalization

The normalization between the S1 vs tdrift (field on, single scattering) histograms and S1late (field off) spectra is done on the basis of the different lifetime of the datasets. Some basic cuts are applied to the full statistics in order to select good triggers, namely the quality cuts Q_CUT 1 (number of channels) and Q_CUT 2 (baseline found) and the physics CUT 9 (good pulse start time). The lifetime of the removed events does not contribute to the integrated lifetime of the datasets.

Table 4.9 summarizes the lifetime of the considered datasets. No further selection cut is applied to build the all-pulses spectrum. In order to build the (S1, drift time) spectra, we instead need to remove multiple scatter events and take this into account for the relative normalization of the datasets.

Three effects can induce systematics in the estimate of the normalization factor between single and multiple scatter datasets:

Dataset	Spectrum	Lifetime [s]	Collected statistics
UAr	S1 vs drift time	5349740	2.415768×10^6
UAr	S1late	372213	4.22471×10^5
AAr	S1 vs drift time	491785	1.9641181×10^7
AAr	S1late	823392	3.7643281×10^7

Tab. 4.9 Lifetime of the S1 vs drift time and S1late datasets. The lifetime is computed after the application of the same basic quality and physics cuts. The collected statistics does not include multiple scatter and pile-up events in the field-on case. The AAr dataset lifetimes are shown for comparison. The fit of the AAr spectra introduce additional systematics, discussed in the last Section of this Chapter.

- We relied on the clustering algorithm run on MC data to estimate the number of reconstructed pulses. The algorithm is tuned in a specific energy range (S1 < 1000 pe) and we can not exclude an energy dependence of the clustering condition. However, we do not expect a large variation: the fraction of simulated events with only two pulses (single scatter) changes for example from $48.9 \pm 0.4\%$ to $46.3 \pm 0.3\%$ when the clustering condition is reduced from 3 mm to 2 mm (for a typical gamma calibration source).
- We already mentioned the non negligible probability for a scintillation pulse (both S1 or S2) to induce an electron emission from the cathode (S3, or echo). The result of having one or more echoes inside the acquisition window is an increase in the number of reconstructed pulses, which does not reflect the number of interactions in the sensitive volume. The echo pulses can be easily identified because of the fixed time difference with respect to pulse which created them. We developed a new algorithm for the identification of echoes and the correct pulse counting, as described in Section/Appendix B.
- During the runs with the drift field, the acquisition window is larger with respect to the one used in field off data. In the field on data analysis we require a minimum time difference between two events of 1.35 ms, in order to reduce the probability of triggering on one echo. This means that the pile-up probability is different among the datasets and must be accounted for in the calculation of the lifetime.

All these effects are expected to have a systematic %-level impact on the estimate of the normalization factor between the two datasets (single scattering field-on and multiple scatter field-off). In order to account for them, we will introduce in the fit minimization a nuisance parameter for each pair of spectra to allow a few-% variation of the predicted single to multiple scatter ratio.

4.2.2 Fit Procedure and Systematics

The fit is based on a χ^2 minimization. The χ^2 is computed at the same time on both the 2D (S1 vs drift time) histogram and the S1late spectrum. The nuisance parameters introduced above are used to weight the ratio between single and multiple scattering for each background components. The fitting intervals (S1, drift time and S1late) and the binning of each histogram can be opportunely changed to determine their impact on the fit result. The free parameters of the fit are the amplitude of each component and the nuisance parameter central values. A Gaussian constraint, with some given weight, included in the χ^2, forces the nuisance to be close to one.

The user can:

- choose which background components are included in the fit;
- set the initial value for each amplitude;
- fix the weight to be assigned to each nuisance parameter in order to have a maximum deviation of the order of few-%.

Figure 4.7 shows one fit example. Data is in dark blue (S1 and drift time) or black (S1late), the sum of the components according to the fit results in red. As already mentioned, the fitting interval for the S1 variable should not exceed 5000 pe, because the S1 variable does not include a correction for the PMT saturation. The drift time fit interval is [20,355] μs and the S1late spectrum is fitted in the [1000, 22000] pe range.

The results of the fit, performed with 12 background components and 24 free parameters, reveal low sensitivity to some components and some degree of degeneracy. We then decided to include in the fitter procedure our knowledge of the specific activity of some detector components (most of them have been γ-counted). We added the possibility to the user to set the starting value of one or more component activity to the expected value from the screening. A Gaussian constraint, included in the calculation of the χ^2, is then applied, with a weight calculated from the error on the screening measurement. I will discuss the comparison between the fit results and the screening measurements in the next Section.

We identified two potential sources of systematic errors related to the fit procedure:

- The MC spectra have different statistics. This is due to the different probability of interacting inside the sensitive volume for gammas coming from different detector materials. We required each simulation to have at least 2×10^4 events depositing energy in the TPC. In some cases (^{39}Ar for example) this number is larger than 500×10^3 events. Thus, the statistical fluctuations can impact in different ways depending on the background component.
- The composition of the χ^2's from the two histograms have a dependence on the binning of each one of them. Moreover, changing the initial value of one component or constraining it to the reference activity affects the fit result too.

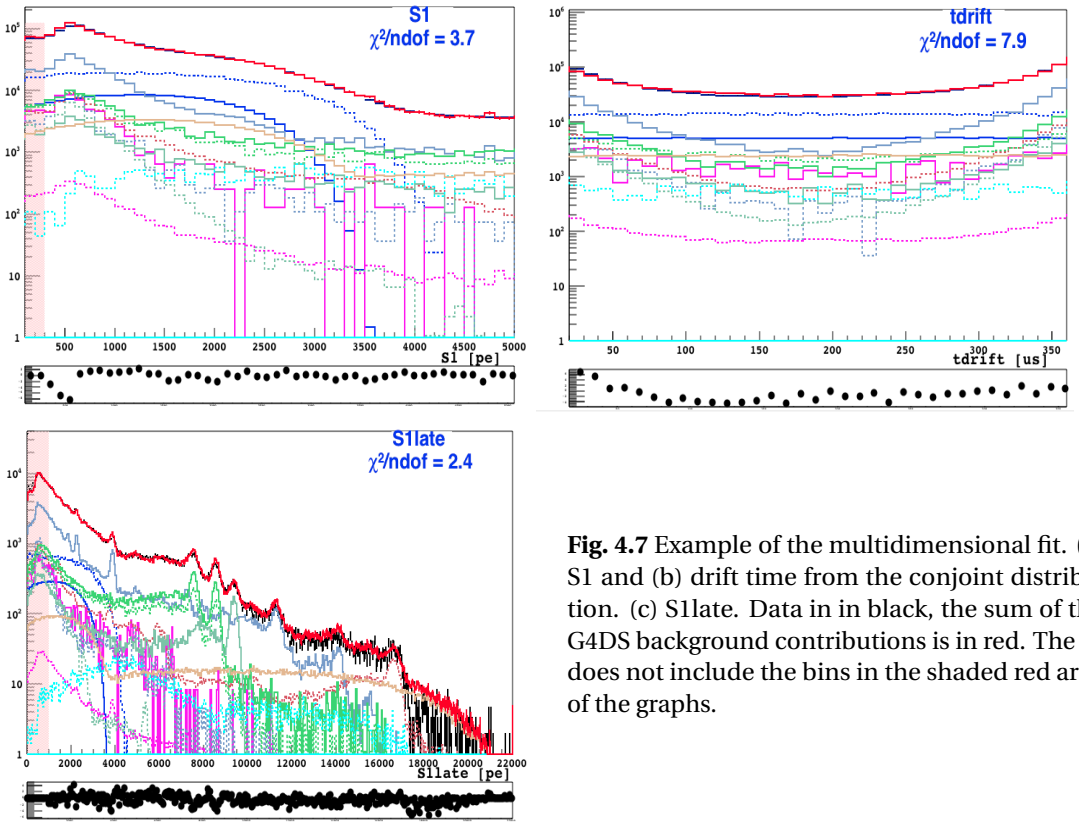

Fig. 4.7 Example of the multidimensional fit. (a) S1 and (b) drift time from the conjoint distribution. (c) S1late. Data in in black, the sum of the G4DS background contributions is in red. The fit does not include the bins in the shaded red area of the graphs.

In order to account for the MC statistics issue, we included the statistical errors of the MC spectra in the χ^2 calculation. We accounted for the systematics related to the second effect by running the fit in many different configurations, changing time after time the number of included components, the binning of the spectra, the fit intervals and the number of components with activity constrained to the reference values.

4.2.3 Comparison with the Screening Results

Table 4.10 summarizes the combined results of the fitter performed several times in different configurations. The measured activity from the fit is compared to the result of the material screening. The statistical uncertainty comes from the fit result in the configuration with the lowest global χ^2. The systematics, computed as described above, does not take into account the uncertainty on the measure of the mass of the detector component.

Figure 4.8 shows the best fit of the data, with the components included in the Table. All the listed radioactive nuclides or decay chains are long lived compared to the lifetime of the experiment, but the ^{60}Co (with half-life of 5.27 years). We took into account the time difference between the screening of the material and the data taking (of the order of 2 years).

In general, we found a good agreement(within the errors) with the screening measurements results. Nonetheless, there are some discrepancy in the case of the ^{238}U chain activity

Component	Activity	Measured	Best Fit (±stat.±sys.)
Cryostats (160 kg) [mBq/kg]	^{238}U top	~2.4	$1.99 \pm 0.23 \pm 1.12$
	^{238}U bottom	~0.4	$2.37 \pm 0.13 \pm 0.23$
	^{232}Th top	0.8 ± 0.3	$0.35 \pm 0.02 \pm 0.4$
	^{232}Th bottom	0.4 ± 0.3	$0.42 \pm 0.02 \pm 0.2$
	^{235}U	< 15	not included
	^{60}Co	13.3 ± 1 (~ 10)^a	$7.66 \pm 0.35 \pm 1.15$
	^{40}K	< 2.5	not included
PMT stems (38) [mBq/PMT]	^{238}U top (^{b})	140 ± 30	$20.5 \pm 0.67 \pm 2.24$
	^{238}U bottom	18.2 ± 1.2	$55.5 \pm 0.7 \pm 7.0$
	^{232}Th	6.0 ± 1.0	$8.93 \pm 0.34 \pm 1.42$
	^{235}U	7.0 ± 1	$6.43 \pm 0.32 \pm 0.11$
	^{60}Co	8.8 ± 0.8 (~ 7)^a	$11.84 \pm 0.72 \pm 1.62$
	^{40}K	79 ± 11	$85.74 \pm 3.7 \pm 1.66$
	^{54}Mn	1.3 ± 0.3	$1.25 \pm 0.5 \pm 0.53$
Windows (3.7 kg) [mBq/kg]	^{238}U	0.370 ± 0.040	$0.11 \pm 0.04 \pm 0.01$
	^{232}Th	0.041 ± 0.004	not included
	^{235}U	0.017 ± 0.002	not included
Inside TPC (46.7 kg) [mBq/kg]	^{39}Ar	?	$0.71 \pm 0.05 \pm 0.10$
	^{85}Kr	$1.92 \pm 0.05\%$	$2.7 \pm 0.06 \pm 0.14$
	^{222}Rn (^{c})	$\sim 2 \times 10^{-3}$	$0.040 \pm 0.005 \pm 0.018$
	^{42}Ar	?	$0.122 \pm \pm 0.005 \pm 0.0133$

Tab. 4.10 The simulated radioactivity for the spectral study compared to the screening measurements. *a*) The cryostat steel and the PMTs have been counted ~ 2 year before the data taking. The ^{60}Co activity is decreasing over time and the expected activity at the time of the data taking is ~ 70% of the measured value. *b*) As already pointed out in the previous section, two measurements are available for the upper part of the ^{238}U decay chain (90 ± 40 and 190 ± 40 mBq/kg). We took the average value, in good agreement with the measurements of the ^{235}U acivity. *c*) The uncertainty on the measurement of the ^{222}Rn chain is hard to evaluate. It changes with time, according to the purification loop status. 2 μBq/kg is the nominal value.

and the ^{60}Co activity in the PMTs. The difference in the ^{238}U case could be due to our lack of information about the breaking of the secular equilibrium. Our assumption is that both the upper part of the chain (down to ^{226}Ra) and the bottom part are independently in equilibrium. Moreover, there is some tension in the reported measurements of the activity of different chain segments. For example, the best fit shown in 4.8 is obtained assuming the secular equilibrium and without any constraint on the chain activity (the fit results is $A(^{238}\text{U}) = 37 \pm 0.5$ mBq/PMT).

There are other hypotheses to explain the discrepancy in the PMTs case. First, even if there is no reason to expect a large variations in the specific activities, only a batch of three devices has been screened. Second: we assumed that the contamination is concentrated in the stems, and this might be wrong, for example in the ^{60}Co case. If the radioactivity is mainly present in the body or in the window of the device, the probability to produce a signal

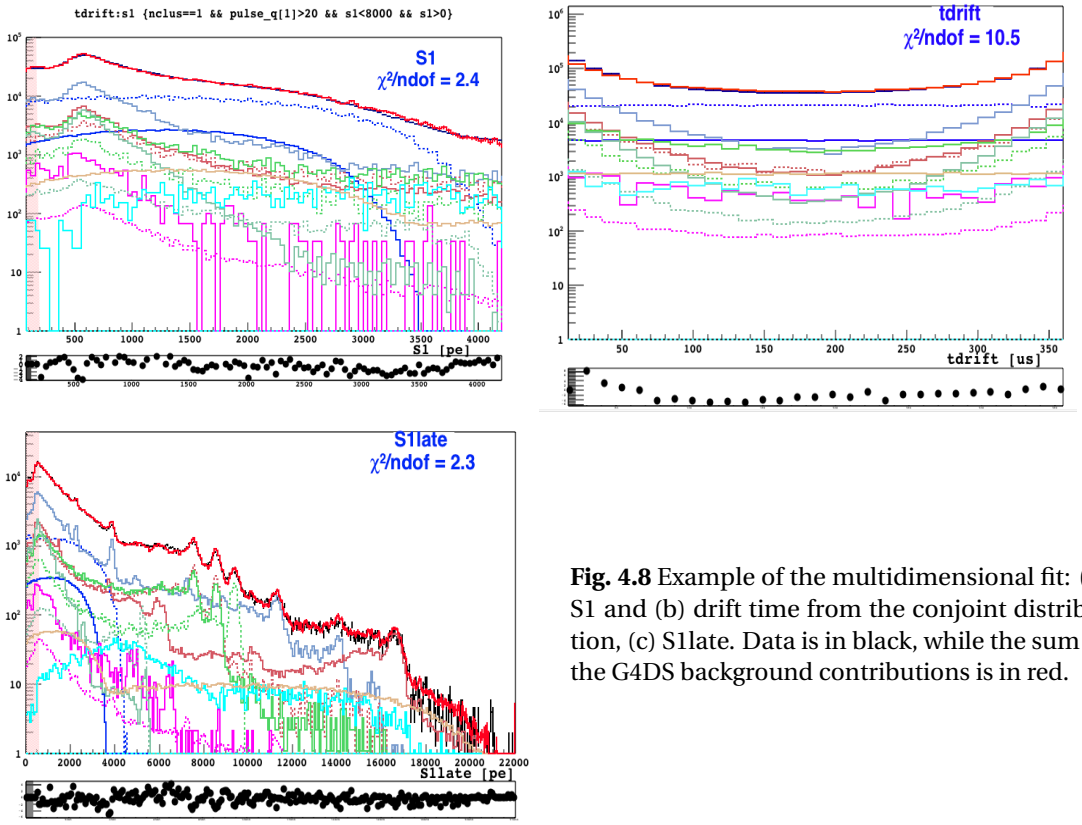

Fig. 4.8 Example of the multidimensional fit: (a) S1 and (b) drift time from the conjoint distribution, (c) S1late. Data is in black, while the sum of the G4DS background contributions is in red.

in the TPC is larger (roughly a factor of 2 for the PMT window). Thus, the required activity to produce the observed spectrum can be lower. Third: close to the PMT stems there is some material which we did not account for, that is the PMT bases, the pre-amplifiers and the cables. We do not expect those components to provide the significant contribution alone (this material has been γ-counted too), but the global contribution might be non negligible.

4.2.4 The ^{85}Kr Activity and the ^{39}Ar Depletion Factor Measurement

The AAr dataset is widely dominated by the ^{39}Ar beta spectrum. This means that the sensitivity to the background components below 565 keV (the decay endpoint) is totally suppressed. In addition to this, because of the higher internal activity, the probability of having pile-up events and thus triggers on echoes or S2's is larger with respect to the UAr sample, resulting in a larger systematic uncertainty on the calculation of the multiple to single scattering ratio.

Thus, in order to compute the ^{39}Ar activity in the UAr and the depletion factor with respect to the AAr we did not fit the AAr spectra. We instead subtracted from the AAr dataset the background components according to the results of the fit to the UAr sample. The background component amplitudes come from the best fit described in the previous sections. Figure 4.10 shows the comparison between the AAr spectrum and the fit of UAr data after the

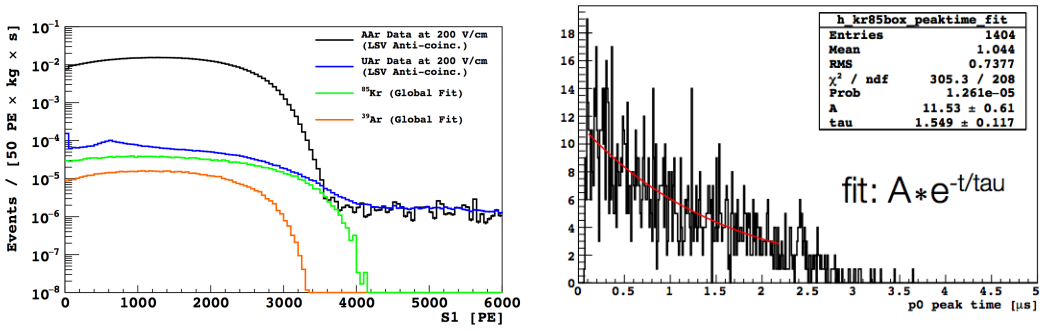

(a) Enpoint of ^{39}Ar (b) Double S1 separation time for ^{85}Kr candidates

Fig. 4.9 The normalized AAr and UAr spectra in the [0,6000] pe S1 range and the time distribution of ^{85}Kr candidates.

normalization. We subtracted all the background components but the ^{85}Kr (not present in the AAr data or present in a negligible amount) and the ^{39}Ar .

We can infer the absence of ^{85}Kr in the atmospheric argon run from the comparison of the AAr and UAr spectra in the region of the ^{39}Ar endpoint. Figure 4.9 (a) shows exactly this portion of the spectra, normalized by the different lifetime. The disagreement around S1 = 4000 pe is due to the shape of the ^{85}Kr beta decay, which has endpoint larger than the ^{39}Ar one. As already mentioned, the presence of ^{85}Kr can be cross checked in real data, thanks to the 0.434% BR for which the decay consists in the emission of one β^- (173 keV endpoint) to the metastable state of ^{85}Rb. Since the ^{85m}Rb decays via γ emission (514 keV) with half-life of 1.015 μs, the decay will induce double-S1 pulse events with short time separation between the two pulses.

We identified this class of events in real data and run a full G4DS simulation to estimate both the escape probability of gammas and the pulse identification efficiency. We simulated 2×10^4 ^{85}Kr $\beta+\gamma$ decays uniformly distributed in the TPC sensitive volume. We evaluate the γ escape probability to be $\sim$ 15%. We then modified the standard pulse-finder algorithm and passed the simulated sample to the full reconstruction chain.

We determined that the combined detection efficiency of the $\beta+\gamma$ decay channel is $\sim$ 75%. Figure 4.9 (b) shows the distribution of the time difference between the γ and the β. The fit with an exponential returns a decay constant of 1.55 ± 0.12 μs, compatible within the errors with the literature value of 1.45 μs. Given the lifetime of the considered dataset, we calculated that the total ^{85}Kr activity is 1.92 ± 0.05 mBq/kg (error is statistical only).

The remaining ^{39}Ar activity in the AAr sample is 985 ± 0.16 mBq/kg (only statistical error) after the background subtraction. In this estimate the content of the first bin is not corrected for the large contamination of very low energy events with unknown origin (these events roughly double the statistics of the first bin, but the effect on the measurement of the ^{39}Ar activity is negligible). This number is in good agreement with the reference value obtained by the WARP Collaboration, namely: A ($\mathrm{Ar_{Atm}}$) $= 1.01\pm0.02\pm0.08$ Bq/kg [79].

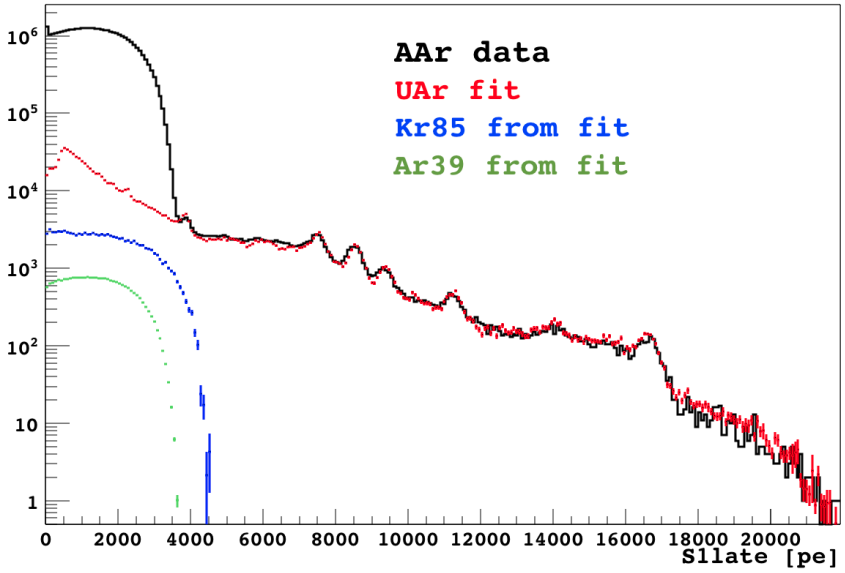

Fig. 4.10 The AAr S1late spectrum compared to the fit of the UAr data, after normalization. ^{39}Ar and ^{85}Kr spectra from the fit are also shown.

The ^{39}Ar activity in the UAr data is 0.710 ± 0.12 mBq/kg (statistical and systematic errors combined). For the second DarkSide publication we calculated the depletion factor with respect to the reference value of 1 Bq/kg for the activity of ^{39}Ar in atmospheric argon. The measured depletion D is then (considering only the errors on the ^{39}Ar activity in UAr):

$$D = 1400 \pm 200. \tag{4.12}$$

4.3 Conclusions

I reported in this Chapter about the results of G4DS-based background estimates for the DarkSide-50 experiment. The neutron background study included the evaluation of the (α, n) neutron yield and the energy spectra for each detector component. We then measured, using the material screening results, the expected number of neutron during the AAr campaign and the liquid scintillator veto efficiency to radiogenic neutrons.

The γ background study is based on a multi-dimensional fit of MC spectra to the real data. We used three different observables to discriminate between the background components. We found a reasonable agreement between the material screening and the fit results and determined the presence of an un-expected contamination of ^{85}Kr in the UAr dataset. We finally extracted the residual ^{39}Ar activity in the UAr sample and measured the depletion factor with respect to the AAr campaign.

Chapter 5

Discussion on the pulse shape discrimination

The pulse shape discrimination allows us to distinguish between nuclear and electronic recoils by looking at the different shape of the primary scintillation pulse (S1).

The first evidence of a double exponential time profile of the argon scintillation light dates back to 1977 [75]. The origin of luminescence is attributed to de-excitation of low-excited molecular states (excitons). Two excited states are available for liquid argon, the $^1\Sigma_u^+$ singlet and the $^3\Sigma_u^+$ triplet states. The decay constants values are $\tau_1 = 7.0 \pm 1.0$ ns for the singlet and $\tau_2 = 1.6 \pm 0.1$ μs for the triplet.

It was later found [76, 77, 74] that the fraction of excitons decaying with the fast decay constant is larger for higher deposited energy density. The average value of the prompt fraction in liquid argon is about 0.3 for electron recoils and about 0.7 for nuclear recoils. The pulse shape discrimination is based on the measurement of the prompt fraction to distinguish nuclear recoils from electron recoils.

To measure the fraction of fast component of the signal, we used the f_{90} parameter, defined as the fraction of scintillation light collected in the first 90 ns of the S1 pulse. The SCENE experiment proved that this choice is more effective than others, such as f_{50} or f_{200} [88].[1]

Our goal is to draw a WIMP search region in the (S1,f_{90}) plane, where the NR acceptance is maximal and where we do not expect any ER background. The f_{90} distributions of nuclear and electron recoils are extremely well separated above ~ 20 keV_{ee}. This energy corresponds to ~ 140 pe in DarkSide-50 at the nominal field. At lower energies, as shown in the (S1,f_{90}) distribution of Fig. 2.8 and 2.9, the two populations tend to overlap. To draw the contours of the WIMP search region we need to estimate the leakage of electron recoils (ER) in the nuclear recoils (NR) band.

[1] The prompt component has a decay time constant of ~ 6 ns. A few tens of nanoseconds are necessary in order to integrate it completely. On the other hand, in order to maximize the separation, the probability of integrating photoelectrons originated from the slow decay component (with decay time of 1600 ns) must be negligible.

We fixed a maximum leakage of 0.01 ER events per S1 bin of 5 pe and computed, for each S1, the f_{90} value above which we expect a number of events lower or equal than the leakage. This value of f_{90} is defined hereafter the leakage position. The WIMP search region is then obtained by intercepting the leakage prediction curves with the 90% (or 99%) nuclear acceptance band.

The extrapolation of the leakage position is done by means of an analytical fit of the f_{90} distribution for each S1 bin. As analytical fit function is usually taken, by this and other Collaborations, the Hinkley model, an approximated form to describe the distribution of two normally distributed correlated variables.

In this section I will discuss our understanding of the f_{90} statistics and the limitations of the Hinkley model. I will then present an alternative analytical model and a procedure to estimate of the systematic error on the prediction of the ER leakages.

5.1 Statistical considerations on f_{90}

The f_{90} variable is differently distributed if expressed as a function of either the true number of photoelectrons, $f_{90}(\text{npe})$, or the reconstructed S1 variable, $f_{90}(\text{S1})$. The latter is exactly the variable used in the DarkSide-50 analysis. In the first case, the distribution can be easily parameterized, taking into account all the statistical effects governing the photon generation, propagation, detection, and reconstruction. For each energy deposit we have to take into account:

- the Poisson distribution of the number of photons,
- the collection efficiency dependence on z,
- the time distribution of the photon emission,
- the possible multiplicative effect of TPB (the wavelength shifter all the internal walls are covered with),
- the quantum efficiency of the PMTs,
- the effect of the single photoelectron response (SER),
- the prompt and late noise, which embed the baseline fluctuations and the reconstruction effects.

For most of these effects, the statistics is well known. For instance, the distinction between fast and slow decay time constants and the quantum efficiency lead to a binomial distribution, while the geometrical effect and the SER sampling are governed by the Poisson statistics for large S1. The electronic noise effect should follow a Gaussian distribution, even though the resolution values in real data are not easily predictable. The simulation of the electronics suggests that the electronics induced noise is small compared to the spread due to the other effects.

As already mentioned, the statistics changes if f_{90} is expressed as function of the reconstructed S1. When we fit the f_{90} distributions, the procedure requires first to fix the S1 to an arbitrary value $S1^0$ for which the f_{90} distribution is projected on a histogram. This means that the prompt and late components are fully anti-correlated since the sum of the prompt and the late is exactly equal to $S1^0$. Ideally, being fully anti–correlated, the variances of the prompt and late components must be identical. The ideality could be broken since $S1^0$ is not exactly equal to a value, but corresponds to a bin, and so to a certain range of S1.

We then expect that the prompt and late resolutions (σ_i, $i = p, l$) can be parameterized by the following equations:

$$\sigma_p = \sqrt{f_P \times (1 - f_P) \times S1 + K_p^2(S1)} \tag{5.1}$$

$$\sigma_l = \sqrt{f_P \times (1 - f_P) \times S1 + K_L^2(S1)} \tag{5.2}$$

where f_P is the prompt fraction. The first term of each resolution originates from the binomial distribution, induced by the integration of the [0,90] ns and [90,7000] ns windows. $K_p(S1)$ and $K_L(S1)$ are the terms accounting for all the other effects. In a first approximation, we expect that:

$$K_i(S1) = k_i \times \sqrt{S1} \qquad (i = p, l). \tag{5.3}$$

where k_i are constants. $K_p(S1)$ and $K_L(S1)$ are ideally equal, because of the full anti–correlation of the prompt and the late variables mentioned before. This also means that we do not have to associate to the resolutions, obtained by fitting the real data, those physical parameters that we estimated for the S1(npe) case. To make a practical example, it would be a mistake to recover a SER nominal resolution of ~0.4 (as expected from the real data), since this resolution value is expressed with respect to the number of photo-electrons and not to the reconstructed S1.

Moreover, in a simplified scenario where the singlet to triplet ratio (the prompt fraction f_P) is constant over the energy, we can draw another conclusion: all the effects which do not interfere with the time distribution of the pe's, but act globally on their total number, do not alter the f_{90} distributions. The initial Poisson fluctuations of the number of scintillation photons, the z dependent collection efficiency and the quantum efficiency of the PMT's induce events with different initial energy to populate different S1 bins. However, the f_{90} statistics is only dependent on the value of S1 in that bin and keeps no memory of all the effects occurring before the conversion of photons to photoelectrons.

In practice, the shape of the f_{90} distribution is only determined by the processes independently acting on the prompt and late parts of the signal: this is the case of the SER and of the noise terms. Figure 5.1 (left) illustrates this behavior.

The black distribution is obtained with a photon-by-photon toy MC that mimic all the effects described above, including the conversion of the energy deposit into scintillation, the sampling of the decay time constant for each photon (with prompt fraction equal to 0.3), the

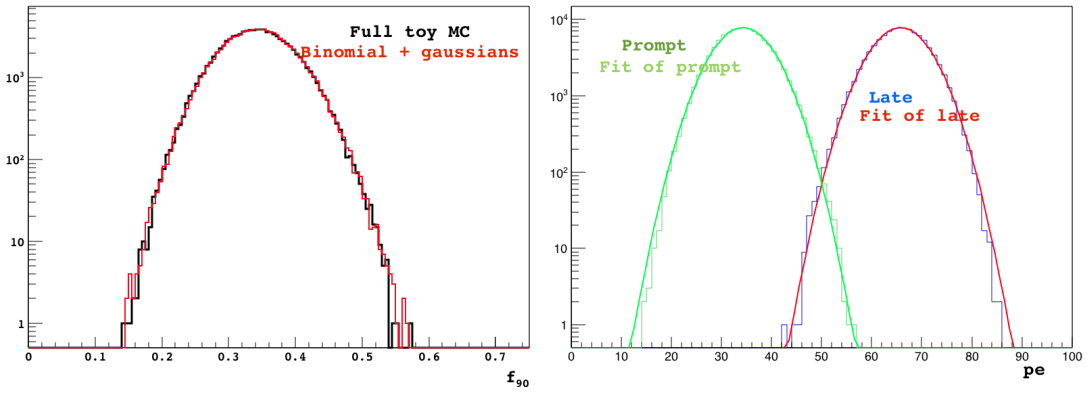

Fig. 5.1 Left: the f_{90} distribution obtained with a photon-by-photon toy MC (black) compared to a simple binomial and Gaussian simulation. Right: the distributions of the prompt and late parts of S1, fit to a Gaussian. The first comparison shows how all the effects affecting the photon propagation before the conversion in photoelectrons do not have impact on the f_{90} distribution. The Gaussian fit of the prompt and late distributions returns equal σ of 5.12 ± 0.01 pe.

quantum efficiency and the charge response of the photo-detectors (with $\sigma_{SER} = 0.4\ \mu_{SER}$), using realistic parameters. Only the baseline noise is not taken into account. Only the f_{90} of the events with S1$= 100 \pm 0.5$ pe are considered in the shown distribution.

The red distribution is obtained starting from a fixed number of 100 pe. Only two processes are simulated: a binomial separation in prompt and late part of the signal (with prompt probability of 0.3) and the sampling of the charge for each photoelectron (with $\sigma_{SER} = 0.4\ \mu_{SER}$). In this case too f_{90} is accepted only when S1$= 100 \pm 0.5$.

The two distributions are perfectly compatible. With the same simulation sample we can study independently the prompt and the late parts of the signal. The right panel of Figure 5.1 shows how they are distributed. They are fit to a Gaussian to measure their spread. The mean values are 34.28 ± 0.02 pe and 65.71 ± 0.02 pe respectively (S1 is fixed to ~ 100), while both the sigmas are 5.12 ± 0.01 pe. Because of the binning, the prompt and late signals are fully anti-correlated and their σ's are equal. Moreover, the value of these σ's does not depend on the input statistics. The relation between input parameter of the simulation and the widths of the binned distributions is completely lost.

5.2 Development of a toy MC

In addition to the binning effect, we observe a variation of the mean f_{90} as a function of S1, which reflects a dependence of f_P on the energy of the event. The maximum variations are at low S1, where the mean value of the f_{90} distributions changes from ~ 0.34 at S1 = 60 pe to ~ 0.30 at S1 = 140 pe. The right panel of Figure 5.2 (right) shows this dependence.

Thus, because of fluctuations, any fixed S1 bin is populated by events with low energy (and higher f_P) and by events with high energy (and lower f_P with respect to the mean value

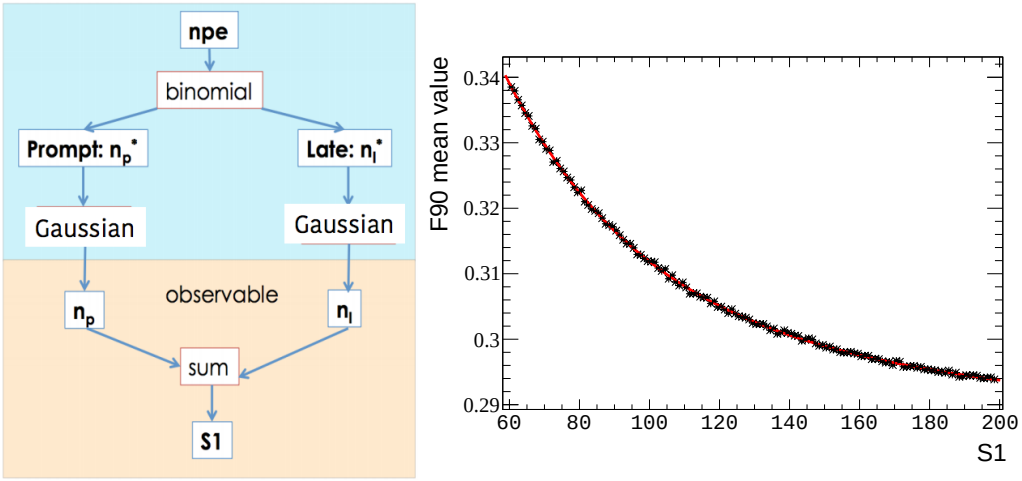

Fig. 5.2 Fit of the mean value of the f_{90} distributions for each S1 1 pe–bin obtained from AAr data (right) and a pictorial representation of the toy MC production procedure (left).

in the bin). This effect is negligible above ~ 100 pe, but it can induce some widening of the distribution at lower S1. We will discuss in a dedicated Section this effect.

On the basis of the assumptions discussed above, we developed a toy MC procedure, illustrated in Figure 5.2 (left), defined as follows:

- random distribution of npe, in [60,300] range, with the same shape of the S1 distribution in the real data;
- binomial random extraction of the prompt component (the late is obtained by subtraction from the total number of pe); the fraction of the prompt, f_P, used in the binomial random sampling, is a function of npe, taken from the real AAr data (f_P is assumed to coincide with the mean of the f_{90} distribution of the real data), as shown in Figure 5.2 (right).
- gaussian smearing of the prompt and of the late components with different and arbitrary (tunable) widths ($m_p \times \sqrt{\text{npe}}$ and $m_L \times \sqrt{\text{npe}}$ for prompt and late, respectively);
- filling of a 2D histogram: f_{90} = prompt / (prompt + late) vs S1 = prompt + late.

We can tune our toy MC on real AAr data in the [60,250] pe S1 energy range. The dataset is supposed to be a pure sample of single scatter events, because of the overwhelming abundance of ^{39}Ar ER events, which dominates the low energy region. The only free parameters are the σ_P and σ_L widths. Under the assumption of their dependence on the $\sqrt{\text{npe}}$, we scanned over m_P and m_L to find the best pair to reproduce real data. This dependence is expected for the SER term and assumed for the noise ones.

The statistics used in each generation is 2×10^8 events. We then evaluated the χ^2 between the f_{90} of each obtained distributions, in the entire S1 range, and the real data. The preliminary obtained χ^2 distribution is shown in the bottom right panel of Figure 5.3. To better identify the real minimum we have to increase the statistics, since the χ^2 is dominated by

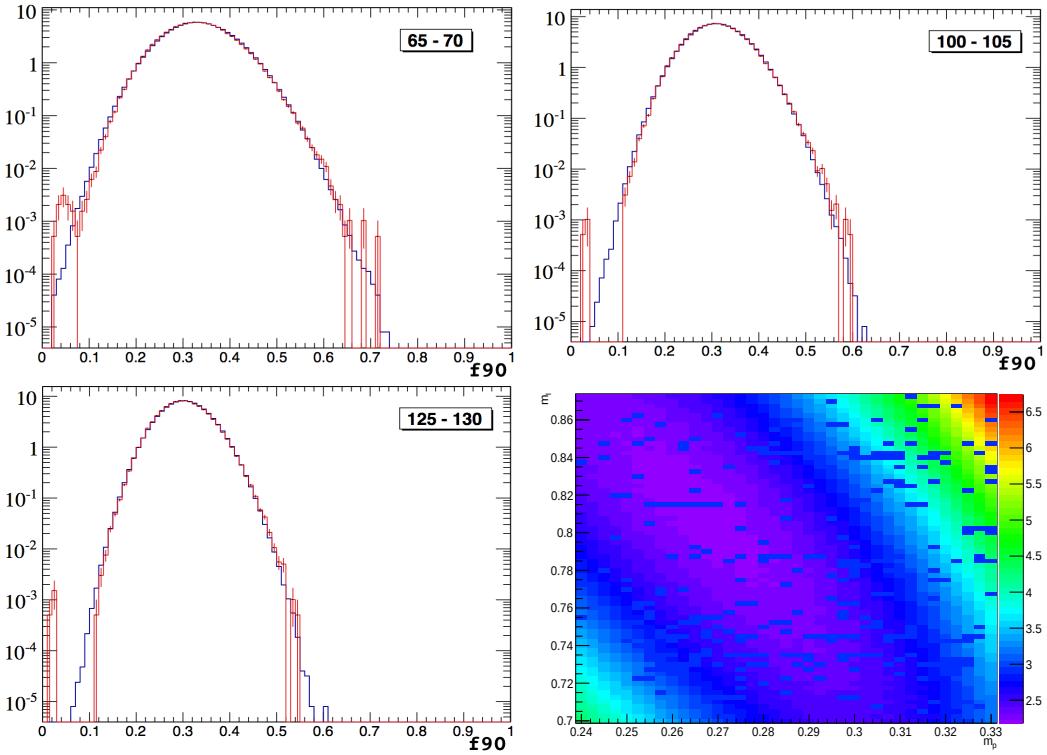

Fig. 5.3 Comparison between data (red) and MC toy (blue) in different S1 ranges for m_P = 0.27 and m_L =0.82. Bottom right: the χ^2/ndf distribution in the (m_P, m_L) plan from the toy MC tuning on AAr data.

the statistical fluctuations of the simulated data, and to reduce the m_P and m_L step sizes. However, a complete scanning of the parameters requires a large amount of cpu. Moreover, a complete toy MC parameter scanning should vary also the f_P values, at least in the 1 σ band from the fitted mean values. This will introduce another degree of freedom, which multiplies the number of simulations.

We opted for a first approximation tuning, identifying a minimum region centered around $m_p \sim 0.27$ and $m_L \sim 0.82$.

The comparison of simulation and real data is shown in Figure 5.3 for different S1 ranges. Thanks to the tuned toy MC we can easily produce a large statistics simulation of the f_{90} distributions and test different analytical fit approaches. In particular we used this model to produce a 5×10^{10} events simulated sample, used as reference for the studies presented in what follows.

5.3 The Hinkley model

Following the scheme adopted in previous works [120, 121], f_{90} can be interpreted as the ratio of two Gaussians (prompt and prompt+late). The ratio of two correlated normal random variables can be expressed with an approximated form developed by Hinkley in 1969 [122].

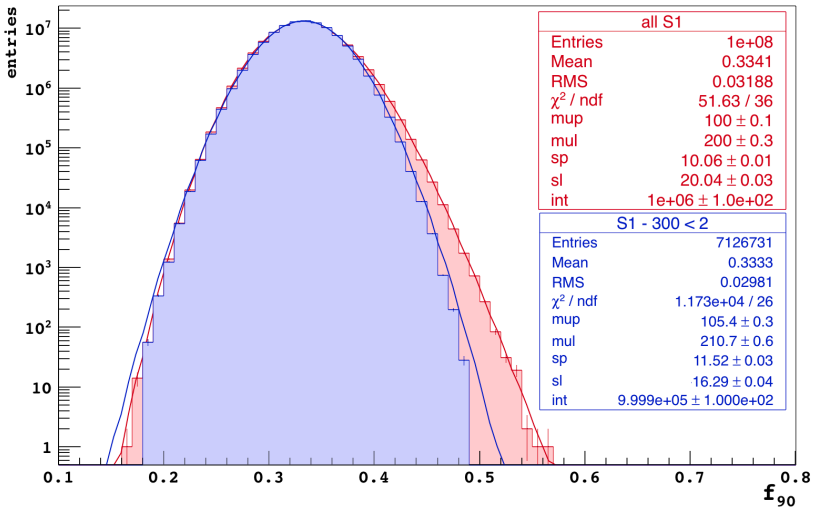

Fig. 5.4 The effect of imposing a binning constraint on the Hinkley model fit. The same data-set (prompt and late from Gaussians with $\mu_p = 100$, $\sigma_p = 10$ and $\mu_L = 200$, $\sigma_L = 20$) is fitted with the Hinkley model. The red histogram contains all the statistics, the blue one only the subset for which (S1 - 300) < 2 (scaled to the full statistics). As long as no binning condition is imposed, the Hinkley model fit allows to recover the true μ_i and σ_i and returns a low χ^2/ndf. When requiring a condition on S1, the fit suffers.

Considering the ratio $P/(P+L)$ and keeping into account the correlation between P and L, the analytical expression of the ratio density function f is the following:

$$f(w) = \frac{1}{\sqrt{2\pi}} \frac{\mu_p \sigma_L^2 w + \mu_L \sigma_p^2 (1-w)}{(w^2\sigma_L^2 + \sigma_p^2(1-w)^2)^{\frac{3}{2}}} e^{-\frac{1}{2}\frac{(\mu_L w - \mu_p(1-w))^2}{(w^2\sigma_L^2 + \sigma_p^2(1-w)^2)}} \tag{5.4}$$

where w represents the ratio prompt/(prompt+late) (alias f_{90}) and μ_i and σ_i are the mean and standard deviation of the prompt ($i = p$) and late ($i = l$) part of the signal.

This analytical description is well suited to describe the ratio variable for a given pair of correlated Gaussians, but we realized that the model diverges from the data when a binning condition is imposed. In particular we identified two effects:

- we can not interpret the fit results as a measure of the true parameters governing the statistics of the process;
- the fit overestimates the tails of the distributions.

The magnitude of the first effect is clear from the comparison shown in Figure 5.4. We generated a large sample of prompt and late values. The prompt is sampled from a Gaussian with $\mu_p = 100$, $\sigma_p = 10$; the late is sampled from a Gaussian with $\mu_L = 200$, $\sigma_L = 20$, so that the sum value fluctuates around the central value of 300. We calculated for each (P, L) pair the ratio $P/(P+L)$ and generated two histograms: one contains all the statistics (red), the second one only the subset for which $P + L = 300 \pm 2$ (blue) fit with the Hinkley model. The fit results are given in the colored boxes in the same Figure. When no binning is applied

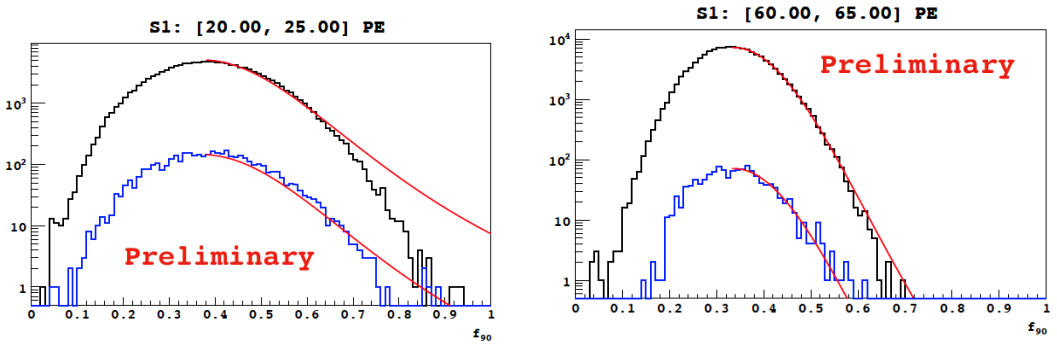

Fig. 5.5 f_{90} distribution at low energy in AAr (black) and UAr (blue) data, for S1 ∈ (20,25) and for S1 ∈ (60,65).

(all S1's accepted), the fit parameters are in good agreement with the input values and the χ^2/ ndof = 1.43.

This is not the case for the distribution obtained requiring an additional constraint on the S1 value (S1= 300 ± 2). The fit returns the wrong parameter values, namely: $\mu_P = 105.4 \pm 0.3$, $\sigma_p = 11.52 \pm 0.03$ and $\mu_L = 210.7 \pm 0.6$, $\sigma_L = 16.29 \pm 0.04$, along with a χ^2/ndf > 450.

The second effect due to the binning condition, already mentioned in [120] as well, is the overestimation of the tails of the f_{90} distributions. In the example of Figure 5.4 the effect is not particularly evident because of the relatively large value of S1 (300). Nonetheless, we can clearly observe this behavior directly in real data. Figure 5.5 shows the f_{90} distributions in two S1 bins at low energy. The fit overestimates the tails of the distributions and the overestimation increases as S1 decreases.

I will further discuss the accuracy of the fit results and evaluate the overestimation of the tails in what follows.

5.3.1 Test of the Hinkley Model

We tested a possible solution to the overestimation of the distribution tails.

Data and model are expected to show discrepancies at low number of pe's (< 10–20 pe) where the gaussian approximation to the Poisson distribution is not valid. This happens at low (high) f_{90} values for the prompt (late), and especially at low values of S1 = prompt + late. Since the prompt component is more subject to the non-Gaussian behavior of the tails (typically $f_p \sim 0.3$), we expect that the analytical function can better approximate the right tail if we move the starting point of the fitting range near the peak of the distribution.

We tested the analytical fit on the large statistics sample generated with the toy MC. The toy MC is tuned on AAr data and the generated statistics is 10^4 times larger with respect to the one acquired in the AAr campaign. This allows us to study the fit performance on tails at the 10^{-6} level. The DarkSide-50 experiment will never collect such a huge amount of data, but

we believe that a good understanding of the fit systematics is a valuable piece of information for this and the future phases of the DarkSide program.

We tested the following f_{90} fitting ranges:

- range 1: [0.18, 1]
- range 2: [0.27, 1]
- range 3: $[peak\,position - 0.014, 1]$
- range 4: $[peak\,position, 1]$

We define the model parameters as follows:

$$\mu_P \equiv f_P \cdot \mathrm{S1} \tag{5.5}$$

$$\mu_L \equiv (1 - f_P) \cdot \mathrm{S1} \tag{5.6}$$

$$\sigma_P \equiv k_P \cdot \sqrt{\mathrm{S1}} \tag{5.7}$$

$$\sigma_L \equiv k_L \cdot \sqrt{\mathrm{S1}} \tag{5.8}$$

In order to minimize the systematics, we projected the f_{90} distributions for each bin of S1 with 1 pe width. Since the non–gaussianity varies as function of S1, we can not assume the same values of k_P and k_L for all the f_{90} distributions. We then fitted independently each f_{90} distribution, with 4 parameters: normalization, f_P, k_P and k_L. The equations 5.7 and 5.8 are only definitions: fitting each distribution with an independent pair (k_P,k_L) removes any constraint on the dependence of σ_i on S1.

Some examples of fits are shown in Figures 5.6 and 5.7, for the ranges 1 and 4, respectively. The plots in the left column show the simulated distribution and the best fit function. The simulated distributions are scaled at the AAr statistics. If we cut the simulated distributions at 1 on the vertical axis (we do not collect fractions of events with our detector), the fit function reproduces reasonably well the shape of the distribution. However, we want an estimate of the f_{90} value above which we expect a fraction of event for each bin (for example we want to estimate the 0.02 events/1 pe bin leakage). The graphs on the right represents the endpoint of the inverse cumulative distribution for both simulated data and the fit function (each bin contains the integral of the histogram from that bin up to 1.).

From these plots we can conclude that relying on the fit of one dataset with the statistics of the order of the AAr sample will lead to an overestimation of the leakage prediction which is as large as 20% in some case (for example in the fitting range 1, the 0.01 events/5 pe bin leakage for S1 < 70). It is worth mentioning that an overestimation of the leakage can eventually be interpreted as a conservative approach (we reduce the probability of having electron recoils in the nuclear expectation region) but also corresponds to a reduction of the detector sensitivity for low WIMP masses.

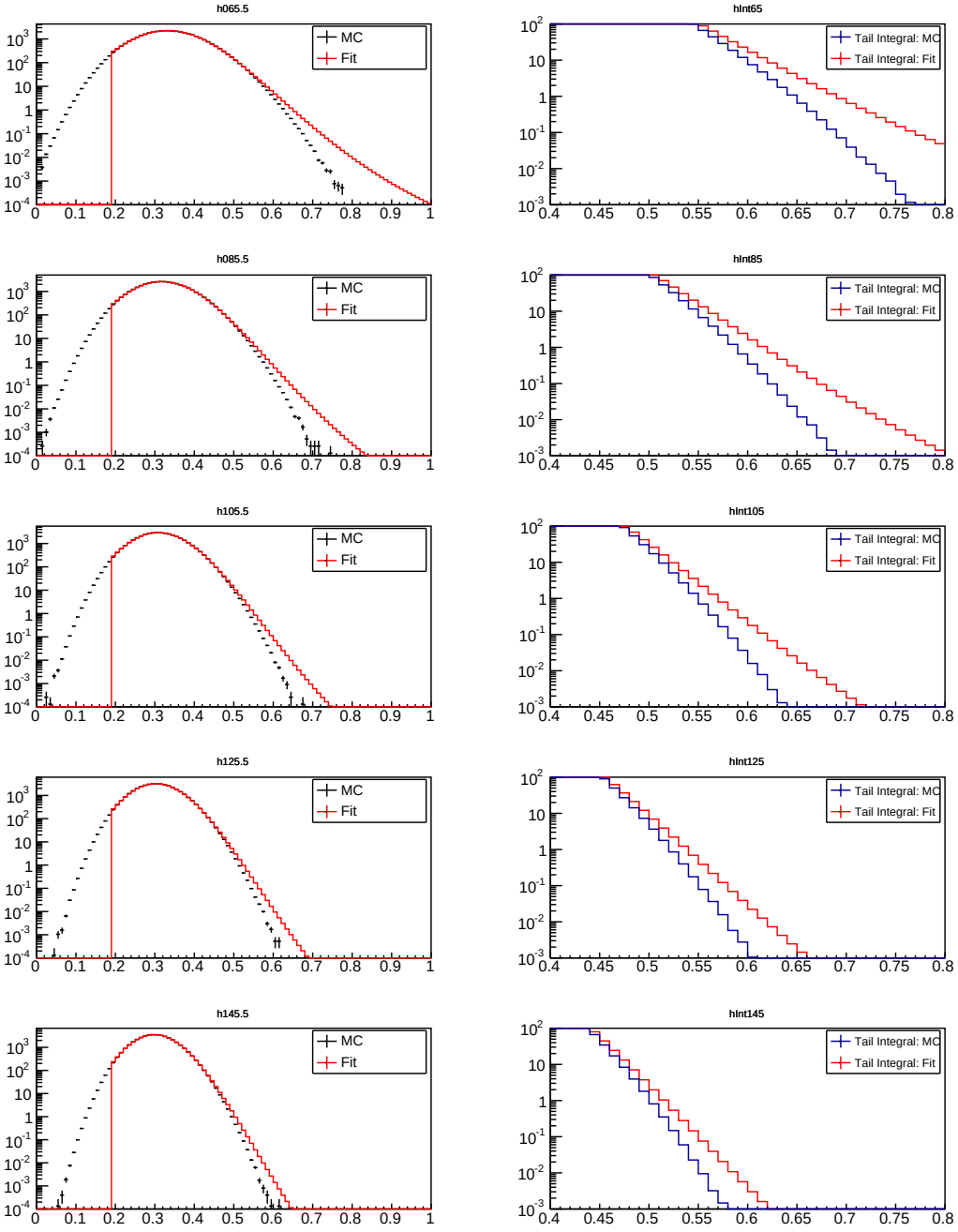

Fig. 5.6 Summary of the simulated f_{90} distribution fit and the comparison of tail integrals over the whole spectrum (from 65 to 145 pe). The fit range is fixed to [0.18, 1] (range 1).

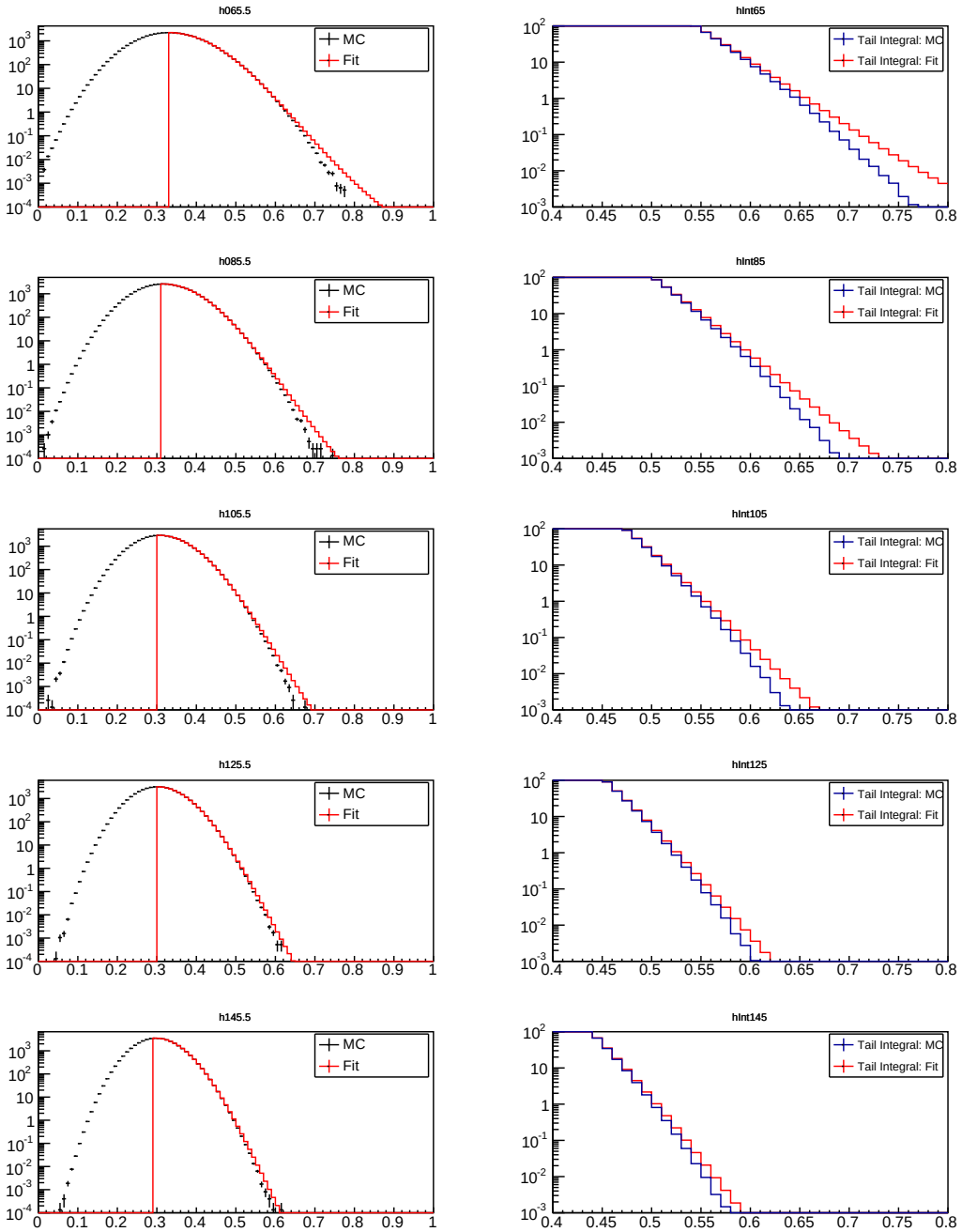

Fig. 5.7 Summary of the simulated f_{90} distribution fit and the comparison of tail integrals over the whole spectrum (from 65 to 145 pe). The fit range low limit corresponds to the center of the maximum bin (range 4) of the f_{90} distribution.

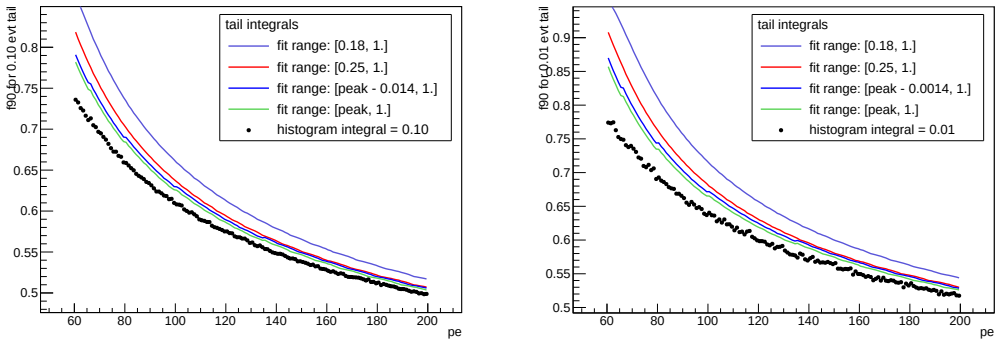

Fig. 5.8 The tail integrals for 0.1 / 5 pe (left) and 0.01 / 5 pe (right) leakage. The simulated data leakages are shown in black dots, while the fit estimates are obtained with different fit intervals.

We now discuss the effect of changing the fitting interval. In order to quantify the disagreement between the model and the simulated data, we extrapolated from the fit the the leakage limits at 0.1 and 0.01 events/5 pe, and we compared them with the true limits from the simulations. In Figure 5.8, we show the ones obtained from the fits, by varying the lower edge of the fit range (solid lines), with respect to the true values of the toy MC (points).

As expected from the considerations that motivated this study, the overestimation of the tails is smaller when the lower edge of the fit interval is closer to the peak position of the distribution. For the 0.1 events/5 pe limit case, the minimum disagreement (in the fitting range 4) varies from ~6% at 60 pe, to ~2% at 200 pe. The disagreement increases for the 0.01 events/5 pe limit case (always for the range 4) up to ~10% at 60 pe and to ~3% at 200 pe.

Moreover, as shown in Figure 5.9, we observe a dependence of σ_P and σ_L on the fitting range. This result is expected, since the two terms try to compensate the non–gaussianity of the tails. However, the behavior shown in the figure rises serious problems in the interpretations of the fit results.

To conclude, in the light of what we have discussed in this Section, we believe that this approach is mis-leading when the data is binned in narrow S1 bins: first, the physical meaning to the fit parameters is lost even when the fitted histogram is obtained with a pure generation of Gaussians. Second, the fit results change when the fit interval changes, revealing that the model is not well suited for the description of the data.

We thus developed an alternative model, described in the following Section.

5.4 The Covariance Model

We developed an analytical model other than the ratio of two Gaussians for the description of the f_{90} distribution. The model is based on the expression of the variance term for the

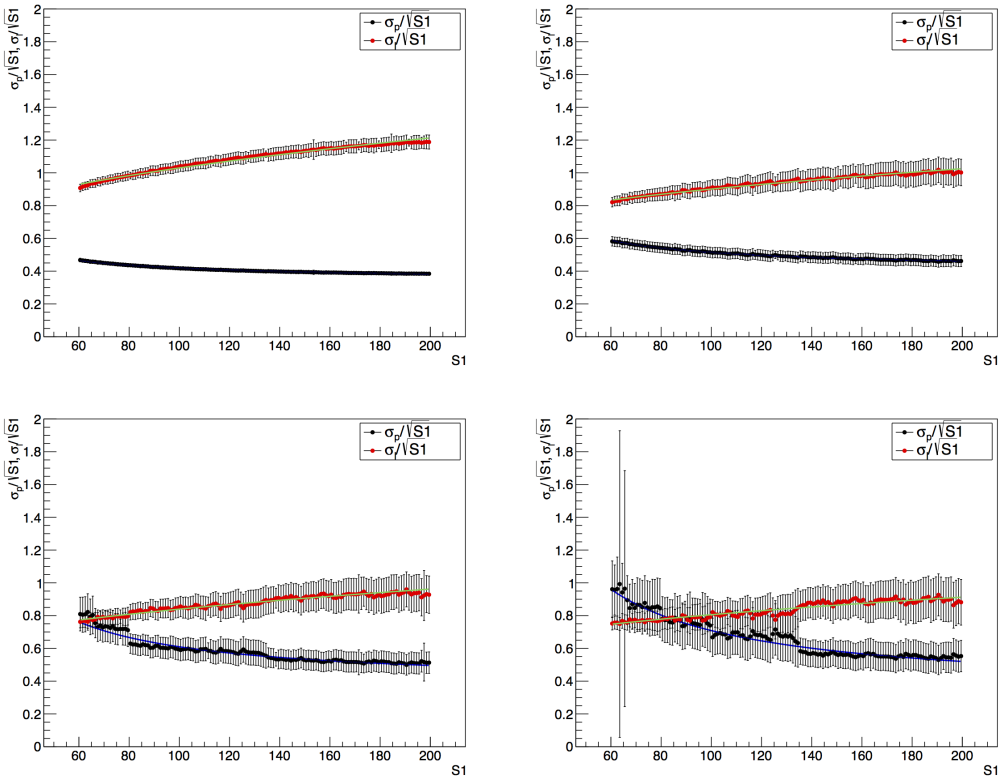

Fig. 5.9 σ_p's and σ_L's, as function of S1, resulting from the fit. Top left: range 1 [0.18, 1]. Top right: range 2 [0.25, 1]. Bottom left: range 3 [$peakposition - 0.014$, 1]. Bottom right: range 4 [$peakposition$, 1].

distribution of a function of two random variable $f(P,L)$. This variance is

$$\mathrm{Var}\left(f(P,L)\right) = f_P^{'2}\mathrm{Var}(P) + f_L^{'2}\mathrm{Var}(L) + 2\cdot f_P^{'} f_L^{'}\mathrm{Cov}(P,L) \tag{5.9}$$

where $f_i^{'}$ represents the partial derivative of f with respect to the i variable and $\mathrm{Cov}(P,L)$ the covariance term.

In our model for f_{90}, f is the ratio between the prompt part of the signal (P) and the total (prompt and late, $P+L$): $f(P,L) = \frac{P}{P+L}$. If we assume that P and L are normally distributed random variables, we can define $\mathrm{Var}(L) = \sigma_L^2$, $\mathrm{Var}(P) = \sigma_P^2$.

Moreover, by selecting a given value of S1 (the sum of $P+L$), we impose that P and L are fully anti-correlated:

$$\mathrm{Corr}(P,L) \equiv \frac{\mathrm{Cov}(P,L)}{\sigma_P \cdot \sigma_L} = -1 \tag{5.10}$$

so that

$$\mathrm{Cov}(P,L) = -\sigma_P \cdot \sigma_L. \tag{5.11}$$

Another consequence of fixing the S1 bin (S1 = $P + L$), is that we can parameterize P and L as follows:

$$P = w \cdot S1 \tag{5.12}$$

$$L = (1-w) \cdot S1 \tag{5.13}$$

where w is the fraction of prompt with respect to the total.

By combining all the above definitions and Equation 5.9, we obtain the expression of the $\sigma = \sqrt{\mathrm{Var}\big(f(P,L)\big)}$ of the distribution of f in the following way:

$$\begin{aligned} \sigma^2(w) &= \frac{L^2}{S1^4}\sigma_P^2 + \frac{P^2}{S1^4}\sigma_L^2 - 2\cdot P\cdot L\cdot \mathrm{Cov}(P,L) \\ &= \frac{1}{S1^2}\left[\left(\frac{(1-w)\cdot S1}{S1}\right)^2 \sigma_P^2 + \left(\frac{w\cdot S1}{S1}\right)^2 \sigma_L^2 + 2\cdot w\cdot(1-w)\cdot\sigma_P\cdot\sigma_L\right] \\ \Rightarrow \sigma(w) &= \frac{1}{S1}\cdot\sqrt{((1-w)\cdot\sigma_P)^2 + (w\cdot\sigma_L)^2 + 2\cdot(1-w)\cdot w\cdot\sigma_P\cdot\sigma_L}, \end{aligned} \tag{5.14}$$

which embeds a dependence on both σ_P, σ_L and w.

The distribution g of the ratio between P and $P+L$ has then the following shape

$$g(w) = A\cdot\frac{1}{\sqrt{2\pi}\sigma^2(w)}\cdot\exp\left(-\frac{\left(\hat{f}_{90}-w\right)^2}{2\sigma^2(w)}\right) \tag{5.15}$$

where A is the arbitrary amplitude of the distribution, $\hat{f}_{90}$ is the mean value of the f_{90} distribution and the σ dependence on w is described by Equation 5.14.

In addition to this, we make the assumption discussed and motivated at the beginning of the chapter, namely that the smearing of the prompt and late parts of the signal follows a Poisson statistics, so that:

$$\sigma_P = k_P\cdot\sqrt{S1} \tag{5.16}$$

$$\sigma_L = k_L\cdot\sqrt{S1}. \tag{5.17}$$

We can then fit any f_{90} distributions with 4 free parameters: the normalization factor A, the mean value of the f_{90} distribution $\hat{f}_{90}$, and the magnitudes k_P and k_L of the prompt and late resolutions.

The assumptions underlying this model make it particularly well suited for the description of a distribution obtained with a narrow binning. The plots in Figure 5.10 show a comparison between a fit with the Hinkley model and the covariance one. The fitted distributions are not meant to accurately reproduce the f_{90} distributions, but they are obtained by computing the ratio $P/(P+L)$ for two normally distributed random variables P and L. It is the same procedure illustrated to produce the histograms of Figure 5.4: the left plot does not include any constraint on the sum of $P+L$, while the second distribution is obtained selecting only the events for which $P+L = 65\pm0.5$. As expected, the Hinkley model fit returns a low

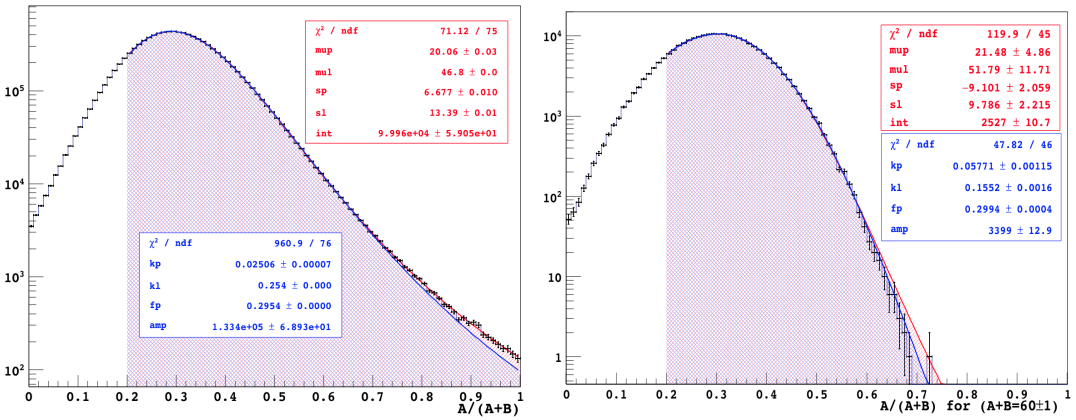

Fig. 5.10 Comparison between a fit with the Hinkley model (red) and the covariance model (blue) for a simulation of $P/(P+L)$ values. P and L are Gaussians, with $\mu_P = 20$, $\sigma_P = 6.5$ and $\mu_L = 45$, $\sigma_L = 13.5$. The left histograms contain all the statistics, the right histograms only the subset for which $P+L = 65 \pm 1$.

χ^2/ndof (71.12/75) for the plot where all the $P+L$ spectrum is accepted. On the contrary, the covariance model returns a lower χ^2/ndof (47.82/46) when the a narrow binning is applied.

In the next Sections we will present the results of a test of the covariance model on the same large statistics toy MC simulation and a method for the evaluation of the systematic error on the prediction of the ER leakages. To some extent, we will make use of G4DS simulations, without discussing the status of the tuning of the f_{90} parameter, already mentioned in chapter 3.

5.4.0.1 Test of the Model on a Large Statistics Sample and with G4DS

We tested the covariance model on the same large statistics sample produced with the toy MC procedure. In order to evaluate the fit accuracy, we compared the same quantities used to evaluate the goodness of fit in the Hinkley model case, namely the overestimation of the distribution tails and the variation of the fit results for different fit intervals: $f_{90} \in [0.2, 1.]$ and $f_{90} \in [a, 1.]$, where a represents the position of the distribution peak. The fit results do not show any bias induced by the variation of the fit intervals and the prediction on the leakage position is accurate, as shown in Figure 5.11.

This is actually the behavior we expect: the covariance model consists exactly in an analytical interpretation of the toy MC. In any case, we consider this is a valuable test: we derived the toy MC procedure from the statistical considerations on the f_{90} distribution discussed at the beginning of the chapter and showed that the model well approximates the data. However, we did not perform a complete study of the systematics, because of the large amount of cpu time required for a full scan of the model parameters (k_P, k_L and the true value of f_P). We then found an analytical description of this model, that accurately fits the simulated distribution and does not induce any bias in the leakage position estimation. The next step is a quantitative validation of the model on real data. Of course this step is

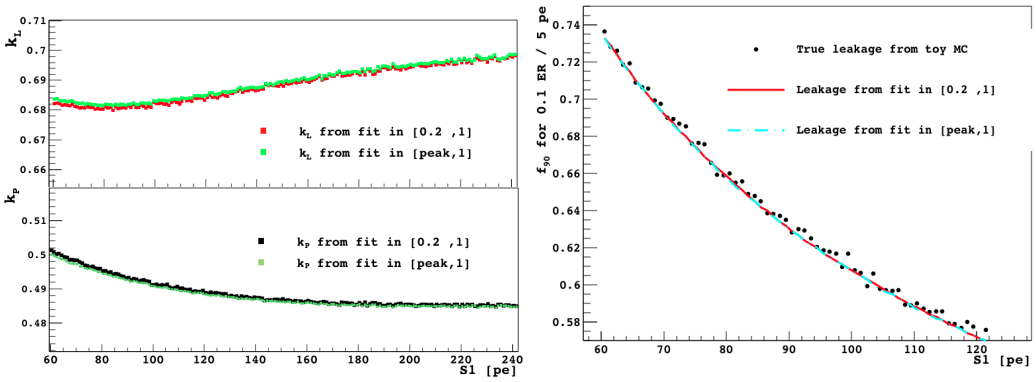

Fig. 5.11 Results of the covariance fit on the large toy MC sample for two different fit intervals $[0.2,1]$ and $[peak,1]$. Left: the k_P and k_L free parameters do not change (as a function of S1) and the curves obtained by fitting in different fit intervals overlap. Right: Prediction of the leakage position (0.1 events / 1 pe) obtained from the fit in two different fit intervals compared to the true leakage.

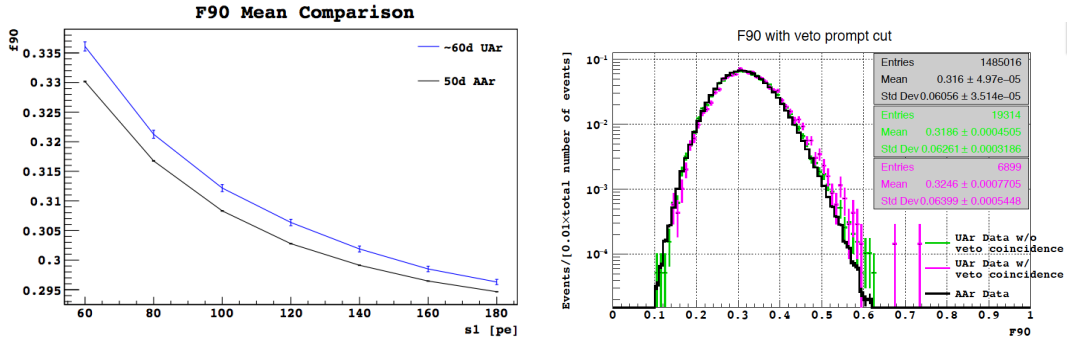

Fig. 5.12 Left: comparison of the f_{90} mean in two datasets (AAr and UAr) and (right) evidence for multi-scatter events in UAr.

impossible, but we can use G4DS for this purpose. Even if the simulation of the pulse shape discrimination is not tuned on data, all the physical effects and the reconstruction effects that may affect the shape of the f_{90} distribution are in fact taken into account.

Moreover, thanks to G4DS , we can test the effect of the shape of the input spectrum on the fit result, as discussed in the next paragraph.

5.4.0.2 The Impact of the Energy Spectral Shape

We observe a different mean value of the f_{90} distributions when moving from the AAr dataset to the UAr one, as shown in Figure 5.12. The difference is of the order of 1% for S1 $\sim$ 60 pe and decreases as S1 increases.

Unlike the AAr dataset, the UAr sample is dominated by external gamma events. We identified a possible explanation for the shift of the f_{90} distribution mean in the different relative abundance of non-single-scatter ER, for example unresolved multiple-scatter events. The combined S1 of a two-scatter event has f_{90} biased upwards, since the mean value of the prompt fraction increases at low energy. The evidence that gammas can enhance the

high tail of the f_{90} distribution is shown in Figure 5.12 (right). The AAr f_{90} distribution for S1 in [60,120] pe is compared to the distribution observed in UAr for events with (pink) and without (green) a coincident signal in the veto. No cut on the number of pulses is applied and all the distributions are normalized to the area. We believe that most of the events tagged by the veto are due to gammas that interact in the veto and once (or more than once) in the TPC. The mean f_{90} for this class of events is larger than the mean of AAr events distribution. The multiple interaction events are removed by the selection of two-pulses events, but some of them may not be correctly identified. However, from the results of MC simulations, it seems unlikely that the unresolved multiple scatter events alone account for the shift observed in data.

We identified another reason for the change in the f_{90} mean in the different energy spectrum of the collected data. Let us consider the singlet to triplet ratio variation as a function of the recoil energy and take a fixed S1 bin. We can assign a reference energy value to the events populating that bin, equal to the ratio S1/light yield. Now, if we consider a flat energy distribution, the bin with fixed S1 will be equally populated by events with lower and higher energy than the reference value, because of fluctuations. If the input energy spectrum changes, the mean of the f_{90} distribution in that bin will be different. For example, if there is an excess of events at energy lower than the reference energy, the mean f_{90} will increase (the mean value of the singlet to triplet ratio increases at low energy).

This dependence on the spectral shape can be reproduced with G4DS , as summarized in Figure 5.13. We prepared two simulation samples: the first one is obtained with a single electron of 8 keV, the second is the sum of two electrons with 5 and 3 keV respectively. For the same S1, the two distributions show a different value of the mean f_{90}, higher in the two electrons case, since $f_P(3\text{ keV}) > f_P(5\text{ keV}) > f_P(8\text{ keV})$. On the other hand, the S1 distribution is similar, centered around S1 $\sim$ 70 pe. This must be considered as an extreme case, since the probability of two ER's to be reconstructed as a single event with energy equal to the sum of their energy is negligible in real data.

We fitted the f_{90} distributions obtained by summing up the single electron sample with a certain amount (of the order of $\sim$ 20%) of the two electrons sample. The fraction of high-f_{90} events is increasing for increasing S1, so that the mean value of the f_{90} distribution for the sum distribution is changing with S1 as shown in figure 5.13 (left). The right panel of the same Figure shows the sum f_{90} distribution in green and the two contributions in blue (single electron sample) and red (double electron sample) in the S1 = 70 pe bin.

As we did in the previous tests, we compared the leakage predictions of the simulation sample to the ones obtained with a fit with the covariance model. We fit a simulated statistics 400 times smaller with respect to the AAr statistics, and derived the prediction of the 0.05 events/5 pe bin leakage. A simulated sample, with large statistics, is available to compare the fit predictions with the true pdf of the distribution. The fits are shown in Appendix C.

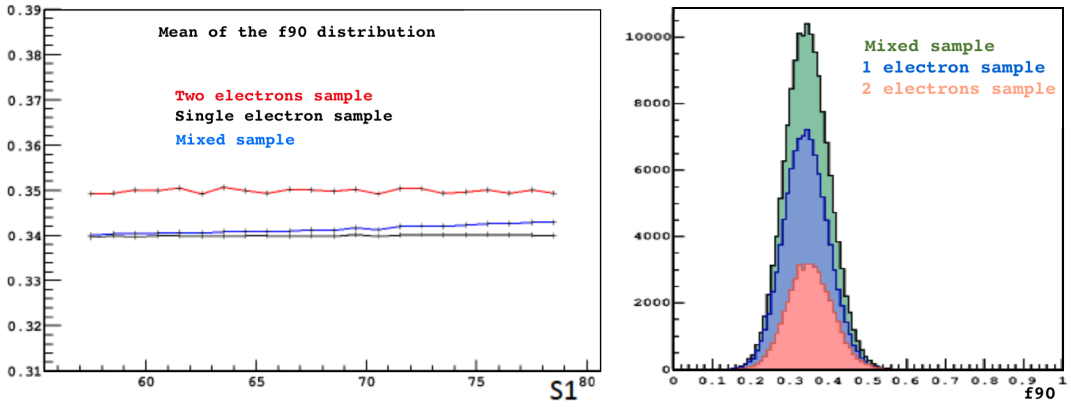

Fig. 5.13 Left: the f_{90} mean of the G4DS simulation sample of single electrons, two electrons and the sum of the two. Right: the f_{90} projection for S1 = 70. The mixed sample (green) is the sum of the single electron sample (blue) and the double electron one (red).

We can compute the 1σ systematic error bands from the fit uncertainties. Figure 5.14 shows the tail integral for the simulated distribution for S1 = 72. The light blue line represents the fitted histogram, while the dark blue line is the larger statistics simulation, or the pdf of the f_{90} distribution in that bin. The red line is the inverse cumulative of the best fit function, while the shaded area represents the 1σ systematic confidence interval.

The error band is computed by uniformly varying the parameters of the fitting function around the best fit value in the 1σ error interval. The true leakage position is the x value of the intercept of the pdf histogram and the dotted line (which represents 0.01 events/1 pe bin). The predicted leakage from the fit function is the intercept of the dotted line with the red line. Thanks to the error band, it is possible to calculate a confidence interval for the leakage position. We fit f_{90} in each S1 bin from 60 to 200 pe. We can count how many times the true leakage falls in the predicted interval (we expect 68% of the times, since it is a 1σ band) and we find that this is true in 95% of the cases. The relative difference between the true leakage and the predicted one in units of σ is shown in Figure 5.16.

We have shown how this fit procedure returns accurate results on the prediction of the leakages, even if the fitted sample is artificially distorted. Moreover, we can calculate a confidence interval for this prediction. We can then apply this method for an estimation of the edges of the ER expectation bands in both the AAr and UAr data.

5.4.1 Prediction of the Electron Recoil Leakage in the AAr Data

We applied this fitting method to the real data. We considered a dataset of AAr data, for a total lifetime of roughly 50 days. Only the events passing all the selection cuts listed in chapter 2 are considered. The total collected statistics is roughly 15×10^6 events in the [60,200] pe S1 range, almost uniformly distributed in energy (the ^{39}Ar β spectrum is almost flat in the WIMP search region).

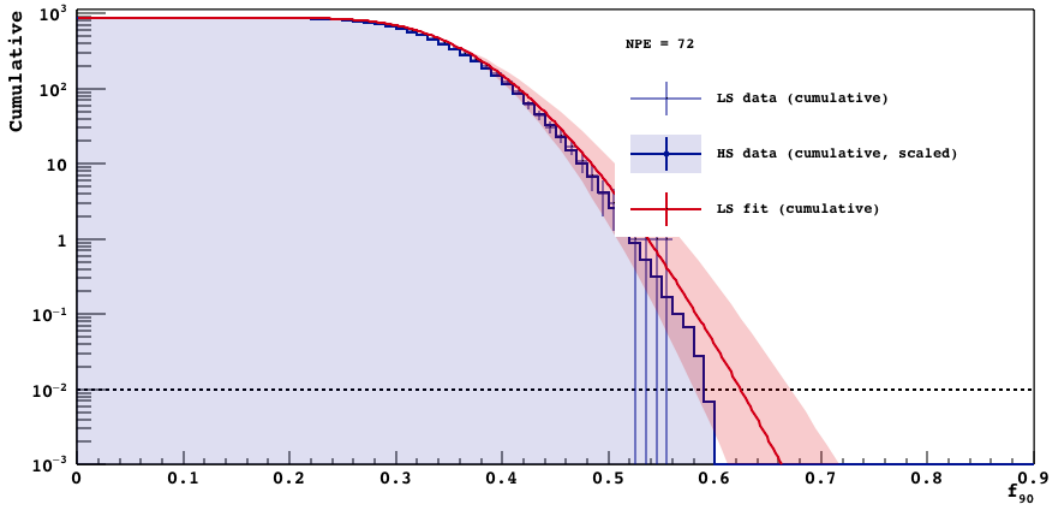

Fig. 5.14 Validation of the covariance model on the G4DS sample. The light blue histogram corresponds to the fitted statistics, while the dark blue line is the pdf for that distribution. The red line is the best fit of the small statistics sample, shown with the 1σ uncertainty band from the fit. All the histograms represent the inverse cumulative of the f_{90} distribution. The dotted line indicates the 0.01 event/1 pe leakage.

We fit with the covariance model vertical slices of the (S1,f_{90}) distribution for each S1 bin of 1 pe and computed the 2σ band corresponding to the 95% CL prediction on the position of the 0.1 events / 5 pe bin leakage. Since the statistics of each bin is larger with respect to the statistics of the G4DS sample, the errors on the fit parameters are smaller and the 2σ expectation band is narrower.

We compare the leakage prediction with the one obtained with the Hinkley fit in Figure 5.16. The latter prediction is systematically above the curve obtained with the covariance model.

We expect 2.8 events above the upper bound of the leakage prediction band and we count 6 events. This might be a hint of some effects which are not included in our model so far. This hypothesis is confirmed by the increase of the number of outliers (events with high-f_{90}) observed in the UAr dataset. The UAr acquired data is no more dominated by the ^{39}Ar β decay: the largest contribution comes from the γ background. A significant fraction of non-single-scatter ER's found in this dataset and mentioned above seems to be due to Cerenkov mixed events, that require an independent model to be described.

The γ interacting in the teflon reflector and in the fused silica windows have been identified as the main responsible of the production of Cerenkov light. The Cerenkov emission spectra extends from the visible blue light to the UV. Some of these photons can hit a PMT and trigger the TPC. If the γ scatters in the fused silica window, close to the PMTs, the emitted light may be concentrated on one of the photo-detectors and, thanks to the cut on the fraction of charge collected by the PMTs, the events can be rejected. The cut is less effective for Cerenkov

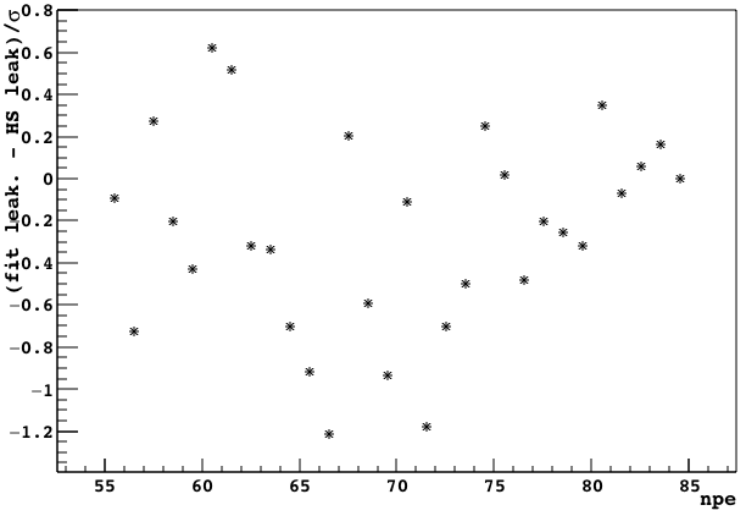

Fig. 5.15 The bias on the prediction of the leakage with the covariance model in units of σ. We fit small statistics sample and compared the predicted leakage with the one of a high statistics (HS) simulation. The σ is obtained thanks to the study of the fit systematics. More than 90% of the leakages predicted from the fit of the small statistics sample falls less than 1σ away from the true value.

emission in the teflon reflectors, since the light pattern on the PMTs is more uniform. In any case, the pure Cerenkov events are in general removed because they only produce one light pulse.

On the oher hand, if the γ interacts both in the detector materials, producing Cerenkov light, and in the TPC active volume, the detected S1 will be the sum of the scintillation and of the Cerenkov light. The Cerenkov signal is fast, lasting a few tens of ns taking into account the light propagation in the detector, resulting in an increase of the f_{90} for that event.

We do not expect an increase of the rate of Cerenkov events in the UAr campaign with respect to the AAr one. Nonetheless, the relative abundance in the datasets is completely different (the rate of β-induced internal single ER is reduced by a factor of 400 in the WIMP search region). The scintillation plus Cerenkov events are not distributed according to the typical f_{90} statistics of pure ER's. We are still developing an independent G4DS-based model for the simulation of the Cerenkov production and propagation in the detector to estimate the effect on the f_{90} distribution. It requires a few modification to the optical properties of some materials, but the preliminary results are promising (not discussed here).

5.5 Conclusions

In this chapter I summarized our findings about the statistics of f_{90}, the pulse shape discrimination parameter used in DarkSide-50. The understanding of this variable is necessary for the determination of the WIMP search region (depicted in Figure 2.8). The low energy side of the WIMP box is in fact obtained by predicting the position of the 0.01 events/5 pe energy bin leakage in the (S1,f_{90}) plane.

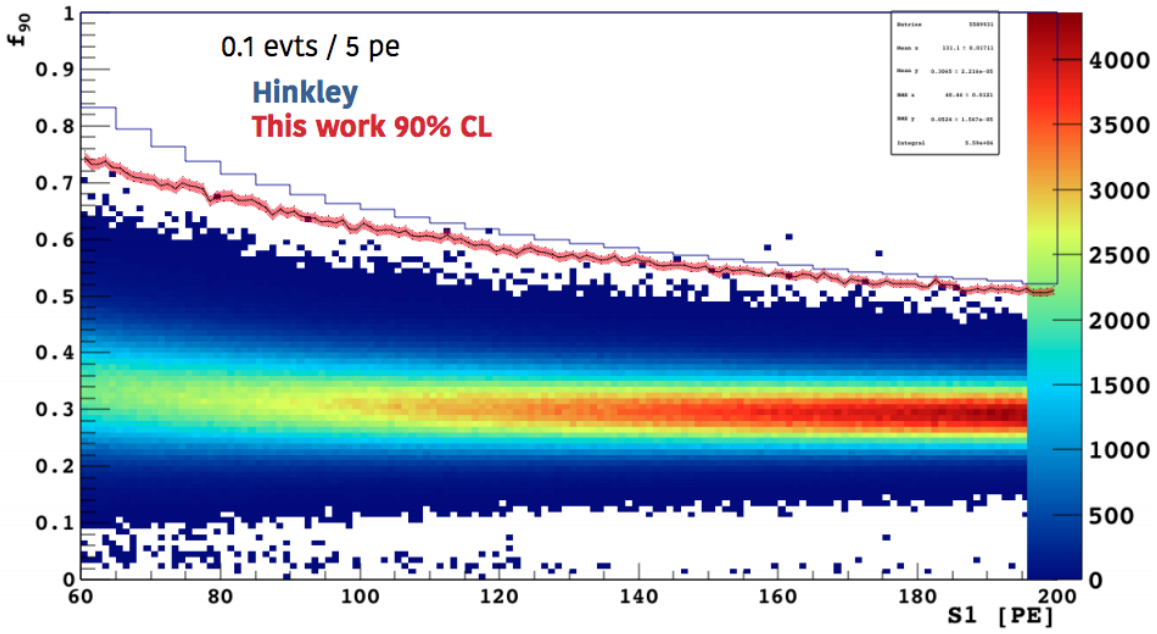

Fig. 5.16 The comparison between the leakage predictions obtained with the Hinkley model (blue) fit and the covariance model fit (black). In red is also shown the 2σ systematic error band.

I firstly discussed which physical effects mostly affect this observable and pointed out the pathologies of the analytical fit traditionally used to fit the data. The fit with the Hinkley function fails in reproducing the tails of the distributions (leading to a systematic overestimation) and implies a bias in the interpretation of the fit parameters. The magnitude of the first effect is dependent on the statistics of the fitted sample. It is actually small for S1 $\geq$ 100 at the AAr dataset statistics, which is the largest statistics DarkSide-50 will ever collect after the filling with UAr. On the other hand, it will be more relevant for the next phase of the experiment.

Because of the dependence on the spectral shape of the f_{90} distribution of the collected data, the optimal solution for the prediction of the electron recoil leakages in the nuclear recoils expectation region would be a full simulation with G4DS. Nonetheless, an accurate tuning of the singlet to triplet ratio requires an immense effort in terms of time and cpu's.

In the last part of the chapter I discussed an alternative analytical method for the fit of the f_{90} distributions. The fit function is derived from the analytical description of a toy MC that reproduces the behavior of f_{90}. According to the validation performed on a G4DS sample, it gives robust results when the fit interval or the input energy spectrum is •changed. A major advantage is the possibility of incorporating the systematic error in the prediction of the leakage. We finally applied this procedure for the determination of the ER leakages in the AAr dataset.

Chapter 6

The Future of DarkSide

The DarkSide-50 experiment performed the most sensitive WIMP search ever realized with a liquid argon target. The plan for the near future is to continue the data collection in order to accumulate 3 years of lifetime (corresponding to and exposure of ~150 kg.y). The design goal of the next phase of the experiment (DarkSide-20k) consists in achieving a background-free exposure of 100 t.y in a 5 years run.

The dual-phase liquid argon technology implemented in DarkSide-50, with the addition of the veto systems, are the key points for a background free exposure, a fundamental requirement to strengthen the robustness of a possible discovery. The projected sensitivity to the WIMP-nucleon cross section is 1×10^{-47} cm^2 (1×10^{-46} cm^2) for a 1 TeV/c^2 (10 TeV/c^2) WIMP. The detector is expected to start the data taking before 2020 and it will be the most sensitive experiment to high-mass WIMPs in the next decade.

In the first part of this Chapter I will give a discussion of the design studies carried out for the DarkSide-20k experiment with particular focus on the minimization of the backgrounds.

The DarkSide-20k run will represent a milestone towards the construction of an ultimate detector (called ARGO), able to reach 1000 t.yr exposure. In the last part of the Chapter I will discuss the physics potential of such a large detector beyond the search for WIMPs. Since a detector with an active volume of ~ 100 t will collect a large statistics of solar-neutrino-induced ERs, we investigated the experiment sensitivity to the CNO cycle neutrinos.

6.1 Design Studies for the DarkSide-20k Detector

The DarkSide-20k dual-phase TPC is designed in order to have a sensitive volume, after the fiducialization, of roughly 20 t of liquid argon. The shape of the TPC is an octagonal prism, with 1.16 m edge and 2.4 m tall (dimensions at warm temperature). The structure will be made of high-reflectivity PTFE, surrounded by copper rings for the uniform drift field (200 V/cm). The top and bottom boundaries of the active volume are two arrays of fused silica tiles. ITO electrodes are deposited on both the top and bottom surfaces of each array and a grid is placed just above the bottom array to serve as cathode.

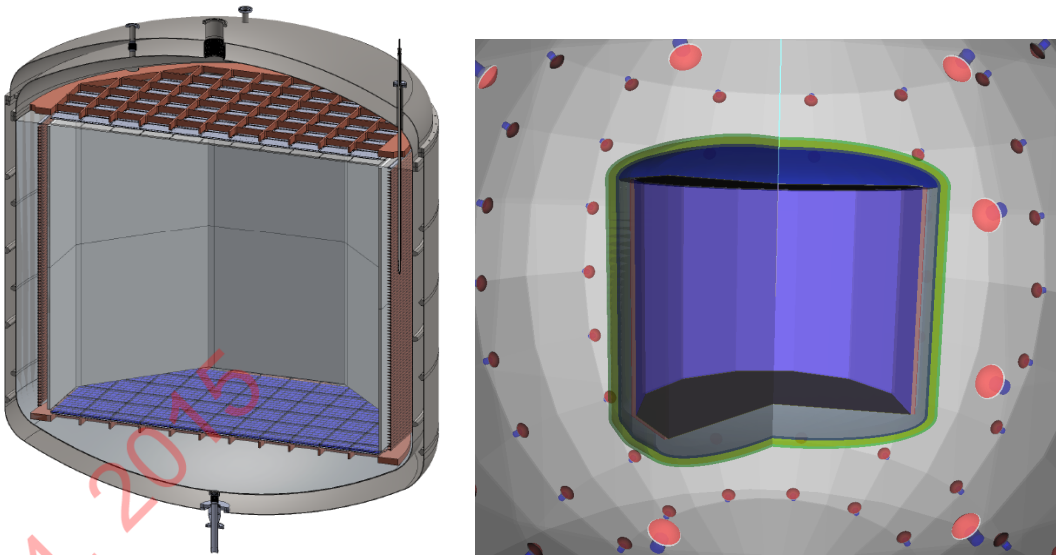

(a) Technical drawing of the DarkSide-20k TPC and cryostat

(b) Preliminary rendering in G4DS

Fig. 6.1 The preliminary DarkSide-20k geometry. On the left, the inner structure of the TPC is visible. The blue plane represents one of the two SiPM arrays, mounted on a copper structure. On the right, the cryostat and the TPC are placed inside a spherical LSV.

The cryostat will be filled with liquid argon up to the top edge of the drift field and gaseous argon will fill the upper part of the cryostat. A second grid is placed 3 mm below the liquid surface and the top array of fused silica tiles is placed 10 mm above the grid. The extraction field will be 2.8 kV/cm in the liquid and the multiplication field about 4.2 kV/cm in the gas.

The design of TPC and cryostat is expected to undergo only minimal modifications in the near future, so that we accurately implemented the geometry of the future detector in G4DS. A technical drawing of the TPC and the corresponding G4DS rendering are shown in Figure 6.1.

We will discuss in Section 6.1.1 the simulation of the TPC response and in Section 6.1.2 the background budget and the related veto design studies.

6.1.1 The Internal Optics

The main change with respect to the DarkSide-50 design is the installation of Silicon PhotoMultipliers (SiPMs) as light detectors. The main features of these devices are the extreme radio-purity, the high quantum efficiency and the fine segmentation. We expect to be able to increase the average photoelectron yield compared to DarkSide-50, so that the pulse shape discrimination (PSD) power would increase. The SiPMs will be grouped in 5×5 cm^2 tiles, in order to cover a total area of 14 m^2 with a reasonable number of channels (roughly 5200). The DarkSide collaboration and its commercial partner FBK [123] are putting an important effort in the development of reliable devices which could match the requirements (low dark

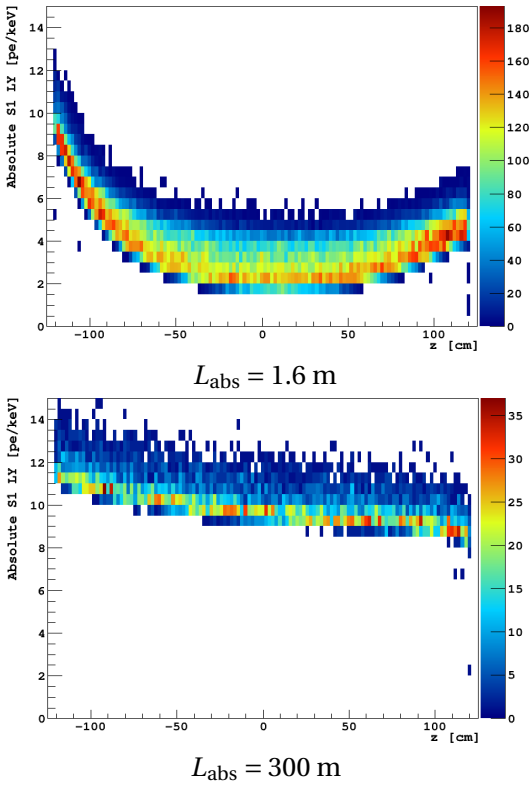

Fig. 6.2 The absolute S1 light yield of DarkSide-20k assuming the same optical simulation of DarkSide-50 for different L_{abs}. The simulations assumes 40% PDE of SiPMs and events with initial energy larger than 100 keV. We expect a $15 \div 20\%$ higher light yield in the energy region of the ^{83m}Kr because of the larger recombination probability.

counts rate of $< 10^{-1}$ Hz/mm^2 and photon detection efficiency (PDE) of about 40% for 420 nm light). However, the status of R&D studies in this field will not be covered in this work and SiPMs will be considered as ideal devices.

The DarkSide-20k TPC is designed to be a larger version of the DarkSide-50 one and it will be build, except for the photosensors, with the same materials (teflon for the walls, fused silica windows coated with ITO for the anode and the cathode, TPB deposition on all the internal TPC walls). We then propagated to the new geometry the description of the internal optics from the simulation of the DarkSide-50 detector. A discussion of the tuning of the optics is given in Chapter 3.

We tracked optical photons until they reach the SiPMs arrays or are absorbed in other materials. The 40% PDE of SiPMs is applied offline. We found that the main parameter affecting the global light yield of the detector is the absorption length of liquid argon at the scintillation wavelength (L_{abs}). We already discussed how the DarkSide-50 TPC is only partially sensitive to this parameter and that the value that allows to better reproduce the TPC response is $L_{\text{abs}} = 1.6$ m. There is actually some tension between the value obtained from the tuning and the expectation one (in principle noble liquids are transparent to their scintillation light).

In the G4DS description of DarkSide-50 a change of L_{abs} from 1.6 m to 300 m implies an increase of the light yield of 11%. The effect is much more important in a larger TPC volume. In DarkSide-20k, the maximum distance an optical photon can travel in a straight line before

reaching the TPC walls and be converted is ~ 4m. We have to keep in mind as well that the Rayleigh scattering length of 128 nm photons is about 55 cm in the liquid, so that the average path is much longer.

Figure 6.2 compares the S1 light yield (given in pe/keV) for a simulation of ^{39}Ar events distributed in a cylinder of 1 m radius at the center of the TPC as a function of the vertical position of the events. We used in turn L_{abs} = 1.6 m, L_{abs} = 4.0 m and L_{abs} = 300 m. We also used the energy calibration tuned on DarkSide-50 data according to the PARIS model, correcting for the increase of the absolute scintillation yield that would occur in DarkSide-50 when L_{abs} is changed (+6% for L_{abs} = 4.0 m and +11% for L_{abs} = 300 m).

6.1.2 Background Budget

To successfully achieve the background-free condition with the DarkSide-20k detector, we set the requirement of less than 0.1 background events in the WIMP expectation region in 100 t.yr exposure.[1] Several classes of possible backgrounds must be taken into account during the design phase of the experiment in order to minimize them.

The external γ induced electron recoils can be successfully suppressed thanks to an attentive selection of ultra-pure materials. Thanks to the self-shielding of a large detector, the large majority of surviving events are efficiently removed by the fiducial volume and multi-sited energy deposition signature. I will demonstrate the efficiency of these cuts in Section 6.1.6.

However, the internal ER, such as β-decays or neutrino induced recoils, are uniformly distributed in the liquid argon volume and are not rejected by the spacial cuts. The main sources of this internal ER background are briefly discussed below.

- The solar pp neutrinos are expected to induce 2.0×10^4 single-sited ER events in a 100 t.yr exposure.
- ^{238}U and ^{232}Th decay chains produce radon, that can escape from materials and enter the sensitive volume. The DarkSide-50 experiment measured a specific activity of the ^{222}Ra decay chain of less than 2 μBq/kg. This value represents an upper limit for the DarkSide-20k detector because of the lower TPC surface-to-volume ratio. However, even assuming this concentration, only 1.0×10^5 events are expected in the 100 t.yr exposure from the β decay of ^{214}Pb (the first β emitter in the decay chain).
- The ^{39}Ar contamination in the argon target represent the main limit to the PSD effectiveness. The present activity of the UAr filling of the DarkSide-50 TPC is (0.71 ± 0.12) mBq/kg, meaning that a 5.5 t.yr exposure will contain the same amount of ^{39}Ar events of the AAr run. The Aria facility will improve the purity and further reduce the

[1] Assuming 5 years of data taking, this translates in 0.02 n/y, the reference number which will be used in what follows.

^{39}Ar contamination by a factor of 10 for each pass through the distillation column. [2] Moreover, the improved photoelectron yield foreseen in the DarkSide-20k TPC will improve the statistical power of the PSD.

- A minor concern is represented by the ^{85}Kr contamination. This β emitter is found in DarkSide-50 with specific activity of (2.7 ± 0.13) mBq/kg, but no removal attempt was performed, since it was unexpected. Calculations show that a reduction by a factor of more than 10^3 per pass is achievable in the Aria distillation column.

According to the DarkSide-50 AAr results, the PSD can be used to efficiently discriminate ER's up to a factor 1.5×10^7 in the WIMP energy region. Moreover, if the internal light yield of DarkSide-20k improves with respect to the light yield of DarkSide-50, the PSD will be more effective. We can conclude that the internal (and external too, as shown in Section 6.1.6) ER background is efficiently removed by the PSD.

Concerning the nuclear recoils, both the cosmogenic and radiogenic neutron backgrounds must be kept well below 0.1 events in the total exposure, since a neutron induced single recoil perfectly mimic a WIMP interaction. The cosmogenic contribution at the LNGS depth is negligible for a detector with a 5 t active mass as demonstrated in [113]. We will repeat this study for the DarkSide-20k experimental setup and discuss the results in Section 6.1.5.

As for the gamma background, the radiogenic neutrons can be minimized by using ultrapure and carefully chosen materials. The irreducible neutrons can be rejected because of their high probability to do multiple interactions within the sensitive volume (the mean interaction length for thermal neutrons in LAr is ~10 cm). We showed that, according to the G4DS simulations, these two features are not enough to guarantee a background free exposure: the experiment must be equipped with a liquid scintillator veto, reproducing the layout of DarkSide-50.

We will discuss the design studies carried out for the minimization of the radiogenic neutron background in the next Section.

6.1.3 Radiogenic Neutron Background

While the design of the DarkSide-20k TPC is fixed, the size and the materials of the other detector components and the veto systems must be optimized in order to minimize the backgrounds. In particular, different possibilities for the veto have been considered (a pure water or Gd-loaded water veto or a liquid scintillator based one). We assumed that the most important sources of (α, n) neutrons are the cryostats, the teflon reflector, the fused silica windows and the SiPMs arrays. Since a preliminary simulation (assuming the same contaminations as the ones found in DarkSide-50) showed that the cryostat is the dominant

[2] The Aria plant consists in a cryogenic distillation column, more than 300 m tall, currently under construction in the Seruci mine (Italy).

contribution, we also identified three different cryostat material candidates (stainless steel, titanium and copper). In this section I will present each alternative and discuss the results of the radiogenic neutron budget for each combination of veto and cryostat materials.

According to the first detector design, the cryostat was directly immersed in the water tank. The self-shielding of a large sensitive volume, along with tuned fiducial volume cuts, were believed to be able to guarantee the suppression of the radiogenic neutron background. Only a small fraction of those neutrons is expected to enter the TPC, interact only once and leave without a second interaction. A preliminary simulation showed that this might not be the case.

The addition of gadolinium in the water could improve the sensitivity to neutrons, since Gd has a large neutron capture cross section (for ^{157}Gd and thermal neutrons it is $\sim 250 \times 10^3$ barns). The capture is followed by a gamma cascade (with total energy of ~ 8 MeV). It is reasonable to assume that a neutron interacting only once in the TPC is captured in the veto by the Gd. If at least one of the gammas from the cascade enters the TPC it would provide an almost coincident signal and increase the neutron rejection.

The liquid scintillator veto (LSV) option, inspired by the current layout of DarkSide-50, is the more expensive solution and implies an higher level of complexity of the detector. In particular, a water Cerenkov (WC) tank larger with respect to the one currently used for DarkSide-50 is required. [3]

Concerning the cryostat material, the stainless steel represents the baseline solution (adopted in the DarkSide-50 experiment too) and good levels of purity can be reached in commercial steel (<1 mBq/kg for U and Th). However, other materials can be a better choice because of the better radiopurity or lightweight. Titanium is for example a valid alternative because of its higher strength-to-mass ratio: assuming the same specific activity, the lower mass would induce less gamma background. On the contrary, the higher (α, n) neutron yield makes the requirement of <1 mBq/kg for U and Th more stringent.

Finally, copper can be ultra-pure (at the level of ~ 0.01 mBq/kg), as demonstrated by the EXO-200 collaboration [124], but with some open questions regarding the feasibility of this solution. The main problems concern the mechanical design (a thicker vessel would be required) and safety (related to the operations inside a scintillator bath).

6.1.3.1 Simulation Procedure

We reproduced the simulation scheme proposed for the DarkSide-50 radiogenic background estimate, propagating neutrons through the DarkSide-20k geometry. The TPC size and shape are fixed, while the dimensions and layout of the cryostats and the vetoes are highly customisable. In particular, the thickness of the cryostat is different according to the material (1 cm for stainless steel, 2 cm for copper and 0.5 cm for titanium). In the water and Gd-loaded

[3] In order to provide enough shielding from the radioactivity coming from the rocks of the cavern, at least 2 m of water are necessary. If the size of the LSV will be increased, the same will happen to the water tank.

Cryostats

Material	Thickness [cm]	Mass [kg]	Chain	Activity [mBq/kg]	Neutron Yield [10^{-6} n/decay]	Production Rate [n/y]
Steel	1.0	5577	^{238}U	0.4	1.123	79.0
			^{232}Th	0.8	2.607	366.8
Titanium	0.5	1400	^{238}U	1.0	4.2	190.0
			^{232}Th	0.25	8.2	90.5
Copper	2.0	11960	^{238}U	0.012	0.06	0.27
			^{232}Th	0.004	0.7	1.1

Other materials

Position	Material	Mass [kg]	Chain	Activity [mBq/kg]	Neutron Yield [10^{-6} n/decay]	Production Rate [n/y]
Field rings	Copper	2795	^{238}U	0.012	0.06	0.06
			^{232}Th	0.004	0.7	0.25
Windows	Fused Silica	189	^{238}U	0.05	1.644	0.49
			^{232}Th	0.01	1.60	0.09
SiPMs	Silicon	11	^{238}U	1.4	3.07	1.5
			^{232}Th	2.1	2.99	2.2
Reflector	**Teflon**	1445	^{238}U	0.07	83.0	**264**
			^{232}Th	0.004	78.1	**14.2**

Tab. 6.1 Input parameters for the simulation of DS20k radiogenic background from the cryostats. For the steel activity, we used the result of the material screening campaign for the DarkSide-50 detector components. The values for titanium are the designed from R&D internal to the collaboration. For the copper we chose to reduce the value reported in [124] by the EXO collaboration by a factor of ∼ 3 after a private communication. Conservative values are used for pure silicon (much lower levels can be reached, see for example [125]), in order to account for the SiPM support. The values for fused silica and teflon come from neutron activation analysis measurement realised by the collaboration on the DarkSide-50 detector materials. The neutron yields are computed with TALYS.

water vetoes simulations, the cryostat is directly immersed in the 11 m height and 10 m diameter tank. In the liquid scintillator case, a sphere with 7 m diameter was chosen as reference option.

The input parameters for the specific activities mostly come from the material assay of the DarkSide-50 experiment. As summarised in Table 6.1, the main sources of radiogenic neutrons are the cryostats and the PTFE reflector. The SiPMs, fused silica and copper field rings contributions will be considered as negligible.

For each combination of cryostat material and veto layout we run a simulation of $1 \div 10 \times 10^6$ neutrons, without the optics, and simulate the basic set of physics cuts to be applied in the real detector, namely:

- **Energy range.** We removed events with a total energy deposit in the TPC outside the WIMP search energy range [10, 70] keV_{ee}.

Cut	Fiducial mass
No FV	23.3 t
5 cm	20.9 t
10 cm	18.7 t
15 cm	16.7 t
20 cm	14.8 t
30 cm	11.4 t

Tab. 6.2 The fiducial mass after the fiducial volume cuts. The same cut is applied both from the lateral walls and the upper/lower part of the active volume.

- **Multi-sited events**. We rejected events with more than a single interaction in the sensitive volume. In order to apply this cut without the simulation of the optics, we relied on algorithm for clustering the energy deposits mentioned in Chapter 3.
- **f_{90} cut.** A rough f_{90} cut (requiring that at least one half of the total energy deposited in the event is due to a nuclear recoil) is applied to remove events induced by gammas (mainly resulting from the capture of neutrons on the detector materials).
- **Fiducialization.** Several fiducial volume cuts have been tested, in order to estimate the self-shielding power of the TPC. We removed events within a fixed distance from the top/bottom windows and lateral walls of the TPC. Obviously a more aggressive cut is more efficient, but implies a stronger reduction of the sensitive volume, as summarized in Table 6.2. We defined an octagonal fiducial volume, used in this work. We also tested a cylindrical fiducial volume and did not observe any significant different. It is evident how a fiducial cut larger than 5-10 cm would prevent to reach an exposure of 100 t.yr in 5 years.
- **Veto cuts.** According to the veto design, different veto cuts were implemented. In the water-based vetoes, the observable is the Cerenkov light produced in the water. The assumed Gd loading was 0.2% (mass fraction). In this preliminary stage, we did not propagate the light within the detector, but only stored the number of Cerenkov photons produced in the detector. The photocathode coverage, required to lower the detection threshold adequately, can be defined in a later stage.

  In the scintillator-based veto simulation, the observable is the visible energy. We assumed the same composition of the DarkSide-50 veto (TMB mass fraction of 5% and PPO loading) and the same light yield (~ 500 pe/keV). The assumed quenching factor for α's of 1.5 MeV is 1./25. In the preliminary analysis, we did not distinguish between the prompt thermalization signal and the capture one, but we summed up all the energy depositions in the veto. A more refined analysis, where the two contributions are separated, did not show a significant difference.

Table 6.3 shows the effect of a 10 cm fiducial volume cut (before the veto cuts) on the radiogenic neutron induced event rate for the nine combinations of veto options and cryostat

Veto	Stainless steel [n/y]	Titanium [n/y]	Copper [n/y]	Teflon only
No FV cut (23.3 t)				
Water	7.3	4.3	0.59	
Gd-water	6.9	4.0	0.58	0.55 n/y
LSV	8.4	5.3	0.64	
10 cm FV cut (18.7 t)				
Water	1.8	1.0	0.14	
Gd-water	1.8	0.95	0.14	0.13 n/y
LSV	2.1	1.25	0.15	

Tab. 6.3 Expected neutron rate before and after a 10 cm octagonal FV cut.

material. The particular values, compatible within the statistical fluctuations in each column, show the weak dependence (as expected) on the veto material. The dominant contribution is, in general, the neutron yield from the cryostat material itself. The ultra-pure copper case is the only one where the cryostat contribution is of the same order of magnitude than the one from the teflon reflector, as shown in the rightmost column.

The results of the simulations, including the effect of the veto cuts, are presented in Figures 6.3, 6.4 and 6.5, in terms of WIMP-like events for different fiducial volume cut as a function of the veto threshold. The typical values of the veto thresholds are 500 Cerenkov photons in the water based vetoes and a few tens of keV in the in liquid scintillator one.

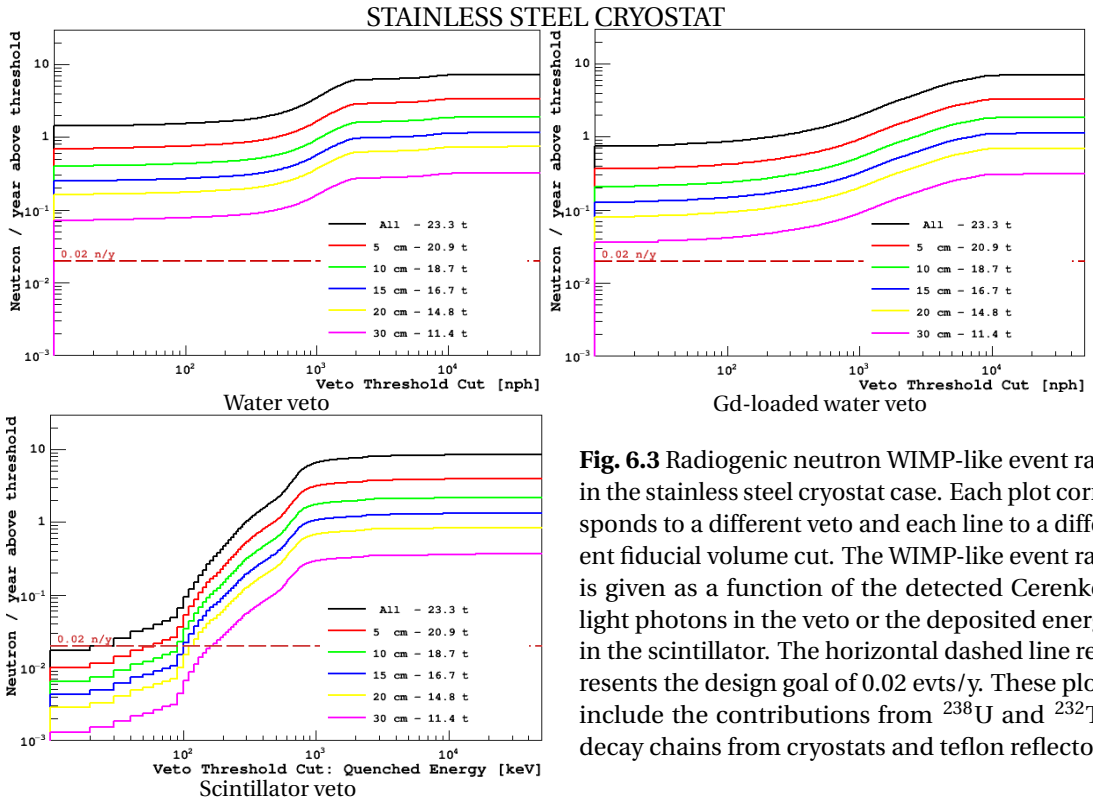

Fig. 6.3 Radiogenic neutron WIMP-like event rate in the stainless steel cryostat case. Each plot corresponds to a different veto and each line to a different fiducial volume cut. The WIMP-like event rate is given as a function of the detected Cerenkov light photons in the veto or the deposited energy in the scintillator. The horizontal dashed line represents the design goal of 0.02 evts/y. These plots include the contributions from ^{238}U and ^{232}Th decay chains from cryostats and teflon reflector.

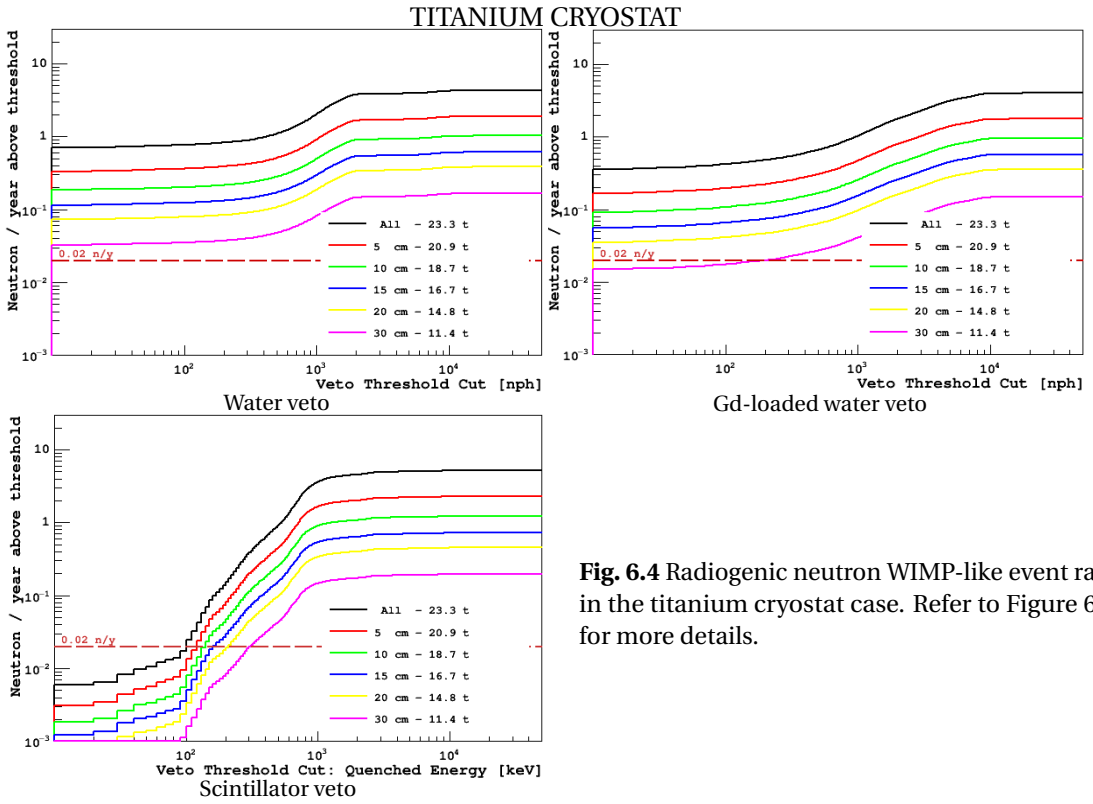

Fig. 6.4 Radiogenic neutron WIMP-like event rate in the titanium cryostat case. Refer to Figure 6.3 for more details.

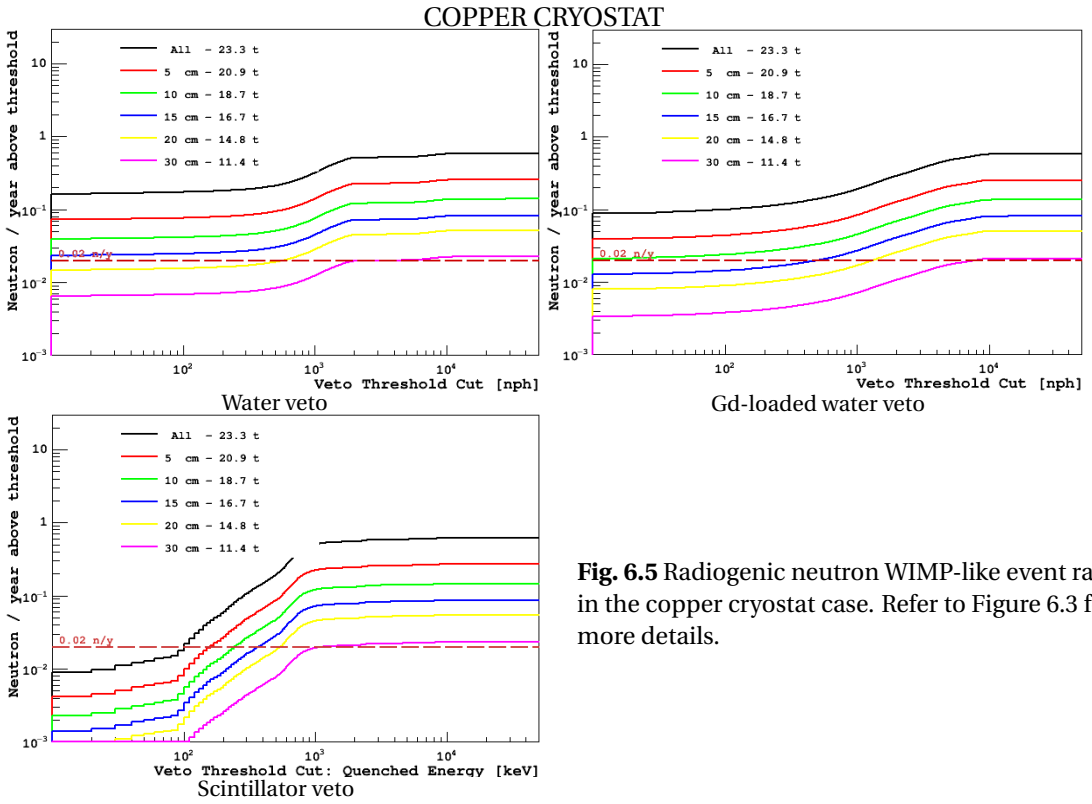

Fig. 6.5 Radiogenic neutron WIMP-like event rate in the copper cryostat case. Refer to Figure 6.3 for more details.

6.1.3.2 Discussion

The results of these simulations must be considered as preliminary. The set of considered sources of background is partial and the geometry description minimal. On the contrary, we tried to minimize the statistical error by producing large simulation samples. The uncertainty on the particular result is then dominated by the systematic errors: the input neutron energy spectra are obtained making assumptions on the material compositions; the detector components sizes and positioning are approximate. Moreover, the radioactive contaminations in materials used for the simulations may be different.

Nevertheless, some unambiguous conclusions can be drawn, only looking at the relative result: the liquid scintillator sphere around the cryostat is the only veto option that guarantees an adequate rejection of the radiogenic neutron background, independently on the cryostat neutron yield.

The design baseline of the DarkSide-20k experiment must be updated with the inclusion of a 7 m diameter LSV around a stainless steel cryostat. The choice of stainless steel is motivated by the fact that, even if it is the less radio-pure, the technology is ready.

6.1.4 Optimal Size of the Liquid Scintillator Veto

The capture of neutrons in the liquid scintillator veto is a very efficient process: the mean capture time (in the DarkSide-50 veto) is ~ 22 μs and neutrons coming from the TPC are

typically captured within 30 cm of liquid. The mean capture length is ~ 3.2 cm for thermal neutrons, as measured with G4DS, for TMB at 5%. With the same concentration, we expect only 8% of the neutrons to capture on H and a negligible fraction on C.

I recall that the capture on ^{10}B produces:

$$n + {}^{10}\mathrm{B} \rightarrow \begin{cases} {}^{7}\mathrm{Li}(1015\ \mathrm{keV}) + \alpha(1775\ \mathrm{keV}) & (6.4\ \%) \\ {}^{7}\mathrm{Li}^{*} + \alpha(1471\ \mathrm{keV}), {}^{7}\mathrm{Li}^{*} \rightarrow {}^{7}\mathrm{Li}(839\ \mathrm{keV}) + \gamma(478\ \mathrm{keV}) & (93.6\ \%) \end{cases} \tag{6.1}$$

Since the energy deposited by the ^{7}Li is heavily quenched, two effects can thus reduce the efficiency of the veto: the missing of the α due to poor light yield and/or high rate in the veto itself and the escape of the gamma from the sensitive volume.

I will describe below the simulations performed to define the optimal size of the veto systems in order to ensure the maximum efficiency.

6.1.4.1 Gamma containment

The mean free path of a 478 keV gamma in the liquid scintillator cocktail (with TMB at 5%) is 10.1 ± 1.1 cm, as measured with G4DS. This means that the required thickness of the scintillator layer outside the cryostat is of the order of some tens of cm in order to assure the maximum gamma containment.

Because of the non-spherical shape of the cryostats and the fluctuations on the position of the neutron capture, a full simulation of radiogenic neutrons is required for our purposes.

We simulated the neutrons from the ^{232}Th decay chain in a steel cryostat, immersed in a LSV of variable diameter. The cryostat shape consists in a cylinder with rounded corners, 3.4 m tall and with 3.6 m dimeter. The diameter of the LSV ranged from 4.50 m to 6.50 m. We implemented the physics cuts described above to select WIMP-like events in the TPC (single sited scattering, recoil energy in the range [10, 70] keV, basic f_{90} cut).

To reproduce the veto response, we distinguished between prompt (thermalization) and late (capture) signals. For this analysis, we only considered the capture signal, defined as the sum of the deposited energy in the veto in a [100 ns, 70 μs] time window. A quenching factor of 1/3.5 is applied to proton energy deposits and a factor of 1/25 is applied to α particles deposits. We did not account for energy depositions by heavier particles.

The results, summarised in Table 6.4, agree with the expectations. Once the thickness of the scintillator exceeds ~ 70 cm in all the directions around the cryostat, the inefficiency of the veto does not improve for increasing radii.[4]

[4] The cryostat, as simulated in G4DS, is a cylinder with rounded edges, 3.4 m tall and with 1.8 m radius. A LSV sphere of 5 m diameter guarantees at least 70 cm of scintillator around the cryostat in all the directions.

LSV diameter	Late signal threshold				
	30 keV	40 keV	50 keV	100 keV	300 keV
6.50 m	**1.00**	**1.00**	**1.00**	**1.00**	**1.00**
6.25 m	0.94	0.93	0.97	0.98	0.99
6.00 m	1.02	1.00	1.02	1.02	1.02
5.75 m	1.02	1.00	1.00	1.02	1.02
5.50 m	1.02	0.98	0.98	1.03	1.00
5.25 m	0.98	0.97	0.98	1.02	1.04
5.00 m	1.04	1.02	1.02	1.06	1.06
4.75 m	**1.13**	**1.11**	**1.11**	**1.12**	**1.14**
4.50 m	**1.28**	**1.23**	**1.26**	**1.23**	**1.34**

Tab. 6.4 Relative number of neutron induced WIMP-like event for decreasing LSV radii and for different detection threshold. The neutron induced event rate are compatible within few % (due to statistical fluctuations) for LSV radii larger than 5 m (assuming a 3.4 m tall, 3.6 diameter, quasi-cylindrical cryostat). The event rate is larger for smaller diameters sphere when compared to the 6.5 m diameter case.

6.1.4.2 Internal Backgrounds

The radioactivity of the veto PMTs can represents a limitation to the veto efficiency, since a high activity in the veto induces high accidental rate.

In order to guarantee a good light yield in the veto, a large photocathode coverage is required. The current LSV is equipped with 110 R5912 Hamamatsu PMTs, with 8 inches area. For the same coverage (~ 10%) in a 6 m sphere, the number of photodetectors must be increased to ~ 500. Table 6.5 reports the specific activities of the PMTs [83] as measured by the manufacturer.

We showed that the PMT-induced total activity in the veto is not the dominant contribution. One must consider in fact the ^{14}C activity due to the PC-TMB mixture and the ^{60}Co for a stainless steel cryostat. We simulated all these components, assuming the same radioactivity levels as in DarkSide-50 (0.25 kBq/(33 t) for ^{14}C and 13 mBq/kg of steel for ^{60}Co).

The result is summarized in Figure 6.6. For a specific veto rate R_V, the accidentals rate is defined as the probability of having one random coincidence event within the veto acquisition window Δt opened by the TPC trigger: $1 - \exp(-\Delta t \cdot R_V)$. To keep the accidentals rate below 10%, with a 200 μs (70 μs) acquisition window a rate lower than ~ 500 Hz (1.5 kHz) at the selected threshold must be obtained. ^{14}C gives the dominant contribution to the veto rate, assuming the same activity found in the DarkSide-50 LSV. Under this assumption, the goal of 10% accidental rate is not achieved. We can either purify the TMB or reduce the acquisition window width.

Isotope	^{40}K	^{238}U	^{235}U	^{232}Th
Activity [mBq/PMT]	649	883	41	110

Tab. 6.5 Activities of the R5912 PMTs as provided by the manufacturer.

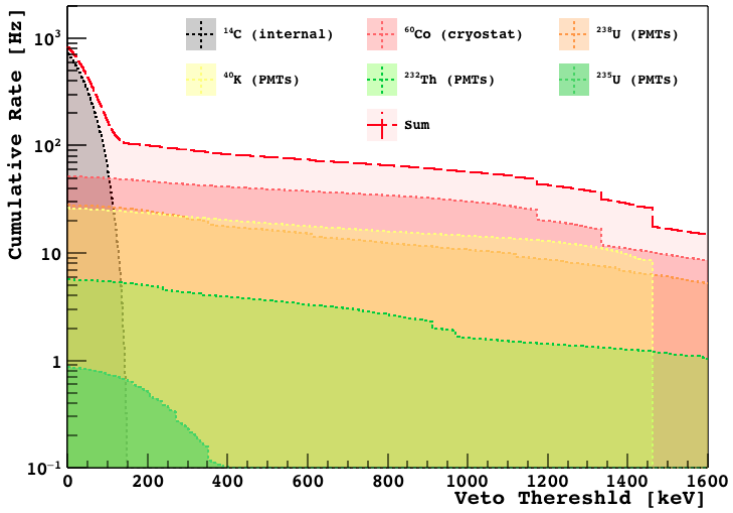

Fig. 6.6 Expected cumulative rate in the veto, assuming the activities from table 6.5 for 500 PMTs, 13 mBq/kg for the stainless steel cryostat and scaling the ^{14}C activity of the TMB from 0.25 kBq/(33 t) to 80 t. To keep the accidentals rate below 10%, with a 200 µs (70 µs) acquisition window a rate lower than ∼ 0.5 kHz (∼ 1.5 kHz) at the selected threshold must be achieved.

6.1.4.3 External Background

The gamma background coming from outside the LSV must be taken into account as well. In particular, the gamma coming from the rocks. Their flux and energy spectrum have been analysed in [126].

Since the water Cerenkov detector offers some shielding from this contamination, we tested the amount of water required for an effective shielding. We simulated isotropic gammas originated in a cylindrical surface around the water Cerenkov detector (WCD) and normalized to the expected flux. This geometry overestimates the side walls. We also tested several WCD dimensions and found that the gamma penetrating in the LSV induce a total rate lower than 10 Hz. Table 6.6 contains a summary of the results.

We decided to adopt a conservative approach for what concerns the WCD dimensions and we decided to opt for a larger tank (14 m diameter, 12 m height). The increased dimensions would imply a larger number of photo-multipliers but the impact on the cost of the experiment is minimal, while the benefit is a more efficient shielding.

In the following section I will describe the evaluation of the cosmogenic neutron background in such a configuration.

6.1.5 Cosmogenic Neutron Background

The mean flux of cosmic rays at the depth of Hall C at LNGS is $(3.41 \pm 0.01) \times 10^{-4}$ µ/s/m^2 [127]. Cosmic muons can produce neutrons by spallation, but most of the neutrons come from interactions of secondary products. It has been shown in [113] that the cosmogenic

WCD radius [m]	WCD height [m]	LSV diameter [m]	Rate in the LSV [Hz]
Large LSV			
5	11	7	**4.5 ± 0.7**
7	11	7	**< 0.15**
Small LSV			
5	11	6	**0.05 ± 0.05**
7	9	6	**0.13 ± 0.07**

Tab. 6.6 Expected rate in the veto induced by gammas from the rocks. The contribution from the walls of the cavern is overestimated.

neutron background is negligible for a detector with either the size of DarkSide-50 and a larger TPC (in this study a 5 t sensitive volume was considered).

That work was based on the results of a large statistics FLUKA [92] simulation (34 years of cosmic muons irradiation of the detector) and particular attention has been devoted to the validation of the simulation with the (few) measured data available.

We reproduced the same study with G4DS and the DarkSide-20k geometry implementation, starting from a large sample of cosmic ray muons and showers simulated with FLUKA. We simulated with FLUKA cosmic ray muons crossing 7 m of rocks above the Hall C of LNGS. The initial energy distribution of muons is scaled in order to have the correct mean value inside the cavern. The output of the simulation included position, energy, time and direction of all the particles, with at least 1 MeV kinetic energy, reaching the WCD for a total exposure of 29.2 years. We used G4DS to propagate those particles through the DarkSide-20k geometry.

We firstly found that events with at least one muon crossing the water Cerenkov veto are efficiently rejected. In order to speed up the simulation, we removed this class of events from the initial data-set and considered only events with at least one neutron entering the WCD. The surviving event fraction is ~ 15% of the total (while the fraction of events with only one neutron entering the WCD is 5%).

We conservatively treated all the events with at least one neutron and no muon as they were single neutrons entering the WCD. By retrieving the energy spectrum and angular distribution of neutrons from the FLUKA data-set we could arbitrarily enlarge the statistics. We finally distinguished between low energy neutrons (with energy lower than 50 MeV, the 90% of the total) and high energy ones (with energy higher than 1 MeV, 28% of the total). In order to simulate the first class of events, the G4DS usual physics lists are adequate and we produced a simulation sample corresponding to 140 years of DarkSide-20k run.

To simulate the high energy neutrons (with energies up to ~ 1 GeV), we had to implement some modifications to the standard G4DS physics lists. To prevent crashes, for instance, we widened the applicability boundaries of the physics lists and we enlarged the physical step in certain materials.

Contaminant	Activity [mBq/kg]	WIMP-like events (before FV and PSD) [ev/day]	WIMP-like events (before PSD , 5 cm FV cut) [ev/day]
^{238}U	0.4	121	1.35
^{232}Th	0.8	447	12.3
^{60}Co	13	49000	607

Tab. 6.7 Expected γ−background induced by ^{238}U, ^{232}Th and ^{60}Co from the cryostats in DarkSide-20k. A WIMP-like event is defined as a single sited recoil in the [10,70] keV energy region. The pulse shape discrimination cut is not applied in this study.

We applied the usual physics cuts to select WIMP-like events (single scattering within [10, 70] keV energy range and basic f_{90} cut). We set a threshold of 1000 Cerenkov photons produced in the WCD and 0.5 MeV energy cut in the LSV. No data-sample provided WIMP-like event in the TPC which was not tagged in one of the vetoes.

6.1.6 External Gamma Induced ER Background

In order to estimate the ER background in the accumulated exposure of 100 t.y, we simulated the γ's coming from the ^{238}U, ^{232}Th and ^{60}Co contamination in the steel cryostat. We discuss here only the cryostat case since the contribution from all other detector materials is one order of magnitude lower.

Table 6.7 summarizes the input parameters of the simulation (activity of the contaminants) and the expected number of background events for a FV cut of 5 cm from the walls of the TPC in the radial direction and from the top and bottom windows. We also applied a cut on the number of clusters (to remove multi-sited events) and on the event energy (the WIMP search region extends from 10 keV to 70 keV).

Is should be mentioned that the ^{60}Co decay consists in the emission of two coincident gammas and the exploitation of the veto coincidence removes roughly the 50% of the events that passes all the other cuts (not shown in the Table). Taking this effect into account we calculated a total number of single ER scattering in the TPC with energy in [10,70] keV lower than 1×10^6. Therefore, this background can be efficiently handled thanks to the pulse shape discrimination.

6.2 Final Design of the Experiment and Projected Sensitivity

The outcome of this simulation work described in the previous Sections is the definition of the DarkSide-20k design baseline. The development of the work is based on several assumptions that limit the prediction reliability. Nonetheless, some unambiguous conclusions can be drawn: the most important is that the only veto system able to assure an efficient neutron rejection is the DarkSide-50-like liquid scintillator sphere surrounding the cryostat. The thickness of the veto must be of the order of ≥ 70 cm to assure the gamma containment. A

ultra-pure copper cryostat or a titanium one can reduce the radiogenic neutron background, but the design goal can be achieved with commercial stainless steel (assuming the same purity as the one found in the current DarkSide-50 experiment).

According to the cryostat dimensions, the LSV can have a diameter as large as 7 m maintaining the same efficiency as the DarkSide-50 veto. The WCD tank will instead be replaced with a larger one (14 m in diameter, 12 m tall).

6.2.1 DarkSide-20k sensitivity to WIMPs

Under the assumption that DarkSide-20k could reach a background-free exposure of 100 t.yr, the experiment sensitivity would be of 1×10^{-47} cm^2 for a WIMP mass of 1 TeV/c^2 and 1×10^{-46} cm^2 for a WIMP mass of 10 TeV/c^2.

The DarkSide collaboration is also making plans to build an ultimate LAr background free detector, Argo, able to reach an exposure of 1000 t.yr. Figure 6.7 shows the projected sensitivity of DarkSide-20k and Argo, compared to the neutrino floor. The only NR background to this experiment would be the neutrino coherent scattering off nuclei. No design study have been yet performed, but the foreseen TPC would have an active (fiducial) volume of the order of 300 (100) t.

In addition to the dark matter physics, Argo will also be sensitive to solar neutrinos. Elastic scattering of neutrinos on electrons will not be a limiting background for the WIMP search, but the detector will be able to measure the low energy solar neutrino flux with unprecedented resolution. The next Section is dedicated to the estimate of the experiment sensitivity.

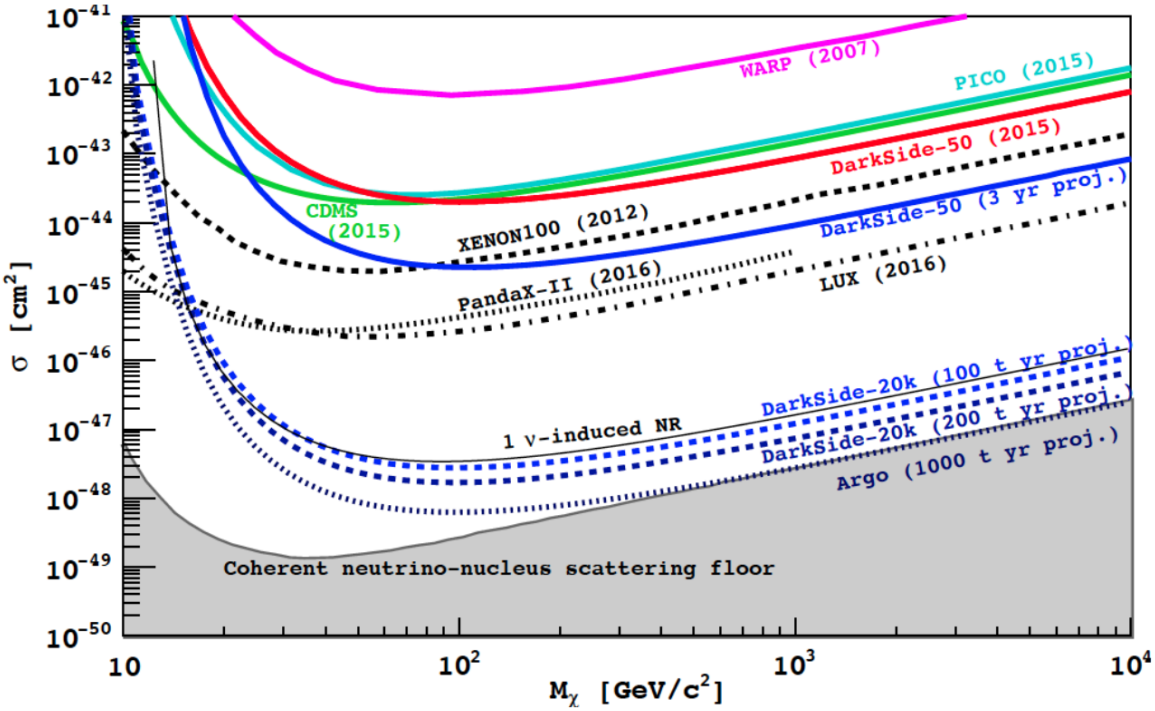

Fig. 6.7 Projected sensitivity of DarkSide-20k and Argo. The exclusion or the projected sensitivity of other experiments is also shown, as the discovery limit for a non directional detector (the gray shaded area [69]).

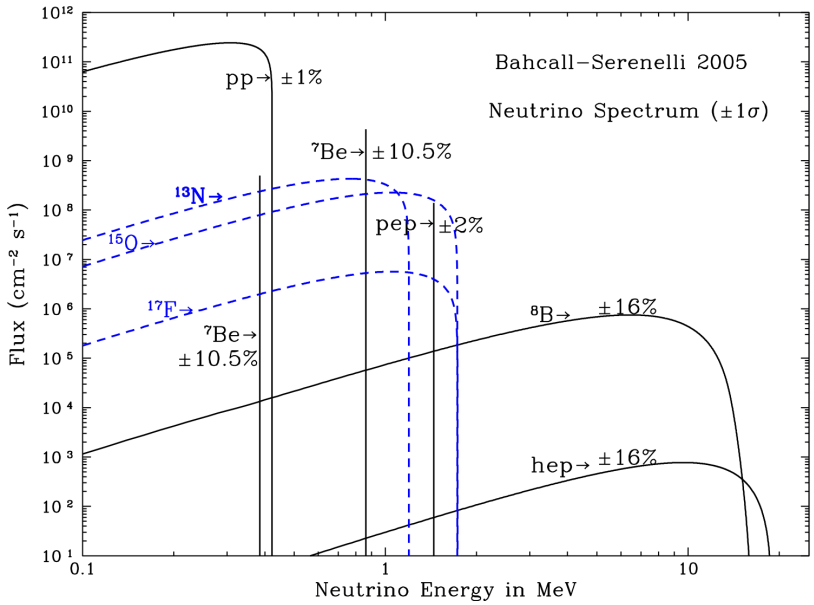

Fig. 6.8 Solar neutrino spectra at the Earth surface. The CNO neutrino spectra are shown in blue.

6.3 Solar Neutrino Physics with Argo

The fusion reaction chains occurring in the nucleus of the Sun imply the production of several electron neutrinos at different energies. The primary fusion chain, summarized in Figure 6.9 (a), starts with the fusion of two protons and leads to the production of two ^{4}He.

Together with the proton-proton (pp) chain, there exist other processes for the conversion of hydrogen into helium, namely the CNO cycles. They differ because of the catalyst nucleus, but the net result is the emission of one ^{4}He for each input proton. A schematic view of the cycles is given in Figure 6.9 (b). The CNO cycle relative intensity to pp depends on the concentration in the Sun of high Z ($Z > 2$) elements. The CNO cycles are believed to be the dominant source of energy in stars with mass larger than $\sim 1.3 M_\odot$ and they produce neutrinos too (from the ^{13}N, ^{15}O and ^{17}F β^+ decays).

A measure of the flux of CNO neutrino components can constraint the chemical composition of the Sun, to date subject to large uncertainties. In particular two different scenarios are favored from spectroscopy analyses for what concerns the fraction of heavy elements ($Z > 2$) in the Sun: the Low Metallicity (LZ) [128] and the High Metallicity (HZ) one [129]. Only an upper limit is available on the flux of CNO neutrinos [111], while a measurement with $10 \div 20\%$ uncertainty could discriminate between the two scenarios.

The differential neutrino energy spectra are shown in Figure 6.8. The flux of solar neutrino at the surface of the Earth is of the order of 6×10^{10} particles/s/cm^2. We show in [130] how a large mass ($\sim$ 100 t fiducial) LAr WIMP detector would detect neutrino interactions with a statistics large enough to measure the CNO neutrinos flux with the required accuracy, if the backgrounds are successfully maintained low. The detector geometry and operation

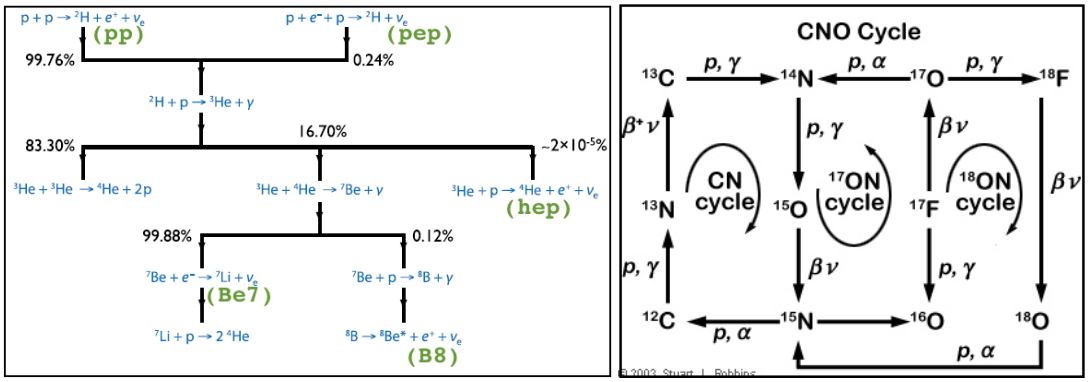

(a) The pp chain (b) The CNO cycles

Fig. 6.9 (a) The pp fusion chain and (b) the CNO cycles.

principles are inspired by the preliminary design of the ultimate dark matter direct detection experiment, Argo. It consists in a cylindrical TPC (3 m height, 3.3 m radius)[5], placed inside a 6 m radius liquid scintillator veto, in turn placed inside a 17 m height, 16 m diameter water tank. I will review in what follows the signal and background estimate and sensitivity for the neutrino physics search. It is important to stress that the WIMP search and the neutrino one can be performed at the same time.

6.3.1 Expected Signal and Backgrounds

Solar electron neutrinos interact with electrons and produce electron recoils in the sensitive target. The total neutrino rate in LAr is expected to be about 150 cpd[6]/(100 t). In 100 t LAr TPC, the event rate induced by ^{39}Ar is many orders of magnitude larger, even with a ^{39}Ar specific activty reduced by a factor of 10 with respect to the one measured in DarkSide-50 (0.07 mBq/kg of ^{39}Ar correspond to 6×10^5 cpd/100 t). However, the ^{39}Ar endpoint is at 565 keV, while neutrinos can induce electron recoils up to several MeV. Assuming a 6000 pe/MeV light yield and a Poisson photon statistics, no ^{39}Ar event is expected to appear above 0.6 MeV in a 400 t.yr exposure due to resolution smearing. On the contrary, both the Compton-like edge of the ^{7}Be and CNO neutrino spectra would be accessible with an energy cut at 0.6 MeV.

Figure 6.10 shows the expected energy spectra of neutrino induced electron recoils and the ^{39}Ar $\beta-$decay, assuming an internal activity of 0.07 mBq/kg in the LAr target and assuming a poissonian resolution.

Other backgrounds could limit the signal to noise ratio above the 0.6 MeV threshold. We included in our study the cosmogenic radionuclides produced by cosmic rays in the sensitive volume, the external gammas due to radioactivity in detector materials and the internal radon contamination. A possible ^{85}Kr internal contamination (found for example in the

[5] The total active mass in this layout is of ~ 140 t. A fiducial volume cut of 30 cm from all the internal walls reduces the fiducial mass down to 100 t.

[6] Counts per day

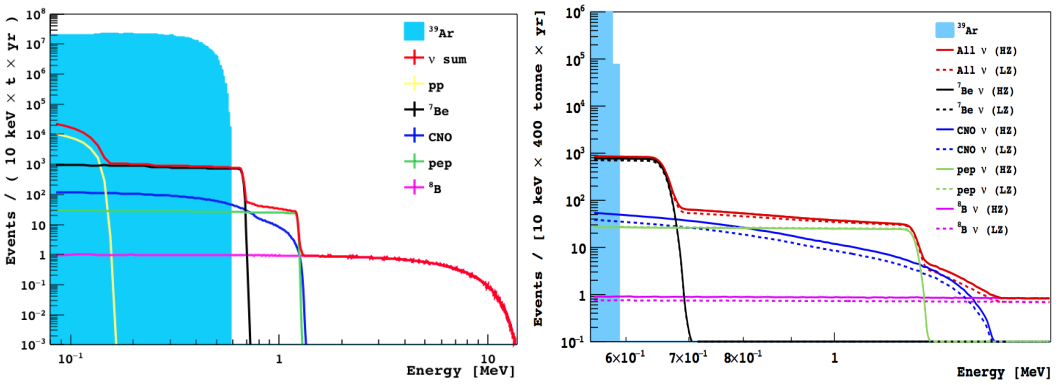

(a) In the whole energy range

(b) In the [0.6, 1.3] MeV range

Fig. 6.10 Energy spectrum of solar neutrino induced events in a LAr target, assuming 6000 pe/MeV. The neutrino spectra are compared to the ^{39}Ar contribution, assuming a specific activity of 7 Bq/(100 t).

UAr filling of DarkSide-50) is not taken into account. Only 1% of the induced events would in fact have energy larger than 0.6 MeV. In the case of a specific activity as large as the one measured in DarkSide-50, the resolution on the ^{7}Be neutrinos would be compromised, but the resolution on CNO neutrinos would remain unchanged.

We performed a detailed study of cosmogenics production in the sensitive volume by means of the FLUKA package. We recorded the radioactive nuclides produced and we propagated them in the G4DS geometry. We found that a significant fraction of events are removed by the multiple scattering cut. We estimated the cosmogenics induced rate to be 4.1 cpd/(100 t) in the full energy range and only 0.73 cpd/(100 t) in the [0.6, 1.3] MeV energy range. In this range we expect 4.63 ± 0.22 cpd/100 t (5.14 ± 0.25 cpd/100 t) in the LZ (HZ) metallicity scenario. We then limited our search to this energy range in order to maximize the neutrino signal-to-background ratio.

To evaluate the external backgrounds we simulated ^{214}Bi, ^{14}K and ^{208}Tl from the photosensors (assumed to be SiPMs) along with ^{60}Co from the cryostats. Because of the small mass of silicon photosensors, we found that the main contribution would arise from the cryostat (up to 510 cpd/100 t in the whole TPC volume assuming the cleanest commercial steel). This class of events can however be suppressed by a factor of 10^5 by applying a fiducial volume cut of the order of 30 cm. Moreover, we assumed a purely passive veto system, meaning that the background rejection power is underestimated. ^{60}Co decays by emitting two $\sim$ 1 MeV gammas and we expect to be able to exploit the anti-coincidence between the TPC and the LSV to improve the rejection.

The most dangerous background source is the internal radon contamination. ^{222}Ra is produced by the ^{238}U decay chain and emanates from all the detector materials. Its decay chain includes two α's (efficiently discriminated by the pulse shape) and two β-decays (^{214}Pb and ^{214}Bi). These β decays are often accompanied by a γ emission, but a significant fraction

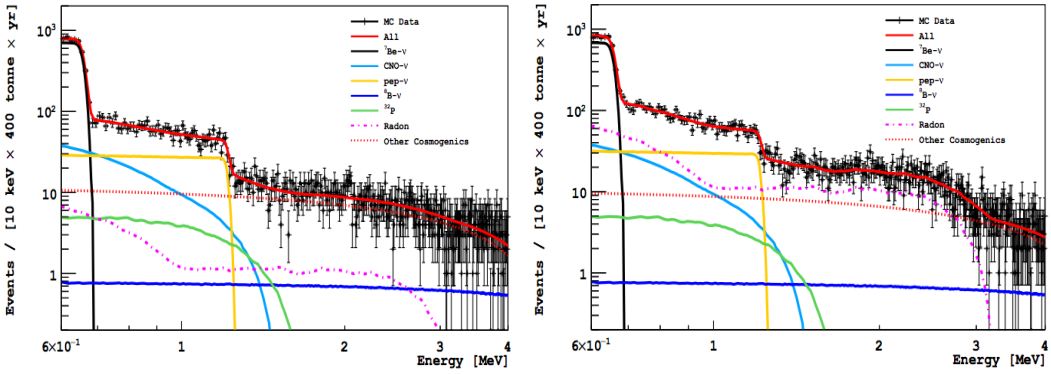

(a) ^{222}Rn activity: 10 µBq/(100 t) (b) ^{222}Rn activity: 100 µBq/(100 t)

Fig. 6.11 Examples of simulated spectra and fits, assuming different values of the radon activity. The calculations assume the low–metallicity solar model. The cosmogenic component is modeled with a first degree polynomial, with the exception of an explicit spectrum for ^{32}P.

of events happens to produce a single recoil within the solar neutrino energy range. We found that a radon contamination at the level of 45 µBq/(100 t) would induce a background rate equivalent to the expected solar neutrino signal.

Fortunately, the ^{222}Rn contamination can be measured by looking for the delayed coincidence between the ^{214}Bi β decay and the ^{214}Po α emission ($\tau_{1/2}$ = 163 µs). An accurate measurement of the ^{222}Rn decay chain activity would allow the discrimination of the neutrino spectral shape even in presence of high contamination, as discussed in the next section.

6.3.2 Expected Sensitivity

A measurement of the solar neutrino spectral components relies on identification of their individual spectral shapes. We attempt to estimate the sensitivity of a 100 t dual–phase LAr TPC to solar neutrinos using a toy Monte Carlo approach. For each solar metallicity model we sampled GEANT4-generated energy spectra for the various signal and background components, to produce simulated data samples. Ten thousand samples were generated with Poisson statistics corresponding to a 400 t.y exposure, and assuming PE-statistics-limited detector resolution with a light yield of 6000 pe/MeV.

The external background was neglected, since, as discussed above, it can be completely suppressed by multi-site and fiducial volume cuts. The radon contribution in the generated data samples was varied from 10 to 200 µBq/(100 tonne) (0.8 - 16 cpd/100 tonne). The simulated spectra were then fit to a model designed to account for the large uncertainty of the cosmogenic background shape. For the present work, only the most abundant cosmogenic contribution from ^{32}P has been explicitly included in the fit function. The aggregate electron recoil spectrum from the remaining cosmogenics was modeled with a linear function of energy. The parameters of the function were left free to vary in the fit which was performed

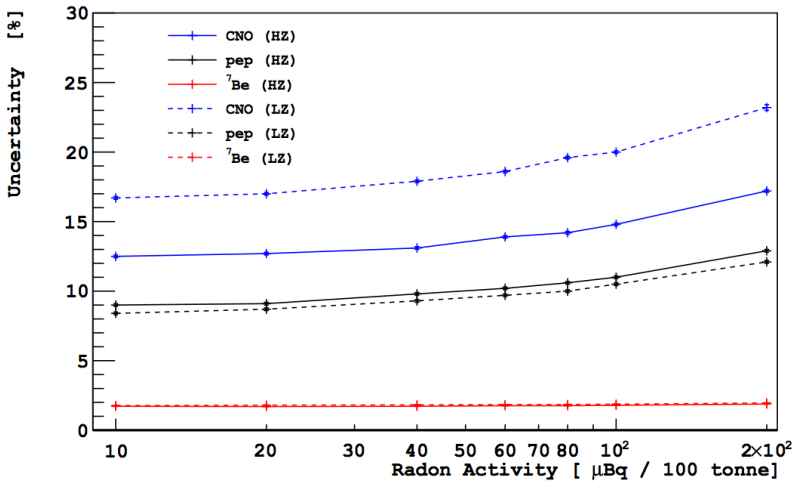

Fig. 6.12 Expected statistical uncertainty on the neutrino flux components as a function of the radon activity. LZ refers to the Sun Low Metallicity scenario and HZ to the High Metallicity one. Figure extracted from [130].

with a maximum likelihood method using the RooFit package. Two examples of the simulated and fitted spectra are given in Figure 6.11.

The radon level in the fitting model was constrained from the simulated number of ^{214}Bi-Po events in each simulated sample. The fit range extended from 0.6 to 5 MeV, so as to better constrain the background contributions.

The CNO spectral shape is similar to the one of the low energy radon component. At radon contamination levels above 200 μBq/(100 t) (16 cpd/100 t), the fit shows a systematic deviation from the central value of the simulated CNO component by a few percent, implying that to guarantee a correct CNO measurement, the radon activity must be reduced below this level. No such systematic deviations are observed for ^{7}Be and *pep* neutrino fluxes, whose spectral shapes have clear characteristic features.

The systematic uncertainty associated with the linear model of the cosmogenic background shape was studied. For this purpose, we generated toy MC samples uniformly varying each cosmogenic isotope activityby a factor between 0.5 and 2, with respect to a reference configuration. The resulting variations in the extracted solar neutrino signals are small compared to the fit errors.

The uncertainty on the flux measurement of each component as a function of the ^{222}Rn activity is given in Figure 6.12. We can conclude that with a 400 t.y exposure is possible a precision at the level of ~2%, ~10%, and ~15% for the ^{7}Be, *pep* and CNO neutrino rates respectively. These expectations can be compared to the best present measurements of the first two components (4.6% and 21.6% from Borexino), and the best upper limit for the CNO neutrinos (currently 1.5 times higher than the prediction in the High Metallicity scenario [131]).

6.4 Conclusions

In this Chapter I focused on the future phases of the DarkSide program.

Since the DarkSide-20k experiment is foreseen to start the data taking before 2020, its experimental setup is currently being finalized. I discussed the simulations that lead the design study of the veto systems of the experiment, aiming to the minimization of the backgrounds. The configuration in which the TPC is surrounded by a liquid scintillator veto is the sole option that guarantees a background free exposure (assuming the current DarkSide-50 levels of internal radioactivity).

In the last part of this Chapter I presented a study of the sensitivity of Argo, the ultimate LAr TPC for direct WIMP search, to the CNO cycle neutrinos. Such a detector could measure the CNO neutrino flux with unprecedented accuracy, allowing the discrimination between the high metallicity and the low metallicity scenarios.

Conclusions

The DarkSide program aims to a background-free WIMP search, using a dual-phase liquid argon TPC. Liquid argon is particularly suited for this kind of search, thanks to the exceptional rejection power between nuclear and electron recoils (WIMP signal and background respectively). However, atmospheric argon contains such a large amount of ^{39}Ar that scaling a dual-phase detector up to the tonne scale would be impossible due to the high internal rate.

The DarkSide Collaboration is operating for the first time a TPC filled with underground argon, depleted in ^{39}Ar. I describe in the first part of this thesis the status and the first results of the DarkSide-50 experiment, the current phase of the DarkSide program.

My involvement in the project has been mainly related to the development of G4DS, the DarkSide simulation tool. It consists in a GEANT4-based simulation of the geometry of all the detectors of the DarkSide program and it is fully integrated within the true data reconstruction software. The non-uniformities of the TPC response are accurately simulated and the energy scale calibration is based on a custom model that we developed to describe the ionization and scintillation mechanisms in liquid argon. The main features of G4DS are discussed in Chapter 3.

I present in Chapter 4 two studies based on G4DS and related to the DarkSide-50 experiment: the estimate of the expected neutron background and the measurement of the residual activity of ^{39}Ar in the UAr sample which currently fills the detector.

Chapter 5 is dedicated to a study about the pulse shape discrimination parameter (f_{90}). We developed an analytical model that accurately describes the statistics of f_{90} and allows to compute the probability for electron recoils to leak in the nuclear recoil expectation region, as well as the related confidence interval.

In the last Chapter I focus on the future of the DarkSide program. I describe the design studies for the next detector (with an active mass of 100 t y), mainly driven by the minimization of the neutron background. We determined that the only design which would allow the experiment to be background-free foresees a liquid scintillator veto, according to the same design of DarkSide-50.

References

[1] D. S. Akerib *et al.*, **(The LUX Collaboration)**, *Results from a search for dark matter in LUX with 332 live days of exposure*, (2016), arXiv:1608.07648.

[2] P. Benetti *et al.*, **(The WArP Collaboration)**, *First results from a dark matter search with liquid argon at 87 K in the Gran Sasso underground laboratory*, Astroparticle Physics **28**, 495 (2008).

[3] P. Agnes *et al.*, **(The DarkSide Collaboration)**, *First results from the DarkSide-50 dark matter experiment at Laboratori Nazionali del Gran Sasso*, Physics Letters B **743**, 456 (2015).

[4] P. Agnes *et al.*, **(The DarkSide Collaboration)**, *Results from the first use of low radioactivity argon in a dark matter search*, Phys. Rev. D **93**, 081101 (2016), arXiv:1510.00702.

[5] F. Zwicky, *Die Rotverschiebung von extragalaktischen Nebeln*, Helvetica Physica Acta **6**, 110 (1933).

[6] V. Rubin and W. K. J. Ford, *Rotation of the Andromeda Nebula from a Spectroscopic Survey of Emission Regions*, Astrophysical Journal **159**, 379 (1970).

[7] F. Iocco, M. Pato, and G. Bertone, *Evidence for dark matter in the inner Milky Way*, Nat Phys **11**, 245 (2015), arXiv:1502.03821.

[8] L. E. Strigari, *Galactic Searches for Dark Matter*, Phys. Rept. **531**, 1 (2013), arXiv:1211.7090.

[9] D. Clowe *et al.*, *A Direct Empirical Proof of the Existence of Dark Matter*, The Astrophysical Journal Letters **648**, L109 (2006), arXiv:astro-ph/0608407.

[10] S. W. Randall *et al.*, *Constraints on the Self-Interaction Cross Section of Dark Matter from Numerical Simulations of the Merging Galaxy Cluster 1E 0657–56*, The Astrophysical Journal **679**, 1173 (2008), arXiv:0704.0261.

[11] M. Bradač *et al.*, *Revealing the Properties of Dark Matter in the Merging Cluster MACS J0025.4–1222*, The Astrophysical Journal **687**, 959 (2008), arXiv:0806.2320.

[12] J. C. Mather *et al.*, *Measurement of the cosmic microwave background spectrum by the COBE FIRAS instrument*, The Astrophysical Journal **420**, 439 (1994).

[13] P. A. R. Ade *et al.*, **(The Planck Collaboration)**, *Planck 2015 results. XIII. Cosmological parameters*, (2015), arXiv:1502.01589.

[14] M. Betoule *et al.*, **(The SDSS Collaboration)**, *Improved cosmological constraints from a joint analysis of the SDSS-II and SNLS supernova samples*, Astron. Astrophys. **568**, A22 (2014), arXiv:1401.4064.

[15] R. Massey, T. Kitching, and J. Richard, *The dark matter of gravitational lensing*, Reports on Progress in Physics **73**, 086901 (2010), arXiv:1001.1739.

[16] K. S. Dawson *et al.*, *The Baryon Oscillation Spectroscopic Survey of SDSS-III*, The Astronomical Journal **145**, 10 (2013), arXiv:1208.0022.

[17] K.A. Olive et al. (Particle Data Group), *Big-bang nucleosynthesis*, Chin. Phys. C **38** (2015).

[18] J. Binney and S. Tremaine, *Galactic Dynamics*, 2nd ed. (Princeton University Press, 2013).

[19] F.-S. Ling, E. Nezri, E. Athanassoula, and R. Teyssier, *Dark matter direct detection signals inferred from a cosmological N-body simulation with baryons*, Journal of Cosmology and Astroparticle Physics **2010**, 012 (2010), arXiv:0909.2028.

[20] M. J. Reid *et al.*, *Trigonometric Parallaxes of Massive Star-Forming Regions. VI. Galactic Structure, Fundamental Parameters, and Noncircular Motions*, The Astrophysical Journal **700**, 137 (2009), arXiv:0902.3913.

[21] C. Savage, K. Freese, and P. Gondolo, *Annual modulation of dark matter in the presence of streams*, Phys. Rev. D **74**, 043531 (2006), arXiv:astro-ph/0607121.

[22] K.A. Olive et al. (Particle Data Group), *Astrophysical Constants and Parameters*, Chin. Phys. C **38** (2015).

[23] J. I. Read, *The local dark matter density*, Journal of Physics G: Nuclear and Particle Physics **41**, 063101 (2014), arXiv:1404.1938.

[24] A. M. Green, *Atrophysical uncertainties on direct detection experiments*, Mod. Phys. Lett. A **27**, 1230004 (2012), arXiv:1112.0524.

[25] M. C. Smith *et al.*, *The RAVE survey: constraining the local Galactic escape speed*, Monthly Notices of the Royal Astronomical Society **379**, 755 (2007), arXiv:astro-ph/0611671.

[26] R. Adhikari *et al.*, *A White Paper on keV Sterile Neutrino Dark Matter*, (2016), arXiv:1602.04816.

[27] E. Bulbul *et al.*, *Detection of an Unidentified Emission Line in the Stacked X-Ray Spectrum of Galaxy Clusters*, The Astrophysical Journal **789**, 13 (2014), arXiv:1402.2301.

[28] M. Klasen, M. Pohl, and G. Sigl, *Indirect and direct search for dark matter*, Progress in Particle and Nuclear Physics **85**, 1 (2015), arXiv:1507.03800.

[29] A. Merle and A. Schneider, *Production of Sterile Neutrino dark matter and the 3.5 keV line*, Physics Letters B **749**, 283 (2015), arXiv:1409.6311.

[30] K.A. Olive et al. (Particle Data Group), *Axions and Other Similar Particles*, Chin. Phys. C **38** (2015).

[31] P. Arias *et al.*, *WISPy cold dark matter*, Journal of Cosmology and Astroparticle Physics **2012**, 013 (2012), arXiv:1201.5902.

[32] J. L. Feng, *Dark Matter Candidates from Particle Physics and Methods of Detection*, Annual Review of Astronomy and Astrophysics **48**, 495 (2010), arXiv:1003.0904v2.

[33] A. Bilal, *Introduction to Supersymmetry*, (2001), arXiv:hep-th/0101055.

[34] S. Chang, R. Edezhath, J. Hutchinson, and M. Luty, *Effective WIMPs*, Phys. Rev. **D89**, 015011 (2014), arXiv:1307.8120.

[35] C. Weniger, *A tentative gamma-ray line from Dark Matter annihilation at the Fermi Large Area Telescope*, Journal of Cosmology and Astroparticle Physics **2012**, 007 (2012), arXiv:1210.3013.

[36] M. Ackermann *et al.*, **(The Fermi-LAT Collaboration)**, *Updated search for spectral lines from Galactic dark matter interactions with pass 8 data from the Fermi Large Area Telescope*, Phys. Rev. D **91**, 122002 (2015), arXiv:1506.00013.

[37] T. A. Porter and S. Murgia, **(The Fermi-LAT Collaboration)**, *Observations of High-Energy Gamma-Ray Emission Toward the Galactic Centre with the Fermi Large Area Telescope*, arXiv:1507.04688.

[38] M. Ajello *et al.*, **(The Fermi–LAT Collaboration)**, *Fermi–LAT Observations of High-energy γ-ray emission toward the galacti centre*, arXiv:1511.02938.

[39] M. Ackermann *et al.*, **(The Fermi-LAT Collaboration)**, *Fermi LAT search for dark matter in gamma-ray lines and the inclusive photon spectrum*, Phys. Rev. D **86**, 022002 (2012), arXiv:1205.2739.

[40] A. Abramowski *et al.*, **(The H.E.S.S. Collaboration)**, *Constraints on an Annihilation Signal from a Core of Constant Dark Matter Density around the Milky Way Center with H.E.S.S.*, Phys. Rev. Lett. **114**, 081301 (2015), arXiv:1502.03244.

[41] K. Choi *et al.*, **(The Super-Kamiokande Collaboration)**, *Search for Neutrinos from Annihilation of Captured Low-Mass Dark Matter Particles in the Sun by Super-Kamiokande*, Phys. Rev. Lett. **114**, 141301 (2015), arXiv:1503.04858.

[42] M. G. Aartsen *et al.*, **(The IceCube Collaboration)**, *Search for Dark Matter Annihilations in the Sun with the 79-String IceCube Detector*, Phys. Rev. Lett. **110**, 131302 (2013), arXiv:1212.4097.

[43] O. Adriani *et al.*, *An anomalous positron abundance in cosmic rays with energies 1.5-100 GeV*, Nature **458**, 607 (2009), arXiv:0810.4995.

[44] L. Accardo *et al.*, **(The AMS Collaboration Collaboration)**, *High Statistics Measurement of the Positron Fraction in Primary Cosmic Rays of 0.5–500 GeV with the Alpha Magnetic Spectrometer on the International Space Station*, Phys. Rev. Lett. **113**, 121101 (2014).

[45] H.-C. Cheng *et al.*, *AMS-02 Positron Excess and Indirect Detection of Three-body Decaying Dark Matter*, (2016), arXiv:1608.06382.

[46] G. Aad *et al.*, **(The ATLAS Collaboration)**, *Summary of the searches for squarks and gluinos using $\sqrt{s} = 8$ TeV pp collisions with the ATLAS experiment at the LHC*, Journal of High Energy Physics **2015**, 1 (2015), arXiv:1507.05525.

[47] J. D. Lewin and P. F. Smith, *Review of mathematics, numerical factors, and corrections for dark matter experiments based on elastic nuclear recoil*, Astropart. Phys. **6**, 87 (1996).

[48] S. Ahlen *et al.*, *The Case for a Directional Dark Matter Detector and The Status of Current Experimental Efforts*, International Journal of Modern Physics A **25**, 1 (2010), arXiv:0911.0323.

[49] A. M. Green and B. Morgan, *Median recoil direction as a WIMP directional detection signal*, Phys. Rev. D **81**, 061301 (2010), arXiv:1002.2717.

[50] R. Bernabei *et al.*, **(The DAMA/LIBRA Collaboration)**, *First results from DAMA/LIBRA and the combined results with DAMA/NaI*, The European Physical Journal C **56**, 333 (2008), arXiv:0804.2741.

[51] C. E. Aalseth *et al.*, **(The CoGeNT Collaboration)**, *Results from a Search for Light-Mass Dark Matter with a p-Type Point Contact Germanium Detector*, Phys. Rev. Lett. **106**, 131301 (2011), arXiv:1002.4703.

[52] R. Bernabei *et al.*, **(The DAMA/LIBRA Collaboration)**, *New results from DAMA/LIBRA*, Eur. Phys. J. **C67**, 39 (2010), arXiv:1002.1028.

[53] S. C. Kim *et al.*, **(The KIMS Collaboration)**, *New Limits on Interactions between Weakly Interacting Massive Particles and Nucleons Obtained with CsI(Tl) Crystal Detectors*, Phys. Rev. Lett. **108**, 181301 (2012), arXiv:1204.2646.

[54] F. Froborg *et al.*, **(The SABRE Collaboration)**, *SABRE: WIMP modulation detection in the northern and southern hemisphere*, (2016), arXiv:1601.05307.

[55] E. B. de Souza *et al.*, **(The DM-Ice Collaboration)**, *First Search for a Dark Matter Annual Modulation Signal with NaI(Tl) in the Southern Hemisphere by DM-Ice17*, (2016), arXiv:1602.05939.

[56] G. Angloher *et al.*, **(The CRESST Collaboration)**, *Results from 730 kg.d of the CRESST-II Dark Matter search*, The European Physical Journal C **72**, 1 (2012), arXiv:1109.0702.

[57] G. Angloher *et al.*, **(The CRESST Collaboration)**, *Results on light dark matter particles with a low-threshold CRESST-II detector*, The European Physical Journal C **76**, 1 (2016), arXiv:1509.01515.

[58] E. Armengaud *et al.*, *Constraints on low-mass WIMPs from the EDELWEISS-III dark matter search*, JCAP **2016**, 019 (2016), arXiv:1603.05120.

[59] Z. Ahmed *et al.*, **(The CDMS and EDELWEISS Collaborations)**, *Combined limits on WIMPs from the CDMS and EDELWEISS experiments*, Phys. Rev. D **84**, 011102 (2011), arXiv:1105.3377.

[60] R. Agnese *et al.*, **(The SuperCDMS Collaboration)**, *New Results from the Search for Low-Mass Weakly Interacting Massive Particles with the CDMS Low Ionization Threshold Experiment*, Phys. Rev. Lett. **116**, 071301 (2016), arXiv:1509.02448.

[61] K. Abe and others", **(The "XMASS" Collaboration)**, *"Direct dark matter search by annual modulation in XMASS-I"*, arXiv:1511.04807.

[62] A. Badertscher *et al.*, **(The ArDM Collaboration)**, *ArDM: first results from underground commissioning*, Journal of Instrumentation **8**, C09005 (2013), arXiv:1309.3992.

[63] P. A. Amaudruz *et al.*, **(The DEAP Collaboration)**, *DEAP-3600 Dark Matter Search*, arXiv:1410.7673.

[64] D. S. Akerib *et al.*, **(The LUX Collaboration)**, *Improved WIMP scattering limits from the LUX experiment*, (2015), arXiv:1512.03506.

[65] E. Aprile *et al.*, **(The XENON100 Collaboration)**, *Dark Matter Results from 225 Live Days of XENON100 Data*, Phys. Rev. Lett. **109**, 181301 (2012).

[66] X. Xiao *et al.*, **(The PandaX Collaboration)**, *Low-mass dark matter search results from full exposure of the PandaX-I experiment*, Phys. Rev. D **92**, 052004 (2015).

[67] A. Tan *et al.*, **(The PandaX-II Collaboration)**, *Dark Matter Results from First 98.7-day Data of PandaX-II Experiment*, (2016), arXiv:1607.07400.

[68] C. Amole *et al.*, **(The PICO Collaboration)**, *Dark Matter Search Results from the PICO-2L* C_3F_8 *Bubble Chamber*, Phys. Rev. Lett. **114**, 231302 (2015).

[69] J. Billard, E. Figueroa-Feliciano, and L. Strigari, *Implication of neutrino backgrounds on the reach of next generation dark matter direct detection experiments*, Phys. Rev. D **89**, 023524 (2014), arXiv:1307.5458.

[70] K. Nakamura *et al.*, *NEWAGE - Direction-sensitive Dark Matter Search Experiment*, Physics Procedia **61**, 737 (2015).

[71] D. Santos *et al.*, **(The MIMAC Collaboration)**, *MIMAC: MIcro-tpc MAtrix of Chambers for dark matter directional detection*, Journal of Physics: Conference Series **469**, 012002 (2013), arXiv:1311.0616.

[72] E. Daw *et al.*, **(The DRIFT Collaboration)**, *Spin-dependent limits from the DRIFT-IId directional dark matter detector*, Astroparticle Physics **35**, 397 (2012), arXiv:1010.3027.

[73] V. Chepel and H. Araújo, *Liquid noble gas detectors for low energy particle physics*, Journal of Instrumentation **8**, R04001 (2013), arXiv:1207.2292.

[74] A. Hitachi *et al.*, *Effect of ionization density on the time dependence of luminescence from liquid argon and xenon*, Phys. Rev. B **27**, 5279 (1983).

[75] S. Kubota, M. Hishida, and J. Raun, *Evidence for a triplet state of the self-trapped exciton states in liquid argon, krypton and xenon*, Journal of Physics C: Solid State Physics **11**, 2645 (1978).

[76] S. Kubota, M. Hishida, and N. A, *Variation of scintillation decay in liquid argon excited by electrons and alpha particles.*, Nucl. Instrum. Methods 150(3): 561-4 (1978) **150**, 561 (1978).

[77] M. Carvalho and G. Klein, *Luminescence decay in condensed argon under high energy excitation*, Journal of Luminescence **18–19, Part 1**, 487 (1979).

[78] T. Alexander *et al.*, **(The SCENE Collaboration)**, *Observation of the dependence on drift field of scintillation from nuclear recoils in liquid argon*, Phys. Rev. D **88**, 092006 (2013).

[79] P. Benetti *et al.*, *Measurement of the specific activity of 39Ar in natural argon*, Nuclear Instruments and Methods in Physics Research Section A: Accelerators, Spectrometers, Detectors and Associated Equipment **574**, 83 (2007), arXiv:astro-ph/0603131.

[80] H. O. Back *et al.*, *First Large Scale Production of Low Radioactivity Argon From Underground Sources*, (2012), arXiv:1204.6024.

[81] H. O. Back *et al.*, **(The DarkSide Collaboration)**, *First Commissioning of a Cryogenic Distillation Column for Low Radioactivity Underground Argon*, (2012), arXiv:1204.6061.

[82] T. Alexander *et al.*, *Light yield in DarkSide-10: A prototype two-phase argon TPC for dark matter searches*, Astroparticle Physics **49**, 44 (2013).

[83] P. Agnes *et al.*, **(The DarkSide Collaboration)**, *The veto system of the DarkSide-50 experiment*, Journal of Instrumentation **11**, P03016 (2016), arXiv:1512.07896.

[84] H. Back *et al.*, **(The Borexino Collaboration)**, *Pulse-shape discrimination with the Counting Test Facility*, Nuclear Instruments and Methods in Physics Research Section A: Accelerators, Spectrometers, Detectors and Associated Equipment **584**, 98 (2008).

[85] L. W. Kastens, S. B. Cahn, A. Manzur, and D. N. McKinsey, *Calibration of a liquid xenon detector with* $^{83}\mathrm{Kr}^{m}$, Phys. Rev. C **80**, 045809 (2009).

[86] P. Agnes *et al.*, **(The DarkSide Collaboration)**, *CALIS - a CALibration Insertion System for the DarkSide-50 dark matter search experiment*, arXiv:1611.02750.

[87] P. Agnes *et al.*, **(The DarkSide Collaboration)**, *Effect of Low Electric Fields on Alpha Scintillation Light Yield in Liquid Argon*, arXiv:1611.00241.

[88] H. Cao *et al.*, **(The SCENE Collaboration)**, *Measurement of scintillation and ionization yield and scintillation pulse shape from nuclear recoils in liquid argon*, Phys. Rev. D **91**, 092007 (2015).

[89] R. Agnese *et al.*, **(The SuperCDMS Collaboration)**, *Improved WIMP-search reach of the CDMS II germanium data*, Phys. Rev. D **92**, 072003 (2015).

[90] D. Akimov *et al.*, *WIMP-nucleon cross-section results from the second science run of ZEPLIN-III*, Physics Letters B **709**, 14 (2012).

[91] S. Agostinelli *et al.*, *GEANT4—a simulation toolkit*, Nucl. Instrum. Meth. A **506**, 250 (2003).

[92] T. Böhlen *et al.*, *The FLUKA Code: Developments and Challenges for High Energy and Medical Applications*, Nuclear Data Sheets **120**, 211 (2014).

[93] A. J. Koning, S. Hilaire, and M. C. Duijvestijn, *TALYS-1.0*, Proceedings of the International Conference on Nuclear Data for Science and Technology - ND2007, Nice, France, 2008, EDP Sciences, pp. 211–214.

[94] C. Green *et al.*, *The art framework*, Journal of Physics: Conference Series **396**, 022020 (2012).

[95] M. Szydagis *et al.*, *NEST: a comprehensive model for scintillation yield in liquid xenon*, Journal of Instrumentation **6**, P10002 (2011), arXiv:1106.1613.

[96] T. Doke *et al.*, *LET dependence of scintillation yields in liquid argon*, Nucl. Instrum. Meth. A **269**, 291 (1988).

[97] P. Sorensen and C. E. Dahl, *Nuclear recoil energy scale in liquid xenon with application to the direct detection of dark matter*, Phys. Rev. D **83**, 063501 (2011), arXiv:1101.6080.

[98] V. Gehman *et al.*, *Fluorescence efficiency and visible re-emission spectrum of tetraphenyl butadiene films at extreme ultraviolet wavelengths*, Nucl. Instrum. Meth. A **654**, 116 (2011).

[99] J. A. N. Emily Grace, *Index of refraction, Rayleigh scattering length, and Sellmeier coefficients in solid and liquid argon and xenon*, arXiv:1502.04213.

[100] B. J. P. Jones *et al.*, *A measurement of the absorption of liquid argon scintillation light by dissolved nitrogen at the part-per-million level*, Journal of Instrumentation **8**, P07011 (2013), arXiv:1306.4605.

[101] R. Acciarri *et al.*, *Oxygen contamination in liquid Argon: combined effects on ionization electron charge and scintillation light*, Journal of Instrumentation **5**, P05003 (2010), arXiv:0804.1222.

[102] G. Seidel, R. Lanou, and W. Yao, *Rayleigh scattering in rare-gas liquids*, Nuclear Instruments and Methods in Physics Research Section A: Accelerators, Spectrometers, Detectors and Associated Equipment **489**, 189 (2002), arXiv:hep-ex/0111054.

[103] A. Neumeier *et al.*, *Attenuation measurements of vacuum ultraviolet light in liquid argon revisited*, Nuclear Instruments and Methods in Physics Research Section A: Accelerators, Spectrometers, Detectors and Associated Equipment **800**, 70 (2015), arXiv:1511.07726.

[104] J. Lindhard *et al.*, Mat. Fys. Medd. K. Dan. Vidensk. Selsk. **33** (1963).

[105] E. Aprile and T. Doke, *Liquid xenon detectors for particle physics and astrophysics*, Rev. Mod. Phys. **82**, 2053 (2010), arXiv:0910.4956.

[106] G. Keefer and A. Piepke, *Beta spectra for* ^{39}Ar, ^{85}Kr *and* ^{210}Bi.

[107] D. Gastler *et al.*, *Measurement of scintillation efficiency for nuclear recoils in liquid argon*, Phys. Rev. C **85**, 065811 (2012), arXiv:1004.0373.

[108] C. Regenfus *et al.*, *Study of nuclear recoils in liquid argon with monoenergetic neutrons*, Journal of Physics: Conference Series **375**, 012019 (2012), arXiv:1203.0849.

[109] D.-M. Mei, Z.-B. Yin, L. Stonehill, and A. Hime, *A model of nuclear recoil scintillation efficiency in noble liquids*, Astroparticle Physics **30**, 12 (2008), arXiv:0712.2470.

[110] J. B. Birks, *Scintillations from Organic Crystals: Specific Fluorescence and Relative Response to Different Radiations*, Proceedings of the Physical Society. Section A **64**, 874 (1951).

[111] G. Bellini *et al.*, **(The Borexino Collaboration)**, *Final results of Borexino Phase-I on low-energy solar neutrino spectroscopy*, Phys. Rev. D **89**, 112007 (2014), arXiv:1308.0443.

[112] V. Tretyak, *Semi-empirical calculation of quenching factors for ions in scintillators*, Astroparticle Physics **33**, 40 (2010), arXiv:0911.3041.

[113] A. Empl, E. V. Hungerford, R. Jasim, and P. Mosteiro, *A Fluka Study of Underground Cosmogenic Neutron Production*, JCAP **1408**, 064 (2014), arXiv:1406.6081.

[114] D. M. Mei, C. Zhang, and A. Hime, *Evaluation of (alpha,n) Induced Neutrons as a Background for Dark Matter Experiments*, Nucl. Instrum. Meth. **A606**, 651 (2009), arXiv:0812.4307.

[115] A. Koning and D. Rochman, *Modern Nuclear Data Evaluation with the TALYS Code System*, Nuclear Data Sheets **113**, 2841 (2012).

[116] J. F. Ziegler, M. Ziegler, and J. Biersack, *SRIM – The stopping and range of ions in matter (2010)*, Nucl. Instrum. Meth. B **268**, 1818 (2010), 19th International Conference on Ion Beam Analysis.

[117] R. Heaton *et al.*, , Nucl. Geophys. V **4**, 499 (1990).

[118] E. Shores, *Data updates for the SOURCES-4A computer code*, Nucl. Instrum. Meth. B **179**, 78 (2001).

[119] K. Palladino, *Comparison of Radiogenic Neutron Background Calculations*.

[120] W. H. Lippincott *et al.*, *Scintillation time dependence and pulse shape discrimination in liquid argon*, Phys. Rev. C **78**, 035801 (2008).

[121] M. G. Boulay *et al.*, **(The DEAP Collaboration)**, *Measurement of the scintillation time spectra and pulse-shape discrimination of low-energy beta and nuclear recoils in liquid argon with DEAP-1*, (2009), arXiv:0904.2930.

[122] D. V. Hinkley, *On the Ratio of Two Correlated Normal Random Variables*, Biometrika **56**, 635 (1969).

[123] *https://www.fbk.eu/it*.

[124] J. B. Albert *et al.*, **(The EXO-200 Collaboration)**, *Investigation of radioactivity-induced backgrounds in EXO-200*, Phys. Rev. **C92**, 015503 (2015), arXiv:1503.06241.

[125] A. Aguilar-Arevalo *et al.*, **(The DAMIC Collaboration)**, *Measurement of radioactive contamination in the high-resistivity silicon CCDs of the DAMIC experiment*, Journal of Instrumentation **10**, P08014 (2015), arXiv:1506.02562.

[126] D. Malczewski, J. Kisiel, and J. Dorda, *Gamma background measurements in the Gran Sasso National Laboratory*, Journal of Radioanalytical and Nuclear Chemistry **295**, 749 (2013).

[127] G. Bellini *et al.*, **(The Borexino Collaboration)**, *Cosmic-muon flux and annual modulation in Borexino at 3800 m water-equivalent depth*, Journal of Cosmology and Astroparticle Physics **2012**, 015 (2012), arXiv:1202.6403.

[128] M. Asplund, N. Grevesse, A. J. Sauval, and P. Scott, *The Chemical Composition of the Sun*, Annual Review of Astronomy and Astrophysics **47**, 481 (2009).

[129] N. Grevesse and A. J. Sauval, *Standard Solar Composition* (Springer Netherlands, Dordrecht, 1998), pp. 161–174.

[130] D. Franco *et al.*, *Solar neutrino detection in a large volume double-phase liquid argon experiment*, Journal of Cosmology and Astroparticle Physics **2016**, 017 (2016), arXiv:1510.04196.

[131] S. Davini *et al.*, *CNO and pep solar neutrino measurements and perspectives in Borexino*, Journal of Physics: Conference Series **675**, 012040 (2016).

Appendix A

The TALYS Program and Some Differential Neutron Energy Spectra

This is one example of input files used in order to obtain neutron spectra:

```
projectile a
ejectiles n
element Fe
mass 58
energy 8
outspectra y
filespectrum n
```

The program is asked to produce the neutron energy spectrum, given in mbarn, for one α of 8.0 MeV in ^{58}Fe. In the following calculations, only neutrons with energy higher than 0.1 MeV are considered.

The command

```
mass 0
```

allows the user to automatically get the neutron energy spectrum for an element with natural isotopic composition. This shortcut should incorporate nuclear structure effects and the result does not always correspond to the weighted sum of spectra for different isotopes. In principle, the first approach is the most exact.[1]

The command

```
elwidth 0.2
```

allows to set the width to 0.2.

In the following figures the spectra computed with the software. When available, the comparison with [114].

[1] As suggested by TALYS people.

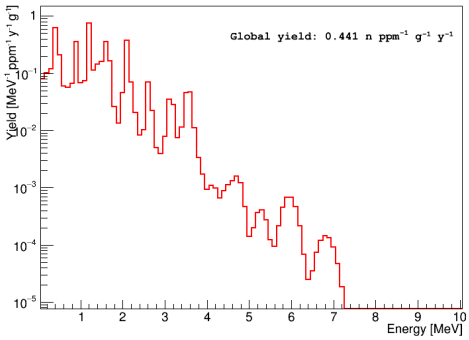

(a) ^{238}U chain, Stainless Steel

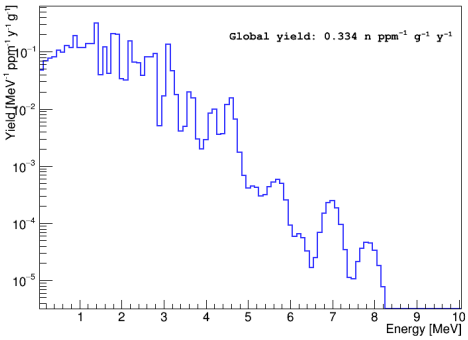

(b) ^{232}Th chain, Stainless Steel

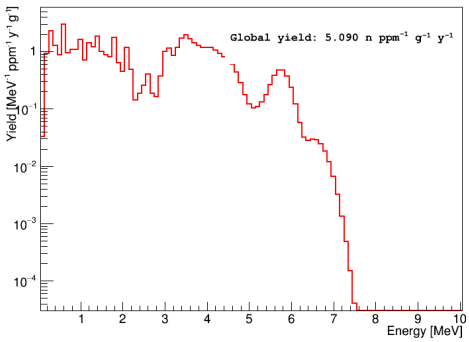

(c) ^{238}U chain, Fused silica

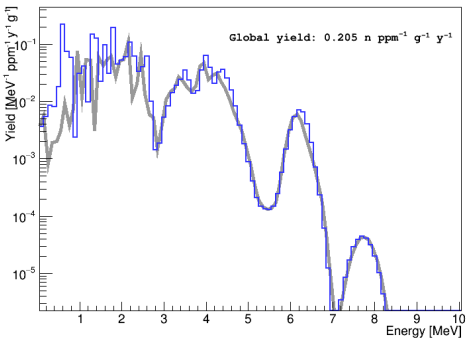

(d) ^{232}Th chain, Fused silica

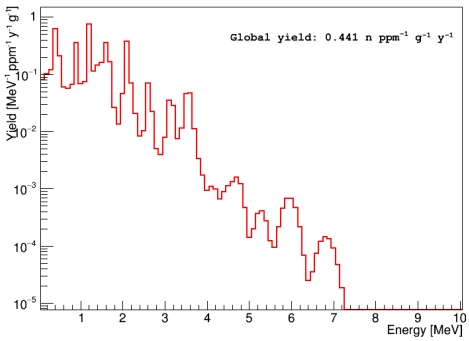

(e) ^{238}U chain, Borosilicate glass

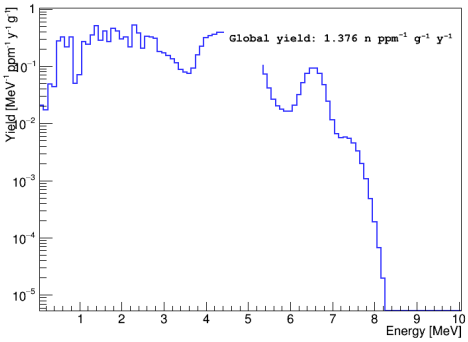

(f) ^{232}Th chain, Borosilicate glass

Fig. A.1 Differential (α, n) neutron energy spectra for some materials. See the text for more details.

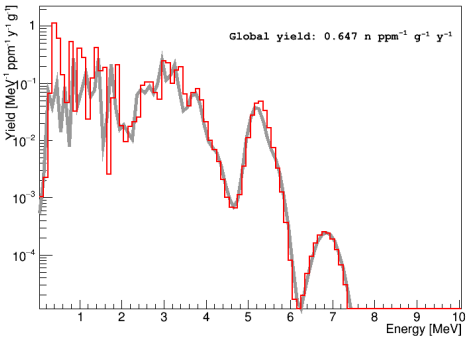

(a) ^{238}U chain, Ceramic

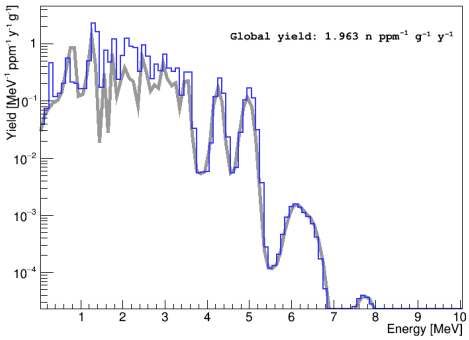

(b) ^{232}Th chain, Ceramic

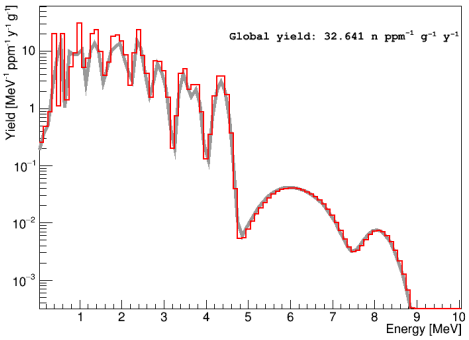

(c) ^{238}U chain, Copper

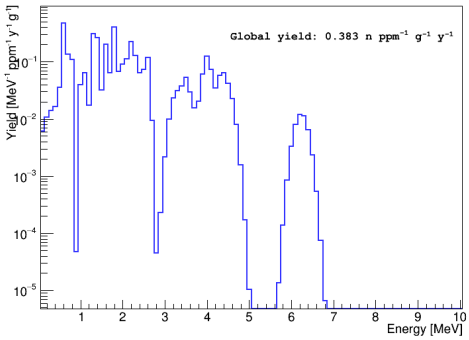

(d) ^{232}Th chain, Copper

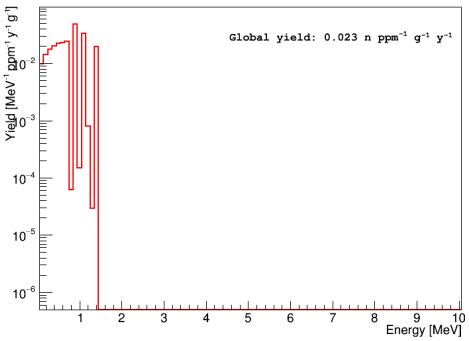

(e) ^{238}U chain, Silicon

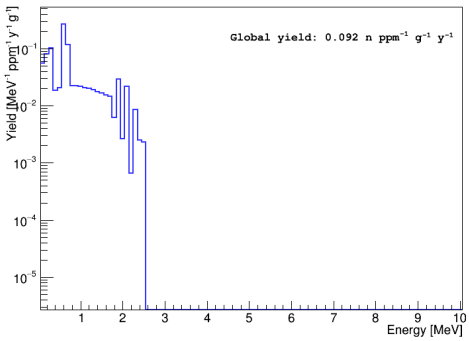

(f) ^{232}Th chain, Silicon

Fig. A.2 Differential (α, n) neutron energy spectra for some materials. See the text for more details.

Appendix B

A Study of Echoes

This is a comparison between data and a simple toy MC. The only observable in real data is the time difference between two (consecutive or not) pulses. Both S1 and S2 can induce photo-ionization from the cathode. This results in an additional pulse separated by 376 μs from the pulse which triggered it.

The acquisition window is roughly 1.5 times the maximum drift time. This means that

- if S1 has an echo, it will happen at tdrift = 376 μs.
- If S2 has an echo, it will be recorded only if $T_{S2} - T_{S1} + 376 <$ acquisition window.

We should also consider the probability of multi-sited events: the first pulse of the waveform is always the S1 triggering the TPC; the second pulse is always an S2; the thrid pulse might be:

- S1-echo ($T_{S3} - T_{S1} = 376$ μs, $T_{S3} - T_{S2} < 376$ μs)
- S2-echo ($T_{S3} - T_{S1} > 376$ μs, $T_{S3} - T_{S2} = 376$ μs)
- another valid S2 ($T_{S3} - T_{S1} < 376$ μs, $T_{S3} - T_{S2} < 376$ μs).

Then the waveform can have a number of pulses equal to double the number of interactions + 2 (if all of them happens at the top of the TPC, otherwise their echoes will not enter in the acquisition window).

I reproduced this behaviour with a toy MC. I generate events sampling the lifetime from the true lifetime in data (to account for the possible pileup of ^{39}Ar events). I sample an S2 time uniformly in the [0,376] μs window (corresponding to a uniform distribution in the TPC volume) and assign some fixed probability to the S1 and to the S2 pulses to generate an echo. These probabilities, roughly tuned in order to reproduce the data behaviour, are 15% for S1 and 60% for S2.

In case an echo is produced, a new pulse is created with time $t_{echoSX} = t|SX + 376$. I build a time ordered vector of pulse arrival times. I then simulate the acquisition window (570 μs for the considered dataset) and the inhibit time (780 μs) and then the number of pulses for each window. I compare with data (black)

- in the case where there are only single-sited ER's (red)
- in the case where in the 3.5% of the cases the interaction is multi-site with 2 ionization signals.

In the next page, some of observables are compared for the three cases, namely:

a) The time difference between the second and the first pulse for waveforms with only two pulses. The step at $\sim$ 200 μs is due to the high probability of an S2 to trigger an echo. However, the S2 is recorded only if $t_{S2} + 376 < 570$ μs.

b) The time difference between the third and the first pulse for events with 3 pulses. The peak at 376 μs corresponds to the echoes of S1, while it is evident how the addition of multi-sited events allows to better reproduce the shape of the data distribution.

c) The time difference between the third and the second pulse in waveforms with 3 pulses. The peak corresponds at the echoes of S2.

d) The time difference between the forth and the second pulse in waveforms with 4 pulses.

e) The time difference between the second and the first pulse in waveforms with 3 pulses.

f) The measured distribution of event lifetime (the time difference between two consecutive events). There is no significant difference between the data and the simulation.

g) The distribution of the number of pulses found in a waveform. The adopted assumptions do not allow to fully reproduce the behavior observed in data, but mean number of pulses is higher in the simulation which includes multi-sited events.

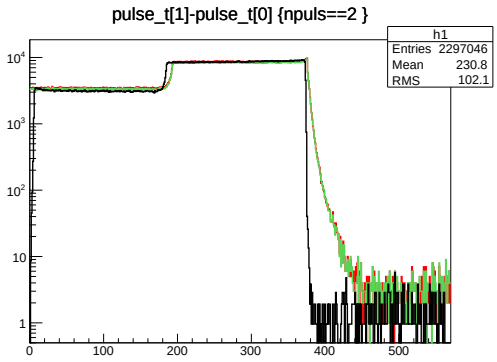
pulse_t[1]-pulse_t[0] {npuls==2 }
h1
Entries 2297046
Mean 230.8
RMS 102.1

(a)

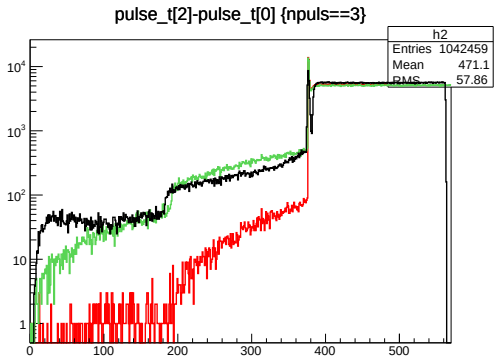
pulse_t[2]-pulse_t[0] {npuls==3}
h2
Entries 1042459
Mean 471.1
RMS 57.86

(b)

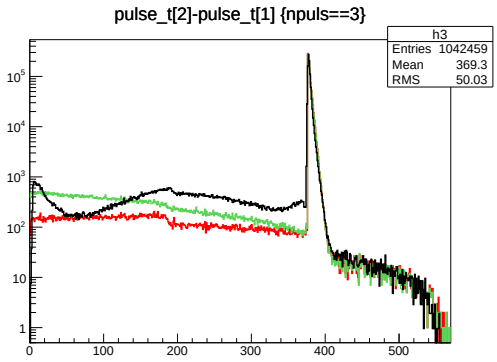
pulse_t[2]-pulse_t[1] {npuls==3}
h3
Entries 1042459
Mean 369.3
RMS 50.03

(c)

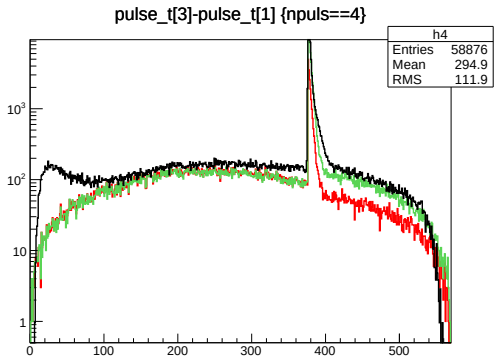
pulse_t[3]-pulse_t[1] {npuls==4}
h4
Entries 58876
Mean 294.9
RMS 111.9

(d)

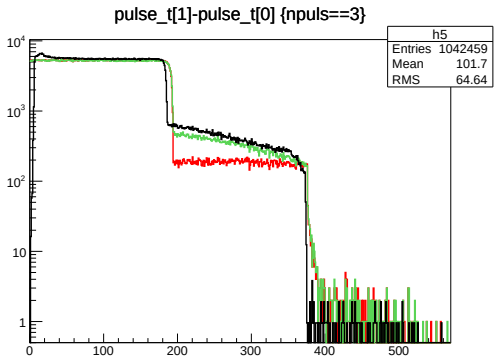
pulse_t[1]-pulse_t[0] {npuls==3}
h5
Entries 1042459
Mean 101.7
RMS 64.64

(e)

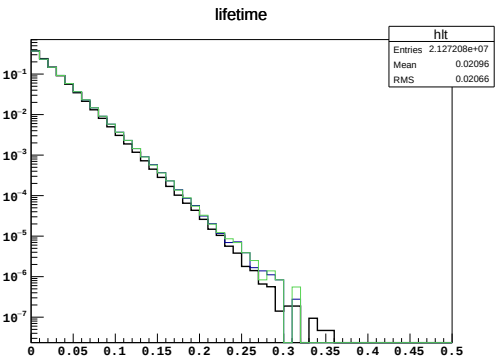
lifetime
hlt
Entries 2.127208e+07
Mean 0.02096
RMS 0.02066

(f)

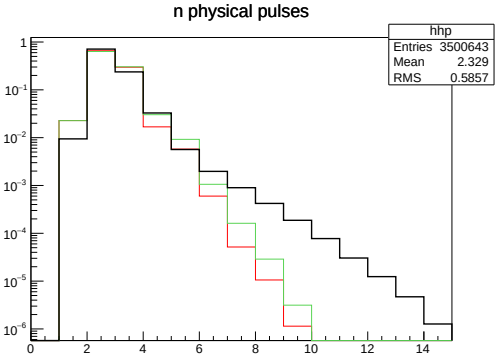
n physical pulses
hhp
Entries 3500643
Mean 2.329
RMS 0.5857

(g)

Appendix C

Plots of the real data fitted f90 distributions

In the following plots I compare the f_{90} distributions for AAr data and the result of the toyMC discussed in Chapter 5. The data are binned in 1 pe slices of S1. The output of the toyMC is truncated at the distribution peak and the χ^2 is computed only for the right tail of the distributions.

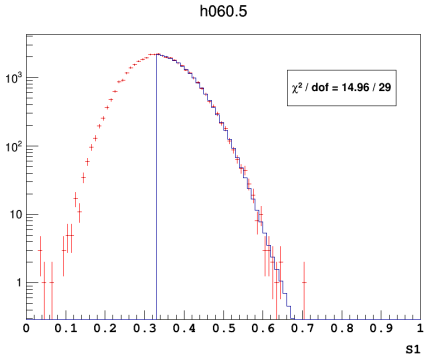
h060.5
χ² / dof = 14.96 / 29
S1

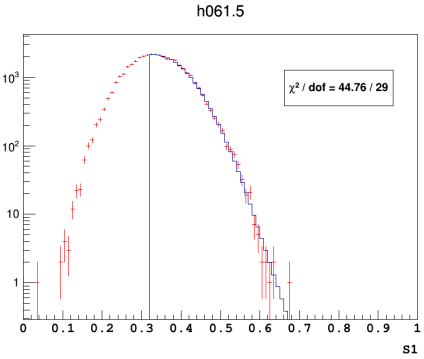
h061.5
χ² / dof = 44.76 / 29
S1

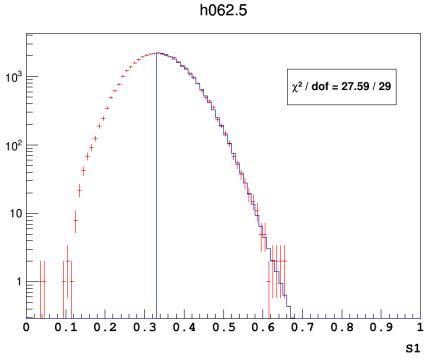
h062.5
χ² / dof = 27.59 / 29
S1

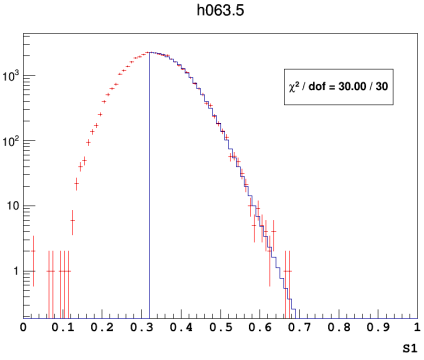
h063.5
χ² / dof = 30.00 / 30
S1

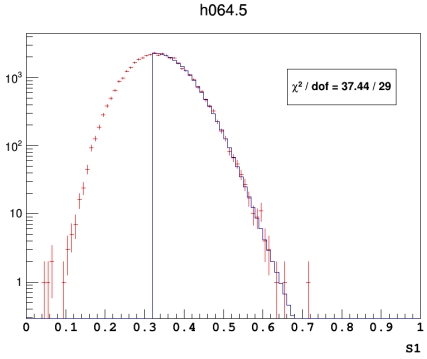
h064.5
χ² / dof = 37.44 / 29
S1

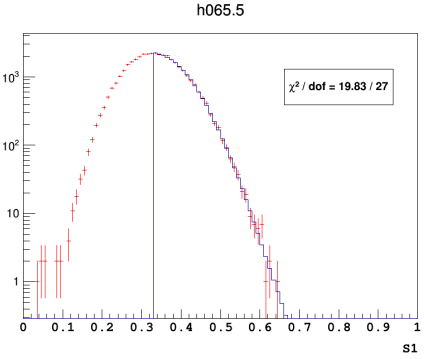
h065.5
χ² / dof = 19.83 / 27
S1

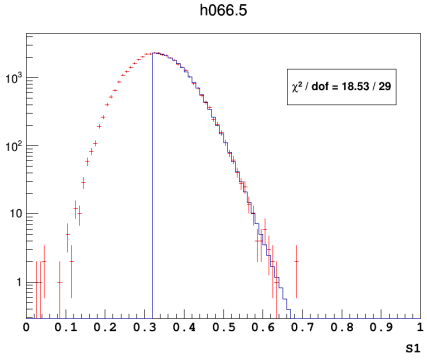
h066.5
χ² / dof = 18.53 / 29
S1

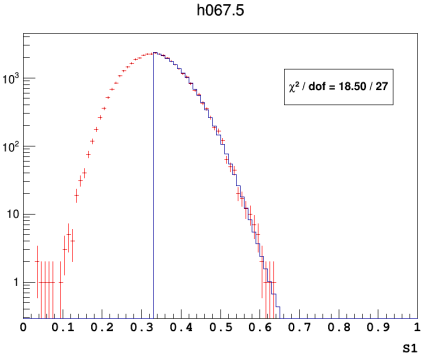
h067.5
χ² / dof = 18.50 / 27
S1

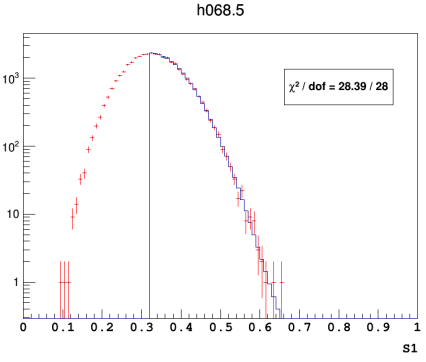
h068.5
χ² / dof = 28.39 / 28
S1

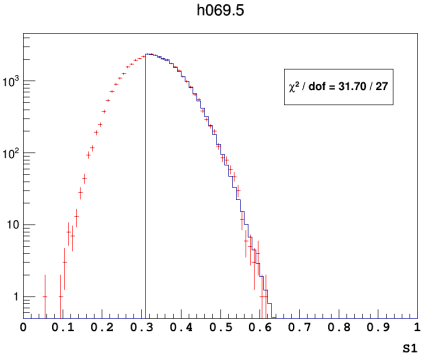
h069.5
χ² / dof = 31.70 / 27
S1

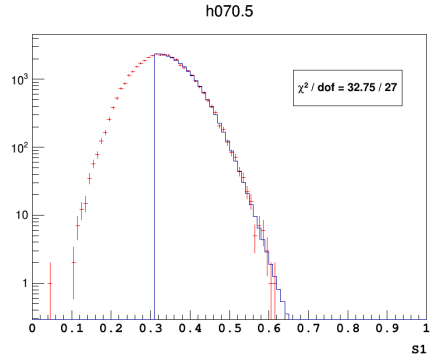
h070.5
χ² / dof = 32.75 / 27
S1

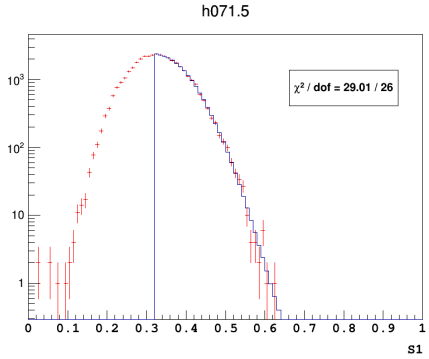
h071.5
χ² / dof = 29.01 / 26
S1

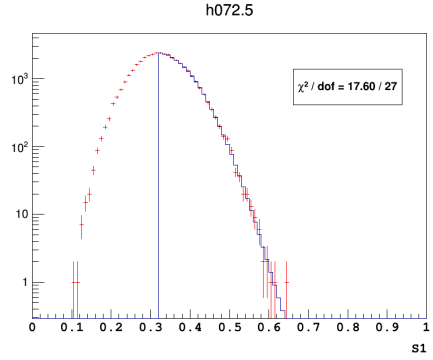
h072.5
χ² / dof = 17.60 / 27
S1

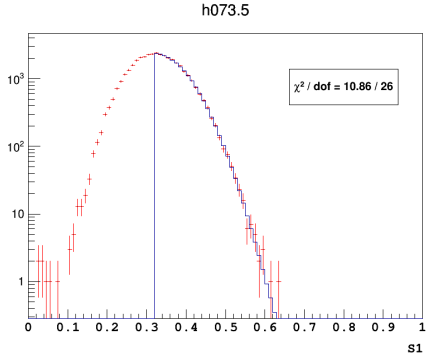
h073.5
χ² / dof = 10.86 / 26
S1

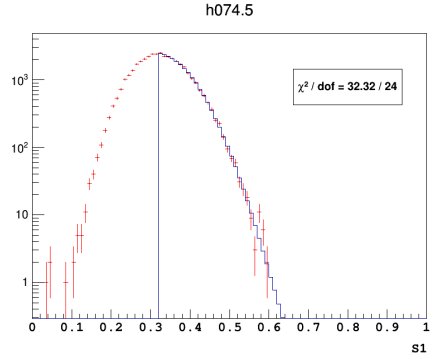
h074.5
χ² / dof = 32.32 / 24
S1

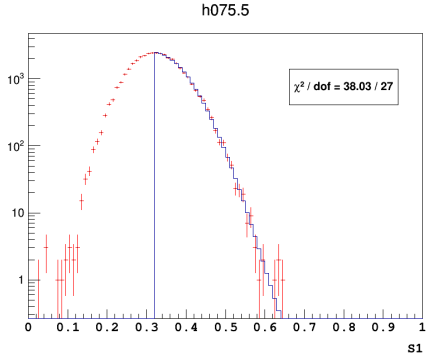
h075.5
χ² / dof = 38.03 / 27
S1

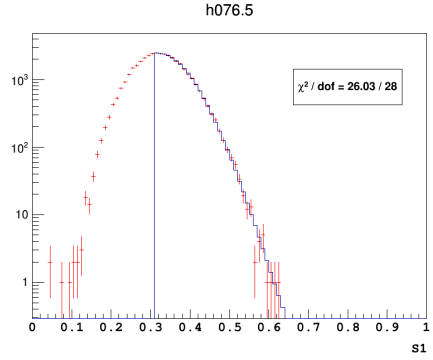
h076.5
χ² / dof = 26.03 / 28
S1

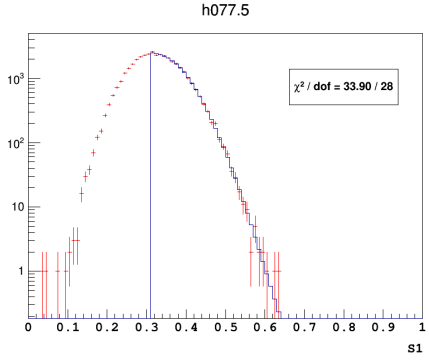
h077.5
χ² / dof = 33.90 / 28
S1

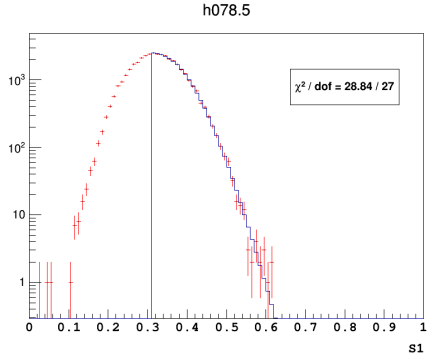
h078.5
χ² / dof = 28.84 / 27
S1

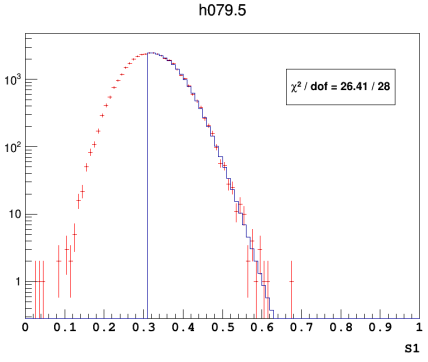
h079.5
χ² / dof = 26.41 / 28
S1

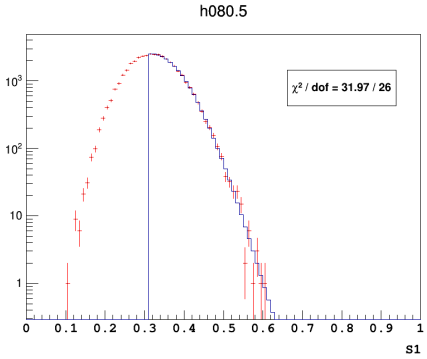
h080.5
χ² / dof = 31.97 / 26
S1

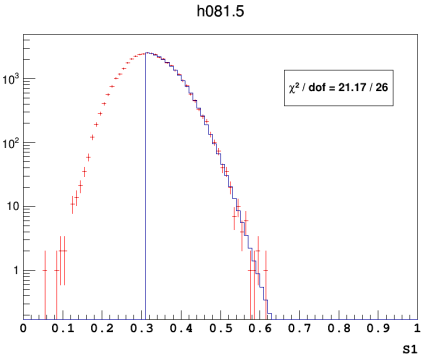
h081.5
χ² / dof = 21.17 / 26
S1

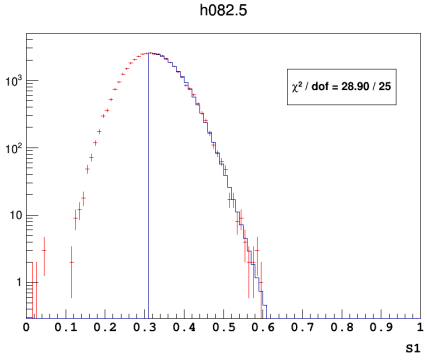
h082.5
χ² / dof = 28.90 / 25
S1

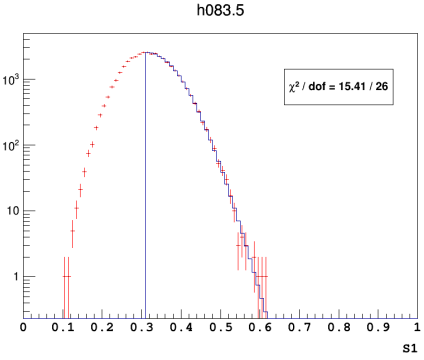
h083.5
χ² / dof = 15.41 / 26
S1

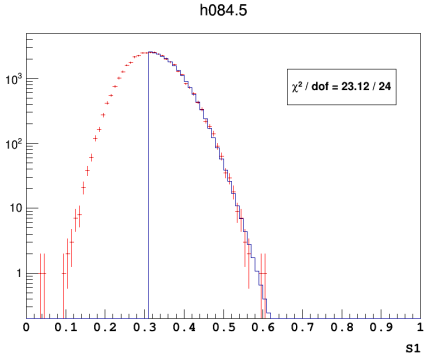
h084.5
χ² / dof = 23.12 / 24
S1

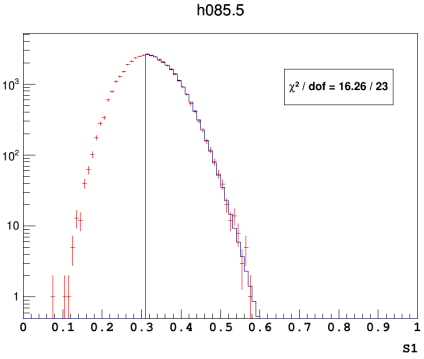
h085.5
χ² / dof = 16.26 / 23
S1

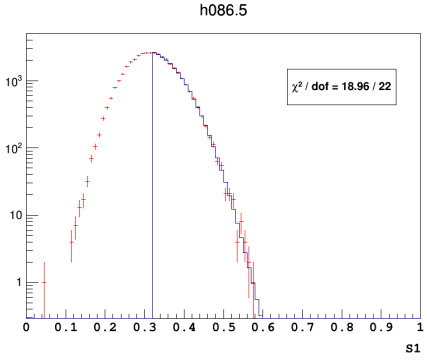
h086.5
χ² / dof = 18.96 / 22
S1

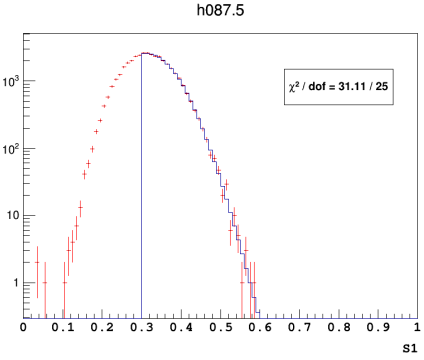
h087.5
χ² / dof = 31.11 / 25
S1

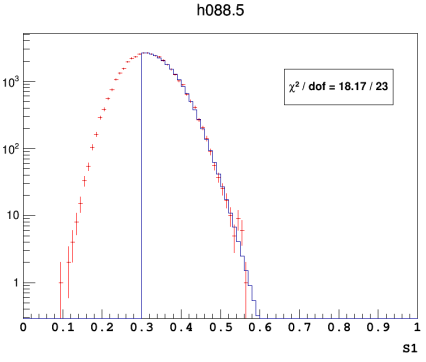
h088.5
χ² / dof = 18.17 / 23
S1

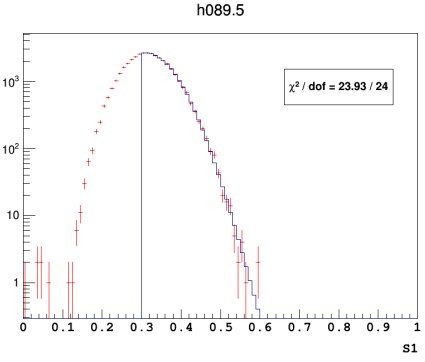
h089.5
χ² / dof = 23.93 / 24
S1

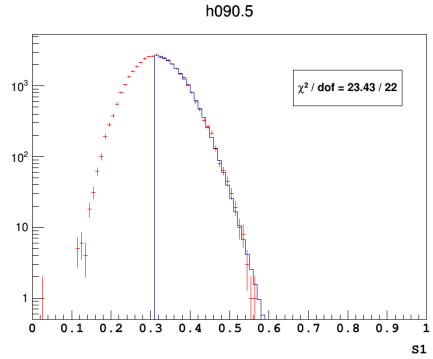
h090.5
χ² / dof = 23.43 / 22
S1

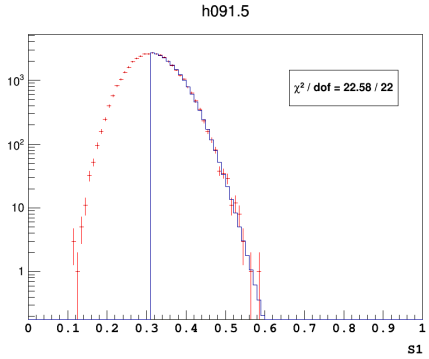
h091.5
χ² / dof = 22.58 / 22
S1

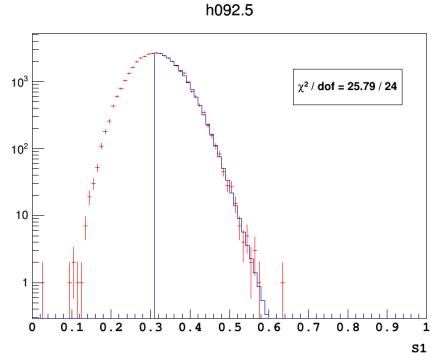
h092.5
χ² / dof = 25.79 / 24
S1

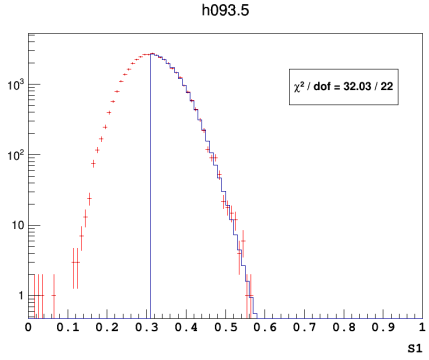
h093.5
χ² / dof = 32.03 / 22
S1

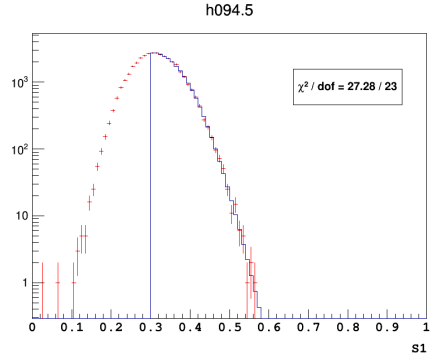
h094.5
χ² / dof = 27.28 / 23
S1

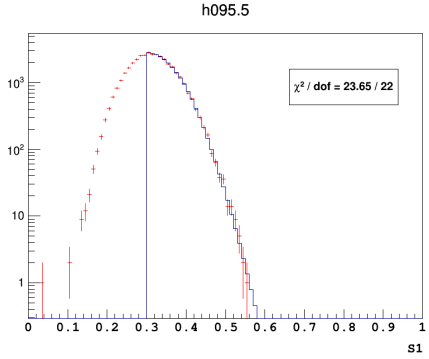
h095.5
χ² / dof = 23.65 / 22
S1

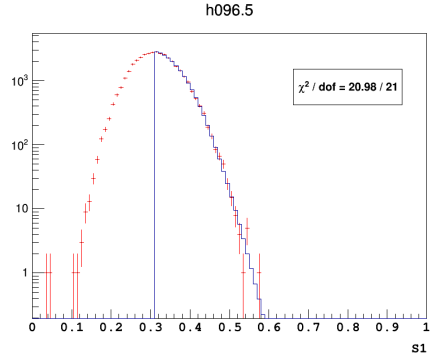
h096.5
χ² / dof = 20.98 / 21
S1

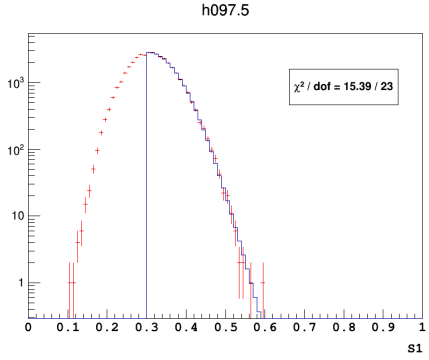
h097.5
χ² / dof = 15.39 / 23
S1

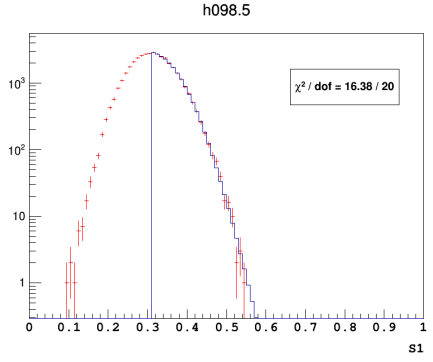
h098.5
χ² / dof = 16.38 / 20
S1

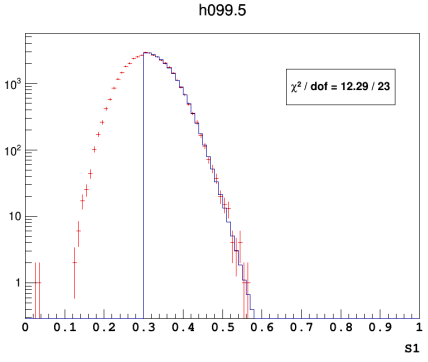
h099.5
χ² / dof = 12.29 / 23
S1

List of figures